

DISSERTATION

Neutron interferometric investigation of phase shifts arising from dynamical diffraction theory

ausgeführt zum Zwecke der Erlangung des akademischen Grades eines
Doktors der technischen Wissenschaften unter der Leitung von

Univ.-Doz. Dipl.-Ing. Dr. Martin Suda
mitwirkender Assistent: Ass.-Prof. Dipl.-Ing. Dr. Michael Zawisky
E141 - Atominstitut

eingereicht an der Technischen Universität Wien
Fakultät für Physik

von

Dipl.-Ing. Josef Springer

Matrikelnummer: 9755472
Siedlungsstrasse 32
A – 4150 Rohrbach

Wien, am 6. Dezember 2009

Kurzfassung

In dieser Arbeit wird der Phasenschub eines nahe einer Braggbedingung transmittierten Neutronenstrahls untersucht. Dieser Fall wird durch die dynamische Beugungstheorie beschrieben und hat an Interesse gewonnen, seit er zur Präzisionsmessung der kohärenten atomaren Streulänge vorgeschlagen wurde.

Zuerst werden die prinzipiellen Eigenschaften dieses Phasenschubes diskutiert. Dabei findet man vor allem eine sehr hohe Winkelsensitivität sowie eine bemerkenswerte Feinstruktur aufgrund von Pendellösungssoszillationen.

Weiters wird der Phasenschub in Hinblick auf eine Messung mit Hilfe eines Neutroneninterferometers diskutiert. Dabei werden vor allem die einhergehenden Herausforderungen in Zusammenhang mit den Kohärenzeigenschaften diskutiert. Innerhalb dieser Arbeit wurde darauf aufbauend ein geeignetes Sechsplatteninterferometer hergestellt und erfolgreich getestet. Dieses Interferometer stellt das momentan größte Perfektkristallinterferometer dar. Zusätzlich können als neue Besonderheit bis zu vier Reflexe im Bereich von 2.72\AA bis in den Subangströmbereich verwendet werden.

Da die für die Phasenmessungen nötigen Strahlablenkungen mit Hilfe von Prismen erfolgen, wurde der Einsatz von Prismen und stark brechenden Materialien in Bezug auf die speziellen Kohärenzanforderungen der Neutroneninterferometrie untersucht.

Schließlich wurden Messungen des Phasenschubs rund um die Braggbedingung für zwei Reflexe durchgeführt und mit numerischen Berechnungen, die die Strahldivergenz berücksichtigen, verglichen.

Abseits dieses Phasenschubes erfolgte zudem eine Messung der vertikalen Kohärenzfunktion bei drei Reflexen.

Abstract

This work investigates the phase shift of a neutron beam transmitted through a perfect crystal under near Bragg condition. This case is described by dynamical diffraction theory. The interest in this feature arose recently due to proposals suggesting a precision measurement of the coherent atomic scattering length.

First the principal properties of this phase shift are investigated. One finds an extreme angular sensitivity and a remarkable finestructure due to Pendellösung oscillations.

This phase shift is then considered in view of a neutron interferometric measurement. Possible setups and related challenges, especially concerning the coherence properties, are discussed. Within this work a suitable six-plate neutron interferometer has been designed, built and successfully tested. This interferometer constitutes the actually largest perfect crystal interferometer. Another new feature is the use of up to four harmonics ranging from 2.72\AA to the sub-angstrom regime.

As prisms are required for the phase measurements, the use of prisms and suitable materials is discussed with respect to the special coherence requirements in neutron interferometry.

As final part measurements of the phase shift around the Bragg condition are presented for two harmonics and compared with numerical calculations taking a divergent beam into account.

Beyond the topic of the phase shift by dynamical diffraction, the vertical coherence function has been measured for three harmonics.

Contents

1	Preface	5
2	Phase shifts by Dynamical diffraction	9
2.1	Dynamical diffraction theory	9
2.1.1	One-beam approximation	11
2.1.2	Two-beam approximation	12
2.2	Phase shift due to Laue transmission	15
2.2.1	General properties of the phase function	20
2.2.2	Pendellösung structures of the Laue phase	24
2.2.3	The asymmetric case	34
2.3	The limits of Dynamical diffraction theory	37
3	Laue phase and interferometry	43
3.1	Review of Related Experiments	43
3.2	Experimental Challenges	45
3.2.1	Defocusing and beam spreading	46
3.2.2	Phase averaging by beam divergence	51
3.2.3	Wavelength distribution	55
3.2.4	Asymmetric intensities	56
3.2.5	Crystal alignment and the prism method	57
4	Numerical interferometer calculation	61
4.1	Spherical wave model	62
4.2	One crystal plate in one beam path	66
4.3	One crystal plate in each beam path	70
4.3.1	Defocused arrangement of two crystal plates	77
5	Interferometer	81
5.1	Interferometer preparation	81
5.1.1	Planning of the interferometer	81

5.1.2	Crystal selection and orientation	84
5.1.3	Crystal machining and fine grinding	86
5.1.4	Etching	88
5.1.5	Final geometric measurements	90
5.2	Interferometer testing	91
5.2.1	Rocking curve	92
5.2.2	Visibility measurements	93
6	Prisms in neutron interferometry	107
6.1	Materials	109
6.1.1	Material candidates	110
6.1.2	Testing materials	112
6.2	Prism design and alignment	120
6.2.1	Preparation of silicon prisms	123
7	Laue phase measurement	127
7.1	Experiment	127
7.1.1	Idea of the experiment	127
7.1.2	Experimental devices	128
7.2	Results	132
7.2.1	Visibility	132
7.2.2	Phase shift	134
7.2.3	Studying the beam divergence	137
7.2.4	Shift of phase and visibility curves	138
7.2.5	An approach beyond Bragg	142
7.3	Outlook: Precision measurements?	145
7.3.1	Future approaches	149
8	Vertical coherence function	151
8.1	Calculation of the spatial shift	151
8.2	Vertical momentum distribution	155
8.3	Outlook	160
A	Laue phase: special cases	163
B	Interferometer cutting drafts	169
C	Rocking curves	171
D	Reflectivity of Laue-USANS	175

E	Position sensitive detector	177
E.0.1	General features	177
E.0.2	Characterization of the resolution	178

Chapter 1

Preface

Laue diffraction on a perfect crystal slab is the basis for perfect crystal neutron interferometry as it coherently splits the incoming neutron wave into a transmitted and a reflected beam. Both wave components can be calculated by dynamical diffraction theory [1, 2, 3, 4]. A special feature is the strong angular dependence of the refracted and transmitted intensities. Furthermore a distinct pattern known as Pendellösung oscillations [5, 6] can be observed.

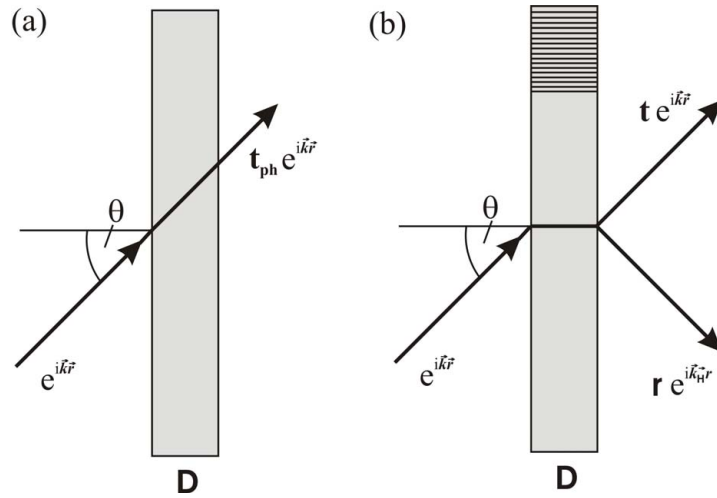


Figure 1.1: Two cases for a neutron beam incident on a medium: (a) far off a Bragg condition only the phase of the wave function changes, whereas in the vicinity of a Bragg condition (b) a transmitted and refracted beam can be observed.

Another important case in neutron optics deals with the beam refraction for non-crystalline media or for crystals far off a Bragg condition. Usually one characterizes such media similar to light optics by an index of refraction. Here the

phase and/or direction of the neutron beam changes, whereas the intensity usually doesn't change¹. There are many applications to neutron optics such as prisms, lenses and phase shifters in interferometry.

In this work we want to investigate a perfect crystal close to a Bragg condition as a "phase shifter", that is to say we are interested in the phase of the transmitted beam. Although this has been always implicit part of the solutions of dynamical diffraction theory, the focus on it shall bring new perspectives. Interest on the explicit phase of the transmitted beam arose via a proposal to measure the neutron-electron scattering length by it [7, 8]. Just recently an even more ambitious suggestion deals with the investigation of non-Newtonian gravity behavior at short distances [9]. Interestingly the main focus so far is on precision measurements, hence on rather tiny effects. However despite some related experiments [10, 11] so far no quantitative measurement and principal investigation of the phase shift has been addressed. Besides the interest in connection with precision measurements of fundamental interactions the extreme angular sensitivity of the phase shift should be noted. This is comparable to the strong angle amplification effect inside a perfect crystal [1]. Therefore this phase shift might find its interest beyond the stated applications, all the more as the same concept is applicable to X-ray physics. From a technical point of view the measurement of such phase shifts involves either the rotation of perfect crystal slabs or beam deflections inside a neutron interferometer, both with an accuracy below the arc second range. Studying such configurations therefore gives also valuable information on the sensitivity of possible future split perfect crystal neutron interferometers which have so far only been realized for X-rays [12, 13, 14].

Moreover phase shifts by dynamical diffraction and related coherence properties might be considered when the neutron beam is diffracted inside a neutron interferometer [15, 16]. Especially the discrepancy concerning the measurement of a confinement induced neutron phase [15, 16] might be analyzed in this respect.

Outline

This thesis is structured in the following way:

Chapter two investigates the phase shift of the transmitted beam theoretically for the plane wave solutions.

Chapter three discusses the phase shift in the context of neutron interferometry, related challenges and possible setups.

Chapter four analyzes several setups by a numerical model, whereby interferometric configurations are simulated by spherical wave theory.

¹Assuming negligible absorption.

Chapter five describes the fabrication and testing of an interferometer especially designed for these experiments. A new feature is here the use of up to four harmonics without changing the beam geometry.

Chapter six deals with prisms in neutron interferometry, where former experiences have been rather limited. Prisms are needed for beam deflection in the discussed experiments.

Chapter seven discusses the concrete experimental setup and the results. Moreover an outlook to future applications is given.

Chapter eight deals with another application of prisms in neutron interferometry: the measurement of the vertical coherence function.

Acknowledgment

First of all I want to thank my thesis advisor Martin Suda for his support, the interest on the subject and especially the time he spent for many discussions. Michael Zawisky gave me the opportunity to participate in his project and guided me through the details of interferometer preparation and experimental neutron interferometry. Dietmar Petrascheck made me aware of the possibility to work in neutron interferometry and gave final input on theoretical aspects. I'm also grateful to Helmut Rauch, Gerald Badurek and Hartmut Abele who gave us the possibility to carry out our experiments at the ILL.

From my colleagues I especially want to mention Hartmut Lemmel, who did not only let me use his program ifsim for the numerical calculations but also participated by many useful discussions and helped during experiments at the ILL. In the beginning of the project Robert Farthofer participated as diploma student and it was a pleasure for me to work together with him.

U. Kuetgens, D. Schulze and J. Hauße from the PTB Braunschweig as well as H. Weiss, W. Eisele and R. Rozenich from G. Rauch company helped with the interferometer preparation and the geometric measurements.

Herbert Hartmann and Erich Tischler helped with our prism holding device. Eva Haberl, Brigitta Buchberger, Friederike Cerny and Tamara Jurschitsch gave support in administrative questions.

In general I want to thank my colleagues: Katharina Durstberger-Rennhofer, Eva Dyrnjaja, Stefan Filipp, Fareeha Hameed, Yuji Hasegawa, Erwin Jericha, Tobias Jenke, Sam Karimzadeh, Rustam Khan, Jürgen Klepp, Rudi Loidl, Simon Mayer, Stephan Sponar, Georg Sulyok, Halit Tatlisu, Mario Villa and Babak Zamani.

The thesis was supported by the Austrian Science Fund FWF, project P18460-N16.

Chapter 2

Phase shifts by Dynamical diffraction

2.1 Dynamical diffraction theory

We are here considering a neutron wave with wave vector \mathbf{k} incident on a perfect crystal under near-Bragg orientation (Fig. 1.1 (b)). This case is described by dynamical diffraction theory [1, 2, 3, 4]. Here a short summary of the most important aspects together with the used notations shall be given.

The neutron wave function $\psi(\mathbf{r})$ inside the crystal is calculated via solving the stationary Schrödinger equation for the crystal potential $V(\mathbf{r})$

$$\left(-\frac{\hbar^2}{2m_n}\Delta + V(\mathbf{r})\right)\psi(\mathbf{r}) = E\psi(\mathbf{r}) \quad (2.1)$$

Due to the periodicity of the potential this equation can be transformed into reciprocal space using a Bloch ansatz

$$\psi(\mathbf{r}) = e^{i\mathbf{K}\mathbf{r}} \sum_{\mathbf{H}} u_{\mathbf{H}} e^{i\mathbf{H}\mathbf{r}} \quad (2.2)$$

where \mathbf{K} is the wave vector inside the crystal and \mathbf{H} are the reciprocal lattice vectors. Thereby one obtains an infinite set of coupled equations for the amplitudes $u_{\mathbf{H}}$

$$\left(\frac{\hbar^2}{2m_n}|\mathbf{K} + \mathbf{H}|^2 - E\right)u_{\mathbf{H}} = -\sum_{\mathbf{H}'} V_{\mathbf{H}'-\mathbf{H}} u_{\mathbf{H}'} \quad (2.3)$$

with the neutron mass m_n and energy E whereas the Fourier components of the potential are determined via

$$V(\mathbf{r}) = \sum_{\mathbf{H}} V_{\mathbf{H}} e^{i\mathbf{H}\mathbf{r}} \quad (2.4)$$

The potential $V(\mathbf{r})$ is determined by the Fermi pseudo potential

$$V_{rigid}(\mathbf{r}) = \frac{2\pi\hbar^2}{m_n} \sum_i b_N \delta(\mathbf{r} - \mathbf{r}_i) \quad (2.5)$$

with b_N the coherent nuclear scattering length. However here we have to regard a static instead of a rigid lattice, as the atoms can move around their equilibrium position

$$\mathbf{r}_i(t) = \mathbf{r}_{0,i} + \mathbf{a}_i(t) \quad (2.6)$$

Consequently the potential reads

$$V_{static}(\mathbf{r}) = \frac{2\pi\hbar^2}{m_n} \sum_i b_N \langle \delta(\mathbf{r} - \mathbf{r}_i) \rangle \quad (2.7)$$

and the Fourier coefficients read

$$\begin{aligned} V_{\mathbf{H}} &= \frac{1}{V_{cryst}} \int d^3r \cdot e^{-i\mathbf{H}\mathbf{r}} V_{static}(\mathbf{r}) \\ V_{\mathbf{H}} &= \frac{2\pi\hbar^2}{m_n V_{cryst}} \int d^3r \cdot e^{-i\mathbf{H}\mathbf{r}} \sum_i b_N \langle \delta(\mathbf{r} - \mathbf{r}_i) \rangle \\ V_{\mathbf{H}} &= \frac{2\pi\hbar^2}{m_n V_{cryst}} F(\mathbf{H}) \sum_i e^{-i\mathbf{H}\mathbf{r}_{0,i}} b_N \langle e^{-i\mathbf{H}\mathbf{a}_i} \rangle \end{aligned} \quad (2.8)$$

with $F(\mathbf{H})$ the structure function and the factor

$$\langle e^{-i\mathbf{H}\mathbf{a}_i} \rangle = e^{-W(\mathbf{H})} \quad (2.9)$$

determines the Debye-Waller factor $W(\mathbf{H})$. For a harmonic crystal the Debye-Waller factor is determined by [1]

$$W(\mathbf{H}) = \frac{1}{2} \langle (\mathbf{H}\mathbf{a}_i)^2 \rangle \quad (2.10)$$

In general this can be understood as a correction to the coherent scattering length

$$b_{atom} \rightarrow b_{atom} \cdot e^{-W} \quad (2.11)$$

where for $H \neq 0$ one has to additionally take the atomic instead of the nuclear scattering length. This will be discussed in more detail in subsec. 2.2.2.

The hitherto obtained system of equations cannot be solved generally. However one only expects a notable contribution of an amplitude $u_{\mathbf{H}}$ if the wave vector of the reflected beam $\mathbf{K} + \mathbf{H}$ is close to a reciprocal lattice point. This leads to the one- and two beam approximations¹.

¹In the following the vectorial notation of the indices is dropped.

2.1.1 One-beam approximation

For the case that only $\mathbf{H} = \mathbf{0}$ is effective, simply the amplitude u_0 is excited. Hence the remaining relevant equation is

$$\left(\frac{\hbar^2}{2m_n} K_0^2 - E \right) u_0 = -V_0 u_0 \quad (2.12)$$

and the solution for the wave vector simply reads

$$K_0 = k \cdot \sqrt{1 - \frac{V_0}{E}} \approx k \cdot \left(1 - \frac{V_0}{2E} \right) \quad (2.13)$$

where the mean crystal potential

$$V_0 = \frac{2\pi\hbar^2 N}{m_n} b_N \quad (2.14)$$

is much smaller than the energy of the incoming neutron. The mean potential characterizing the medium is determined by the atomic density N and the coherent nuclear scattering length b_N . One can characterize the effect of such a potential by an index of refraction

$$n = \frac{K_0}{k} \approx 1 - \lambda^2 \frac{N b_N}{2\pi} \quad (2.15)$$

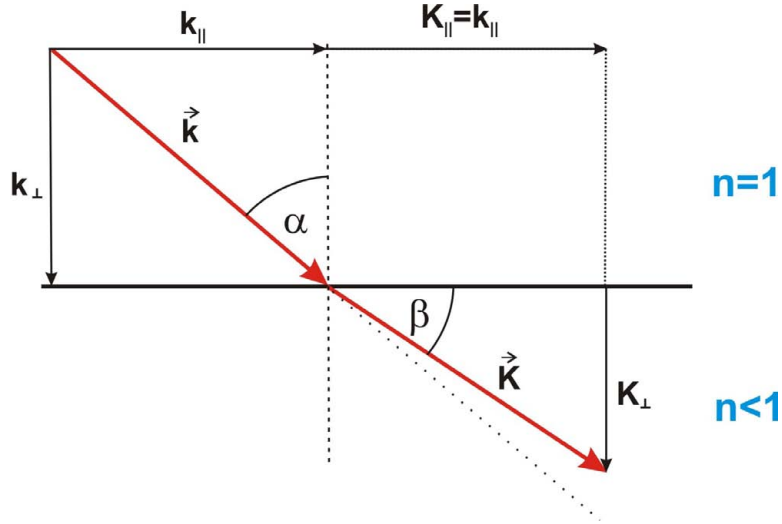


Figure 2.1: A neutron wave incident on a medium with index of refraction $n < 1$ is refracted off the surface normal.

As in light optics only the wave vector component normal to the crystal surface changes while the tangential component remains constant (Fig. 2.1). Thereby the

wave vector in general changes both direction and magnitude - the neutron wave is refracted. This case is valid for a perfect crystal far off any Bragg condition as well as for homogeneous non-crystalline media. Neutron refraction is used in neutron optics for example for prisms and in interferometry for phase shifters.

2.1.2 Two-beam approximation

A Bragg reflection is determined by Bragg's equation

$$\lambda = 2d_{hkl} \sin \theta_B \quad (2.16)$$

with the lattice plane distance

$$d_{hkl} = \frac{a}{\sqrt{h^2 + k^2 + l^2}} \quad (2.17)$$

according to the miller indices (h,k,l) and the lattice constant a . Close to a Bragg condition two reciprocal lattice points lie near the Ewald sphere and two amplitudes have to be considered. These amplitudes u_0 and u_H belong to the forward and reflected direction, respectively

$$\begin{aligned} \left(\frac{\hbar^2}{2m_n} K_0^2 - E \right) u_0 &= -V_0 u_0 - V_{-H} u_H \\ \left(\frac{\hbar^2}{2m_n} K_H^2 - E \right) u_H &= -V_H u_0 - V_0 u_H \end{aligned} \quad (2.18)$$

where $\mathbf{K}_H = \mathbf{K}_0 + \mathbf{H}$ denotes the reflected wave vector inside the crystal². The crystal potential $V_{\pm H}$ is given by

$$V_{\pm H} = \frac{\pi N \hbar^2}{4m_n} b_{atom}(H) F(H) \quad (2.19)$$

where $b_{atom}(H)$ denotes the atomic scattering length (compare section 2.2.2) and $F(H)$ the structure factor. The latter can take three values: $F = 8$ if the sum of the Miller indices (h, k, l) is divisible by 4, $F = 4 \pm 4i$ for h, k, l all odd and $F = 0$ for all other cases. Hence for the most commonly used (220) and (111) reflections one obtains

$$\begin{aligned} V_{\pm 220} &= \frac{2\pi N \hbar^2}{m_n} b_{atom}(220) \\ V_{\pm 111} &= \frac{2\pi N \hbar^2}{m_n} b_{atom}(111) \frac{1 \pm i}{2} \end{aligned} \quad (2.20)$$

² \mathbf{K}_0 is the wave vector in forward direction whereas the remaining \mathbf{H} is the reciprocal lattice vector of the reflecting lattice planes.

In the following we assume the symmetric Laue case where the crystal surface is oriented exactly perpendicular to the crystal surface. Then the coupled equations 2.18 lead to the standard formulas for the transmission and reflection amplitudes of the neutron wave behind a crystal of thickness D

$$t(y) = \exp[-i(A_0 + A_H y)] \left\{ \cos\left(A_H \sqrt{1 + y^2}\right) + \frac{iy}{\sqrt{1 + y^2}} \sin\left(A_H \sqrt{1 + y^2}\right) \right\} \quad (2.21)$$

$$r(y) = \exp[-i(A_0 + A_H y)] \sqrt{\frac{V_H}{V_{-H}}} \cdot \frac{-i}{\sqrt{1 + y^2}} \sin\left(A_H \sqrt{1 + y^2}\right) \quad (2.22)$$

where the scaled miset angle³ $\delta\theta = \theta - \theta_B$, namely

$$y = -\delta\theta \sin 2\theta_B / v_H \quad (2.23)$$

and

$$\begin{aligned} A_{0,H} &= \frac{Dkv_{0,H}}{2 \cos \theta_B} \\ v_H &= \frac{|V_H|}{E}, \quad v_0 = \frac{V_0}{E} \end{aligned} \quad (2.24)$$

have been introduced. From the amplitudes 2.21 and 2.22 one can calculate the intensities in the forward and reflected direction which in a non-absorbing medium have to fulfill the relation

$$|t(y)|^2 + |r(y)|^2 = 1$$

The reflected beam shows a Lorentzian-shaped peak with rapid oscillations (Fig. 2.2). These oscillations are known as Pendellösung oscillations and depend on the ratio between crystal thickness D and the so called Pendellösung length Δ_H :

$$\begin{aligned} A_H &= \frac{\pi D}{\Delta_H} \rightarrow \\ \Delta_H &= \frac{2\pi \cos \theta_B}{kv_H} \end{aligned} \quad (2.25)$$

These oscillations are due to the interference of two internal wave fields with slightly different wave vectors [1, 3]. This constitutes an important result of

³Throughout most presentations of dynamical diffraction theory equations and figures are given in terms of this y -parameter. However according to the discussion of higher order reflections and in view of the experimental realization, the miset angle dependence will be discussed more explicitly in the following chapters.

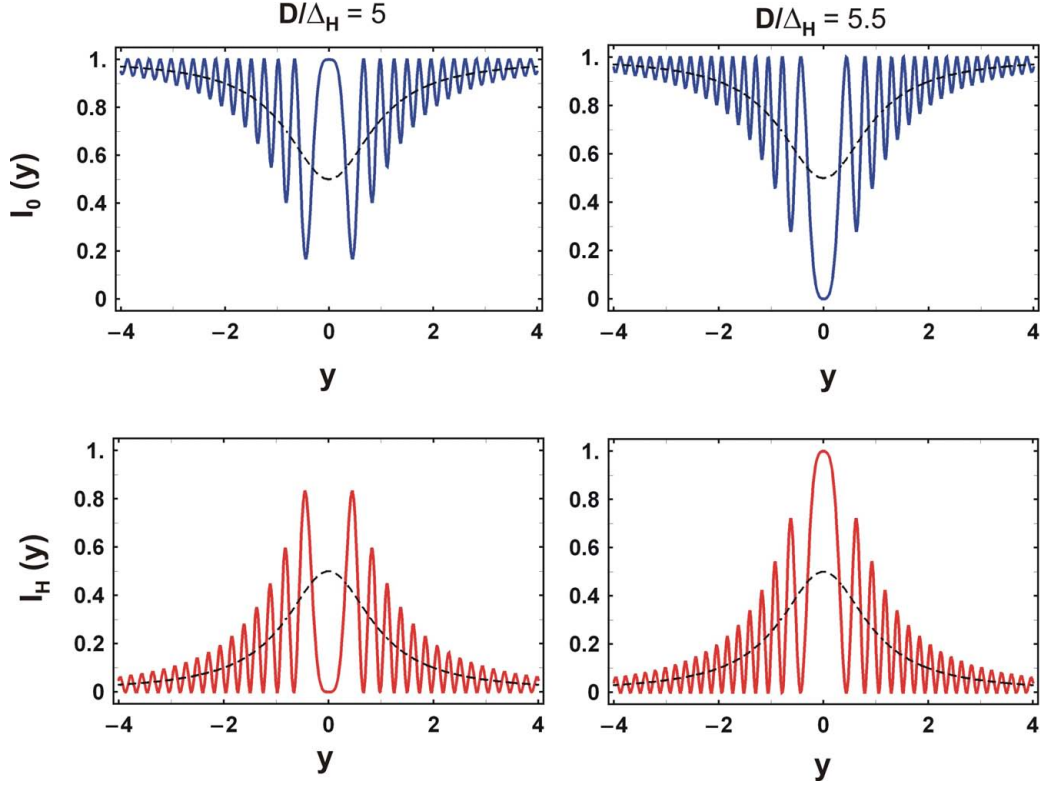


Figure 2.2: Intensities of the forward ($I_0(y) = |t(y)|^2$) and reflected ($I_H(y) = |r(y)|^2$) beam behind a perfect crystal slab for two thicknesses D in ratio to Δ_H . The dashed line shows the average taken over the Pendellösung oscillations.

dynamical diffraction theory and has been experimentally demonstrated in several experiments [5, 6].

An average over these oscillations yields

$$\begin{aligned}\langle I_H(y) \rangle &= \frac{1}{2} \frac{1}{1 + y^2} \\ \langle I_0(y) \rangle &= \frac{1}{2} \left(1 + \frac{y^2}{1 + y^2} \right)\end{aligned}\tag{2.26}$$

which is compared with the oscillating functions in Fig. 2.2. The average reflected intensity falls to half its maximum value when the y -parameter is unity or equivalently the miset angle is

$$\Delta\theta_{1/2} = \frac{\lambda^2 N F(H) b_{atom}(H)}{8\pi \sin 2\theta_B}\tag{2.27}$$

This is known as the Darwin width of the reflection and depends on both the Bragg angle and the type of reflection. Thereby higher order reflections such as

the (440) reflection have a strongly reduced width. The Darwin width describes the angular acceptance of a crystal and will thereby become important for the subsequent discussion of the phase shift.

2.2 Phase shift due to Laue transmission

So far a brief description of the transmission and reflection amplitudes and thereby the related intensities has been given. Here we want to focus on a different aspect. The transmission amplitude does not only describe the intensity but also contains the phase factor of the neutron wave in forward direction. This phase shift - modulo π - is given by the argument of the transmission factor

$$\phi(y) \equiv \arg[t(y)] \quad (2.28)$$

which is shown in Fig. 2.3. This phase has been mentioned in [8, 7] as "dynamical phase", which might be misleading in the sense of distinguishing dynamical from topological phase shifts [1]. Therefore we refer to a phase that arises by a Laue transmission as "Laue transmission phase" or short as "Laue phase"⁴.

To obtain an explicit form for the Laue phase the transmission factor has to be rewritten as

$$t(y) = A(y) \cdot e^{i\phi_{Laue}(y)} \quad (2.29)$$

In general the phase ϕ of a complex number $z = a + ib = r \cdot e^{i\phi}$ in the interval $]-\pi, \pi]$ can be expressed using the arctan function $]-\pi, \pi]$ can be expressed using the arctan function:

$$\phi = \begin{cases} \arctan \frac{b}{a} & \text{for } a > 0, b \text{ arbitrary} \\ \arctan \frac{b}{a} + \pi & \text{for } a < 0, b \geq 0 \\ \arctan \frac{b}{a} - \pi & \text{for } a < 0, b < 0 \\ \pi/2 & \text{for } a = 0, b > 0 \\ -\pi/2 & \text{for } a = 0, b < 0 \\ \text{undetermined} & \text{for } a = 0, b = 0 \end{cases} \quad (2.30)$$

⁴Also within the reflected term there is a phase relationship between the different y , the wave vector \mathbf{k}_H however is not in the original direction. Analogous to the "Laue transmission phase" arising in Laue geometry, also a "Bragg transmission phase" arising in Bragg geometry can be defined. Nevertheless it is important to note, that closely around the exact Bragg position $-1 < y < 1$ the transmitted beam vanishes. Outside this region a "Bragg phase" might be of interest.

Alternatively the phase can be expressed using the arccos function, where one needs only three distinctions of cases:

$$\phi = \begin{cases} \arccos \frac{a}{\sqrt{a^2+b^2}} & \text{for } b \geq 0 \\ -\arccos \frac{a}{\sqrt{a^2+b^2}} & \text{for } b < 0 \\ \text{undetermined} & \text{for } \sqrt{a^2+b^2} = 0 \end{cases} \quad (2.31)$$

Hence one can write the Laue phase in the interval $]-\pi, \pi]$ as

$$\begin{aligned} \phi_{Laue}(y) &= \text{sgn}[\beta(y)] \arccos \left(\frac{\alpha(y)}{\sqrt{\alpha^2(y) + \beta^2(y)}} \right) \\ \beta(y) &= \cos(A_0 + A_H y) \frac{y}{\sqrt{1+y^2}} \sin(A_H \sqrt{1+y^2}) \\ &\quad - \sin(A_0 + A_H y) \cos(A_H \sqrt{1+y^2}) \\ \alpha(y) &= \cos(A_0 + A_H y) \cos(A_H \sqrt{1+y^2}) \\ &\quad + \sin(A_0 + A_H y) \frac{y}{\sqrt{1+y^2}} \sin(A_H \sqrt{1+y^2}) \end{aligned}$$

where one can simplify the amplitude of the transmitted beam according to

$$\sqrt{\alpha^2(y) + \beta^2(y)} = \sqrt{1 - \frac{\sin^2(A_H \sqrt{1+y^2})}{1+y^2}} \quad (2.32)$$

However we aim here for a continuous presentation of the Laue phase as one can directly extract the phase term $-A_0 - A_H y$ from the exponential part of Eq. 2.21. For the remaining term one can apply the arctan function according to (2.30). This yields

$$\phi_{Laue}(y) = \phi_{Laue}(0) - A_H y + \arctan \left[\frac{y}{\sqrt{1+y^2}} \cdot \tan(A_H \sqrt{1+y^2}) \right] \quad (2.33)$$

The term $\phi_{Laue}(0)$ is in principle determined by $-A_0$ which is the phase shift that would occur in the case of a phase shifter at an angle θ_B ⁵. However according to (2.30) a constant $\pm\pi$ adds depending on the ratio between crystal thickness and Pendellösung length. This can be seen from

$$\begin{aligned} \lim_{y \rightarrow 0} \left\{ \cos(A_H \sqrt{1+y^2}) + \frac{iy}{\sqrt{1+y^2}} \sin(A_H \sqrt{1+y^2}) \right\} &= \\ \lim_{y \rightarrow 0} \{ \cos A_H + iy \sin A_H \} &= \cos A_H \end{aligned} \quad (2.34)$$

⁵This can be shown by inserting v_0 into $\phi_{Laue}(0) = -A_0 = -\frac{Dkv_0}{2\cos\theta_B}$ yielding $\phi_{Laue}(0) = -\frac{D}{\cos\theta_B}Nb_N\lambda$ which is exactly the phase shift of a phase shifter of thickness D at an angle θ_B .

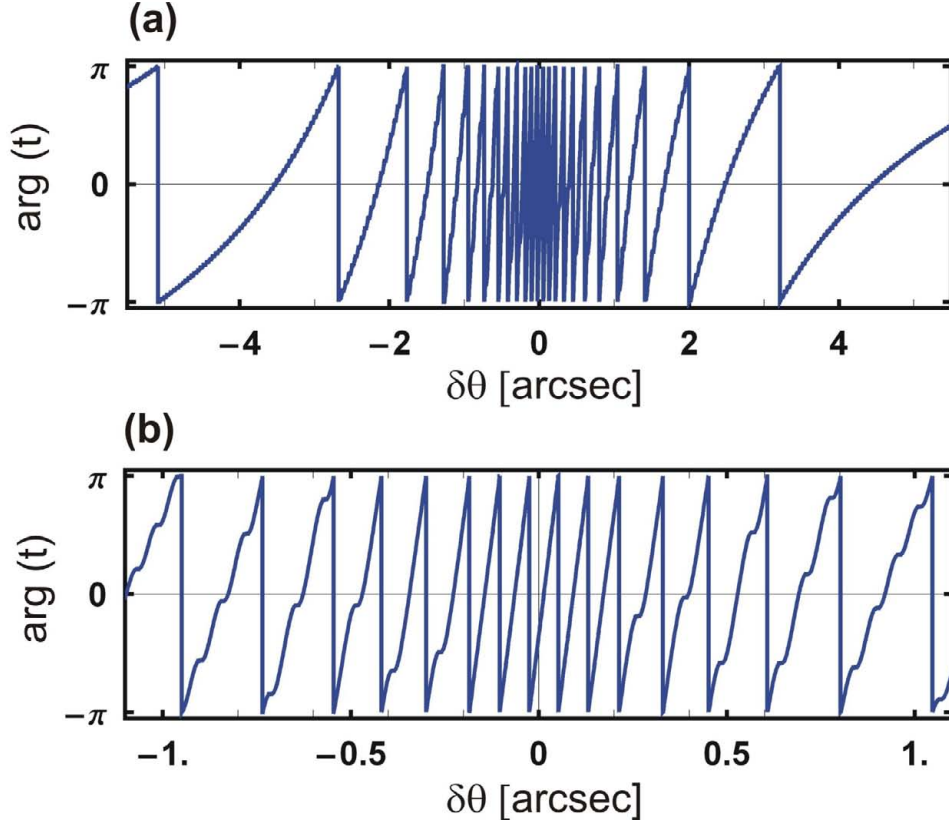


Figure 2.3: Plot of the argument of the transmission factor around the Bragg position (b) and over a larger region of $\delta\theta$ (a). The parameters are $D = 1\text{mm}$, $\theta_B = 45^\circ$ for a silicon-(220) reflection. The vertical lines do not indicate a discontinuity of the phase, as the difference is just 2π .

According to (2.30) in the case $\cos A_H < 0$ a constant $\pm\pi$ adds. Consequently

$$\phi_{Laue}(0) = -A_0 \quad \text{for} \quad \frac{4n-1}{2} < \frac{D}{\Delta_H} < \frac{4n+1}{2} \quad (2.35)$$

for n natural numbers. Otherwise one has to add $\pm\pi$. This is insofar interesting as the phase shift at $\delta\theta = 0$ differs from the phase shift of an equivalent phase shifter $-A_0$ depending on the crystal thickness. The transition between cases where the phase shift is equal or differs by a constant $\pm\pi$ happens exactly at the minima of the transmitted beam for $\delta\theta = 0$. However in the following only the angular dependence of the Laue phase is of interest. Here one finds that besides the constant $\phi_{Laue}(0)$ the Laue phase is antisymmetric with respect to y and thereby $\delta\theta$. Still the phase function (Eq. 2.33) is not continuous. Due to the periodicity of the arctan term in Eq. 2.33 artificial phase jumps of height π would appear at the poles of the tan term, if plotting expression 2.33 directly.

One therefore has to continue the function, which can for example be achieved by

$$\begin{aligned}\phi_{Laue}(y) = & \phi_{Laue}(0) - A_H y + \arctan\left[\frac{y}{\sqrt{1+y^2}} \cdot \tan\left(A_H \sqrt{1+y^2}\right)\right] \\ & + \pi \cdot \text{sgn}(y) \cdot \left(\left\lfloor \frac{A_H \sqrt{1+y^2} + \frac{\pi}{2}}{\pi} \right\rfloor - \left\lfloor \frac{A_H + \frac{\pi}{2}}{\pi} \right\rfloor\right)\end{aligned}\quad (2.36)$$

It is interesting to note, that the arctan term of Eq. 2.36 or equivalently the term $\cos\left(A_H \sqrt{1+y^2}\right) + \frac{iy}{\sqrt{1+y^2}} \sin\left(A_H \sqrt{1+y^2}\right)$ in the transmission amplitude (2.21) contains the whole nonlinearity of the Laue phase. Moreover it contains the relevant dependences on the crystal potential and the wavelength as we will see later.

Recently in [7] a formula different from ours has been given⁶

$$\phi_{Laue,approx}(y) = \phi_{Laue,approx}(0) - A_H \left(y \pm \sqrt{1+y^2}\right) \quad (2.37)$$

with the plus (minus) sign corresponding to positive (negative) y .

This approximation is identical to Eq. 2.33 in the limit $|y| \rightarrow \infty$ where $\left|\frac{y}{\sqrt{1+y^2}}\right| \rightarrow 1$. In this case Eq. 2.21 can simply be written as

$$\begin{aligned}t(y) &= \exp[-i(A_0 + A_H y)] \left\{ \cos\left(A_H \sqrt{1+y^2}\right) + i \cdot \text{sgn}(y) \cdot \sin\left(A_H \sqrt{1+y^2}\right) \right\} \\ &= \exp\left[-i\left(A_0 + A_H y - \text{sgn}(y) \cdot A_H \sqrt{1+y^2}\right)\right]\end{aligned}\quad (2.38)$$

directly yielding the phase Eq. 2.37. Besides the limit $|y| \rightarrow \infty$, Eq. 2.37 is also exact for

$$A_H \sqrt{1+y^2} = n\pi \quad \implies \quad \sin\left(A_H \sqrt{1+y^2}\right) = 0. \quad (2.39)$$

Thereby we expect a significant difference between Eq. 2.33 and Eq. 2.37 closely around Bragg for the case $A_H \sqrt{1+y^2} \approx (2n+1) \cdot \frac{\pi}{2}$. Indeed Fig. 2.4 shows a remarkable fine structure in the form of small plateaus in the phase function by Eq. 2.33 (or Eq. 2.36, see below) which is not contained in Eq. 2.37. This fine structure - that can also be observed in Fig. 2.3 - will be discussed in detail in subsection 2.2.2.

⁶Here the formula of [7] is written in the notations used in this work.

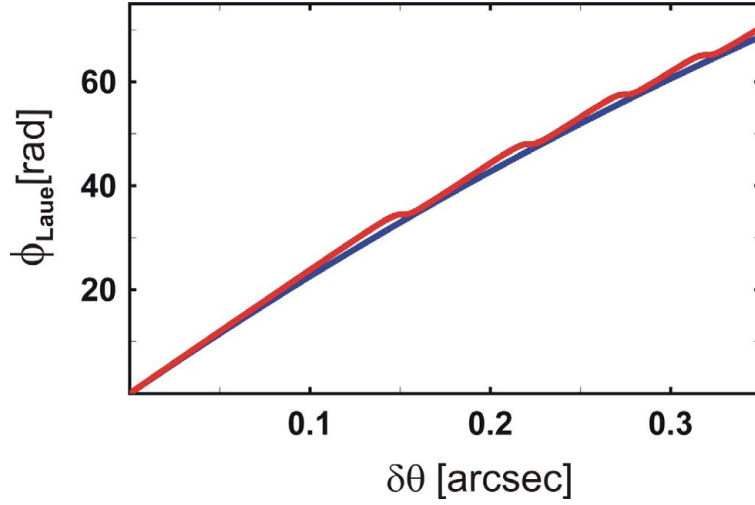


Figure 2.4: Comparison of the phase functions by Eq. 2.37 (blue curve) and Eq. 2.36 (red curve) closely around the Bragg condition. The parameters are $D = 3\text{mm}$, $\theta_B = 45^\circ$ for a Si-(220) reflection, corresponding to $\lambda = 2.72\text{\AA}$. Here the constant $\phi_{Laue}(0)$ is subtracted.

Plotting the phase function

Before we discuss the principal properties and dependences of the Laue phase some comments on plotting the phase function are necessary.

One possibility consists in plotting the phase modulo π as shown in Fig. 2.3. On the other hand the progress of the phase function is better visible if the phase function is plotted as a continuous function. This can for example be done by using approximation 2.37. Omitting the constant value $-A_0$ the phase shift is plotted in Fig. 2.5(a). In this depiction the limits $\delta\theta \rightarrow \pm\infty$ are equal and zero. This can be easily seen from Eq. 2.37 as

$$\lim_{y \rightarrow \pm\infty} \left\{ y \mp \sqrt{1 + y^2} \right\} = \lim_{y \rightarrow \pm\infty} \frac{1}{2y} = 0. \quad (2.40)$$

On the other hand one obtains a huge jump at $\delta\theta = 0$. In contrast to this Fig. 2.3 shows that the phase function is continuous at $\delta\theta = 0$. To emphasize the continuity of the phase function at $\delta\theta = 0$ it is preferable to choose the representation shown in Fig. 2.5 (b) by using Eq. 2.36.

Here the two asymptotes $|\delta\theta| \rightarrow \infty$ are separated by a large value. This seems to be a contradiction. However the two asymptotes - or alternatively the huge jump at $\delta\theta = 0^7$ (Fig. 2.5(a)) - are separated exactly by a multiple of 2π . The

⁷Using approximation Eq. 2.37 one in fact obtains $\lim_{\delta\theta \rightarrow 0} \phi_{Laue}(\delta\theta) - \lim_{\delta\theta \rightarrow \infty} \phi_{Laue}(\delta\theta) = A_H$

reason is that according to Eq. 2.33 $\lim_{\delta\theta \rightarrow 0} \phi_{Laue}(\delta\theta) = \phi_{Laue}(0) = -A_0 (\pm\pi)$ and $\lim_{|\delta\theta| \rightarrow \infty} \phi_{Laue}(\delta\theta) = -A_0$. Thereby these two limits can only be separated by a multiple of π (periodicity of the arctan-term in Eq. 2.33). Consequently the separation between the two asymptotes in Fig. 2.5(b) is exactly a multiple of 2π . This means that they are identical. During most of this work the representation of Fig. 2.5(b) will be used but in some cases it is more convenient to use another representation.

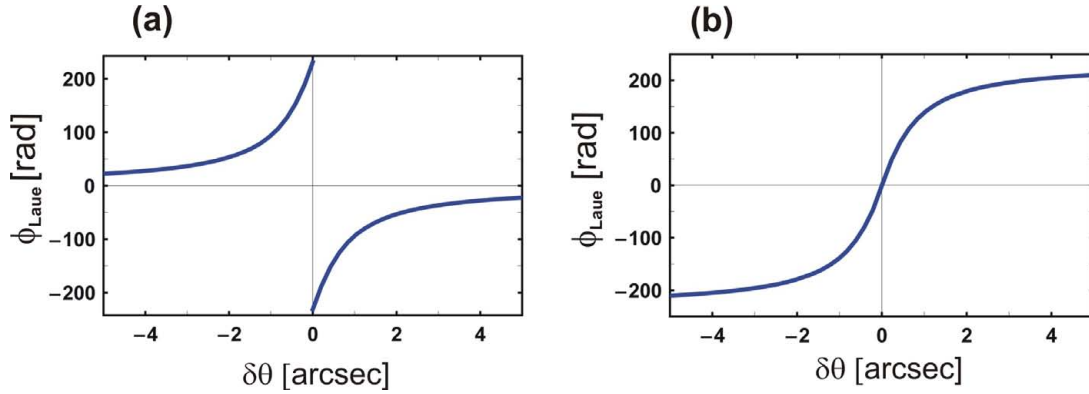


Figure 2.5: Two possibilities to plot the Laue phase over a large range of $\delta\theta$: (a) with a discontinuity at $\delta\theta = 0$ but equal asymptotes or (b) continuous at $\delta\theta = 0$ but with separated asymptotes. In these two representations Eq. 2.33 can not be distinguished from Eq. 2.37. The huge jump at $\delta\theta = 0$ in (a) and the difference between the asymptotes in (b) is equal to a multiple of 2π . Parameters as in Fig. 2.4.

2.2.1 General properties of the phase function

The angular dependence

The most significant feature of the Laue phase is its dependence on y (Eq. 2.23) and thereby small deviations $\delta\theta$ from the Bragg condition. A first observation is the antisymmetry of the Laue phase with respect to the Bragg condition. There the angular dependence reaches its maximum. Fig. 2.4 shows that for a plate of 3 mm thickness already a deviation $\delta\theta = 0.1''$ leads to phase differences in the order of 20 rad ($\approx 3 \cdot 2\pi$) relative to $\delta\theta = 0''$ and $\delta\theta = 0.0001''$ would still lead to relative phase shifts in the order of 1° ! This extreme sensitivity to angular

which is in general not a multiple of 2π . This is due to the fact that this expression is only a good approximation for large $\delta\theta$. However due to the argument presented also 2.33 can be plotted as in Fig. 2.5(a).

deviations is the main difference to the phase shift induced by a non crystalline material or a perfect crystal far off any Bragg condition. In this case the angular sensitivity for an equally thick plate in the same configuration is of the order of 1 degree phase shift per angular deviation by 15 arc seconds, which means that the angular dependence here is by an order of 10^{-5} weaker. Closely around Bragg the Laue phase can be approximated by

$$\begin{aligned}\phi_{Laue}(y) &= \phi_{Laue}(0) - y(A_H - \tan A_H) + \\ &+ y^3 \left(\frac{A_H}{2} - \frac{\tan A_H}{2} + \frac{1}{2}A_H \tan^2 A_H - \frac{\tan^3 A_H}{3} \right) + \\ &+ O(y^5)\end{aligned}\tag{2.41}$$

In terms of $\delta\theta$ this reads

$$\begin{aligned}\phi_{Laue}(\delta\theta) &= \phi_{Laue}(0) + \delta\theta \cdot \frac{\sin 2\theta_B}{v_H} (A_H - \tan A_H) + \\ &- \delta\theta^3 \cdot \frac{\sin^3 2\theta_B}{v_H^3} \left(\frac{A_H}{2} - \frac{\tan A_H}{2} + \frac{1}{2}A_H \tan^2 A_H - \frac{\tan^3 A_H}{3} \right) + \\ &+ O(\delta\theta^5)\end{aligned}\tag{2.42}$$

Consequently the phase is to second order linear in $\delta\theta$ at $\delta\theta = 0$. As for thick crystals⁸ $A_H \gg \tan A_H$ - beside the case $A_H \approx (2n+1)\frac{\pi}{2}$ which will be discussed separately (Appendix A) - one can use the approximation

$$\phi_{Laue}(y) \approx \phi_{Laue}(0) - yA_H + O(y^3)\tag{2.43}$$

and

$$\phi_{Laue}(\delta\theta) \approx \phi_{Laue}(0) + \delta\theta \cdot \frac{\pi D}{d} + O(\delta\theta^3)\tag{2.44}$$

respectively. In the last step Eq. 2.16 and $k = \frac{2\pi}{\lambda}$ has been used. An important observation here is that in the immediate surrounding of Bragg, the angular dependence of the Laue phase is described simply by the crystal thickness D and the lattice plane distance d . The ratio D/d is under usual conditions of the order of 10^7 and thereby leads to the high phase sensitivity around $\delta\theta = 0$. For larger $\delta\theta$ the higher order contributions lead to a flattening of the phase function and finally to the asymptotic behavior (Eq. 2.40) shown in Fig. 2.5. Nevertheless the angular dependence of the Laue phase is still effective many arc seconds away. Another important observation can be made by Eq. 2.37 for the phase progress from the Bragg condition to the asymptotes. Using approximation 2.37 one can estimate

$$\lim_{\delta\theta \rightarrow \infty} \phi_{Laue}(\delta\theta) - \phi_{Laue}(\delta\theta = 0) \approx A_H \propto DNb_{atom}d \tan \theta_B\tag{2.45}$$

⁸Here: $D \gg \Delta_H$.

It is important to note that besides the fact that the exact value is a multiple of π (App. A) this is not an absolute phase difference between the asymptotes and $\delta\theta = 0$ as it does not constitute a shift by a potential. It rather constitutes a measure for the effective region of the Laue phase. Thereby this asymptotic behavior together with Eq. 2.44 is an useful estimation for an understanding of the phase dependences discussed in the following. Close to Bragg the phase is dominated by an almost energy independent lattice scattering, further away the influence of the neutron energy and the crystal potential via the wavelength (or θ_B) and the scattering length density Nb_{atom} gain importance.

Crystal thickness

Of course the phase shift depends on the crystal thickness D which is contained in A_H (2.24). Thus the phase shift is - apart from the fine structure discussed in subsection 2.2.2 - proportional to D . This will become important for the correct limit to the phase shifter case (section 2.3). Fig. 2.6 (a) shows the Laue phase for several crystal thicknesses.

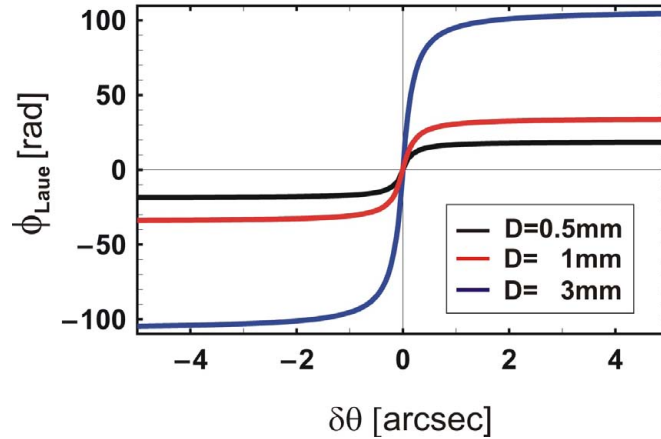


Figure 2.6: Laue phase for several thicknesses D . Other parameters as in Fig. 2.4.

Bragg angle

Closely around the Bragg condition the Laue phase is to first order independent of the Bragg angle θ_B and thereby the wavelength. This means that the phase shift is almost non dispersive⁹. On the other side due to the higher order contributions

⁹There is almost no dispersion with respect to λ . However there is a large "dispersion" - according to the "dispersion surfaces" [1, 3] - with respect to the energy independent angle

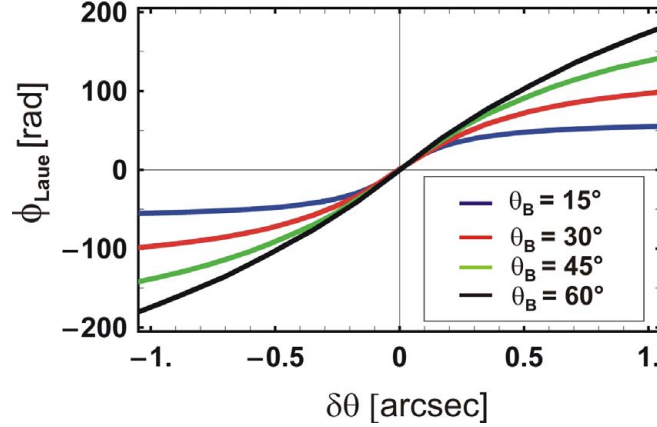


Figure 2.7: The Laue phase for different Bragg angles θ_B . Other parameters as in Fig. 2.4.

the phase function bends off into the asymptotes earlier for smaller Bragg angle (Fig. 2.7). From Eq. 2.45 it can be observed that the phase difference to the asymptotes is approximately proportional to $\tan \theta_B$. This means that for larger θ_B the Laue phase is effective over a larger region of $\delta\theta$. This is related to the Darwin width (Eq. 2.27) given explicitly in terms of θ_B by

$$\Delta\theta_{1/2} = \frac{d^2 N F(H) b_{atom}(H)}{4\pi} \tan \theta_B \quad (2.46)$$

Crystal properties

Different types of lattice plane orientations - entering via the structure function $F(H)$ - will naturally influence the steepness of the Laue phase. As with our neutron interferometers we use the (110) orientation, we will concentrate on this lattice plane orientation. However higher order reflections m are of great interest. In our case these are the $(2m, 2m, 0)$ reflections, leading via the Bragg equation (Eq. 2.16) to

$$\lambda_m = \frac{\lambda_{(220)}}{m}. \quad (2.47)$$

As the phase around Bragg is inversely proportional to the lattice plane distance d there is a strong dependence on the order of reflection

$$\phi_{Laue}(|\delta\theta| \gtrsim 0) \propto \frac{\delta\theta}{d} \propto m\delta\theta \quad (2.48)$$

Fig. 2.8 displays the fact that higher order reflections show a higher steepness of the phase close to Bragg¹⁰ but on the other hand bend off earlier into the distribution $\delta\theta$ and hence the direction of the wave vector.

¹⁰This would not be the case, if plotting $\phi_{Laue}(y)$ as $y \propto m^2 \cdot \delta\theta$.

asymptotes due to the higher order contributions of $\delta\theta$. This can easily be seen from Eq. 2.45, whereby

$$\lim_{\delta\theta \rightarrow \infty} \phi_{Laue}(\delta\theta) - \phi_{Laue}(\delta\theta = 0) \propto d \propto \frac{1}{m} \quad (2.49)$$

The larger steepness close to Bragg and the smaller value of the asymptotes on the other hand is reflected via the effective range of the Darwin width (Eq. 2.46).

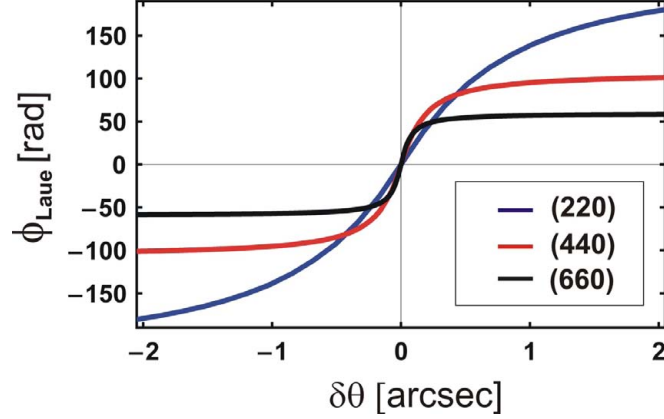


Figure 2.8: The Laue phase for the (220), (440) and (660) reflection. Other parameters as in Fig. 2.4.

Certainly the special material properties such as the atomic number density N and the atomic scattering length b_{atom} entering via the mean crystal potentials $V_{0,H}$ are relevant for the phase shift. Interestingly the angular dependent part of the phase shift is independent of the mean potential in the immediate vicinity of the Bragg condition, as it is only described by the lattice geometry and crystal thickness. For larger $\delta\theta$ where the higher order terms become relevant - and especially in the case of the fine structure discussed in 2.2.2 - the material properties show a significant influence as according to (2.45)

$$\lim_{\delta\theta \rightarrow \infty} \phi_{Laue}(\delta\theta) - \phi_{Laue}(\delta\theta = 0) \propto Nb_{atom} \quad (2.50)$$

Fig. 2.9 shows that for larger crystal potential (b_{atom} or equivalently N) the Laue phase is more effective for larger $\delta\theta$. This will become important for the correct limit to the phase shifter case discussed in 2.3.

2.2.2 Pendellösung structures of the Laue phase

In Fig. 2.4 we have observed a remarkable structure in the form of small plateaus in the phase function. These only occur in the exact expression for the Laue

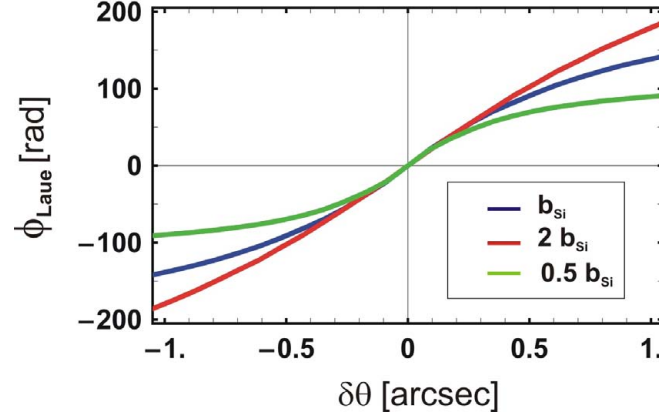


Figure 2.9: Dependence of the Laue phase on the nuclear scattering length. $b_{Si} = 4.1507 \cdot 10^{-15}m$ is the value for silicon. Other parameters as in Fig. 2.4.

phase (Eq. 2.33). There one has to consider the arctan term:

$$\arctan \left[\frac{y}{\sqrt{1+y^2}} \tan \left(A_H \sqrt{1+y^2} \right) \right] \quad (2.51)$$

At the poles of the tangent term

$$A_H \sqrt{1+y^2} = (2n+1) \frac{\pi}{2} \quad (2.52)$$

the scaling factor $\frac{y}{\sqrt{1+y^2}}$ prevents a simple extraction of the argument of the tangent function by the arc tangent. At these positions the phase becomes very sensitive to small changes in the argument of the tangent and this fine structure in the form of plateaus appears. These positions are just where we expect the most striking deviations from Eq. 2.37. Using Eq. 2.24 it becomes obvious that similar to the reflected and transmitted intensities the ratio between the crystal thickness and Pendellösung length Δ_H affects this behavior

$$\frac{D}{\Delta_H} = \frac{(2n+1)}{2\sqrt{1+y^2}} \quad (2.53)$$

It is interesting to note, that the positions of this fine structure

$$\begin{aligned} y_{Pend}(n) &= \sqrt{\frac{(2n+1)^2 \Delta_H^2}{4D^2} - 1} \\ n_{min} &= \left\lceil \frac{1}{2} \left(\frac{2D}{\Delta_H} - 1 \right) \right\rceil \end{aligned} \quad (2.54)$$

are exactly identical with the minima of the transmitted intensity (Fig. 2.10) and thereby the maxima of the reflected intensity. Apparently the interference of the α and β wave functions inside the crystal [1, 3] does not only explain the Pendellösung oscillations of the reflected and transmitted intensities but also the structure of the Laue phase.

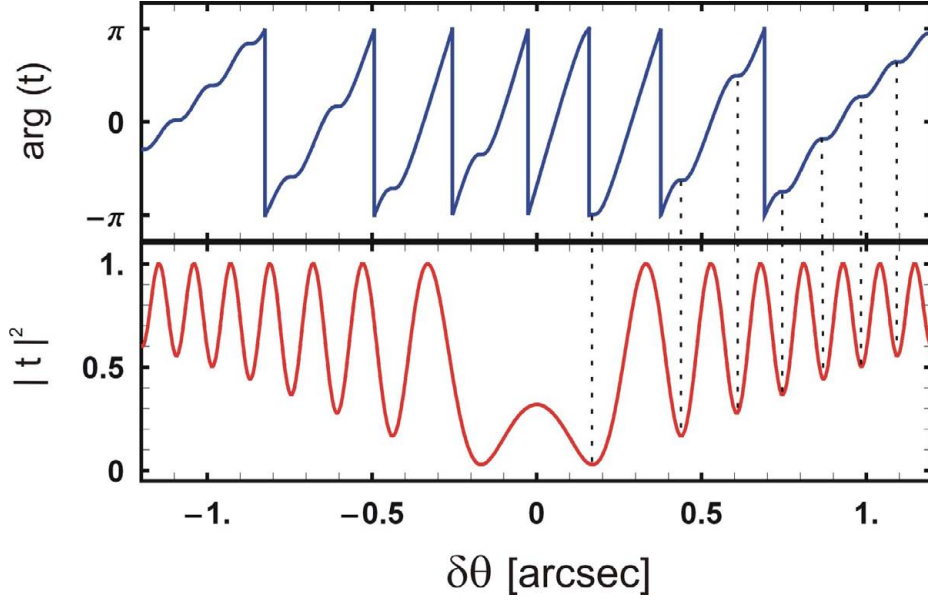


Figure 2.10: The fine structure of the Laue phase appears exactly at the minima of the transmitted intensity. Parameters: $D = 0.5\text{mm}$, $\theta_B = 45^\circ$, Si-(220) reflection.

Position of Pendellösung structures

The positions of the plateaus (2.54) depend sensitively on the crystal thickness D and all parameters relevant for the Pendellösung length Δ_H , such as b_{atom} , θ_B and the order of reflection m . If

$$D_1 = \left(n + \frac{1}{2}\right) \Delta_H \quad (2.55)$$

this structure (compare Appendix A) will directly occur at $y = 0$ ¹¹. The same is valid for $D_2 = (n + \frac{3}{2})\Delta_H$ where the difference between D_2 and D_1 is just one Pendellösung length Δ_H . Between these two thicknesses the first plateau will roam continuously between 0 and a maximum of $y_{Pend}(D_2, n = n_{min}(D_2) + 1)$ (Eq. 2.54). Fig. 2.11 shows the Pendellösung structure for two crystal thicknesses.

¹¹In this special case Eq. 2.44 is no more an appropriate approximation for the phase around Bragg.

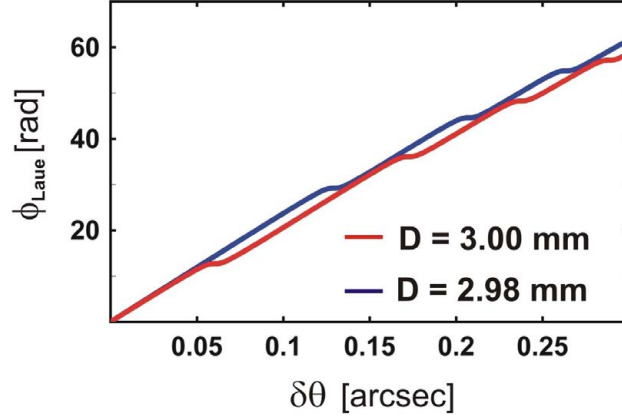


Figure 2.11: The Pendellösung structure of the Laue phase for two crystal thicknesses D . Other parameters as in Fig. 2.4.

The distance between successive plateaus decreases with rising y and finally becomes a constant value

$$\lim_{n \rightarrow \pm\infty} \{y_{Pend}(n+1) - y_{Pend}(n)\} = \lim_{n \rightarrow \pm\infty} \left\{ \sqrt{\frac{(2n+3)^2 \Delta_H^2}{4D^2} - 1} - \sqrt{\frac{(2n+1)^2 \Delta_H^2}{4D^2} - 1} \right\} = \frac{\Delta_H}{D} \quad (2.56)$$

Hence the plateaus are the denser, the larger the thickness D in comparison to Δ_H . As $\Delta_H \propto m$ and $\delta\theta \propto \frac{1}{m^2} y$ for higher order reflections m , for these the distances between the plateaus are denser by a factor $\frac{1}{m}$. The limit calculated above nevertheless is just the case where the plateaus vanish as it corresponds to the limit $y \rightarrow \infty$ where approximation 2.37 is valid. Fig. 2.11 shows this fine structure for two crystal thicknesses. It can be observed that an extraordinary phase difference between the two curves occurs in the vicinity of the plateaus. This difference is the more pronounced the closer the structure to the Bragg position. This additional phase sensitivity due to the Pendellösung structure depends not only on the crystal thickness but on all parameters contained in Δ_H . The sensitivity due to the neutron-electron scattering length b_{ne} contained via the atomic scattering length b_{atom} is discussed in the following part.

The neutron-electron scattering length

The relevant scattering length in the regime described by dynamical diffraction theory is the atomic scattering length

$$b_{atom} = b_N - Z[1 - f(q)]b_{ne}$$

Besides the nuclear scattering length the neutron-electron scattering length b_{ne} ¹² is contained in this expression. This contribution describes the interaction of a charged particle with the internal charge separation within the neutron [1, 17]. There is still a clear disagreement between measurements of b_{ne} by different methods. The two disputed values are [18, 19, 20, 21, 22]

$$\begin{aligned} b_{ne}(1) &= -0.00131(3)\text{fm} \quad [\textit{Garching} - \textit{Argonne}] \\ b_{ne}(2) &= -0.00159(4)\text{fm} \quad [\textit{Dubna}] \end{aligned} \quad (2.57)$$

Therefore S. A. Werner [7]¹³ and A. Ioffe [8] proposed to determine b_{ne} by a precision measurement of the phase shift arising from dynamical diffraction theory. This gives additional motivation for the investigation of the Laue phase. The contribution of b_{ne} to b_{atom} depends on the atomic number Z and on the atomic form factor $f(q)$. According to [17] the latter is given by

$$\begin{aligned} f(q) &= \frac{1}{\sqrt{1 + 3\frac{q^2}{q_0^2}}} \\ q &= \frac{4\pi \sin \theta_B}{\lambda} = \frac{2\pi}{d} \\ q_0 &= 19 \cdot Z^{1/3} \text{nm}^{-1} \end{aligned} \quad (2.58)$$

where d is the lattice constant (Eq. 2.17). As $f(q = 0) = 1$ the contribution of b_{ne} vanishes off Bragg and $b_{atom} = b_N$ there. The contribution to the Laue phase vanishes as well:

$$\begin{aligned} \lim_{y \rightarrow \pm\infty} \phi_{Laue}(y) &= \lim_{y \rightarrow \pm\infty} \left\{ -A_0 + A_H(\mp y \pm \sqrt{1 + y^2}) \right\} \\ &= -A_0 \end{aligned} \quad (2.59)$$

and $-A_0$ contains the nuclear scattering length only. This is an important fact for the correct limit to the phase shifter case treated in section 2.3. Estimating in general the influence of small scattering length corrections

$$b_{atom}^* = b_{atom}(1 + \epsilon) \quad (2.60)$$

where for the case of the neutron electron scattering length

$$\epsilon \approx \frac{Z \cdot [1 - f(q)] \cdot [b_{ne}(1) - b_{ne}(2)]}{b_N} \approx 3.8 \cdot 10^{-4} \quad (220) \quad (2.61)$$

¹²Here b_{ne} is used for the bound scattering length similar to the bound nuclear scattering length b_N . The relation between the bound and free (a_{ne}) scattering length is $b_{ne} = a_{ne} \frac{A+1}{A}$ where A is the mass number of the nucleus.

¹³These proposals do not mention the here discussed Pendellösung structures, however the extraordinary phase sensitivity there is a good reason to give a discussion in this context.

one finds for the phase difference:

$$\Delta\phi_{Laue}(y, \epsilon) = \phi_{Laue}(y, \epsilon) - \phi_{Laue}(y, 0) \quad (2.62)$$

According to the first order expansions $y(\epsilon) = y \cdot (1 - \epsilon)$ and $A_H(\epsilon) = A_H \cdot (1 + \epsilon)$ the resulting first order expansion of Eq. 2.37 yields

$$\Delta\phi_{Laue}(y, \epsilon) = A_H \frac{1}{\sqrt{1 + y^2}} \cdot \epsilon \approx \frac{A_H \cdot \epsilon}{y} \quad y \gg 1 \quad (2.63)$$

As $y \propto m^2 \delta\theta$ the sensitivity for higher order reflections m is significantly reduced. Furthermore there is almost¹⁴ no contribution at the exact Bragg position, due to the independence of the atomic scattering length there. Close to Bragg one has to regard the full first order expansion (Eq. 2.41)

$$\phi_{Laue}(y) = -y(A_H - \tan A_H) + O(y^3) \quad (2.64)$$

The phase difference to first order in ϵ and y then reads

$$\Delta\phi_{Laue}(y, \epsilon) = y (A_H[1 + \tan^2 A_H] - \tan A_H) \cdot \epsilon \quad y \ll 1 \quad (2.65)$$

This is a linear phase term strongly depending on the ratio D/Δ_H . Considering the wavelength dependence, the atomic scattering length is independent of the Bragg angle but depends according to Eq. 2.58 on the lattice constant d and thereby the order of reflection m (Tab. 2.1).

reflection	$f(q)$	$b_{atom}(b_{ne}(2) = -0.0013 fm)$	$b_{atom}(b_{ne}(1) = -0.0016 fm)$
0	1	$4.1507 fm$	$4.1507 fm$
(220)	0.6284	$4.1575 fm$	$4.1590 fm$
(440)	0.3746	$4.1621 fm$	$4.1647 fm$
(660)	0.2600	$4.1642 fm$	$4.1673 fm$
(880)	0.1980	$4.1653 fm$	$4.1687 fm$

Table 2.1: Form factor and atomic scattering length for the (220) and higher order reflections in the case of Si. The Debye-Waller factor is here omitted.

Fig. 2.12 shows that due to a small shift of the plateaus of the fine structure a remarkable phase difference in the Laue phase between the two b_{ne} values in discussion appears. This difference decreases with the order of reflection m , although the influence on b_{atom} is larger for higher order reflections m . Additionally

¹⁴Unless the case that a Pendellösung structure is very close to $\delta\theta = 0$. However then also the transmitted beam vanishes at $\delta\theta = 0$.

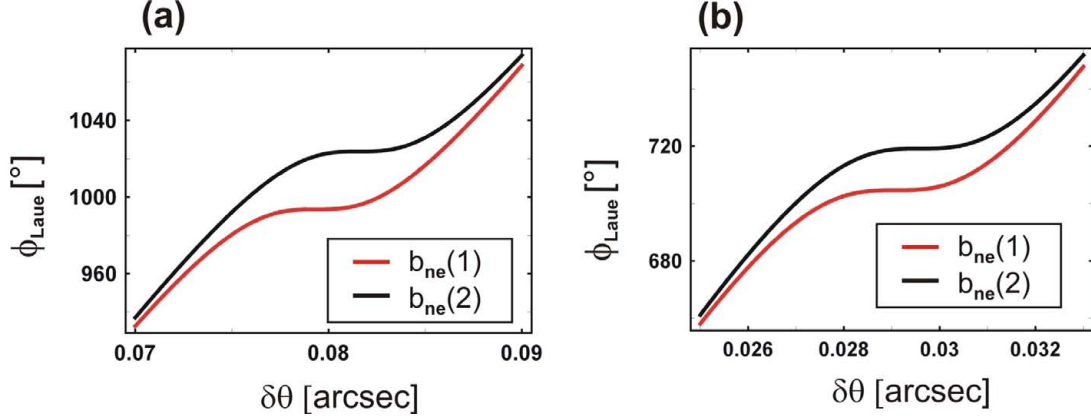


Figure 2.12: Laue phase for two disputed values of b_{ne} (2.57) around a plateau of the Pendellösung structure for (a) Si-(220) reflection and (b) Si-(440) reflection. Other parameters as in Fig. 2.4.

the Laue phase close to Bragg is by a factor m steeper, thereby a shift of the plateaus should yield a higher phase difference. However the phase difference also depends on the width of these plateaus, which is - according to the reflection width - significantly narrower. Thus the phase difference for higher order reflections is smaller. The phase difference at plateaus close to Bragg can be estimated by the phase difference caused by the magnitude of the plateau shift. For this the position of the plateaus (Eq. 2.54 written in the explicit dependences)

$$\begin{aligned}\delta\theta_{Pend} &= \sqrt{\alpha + \beta} \\ \alpha &= \frac{(2n+1)d^2}{4D^2} \\ \beta &= -\frac{4N^2b_{atom}^2d^4}{\pi^2} \tan^2\theta_B\end{aligned}\quad (2.66)$$

is expanded in ϵ (2.61):

$$\Delta\delta\theta_{Pend}(\epsilon) = \delta\theta_{Pend}(\epsilon) - \delta\theta_{Pend}(0) = \delta\theta_{Pend}(0) \frac{\beta}{\alpha + \beta} \cdot \epsilon \quad (2.67)$$

The resulting phase difference can then be estimated by

$$\Delta\phi_{Laue}(\delta\theta, \epsilon) \approx \Delta\delta\theta_{Pend}(\epsilon) \frac{\pi D}{d} = \delta\theta_{Pend}(0) \frac{\beta}{\alpha + \beta} \cdot \epsilon \cdot \frac{\pi D}{d} \quad (2.68)$$

Furthermore it can be observed (Fig. 2.13) that this phase difference becomes smaller at successive plateaus, which can be understood by the decreasing phase slope for larger $\delta\theta$. As already discussed there is no sensitivity to b_{ne} in the limits

$\delta\theta \rightarrow 0$ and $|\delta\theta| \rightarrow \infty$, although a notable contribution can still be observed as far as 10 arc seconds away from Bragg. This range of influence depends in turn on the Darwin width. It is also around the Darwin width, where the largest average sensitivity can be found and in general the phase sensitivity for higher order reflections is reduced.

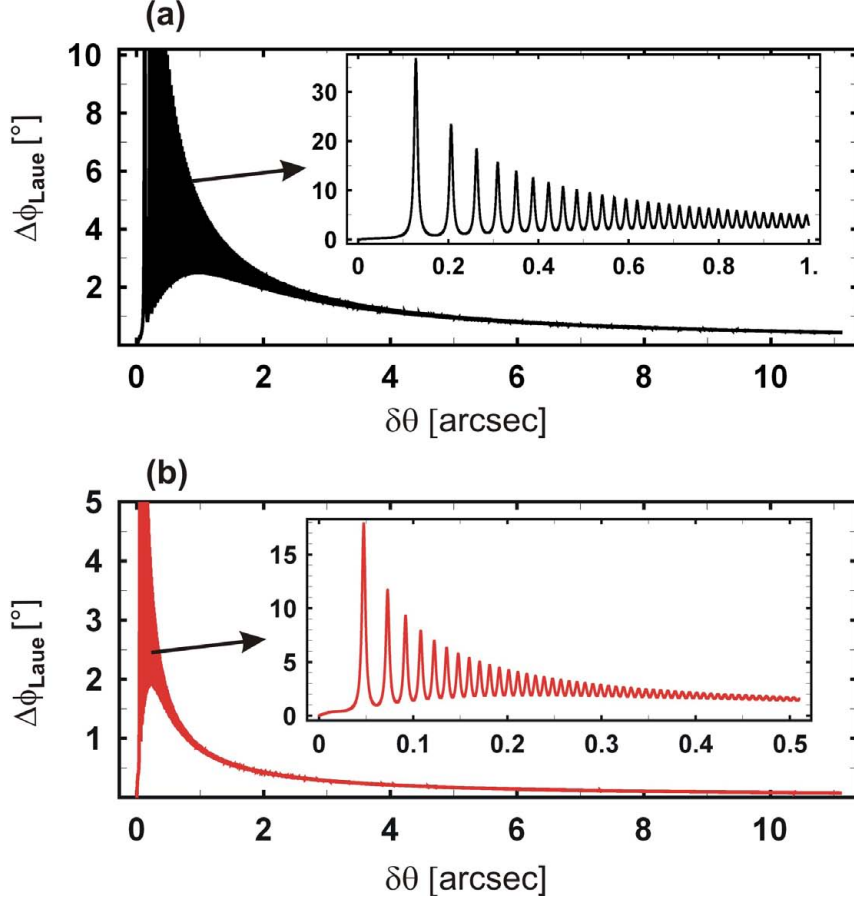


Figure 2.13: Difference in Laue phase for two disputed values of b_{ne} (2.57) for (a) Si-(220) reflection and (b) Si-(440) reflection. Other parameters as in Fig. 2.4.

The phase sensitivity due to b_{ne} at the fine structure plateaus could give rise to the hope that a precise measurement of b_{ne} could be possible there. Unfortunately the parameters D and θ_B (or equivalently λ) lead to a similar sensitivity of the Pendellösung structure position to small changes as b_{atom} , which can be shown by expanding Eq. 2.66. According to the relative difference in the scattering length (2.61) one would need to know $\tan \theta_B$ and D with a precision of the order 10^{-4} . In the case of a plate of 3 mm thickness this would mean a precision of $0.3\mu\text{m}$, for the Bragg angle or wavelength this would mean $\Delta\lambda/\lambda \approx 10^{-4}$. In principle

the thickness can be measured to such an accuracy. Uncertainties due to etching errors and surface roughness in usual interferometer preparation are nevertheless $> 1\mu\text{m}$ (compare chapt. 5). A precise wavelength measurement can yield a precision approximately the desired precision [23]. However the wavelength distribution in an experimental situation is normally of the order $\frac{\Delta\lambda}{\lambda} \approx 10^{-3} - 10^{-2}$. This distribution of thicknesses, wavelengths and finally most important $\delta\theta$ is the main reason for difficulties in an approach to determine the neutron-electron scattering length by a precision measurement of the Laue phase.

The Debye Waller factor

The neutron-electron scattering length only contributes to the phase shift in the range around a Bragg/Laue reflection but not far off in the limit of a phase shifting slab. Another parameter that only adds in this regime is the Debye Waller factor W . This factor is due to the fact that at finite temperature T atoms move around their equilibrium position. The Debye Waller factor for a harmonic crystal depends on the displacement \mathbf{r} of the single atoms and - similar to b_{ne} - on the momentum transfer \mathbf{q} (Eq. 2.10) :

$$W = \frac{1}{2} \langle (\mathbf{q} \cdot \mathbf{r})^2 \rangle_{\mathbf{T}} \quad (2.69)$$

This leads to a further correction of the atomic scattering length

$$b_{atom} \rightarrow b_{atom} e^{-W} \quad (2.70)$$

but not the nuclear scattering length b_N contained in A_0 . For room temperature the Debye Waller factor can be calculated by [24]

$$W = B \frac{\sin^2 \theta_B}{\lambda^2} = \frac{B}{4d^2} \quad (2.71)$$

where Eq. 2.16 has been used. In the case of silicon $B = 0.45(1)\text{\AA}^2$ [24]. As $W \propto 1/d^2$ the correction to the scattering length increases significantly with the order of reflection (Tab. 2.2) but as the b_{ne} contribution is independent of the Bragg angle.

Similar to the neutron-electron scattering length one could also consider a precision measurement of the Laue phase for a precise determination of the Debye Waller factor. An uncertainty in the Debye Waller factor δW by δB leads to

$$b_{atom} e^{-W \pm \delta W} \approx b_{atom} e^{-W} (1 \pm \delta W) = b_{atom} e^{-\frac{B}{4d^2}} \left(1 \pm \frac{\delta B}{4d^2} \right) \quad (2.72)$$

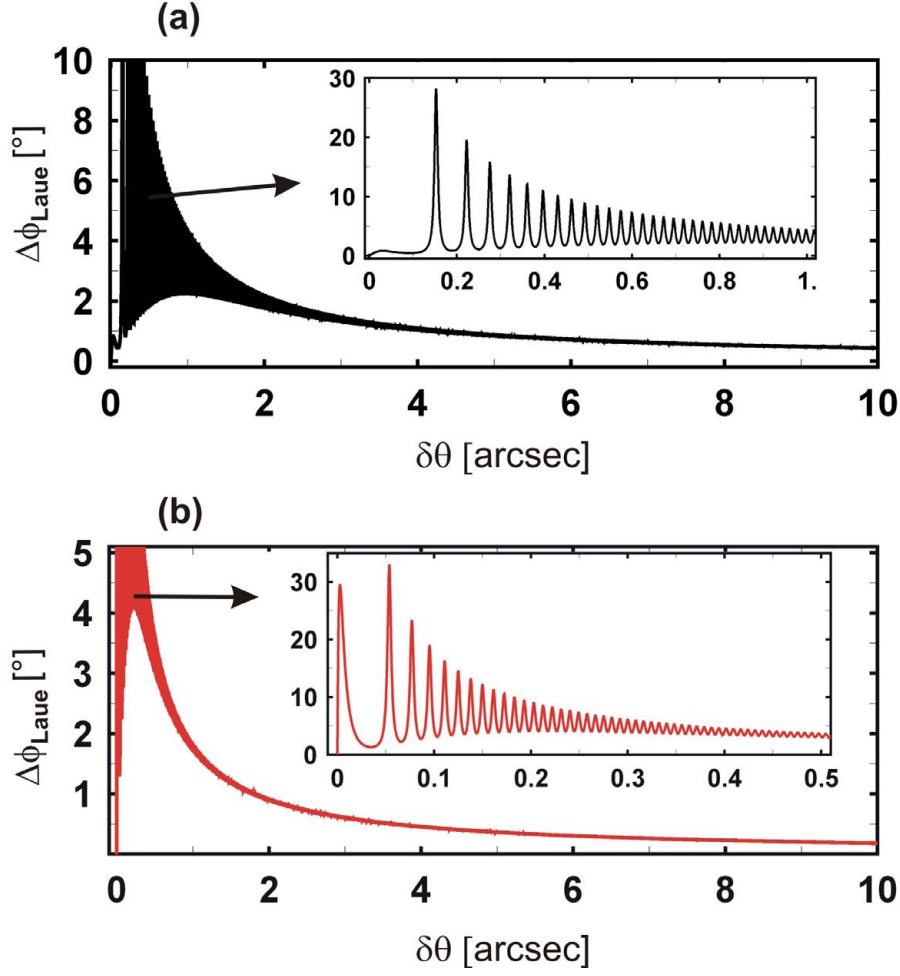


Figure 2.14: Difference in Laue phase for $B = 0.45\text{\AA}^2$ and $B = 0.455\text{\AA}^2$ for (a) the Si-(220) and (b) Si-(440) reflection. Both values are within the given error of B . Other parameters as in Fig. 2.4.

The relative uncertainty due to the given error of B (0.01\AA^2) for the (220) reflection is thereby in the order of $7 \cdot 10^{-4}$. Thus the uncertainty created by the Debye Waller factor is approximately twice as large as the present uncertainty due to b_{ne} . This uncertainty is even more pronounced at higher order reflections. Fig. 2.14 shows the phase difference created by two values of B within the given error. By the chosen value the phase difference in the (220) case is similar to the phase difference by the two disputed b_{ne} values (Fig. 2.13). For the (440) reflection the maximum phase difference is even larger than the one for the (220) reflection. This is just the other way round than for the b_{ne} difference. The reason is that the influence of the reflection order on b_{atom} is much stronger by the Debye Waller factor. According to the same argument as for the neutron-electron scattering

reflection	e^{-W}	$b_{atom}(b_{ne} = -0.0013 fm)$	$b_{atom}(b_{ne} = -0.0016 fm)$
0	1	$4.1507 fm$	$4.1507 fm$
(220)	0.9699	$4.0325 fm$	$4.034 fm$
(440)	0.8851	$3.6838 fm$	$3.6862 fm$
(660)	0.7599	$3.1642 fm$	$3.1665 fm$
(880)	0.6137	$2.5563 fm$	$2.5584 fm$

Table 2.2: Debye Waller factor for silicon ($B = 0.45 \text{\AA}^2$) and thereby corrected atomic scattering length for the (220) and higher order reflections.

length, the Debye Waller factor gives no contribution in the limits $\delta\theta \rightarrow 0$ and $\delta\theta \rightarrow \pm\infty$. To measure either the neutron-electron scattering length or the Debye Waller factor independent methods have to be applied. Alternatively one could investigate the possibility of using the inverse behavior concerning the reflection order to extract both of them by performing measurements at several orders of reflection. Anyhow it is interesting to note that a possible measurement of the Laue phase is one of very few experiments in neutron interferometry where the Debye Waller factor and the neutron-electron scattering length enter.

2.2.3 The asymmetric case

So far dynamical diffraction theory in the Laue geometry has been considered. In this case the lattice planes are assumed to be orthogonal to the surface of the crystal plate. Now we will examine deviations from this condition (Fig. 2.15) and their influence on the Laue phase. For this the transmission factor for the asymmetric case is considered [3, 25]

$$\begin{aligned}
t(\delta\theta, \gamma) = & \exp[-i(A_{0,as}(\gamma) + A_{H,as}(\gamma)y_{as}(\delta\theta, \gamma))] \cdot \\
& \cdot \left\{ \cos \left[A_{H,as}(\gamma) \sqrt{1 + y_{as}^2(\delta\theta, \gamma)} \right] \right. \\
& \left. + \frac{iy_{as}(\delta\theta, \gamma)}{\sqrt{1 + y_{as}^2(\delta\theta, \gamma)}} \sin \left[A_{H,as}(\gamma) \sqrt{1 + y_{as}^2(\delta\theta, \gamma)} \right] \right\} \quad (2.73)
\end{aligned}$$

with

$$b(\gamma) = \frac{\cos(\theta_B - \gamma)}{\cos(\theta_B + \gamma)} \quad (2.74)$$

and

$$\begin{aligned}
y_{as}(\delta\theta, \gamma) &= -\frac{(b(\gamma) - 1)v_0 + 2b(\gamma) \sin 2\theta_B \delta\theta}{2\sqrt{|b(\gamma)|}v_H} \\
\Delta_{H,as}(\gamma) &= \frac{2\pi\sqrt{|\cos(\theta_B - \gamma) \cdot \cos(\theta_B + \gamma)|}}{kv_H} \\
A_{H,as}(\gamma) &= \frac{\pi D}{\Delta_{H,as}(\gamma)} \quad A_{0,as}(\gamma) = \frac{v_0 k D}{2 \cos(\theta_B - \gamma)} \quad (2.75)
\end{aligned}$$

The lattice orientation relative to the surface normal is denoted by γ . For $\gamma = 0$ the expressions reduce to the ones of the symmetric theory.

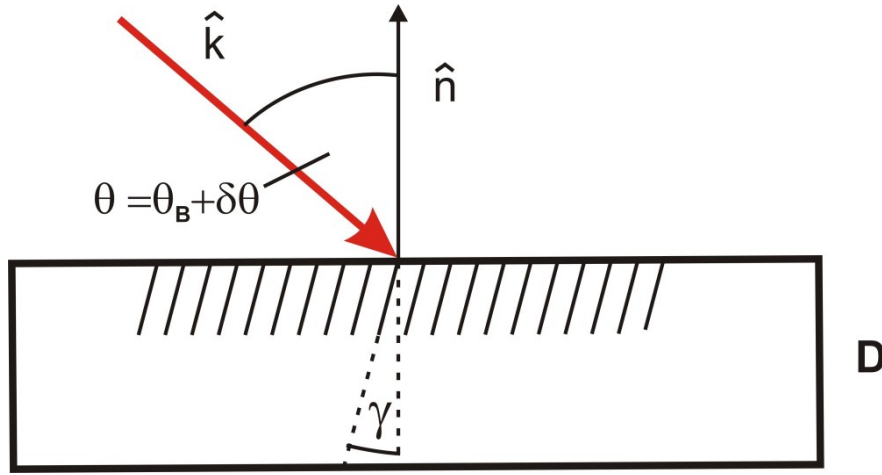


Figure 2.15: If the lattice planes enclose an angle γ with the surface normal \hat{n} , slightly modified equations of dynamical diffraction theory have to be used.

The asymmetric Laue phase $\phi_{Laue,as}$ is obtained by substituting $A_{0,H}$ and y in the symmetric formula (Eq. 2.33) by the corresponding asymmetric terms (Eq. 2.75):

$$\begin{aligned}
\phi_{Laue,as}(\delta\theta, \gamma) &= \phi_{Laue,as}(0, \gamma) - A_{H,as}(\gamma)y_{as}(\delta\theta, \gamma) + \arctan \left[\frac{y_{as}(\delta\theta, \gamma)}{\sqrt{1 + y_{as}^2(\delta\theta, \gamma)}} \cdot \right. \\
&\quad \left. \cdot \tan \left(A_{H,as}(\gamma) \sqrt{1 + y_{as}^2(\delta\theta, \gamma)} \right) \right] \quad (2.76)
\end{aligned}$$

The Laue phase in the asymmetric case is still antisymmetric with respect to y_{as} but due to (Eq. 2.75) no more antisymmetric with respect to $\delta\theta$. The center of antisymmetry is shifted to

$$\delta\theta_{center}(\gamma) = -v_0 \frac{1 - b(\gamma)}{2b(\gamma) \sin 2\theta_B} \quad (2.77)$$

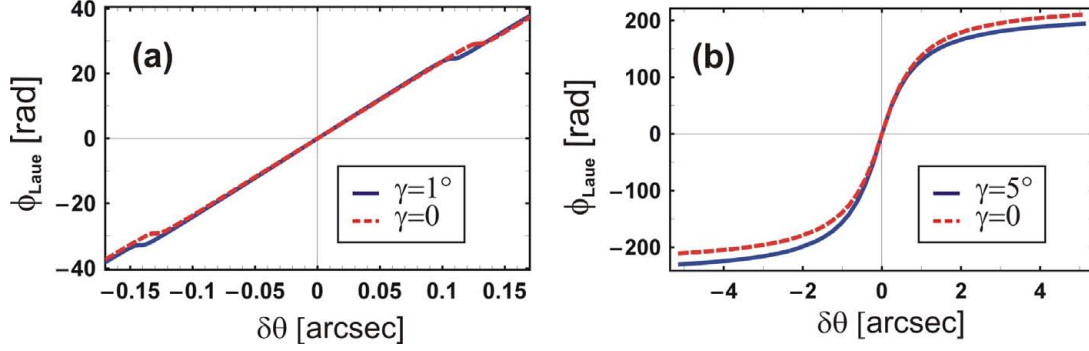


Figure 2.16: Laue phase for $\gamma = 0$ (symmetric case) and $\gamma = 1^\circ$ around Bragg (a) and in the limit of the asymptotes $\gamma = 5^\circ$ (b). Other parameters as in Fig. 2.4.

in the asymmetric case. This can be observed in Fig. 2.16 where a shift of the asymmetric curve relative to the symmetric occurs¹⁵. Thereby a significant phase difference relative to the Laue phase in the symmetric geometry - mainly at the positions of the plateaus (a) and in the limit of the asymptotes (b) - is generated.

It should be noted here, that the asymmetric shift depends on θ_B and especially on the order of reflection m :

$$\delta\theta_{center}(\gamma) \propto \frac{1}{m^2 \cdot \sin 2\theta_B} \quad (2.78)$$

Thus the shift reduces by $1/m^2$ for higher order reflections m . Fig. 2.17 shows the (220) phase difference between the symmetric and asymmetric case for a typical accuracy of lattice plane orientation $\gamma = 10'$ and for $\gamma = 10''$. For $\gamma = 10'$ the corrections from the asymmetric theory are not negligible in a precision measurement. At a higher precision of approximately $\gamma < 30''$ the symmetric theory can be used, if the goal is not a phase precision significantly below 1° . The aimed precision of crystal orientation in our experiment is within this limit. Hence the symmetric theory is sufficient for the further treatment.

¹⁵Secondary also the crystal potentials v_H and v_0 are scaled by - however different - γ dependent cosine terms. This yields a similar effect as a change in the scattering length and thereby also leads to a slight shift of the Pendellösung structure.

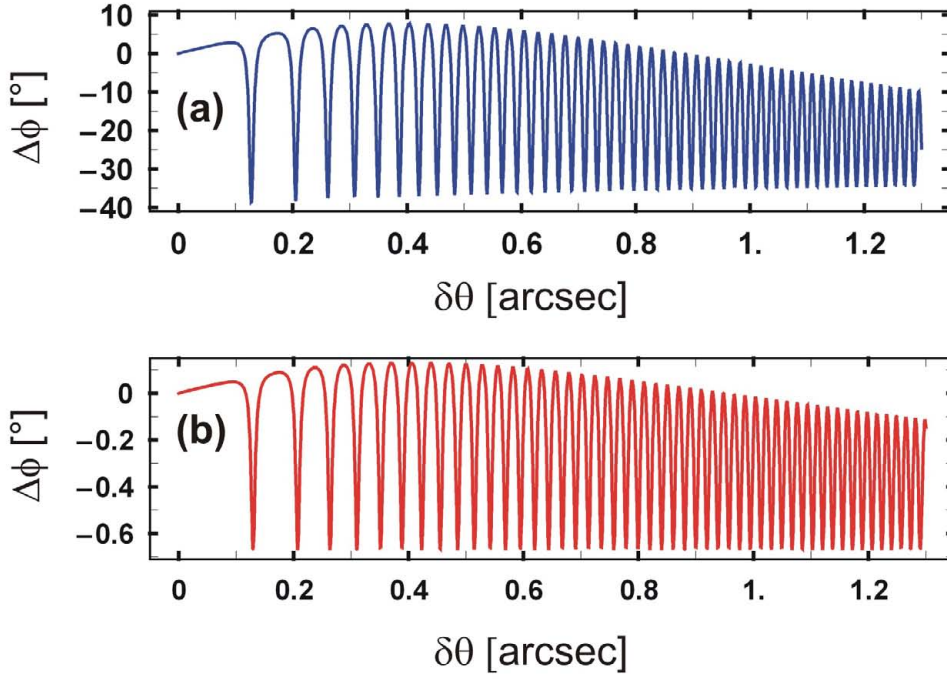


Figure 2.17: (a) Phase difference between the symmetric and asymmetric case for $\gamma = 10'$ (b) and $\gamma = 10''$. Parameters: (220) reflection, $\theta_B = 45^\circ$, $D = 3\text{mm}$.

2.3 The limits of Dynamical diffraction theory

In section 2.1 we have discussed the one- and two beam approximation as descriptions for the case of a phase shifter and a perfect crystal close to Bragg respectively. The two beam approximation is the more general ansatz and should thereby also yield the results of the one beam approximation in the limit far off Bragg. Indeed the reflected intensities vanish for this case. However also the phase shift should yield the correct limit of a phase shifter. We have already shown that for large y or $\delta\theta$ the phase approaches a constant value¹⁶

$$\lim_{y \rightarrow \pm\infty} \phi_{Laue}(y) = -A_0 \quad (2.79)$$

¹⁶In the following the potential constant $\pm\pi$ in $\phi_{Laue}(0)$ is omitted.

In the case of a phase shifter around an angle of the same value $\theta = \theta_B + \delta\theta$ there should be however to first order in $\delta\theta$ an angular dependence

$$\begin{aligned}
\phi_{\text{phaseshifter}}(\delta\theta) &= D(K_z - k_z) = D\left(\sqrt{K^2 - k_x^2} - k_z\right) \\
&= D\left[\sqrt{k^2(1 - v_0) - k^2 \sin^2 \theta} - k \cos \theta\right] \\
&= Dk\left(\sqrt{\cos^2 \theta - v_0} - \cos \theta\right) \\
&\approx -Dk \frac{v_0}{2 \cos \theta} = -A_0 \frac{\cos \theta_B}{\cos \theta} = -A_0 \frac{\cos(\theta - \delta\theta)}{\cos \theta} \\
&\approx -A_0(1 + \tan \theta_B \delta\theta)
\end{aligned} \tag{2.80}$$

where Eq. 2.13 and Eq. 2.24 have been used. This observation lead us to the conclusion, that the derivation of the equations of standard dynamical diffraction theory must include approximations that prevent a correct description in the transition range between these two cases. H. Lemmel [26] realized that a first order expansion of v_0 and v_H in the derivation is the main source of the stated problem. By a second order expansion one arrives at the following transmission and reflection amplitudes

$$\begin{aligned}
t_{\text{trans}}(\eta) &= \exp[-iA_0(1 + \bar{\epsilon}) - iA_H\eta] \left\{ \cos \left[A_H \sqrt{1 + \eta^2} (1 + \epsilon) \right] + \right. \\
&\quad \left. \frac{i\eta}{\sqrt{1 + \eta^2}} \sin \left[A_H \sqrt{1 + \eta^2} (1 + \epsilon) \right] \right\} \\
r_{\text{trans}}(\eta) &= \exp[-iA_0(1 + \bar{\epsilon}) - iA_H\eta] \sqrt{\frac{V_H}{V_{-H}}} \cdot \\
&\quad \frac{-i}{\sqrt{1 + \eta^2}} \sin \left[A_H \sqrt{1 + \eta^2} (1 + \epsilon) \right]
\end{aligned} \tag{2.81}$$

where

$$\begin{aligned}
\eta &= 2 \sin \theta_B (\sin \theta_B - \sin(\theta_B + \delta\theta)) / v_H \\
\epsilon &= \frac{v_0}{2 \cos^2 \theta_B}, \quad \bar{\epsilon} = \epsilon \frac{1 + v_H^2/v_0^2}{2}
\end{aligned} \tag{2.82}$$

Instead of y (2.23), η is now the new dimensionless representation of the miset angle $\delta\theta$. Though y was directly proportional to $\delta\theta$, the new quantity includes higher order terms:

$$\begin{aligned}
\eta &= \frac{2 \sin \theta_B}{v_H} \left(-\cos \theta_B \delta\theta + \frac{1}{2} \sin \theta_B \delta\theta^2 + \frac{1}{6} \cos \theta_B \delta\theta^3 \right) + O(\delta\theta^4) \\
&= y + y^2 \frac{v_H}{4 \cos^2 \theta_B} - y^3 \frac{v_H^2}{6 \sin^2 2\theta_B} + O(y^4)
\end{aligned} \tag{2.83}$$

As v_H is of the order 10^{-6} , the higher order contributions will only be recognized for $y \gg 1$. The Laue phase within the new approximations now reads

$$\begin{aligned} \phi_{Laue,trans}(\eta) = & -A_0(1 + \bar{\epsilon}) - A_H\eta + \arctan\left[\frac{\eta}{\sqrt{1 + \eta^2}}\right] \\ & \cdot \tan\left(A_H\sqrt{1 + \eta^2}(1 + \epsilon)\right) \end{aligned} \quad (2.84)$$

The main difference to expression 2.33 is contained in the parameters ϵ and $\bar{\epsilon}$. The term $A_0\bar{\epsilon}$ can be neglected as it contains no angular dependence and additionally $A_0\bar{\epsilon} \ll 1$. The relevant correction to the angular dependence of Eq. 2.33 is contained in the term

$$A_H\sqrt{1 + \eta^2}(1 + \epsilon) = A_H\sqrt{1 + \eta^2} + A_H\sqrt{1 + \eta^2} \cdot \epsilon \quad (2.85)$$

The ϵ dependent correction $A_H\sqrt{1 + \eta^2} \cdot \epsilon$ gives a remarkable contribution to the phase for large η . In this case the phase correction to (2.33) amounts to¹⁷

$$\phi_{Laue,corr} \approx A_H\eta\epsilon \approx A_H y\epsilon \quad (2.86)$$

and is thereby to first order linear in $\delta\theta$. This already reflects the linear correction that will lead to the proper limit of the phase shifter case. For a typical configuration ($D = 3\text{mm}$, (220)-reflection, $\theta_B = 45^\circ$) the parameters are $A_H \approx 240$, $\epsilon \approx 4.9 \cdot 10^{-6}$ and $\eta \approx 2.06 \cdot 10^5 \cdot \delta\theta$. Thus a significant correction in the order of 1° will be recognized at $\delta\theta \gtrsim 15''$. Fig. 2.18 shows the phase difference to (2.33). Due to tiny shifts of the Pendellösung structure also small phase differences can be observed at the positions of the plateaus:

$$\begin{aligned} A_H\sqrt{1 + \eta^2}(1 + \epsilon) & \approx A_H\sqrt{1 + y^2}(1 + \epsilon) = (2n + 1)\frac{\pi}{2} \implies \\ y_{Pend,Laue,trans} & \approx \sqrt{\frac{(2n + 1)^2\Delta_H^2}{4D^2(1 + \epsilon)^2} - 1} \approx \sqrt{\frac{(2n + 1)^2\Delta_H^2}{4D^2}(1 - 2\epsilon) - 1} \\ & \approx y_{Pend,Laue} \left\{ 1 - \frac{(2n + 1)^2\Delta_H^2}{(2n + 1)^2\Delta_H^2 - 4D^2} \cdot \epsilon \right\} \end{aligned} \quad (2.87)$$

¹⁷The difference between the parameter η and y is of minor relevance for the phase correction. As

$$\eta = y + y^2 \frac{v_H}{4 \cos^2 \theta_B} + O(y^3) \approx y + y^2 \cdot \frac{\epsilon \cdot e^{-W}}{2} + O(y^3)$$

and

$$\lim_{\eta \rightarrow \pm\infty} \phi_{Laue}(\eta) - \phi_{Laue}(0) = \lim_{\eta \rightarrow \pm\infty} \mp A_H\eta \pm A_H\sqrt{1 + \eta^2}(1 + \epsilon) = \lim_{\eta \rightarrow \pm\infty} \pm A_H\eta\epsilon$$

the second order contribution in y is also second order in ϵ . Thus there will only be a further significant correction at $\delta\theta \gg 1^\circ$.

Now we will show that these new approximations indeed give the correct limit to the one beam approximation by a continuous phase shift. Using

$$\begin{aligned}
A_H \eta \epsilon &= -\frac{Dk v_H}{2 \cos \theta_B} \frac{2 \sin \theta_B [\sin(\theta_B + \delta\theta) - \sin \theta_B]}{v_H} \frac{v_0}{2 \cos^2 \theta_B} \\
&= -\frac{A_0}{2 \cos^2 \theta_B} 2 \sin \theta_B [\sin(\theta_B + \delta\theta) - \sin \theta_B] \\
&= \frac{A_0}{\cos^2 \theta_B} \sin \theta_B \left(-\cos \theta_B \delta\theta + \frac{1}{2} \sin \theta_B \delta\theta^2 \right) + O(\delta\theta^3) \quad (2.88)
\end{aligned}$$

we find for $\eta \gg 1$

$$\begin{aligned}
\phi_{Laue,trans}(\eta) &\approx -A_0 + A_H \left[\text{sgn}(\eta) \cdot \sqrt{1 + \eta^2} (1 + \epsilon) - \eta \right] \quad (2.89) \\
&\approx -A_0 + A_H \eta \epsilon \\
&= -A_0 \left\{ 1 - \frac{\sin \theta_B}{\cos^2 \theta_B} \left(-\cos \theta_B \delta\theta + \frac{1}{2} \sin \theta_B \delta\theta^2 \right) \right\} + O(\delta\theta^3) \\
&\approx -A_0 (1 + \delta\theta \tan \theta_B), \quad |\delta\theta| \lesssim 1^\circ
\end{aligned}$$

This is just the expected result for the case of a simple phase shifter (2.80), where the dependence on the atomic scattering length cancels and only the nuclear part is left via A_0 .

Fig. 2.19 shows the transition range between the case of a phase shifter and the region around Bragg. Only the new approximations treat the whole angular range of the phase shift correctly. As the higher order terms of Eq. 2.84 are negligible in the interesting transition range $|\delta\theta| \lesssim 1^\circ$ the transmission and reflection amplitudes can be written as

$$\begin{aligned}
t_{trans}(y) &= \exp \left[-iA_0 - iA_H y \right] \left\{ \cos[A_H \sqrt{1 + y^2} (1 + \epsilon)] \right. \\
&\quad \left. + \frac{iy}{\sqrt{1 + y^2}} \sin \left[A_H \sqrt{1 + y^2} (1 + \epsilon) \right] \right\} \quad (2.90)
\end{aligned}$$

$$\begin{aligned}
r_{trans}(y) &= \exp \left[-iA_0 - iA_H y \right] \sqrt{\frac{V_H}{V_{-H}}} \cdot \\
&\quad \frac{-i}{\sqrt{1 + y^2}} \sin \left[A_H \sqrt{1 + y^2} (1 + \epsilon) \right] \quad (2.91)
\end{aligned}$$

and the Laue phase

$$\begin{aligned}
\phi_{Laue,trans}(y) &= -A_0 - A_H y + \arctan \left[\frac{y}{\sqrt{1 + y^2}} \cdot \right. \\
&\quad \left. \cdot \tan \left[A_H \sqrt{1 + y^2} (1 + \epsilon) \right] \right] \quad (2.92)
\end{aligned}$$

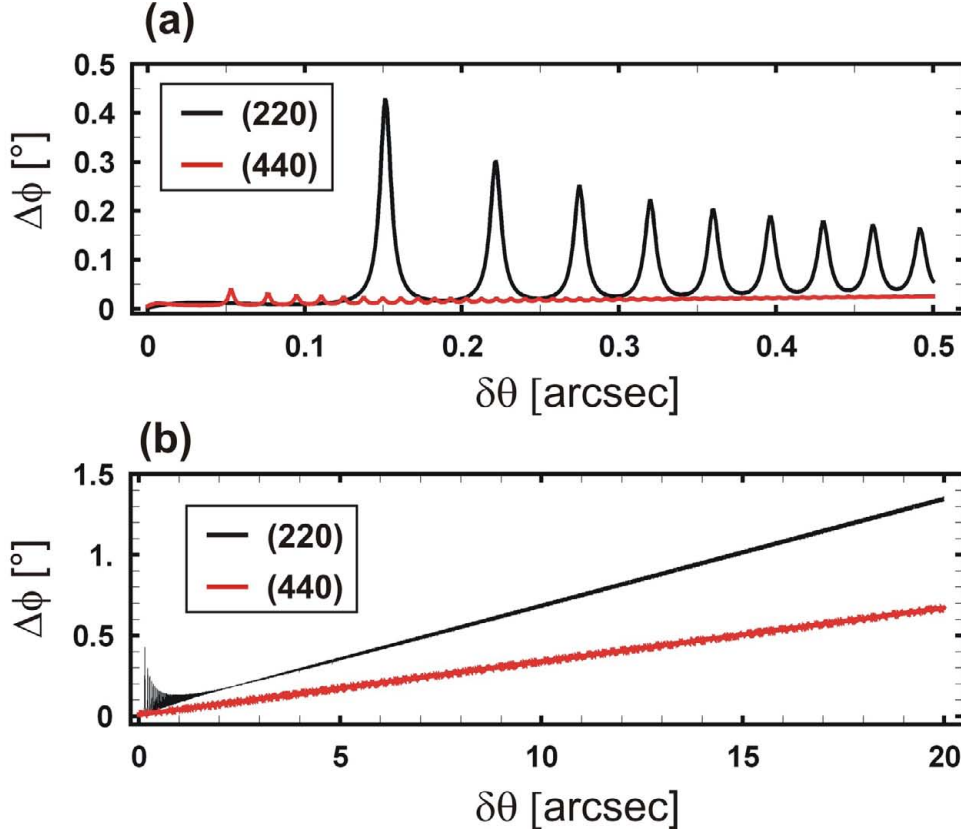


Figure 2.18: (a) Phase difference between the new approximations (2.92) and (2.33) closely around Bragg (a) and over a larger range of $\delta\theta$ (b). Parameters as in Fig. 2.4.

For the description of our experiments these approximations are sufficient, as even the corrections to the original equations will be hardly noticeable. In most cases even

$$\begin{aligned}\phi_{Laue,trans}(\delta\theta) &\approx \phi_{Laue}(\delta\theta) - A_0\delta\theta \tan \theta_B \\ &= \phi_{Laue}(\delta\theta) + A_0 + \phi_{phaseshifter}(\delta\theta)\end{aligned}\quad (2.93)$$

is a good approximation. This additionally defines the transition-range between the case where the phase effects are dominated by dynamical diffraction to the case of a simple phase shifter. The condition

$$\phi_{Laue,trans}(y_t) = \phi_{phaseshifter}(y_t) \quad (2.94)$$

is well approximated by

$$-A_H \left(y_t - \sqrt{1 + y_t^2} \right) = A_H y_t \epsilon \quad (2.95)$$

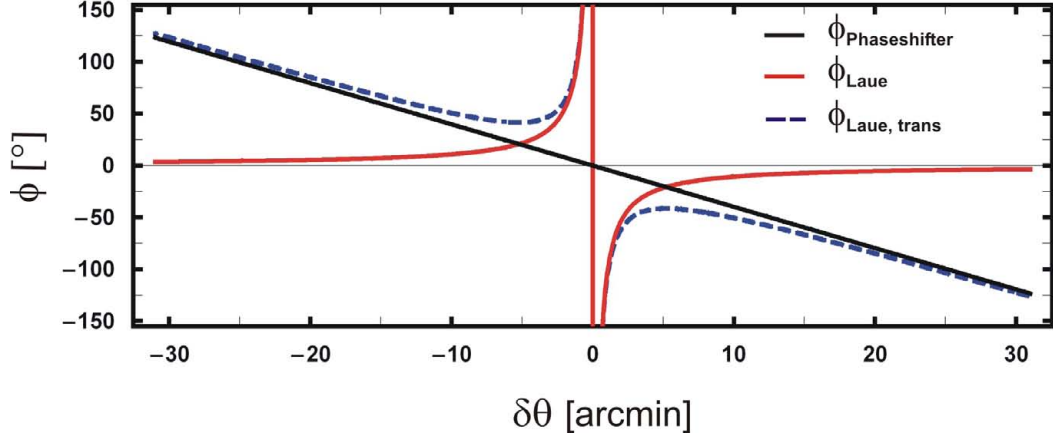


Figure 2.19: Comparison of the Laue phase by the standard approximations (2.33), the case of a phase shifter (2.86) and the new approximations (2.92). The constant $\phi_{Laue}(0)$ is subtracted. Parameters as in Fig. 2.4.

This yields

$$|y_t| = \frac{1}{\sqrt{2\epsilon + \epsilon^2}} \approx \frac{1}{\sqrt{2\epsilon}} = \frac{\cos \theta_B}{\sqrt{v_0}} \quad (2.96)$$

and in terms of $\delta\theta$

$$|\delta\theta_t| = \frac{v_H}{\sqrt{v_0}} \frac{1}{2 \sin \theta_B} \approx \frac{\sqrt{v_0} \cdot e^{-W}}{2 \sin \theta_B} \propto \frac{e^{-m^2 B / 4d_{220}^2}}{m \cdot \sin \theta_B} \quad (2.97)$$

Although in the case of higher order reflections m the pure nuclear phase shift is weaker (proportional to m), the effective range of the reflection falls off even faster according to the Darwin width (proportional to $1/m^2$). On the other hand in the case of the (220) reflection at $\theta_B = 45^\circ$ the nuclear phase shift is dominated by the Laue phase more than 5 arc minutes off Bragg! For thick samples corrections from dynamical diffraction to the ordinary phase shift can still be of the order of 1° for $\delta\theta \approx 1^\circ$. This should be accounted for in high precision measurements of nuclear scattering lengths of single crystals by proper orientation of the pieces.

Chapter 3

Laue phase and interferometry

3.1 Review of Related Experiments

In the first chapter the theoretical concept of a phase shift by Laue transmission has been discussed. So far there have been no quantitative measurements of this phase shift. However there have been a few related interferometric experiments that are interesting from a qualitative point of view.

Laue geometry

Graeff et. al [10] have performed the only directly related experiment. For the goal of studying the crystal structure function a perfect silicon crystal sample in Laue orientation has been rotated through the Bragg condition (Fig. 3.1). Although no phase shift has been extracted from the data, one can qualitatively interpret the data by an increasing phase shift in the surrounding of the Bragg condition. The interference pattern has been destroyed completely in a surrounding of approximately 5 arc seconds around the expected Bragg condition. Moreover the interference pattern is not even symmetric around the indicated Bragg condition, which is probably a result of the difficult alignment requirements. An interpretation of the data was given by a superimposition of the usual sinusoidal oscillation "with sharp oscillations caused by the diffraction induced length change of k-vectors within the sample". This variation of the k-vectors on the dispersion surface [1, 3] is of course the cause for the distinct phase shift in the surrounding of Bragg.

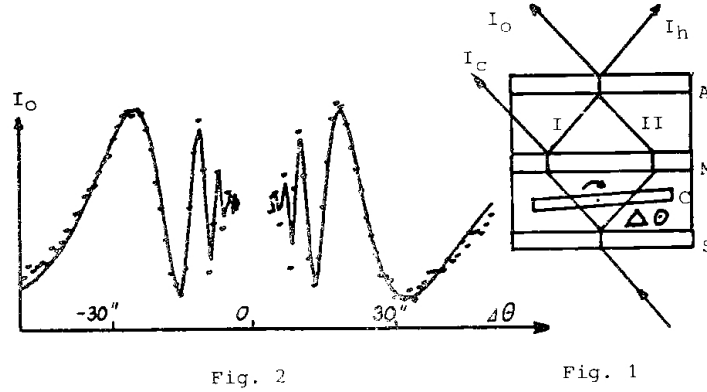


Figure 3.1: Interference pattern for a perfect silicon crystal in Laue geometry rotated through the Bragg condition [10].

Bragg geometry

In a similar experiment [11] a thick perfect crystal silicon sample in Bragg orientation has been rotated in one of the beam paths (Fig. 3.2). Similar to the Graeff experiment qualitatively an increasing phase shift can be observed when the Bragg condition is approached, on the other hand the interference pattern is rapidly destroyed in the surrounding of Bragg. Already 0.5 arc minutes away from the indicated Bragg condition the visibility is almost destroyed completely and it becomes difficult to extract data for an information on a phase shift there. This is probably due to the chosen sample thickness, which is not explicitly mentioned in the article. Judging the sketch it seems to be in the range of 1 cm. This has the benefit that remarkable deviations from the usual phase shifter behavior become already obvious more than 2 arc min away from Bragg. In contrast to the Laue experiment here the destruction of the interference pattern at least at the exact Bragg condition has an obvious reason. The transmitted beam in Bragg geometry in principle vanishes at exact Bragg which is almost similar to placing an absorber into one of the beam paths of an interferometer. This is not the case in Laue geometry¹. In [1] a qualitative interpretation of the decreasing oscillation period of the interference pattern has been given. Thus the index of refraction deviates from its normal value $n = 1 - \lambda^2 \frac{Nb_N}{2\pi}$ to $n \approx 1 - 2\lambda^2 \frac{Nb_N}{2\pi}$ at the edges of the Darwin reflection curve at $|y| = 1$.

¹In the experiment by Graeff et al. [10] additionally the change of the transmission amplitudes is equal in both interferometer paths.

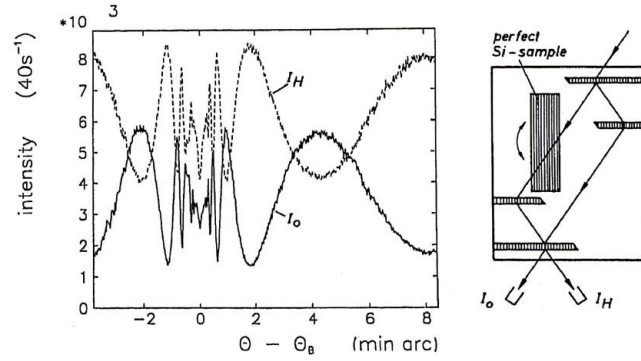


Figure 3.2: Interference pattern for a perfect silicon crystal in Bragg geometry rotated through the Bragg condition [11].

X-ray interferometer

In addition there has been a similar experiment for X-rays [27] that is interesting as explicitly a "phase shift in X-ray forward diffraction" is mentioned. Similar to the Bragg case for neutrons a model with a modified index of refraction n has been discussed. Qualitatively good agreement with the measured interference pattern could be achieved and similar to the neutron experiments an increasing phase shift can be observed. However quantitatively there is a clear disagreement as far as 0.5 arc minutes away from the indicated Bragg condition. Furthermore, similar to the neutron experiments so far, the interference pattern has been destroyed rapidly in the surrounding of Bragg. Though dynamical diffraction theory for X-rays is entirely different from the neutron case, due to the not negligible absorption in the X-ray case.

Suggested setup

Apart from these experiments, just recently a new experiment [7] has been proposed to determine the already mentioned neutron-electron scattering length. The proposed setup is similar to the Graeff experiment [10], but employs an auxiliary phase shifter, to determine the phase shift directly (Fig. 3.3).

3.2 Experimental Challenges

In chapter 2 the Laue phase for one monochromatic plane wave and its dependence on deviations from the exact Bragg condition has been discussed. In fact in any realistic experimental situation, one has to deal with a distribution of both wavelengths and misset angles relative to Bragg. Taking this into account

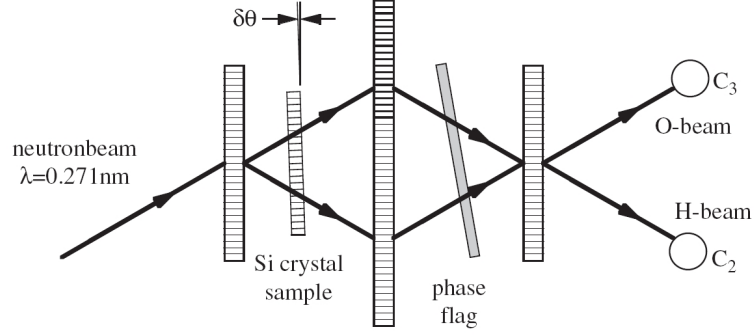


Figure 3.3: Proposed setup for a measurement of the neutron-electron scattering length in [7]. A silicon crystal sample in Laue geometry is rotated through the Bragg condition.

leads to a much more complex treatment of the phase shift than simply applying 2.33. Furthermore the experiments discussed so far have shown, that one might expect severe problems concerning the visibility of the interference pattern in the interesting region around the Bragg condition. As for an interferometer - which we are here regarding as the suitable measurement tool - the visibility is the most crucial quantity, an understanding of this problem is essential. Although some of the troubles might be addressed to alignment problems [8], there remain fundamental challenges that have to be considered in any experimental approach.

3.2.1 Defocusing and beam spreading

The first challenge is devoted to interferometer and beam geometry. One of the results of dynamical diffraction theory consists in a pronounced sweep of the probability current density

$$\mathbf{J} = \frac{i\hbar}{2m}(\Psi\nabla\Psi^* - \Psi^*\nabla\Psi) \quad (3.1)$$

within the Borrmann triangle [1, 3]. As this sweep takes place inside the crystal, Ψ labels the wave function there. Fig. 3.4 shows how a single plane wave incident on a crystal in Laue geometry is split up into two probability currents α and β inside. Defining Ω as the angle with respect to the lattice planes, and

$$\Gamma \equiv \frac{\tan \Omega}{\tan \theta_B} \quad (3.2)$$

leads in the symmetric case² to

$$\Gamma(\delta\theta) = \frac{\pm y(\delta\theta)}{\sqrt{1 + y(\delta\theta)^2}} \quad (3.3)$$

where the plus (minus) sign corresponds to the α (β) wave currents. The currents are limited to the range $-1 < \Gamma < 1$ corresponding to $-\theta_B < \Omega < \theta_B$, known as the "Borrmann fan". In the special case of a neutron wave incident at the exact Bragg condition $\delta\theta = 0$ both currents are going straight in the direction of the lattice planes.

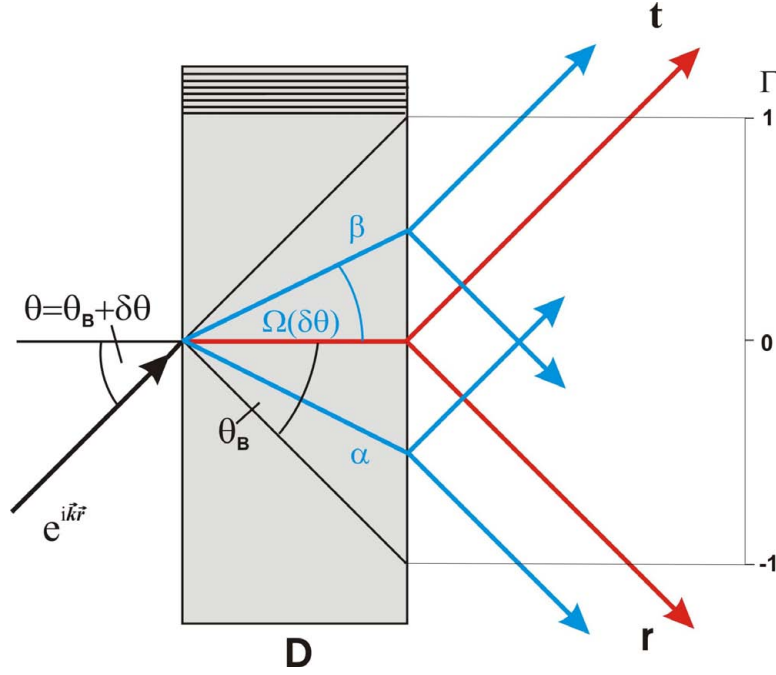


Figure 3.4: A plane wave at miset angle $\delta\theta$ relative to θ_B is split up into an α and β current. The red line shows the current directions for $\delta\theta = 0$.

The angle Ω within the crystal can be explicitly written as

$$\Omega(\delta\theta) = \pm \arctan \left(\tan \theta_B \frac{y(\delta\theta)}{\sqrt{1 + y^2(\delta\theta)}} \right) \quad (3.4)$$

This yields in the surrounding of Bragg an enormous angle amplification effect by the order of 10^6 relative to the miset angle $\delta\theta$ assuming practical conditions. Fig. 3.5 shows $|\Omega(\delta\theta)|$ for the (220) and higher order reflections. In all cases the asymptotic behavior $\lim_{\delta\theta \rightarrow \infty} |\Omega(\delta\theta)| = \theta_B$ can be observed. But it is also

²The results for the asymmetric case are treated in [3].

apparent that the angle amplification is stronger for higher order reflections m . This is due to the fact that to first order $\Omega \propto y$ and $y \propto m^2 \delta\theta$. The behavior is thereby similar to the one of the Laue phase, which shows a strong correlation between angle amplification and phase shift.

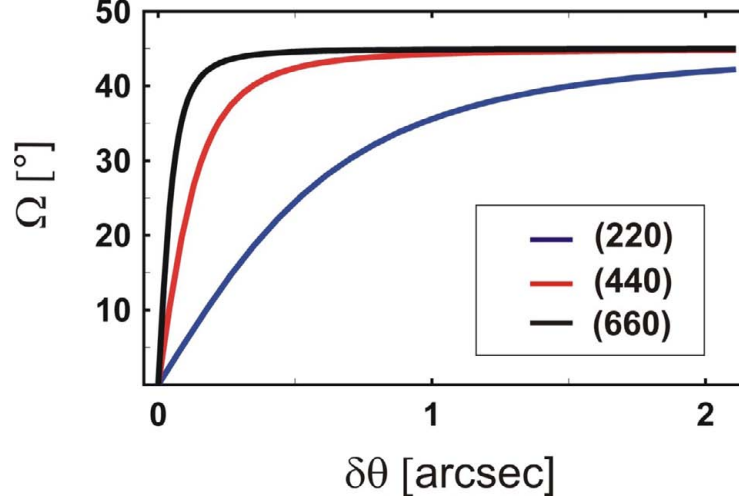


Figure 3.5: Angle amplification effect $\Omega(\delta\theta)$ for Si (220) and higher order reflections at $\theta_B = 45^\circ$.

This distinct behavior of the probability density currents is important for the consideration of an experimental setup to measure the Laue phase. The most simple approach may consist in putting one Laue crystal of thickness D inside a neutron interferometer and rotate it through the Bragg condition as in principle performed in the experiments cited in section 3.1. Fig. 3.6 now shows for such a configuration that a ray at $\delta\theta = 0$ experiences a macroscopic parallel shift of $D \sin \theta_B$. This arrangement represents basically a new interferometer geometry. The visibility of a neutron interferometer depends on the accurate compliance of the focusing conditions in the micrometer range. By this additional Laue crystal the interferometer becomes in principle "defocused". However this is not a simple defocusing constant for all wave components. In fact this defocusing depends strongly on the miset angle and is different for α ($D \cdot [\tan \theta_B + \tan |\Omega|]$) and β ($D \cdot [\tan \theta_B - \tan |\Omega|]$) contributions. This defocusing distance D_d (Fig. 3.6) has thereby a variation between

$$0 < D_d < 2D \tan \theta_B \quad (3.5)$$

In principle the beam is fanned out by the additional crystal.

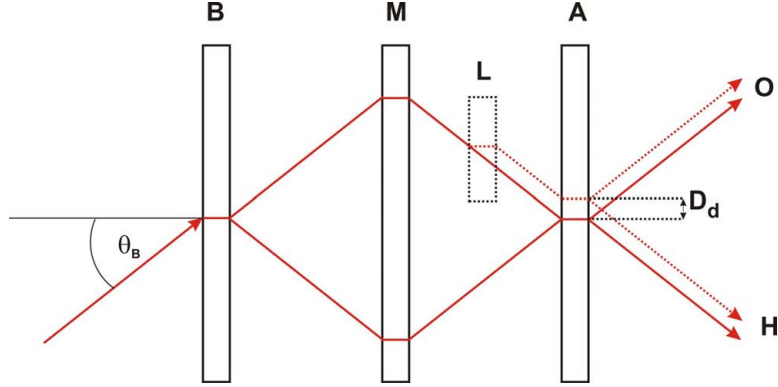


Figure 3.6: A ray exactly at the Bragg angle $\delta\theta = 0$ is shown for a three plate interferometer (full line, plates B, M and A) and with an additional lamella (L) of thickness D in Laue orientation inserted (dotted lines). In the case of the additional lamella, the rays do not meet at the analyzer plate (A), the interferometer is defocused.

Although there are contributions with very small defocusing left³, one will expect a significant decrease of the visibility in this arrangement. One approach could consist in choosing a very thin crystal plate to keep the defocusing as small as possible. However due to the magnitude of the angle amplification effect one would need impractically thin plates. Another approach could consist in inserting an equally thick crystal plate into the other beam path to compensate for the defocusing effect. Fig. 3.7 shows that for ensuring the correct focusing condition, it is essential, that in one beam path, the crystal plate is inserted before the mirror plate, in the other after the mirror plate. In general one has to insert the crystal plates in parallel beams. Otherwise the defocusing would be even twice as large as for a single crystal. The setup used in [10]⁴ and the one suggested in [7] (Fig.3.3) are just defocused arrangements in this sense. Thus the encountered visibility reduction around the Bragg condition is not just a problem of accurate alignment or inhomogeneous crystal strains, but has fundamental reasons. Though this setup could be used to measure the phase shift sufficiently far off Bragg.

Inserting two equally thick crystal plates into the interferometer as shown in Fig. 3.7 would lead to zero net phase shift. Hence it is necessary to rotate one crystal plate while the other is kept in exact Bragg condition and measure

³These are however contributions with large $\delta\theta$ which give almost no contribution to the interference pattern due to successive reflection in the interferometer.

⁴The authors claim, that in this setup "defocusing effects compensate". They probably refer to the spatial shift by the sample far off the Bragg condition and not the much stronger effect around Bragg.

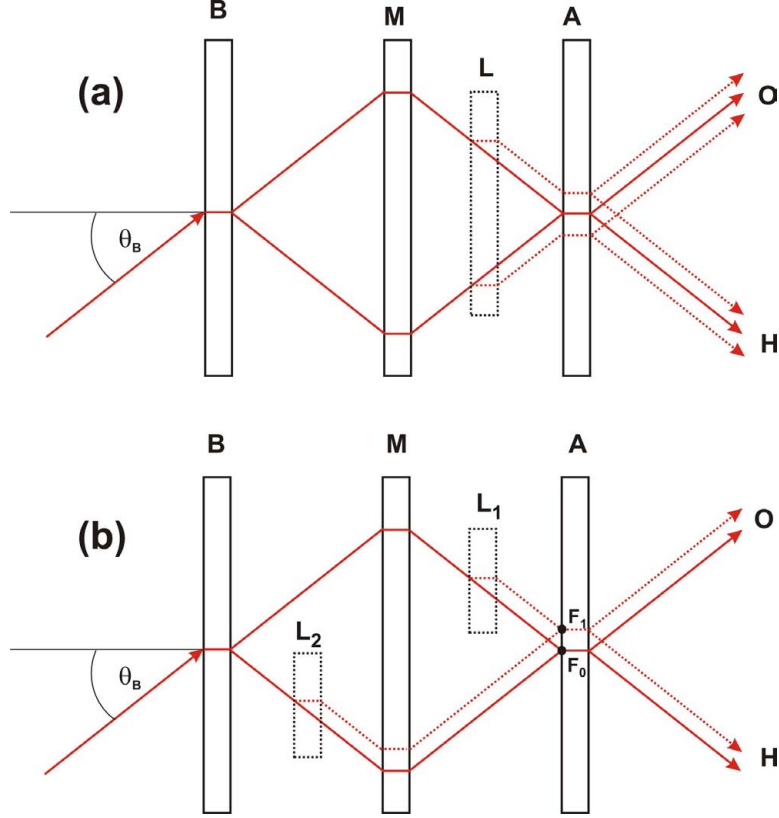


Figure 3.7: Introducing another crystal plate in the other beam path after the mirror leads to an even stronger defocusing (a) while before the mirror plate (b) the interferometer is focused again (new focuspoint F_1).

the relative phase shift. While the first plate is rotated away from the Bragg condition, the interferometer will certainly become defocused again. Nevertheless it should be possible to start in Bragg condition and measure the Laue phase closely around it. One could use even more crystal plates to compensate for all defocusing [26], but the practical realization would be rather difficult. In general this defocusing effect will be of importance for very narrow, localized beams. In this case the overlap of the two beam path contributions of the interferometer will decrease faster than for a large beam divergence. In general it should be noted that this is a more graphic illustration of the subsequent discussion as the focusing conditions are inevitably coupled to phase and intensity relations. For example the configurations shown in Fig. 3.7 can be understood by the antisymmetry of the Laue phase with respect to y :

$$\phi_{Laue}(-y) = -\phi_{Laue}(y) + 2\phi_{Laue}(0) \quad (3.6)$$

Writing down the total wave functions $\psi_{a,b}$ for the two configurations (Fig. 3.7

a, b) yields

$$\begin{aligned}
\psi_a &= \psi_{a,I} + \psi_{a,II} = \psi_0 \{t(y) + t(-y)\} \\
&= \psi_0 \cdot A(y) \{e^{i\phi_{Laue}(y)} + e^{i\phi_{Laue}(-y)}\} \\
&= \psi_0 \cdot A(y) \{e^{i\phi_{Laue}(y)} + e^{-i[\phi_{Laue}(y) - 2\phi_{Laue}(0)]}\} \\
\psi_b &= \psi_{b,I} + \psi_{b,II} = \psi_0 \{t(y) + t(y)\} \\
&= \psi_0 \cdot A(y) \{e^{i\phi_{Laue}(y)} + e^{i\phi_{Laue}(y)}\} = 2\psi_0 \cdot t(y)
\end{aligned} \tag{3.7}$$

with ψ_0 as the wave function of one beam (I,II) of the empty interferometer. While ψ_b fulfills the focusing conditions of a neutron interferometer (equal phases and amplitudes in both beam paths), ψ_a does not fulfill the phase equality due to the antisymmetry of the Laue phase. The phase difference

$$\Delta\phi_b(y) = \phi_{Laue}(y) - \phi_{Laue}(-y) = 2 \{ \phi_{Laue}(y) - \phi_{Laue}(0) \} \tag{3.8}$$

here is strongly dispersive with respect to y . The consequences of this will be discussed in the next subsection.

3.2.2 Phase averaging by beam divergence

The Laue phase shows a strong dependence on the misset angle. In any realistic experiment one has to consider divergent beams where the phase shift is averaged over the beam divergence⁵. This is analogous to the case of a phase shifter, where the phase shift is averaged over the wavelength distribution and leads to the definition of coherence lengths [1]. For a distribution of phase shifts $P(\phi)$, one obtains an average phase factor

$$\langle e^{i\phi} \rangle = \int d\phi P(\phi) e^{i\phi} \tag{3.9}$$

which can be rewritten [1] as⁶

$$\langle e^{i\phi} \rangle = e^{i\langle\phi\rangle} \int d\phi P(\phi) e^{i(\phi - \langle\phi\rangle)} \approx e^{i\langle\phi\rangle - \langle\delta\phi^2\rangle/2} \tag{3.10}$$

where the average phase shift

$$\langle\phi\rangle \equiv \int \phi P(\phi) d\phi \tag{3.11}$$

⁵In this work "beam divergence" denotes the distribution of misset angles on an arc second scale for a single wavelength. The distribution of possible Bragg angles and wavelengths is referred to as "wavelength distribution". In the following the angle $\delta\theta$ stands for the rotation of a crystal plate or the beam deflection relative to one, while $\delta\theta^*$ denotes an angle within the incoming beam distribution.

⁶This relation is only a good approximation for a narrow distribution $P(\phi)$.

and the mean fluctuation

$$\begin{aligned}\langle \delta\phi^2 \rangle &\equiv \langle \phi^2 \rangle - \langle \phi \rangle^2 \\ \langle \phi^2 \rangle &\equiv \int \phi^2 P(\phi) d\phi\end{aligned}\tag{3.12}$$

have been introduced. The term $e^{-\langle \delta\phi^2 \rangle / 2}$ describes the reduction of the visibility. Thus phase distributions in the order of radian will lead to a significant reduction of the visibility. One can understand this easily as for example a phase distribution in the order of 2π leads to an phase averaging over a whole period, which destroys the visibility. Despite the knowledge of the defocusing problem, lets consider the configuration of Fig. 3.6 for a 3mm thick crystal plate and $\theta_B = 45^\circ$. Fig. 2.4 shows that the phase shift within a beam divergence of just $-0.1'' < \delta\theta^* < 0.1''$ would already vary by approximately 40rad. One would therefore need beam divergences smaller than 10^{-2} arc seconds to not significantly decrease the visibility by phase averaging. On the other hand using realistic beam divergences in the order of 1 arc second one would need to choose the thickness of the crystal plate below $50\mu\text{m}$ to keep the phase averaging adequately small within the beam divergence.

Another strategy - as already proposed during the discussion of the defocusing effect - is to use another crystal plate in the other beam path for compensation. This creates the same steepness of the Laue phase in both beam paths. Now one can rotate one plate while keeping the other in exact Bragg condition. If the Laue phase would be strictly linear, the phase difference within the beam divergence would be constant. Indeed the Laue phase shows a nonlinear behavior for $|\delta\theta| > 0$ (Fig. 3.8).

Thus the phase difference

$$\Delta\phi_{Laue}(\delta\theta, \delta\theta^*) = \phi_{Laue}(\delta\theta + \delta\theta^*) - \phi_{Laue}(\delta\theta^*)\tag{3.13}$$

is not constant within the $\delta\theta^*$ distribution of the beam. This fact is especially pronounced at the plateaus of the Pendellösung structure and far off Bragg (Fig. 3.8, 3.9). In the latter case the phase difference tends to zero⁷. This phase averaging is the stronger, the larger the relative rotation angle $\delta\theta$ and depends on the considered beam divergence σ_θ

$$-\sigma_\theta < \delta\theta^* < \sigma_\theta\tag{3.14}$$

⁷The corrections from the correct limit to the phase shifter case - the angular dependence of the pure nuclear phase shift - are negligible.

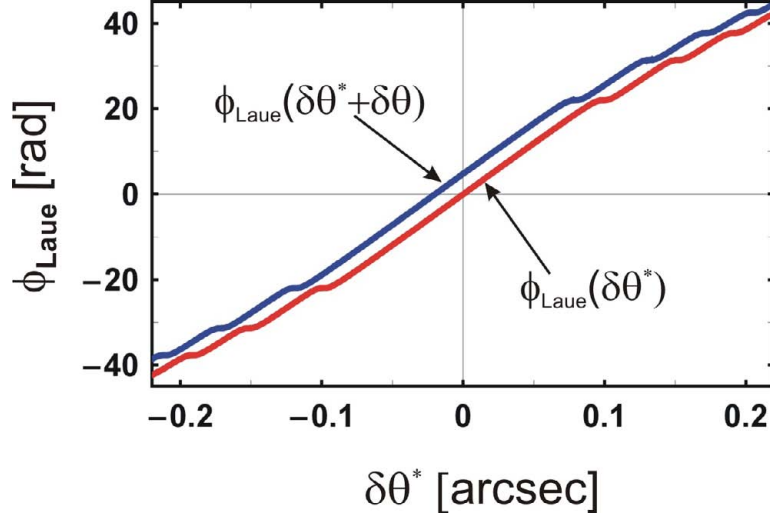


Figure 3.8: Laue phase as a function of the incoming angular beam distribution $\delta\theta^*$ for a crystal plate in exact Bragg condition ($\delta\theta = 0$) and slightly rotated off Bragg ($\delta\theta = 0.02$ arc sec). (Parameters: $\theta_B = 45^\circ$, $D = 3\text{mm}$, Si-(220) reflection, $\phi_{Laue}(0)$ is subtracted).

Furthermore Fig. 3.10 (a) shows that for the same relative crystal rotation $\delta\theta$ the phase averaging is stronger for higher order reflections. Considering large beam divergences, one can qualitatively regard the phase distribution averaged over the Pendellösung structures Fig. 3.10 (b). While in the case of very small beam divergences, one will expect the measured value to be close to $\phi_{Laue}(\delta\theta)$, the measured value will decrease with increasing divergence σ_θ . Within this simple picture one might suspect

$$\langle\phi(\delta\theta)\rangle_{\sigma_\theta \rightarrow \infty} = \lim_{\sigma_\theta \rightarrow \infty} \frac{1}{2\sigma_\theta} \int_{-\sigma_\theta}^{\sigma_\theta} \Delta\phi_{Laue}(\delta\theta, \delta\theta^*) d\delta\theta^* = 0 \quad (3.15)$$

This neglects that with increasing $\delta\theta^*$ the contribution to the interference pattern decreases, due to successive reflection at the interferometer lamellas. Fig. 3.10 (c) shows that the width of the averaged reflectivity of one crystal plate is just according to the width of the associated phase distribution (b). In a standard neutron interferometer the neutron beam experiences two reflections and two transmissions (one because of the sample crystal). Omitting the Pendellösung structures one can in this case for $|\delta\theta| \gtrsim 0$ estimate the limit of large beam divergences by

$$\langle\phi(\delta\theta)\rangle_{\sigma_\theta \rightarrow \infty} \approx \frac{\int_{-\infty}^{\infty} P(\delta\theta, \delta\theta^*) \Delta\phi_{Laue}(\delta\theta, \delta\theta^*) d\delta\theta^*}{\int_{-\infty}^{\infty} P(\delta\theta, \delta\theta^*) d\delta\theta^*} \approx 0.4 \cdot \Delta\phi_{Laue}(\delta\theta, 0) \quad (3.16)$$

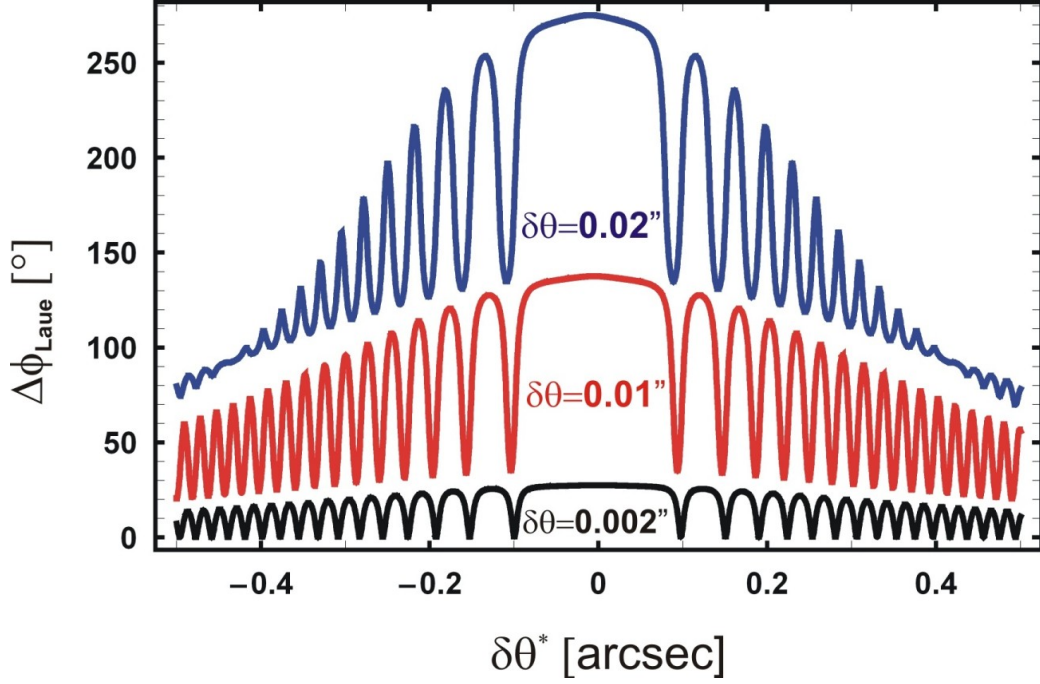


Figure 3.9: Phase difference $\Delta\phi_{Laue}(\delta\theta, \delta\theta^*)$ (3.13) within an angular distribution $\delta\theta^*$ for a crystal plate rotated by $\delta\theta$ relative to another in exact Bragg condition. (Parameters: $\theta_B = 45^\circ$, $D = 3\text{mm}$, Si-(220) reflection).

Here

$$P(\delta\theta, \delta\theta^*) = R^2(\delta\theta^*) \cdot T(\delta\theta^*) \cdot T(\delta\theta + \delta\theta^*) \quad (3.17)$$

where the averaged intensities 2.26 are used for reflected and transmitted intensities R and T and Eq. 2.37 for the phase average. In fact the average - which also depends on $\delta\theta$ - will be somewhat lower as the Pendellösung structures closely around Bragg push the average down further (Fig. 3.9). Concerning the visibility one can qualitatively suspect a significant reduction when $\Delta\phi_{Laue}(\delta\theta, 0) = \phi_{Laue}(\delta\theta)$ is of the order of 2π . In the case of a three millimeter thick plate for the (220) reflection this is already the case for $\delta\theta \approx 0.03$ arc sec. Thus one expects in the discussed arrangement a significant visibility reduction already for relative rotations of the order 0.01 arc seconds!

This qualitative analysis shows that the beam divergence has a crucial influence on the measurable phase shift and the expected visibility. However it is important to note that the concrete influence of the beam divergence depends on the special experimental configuration.

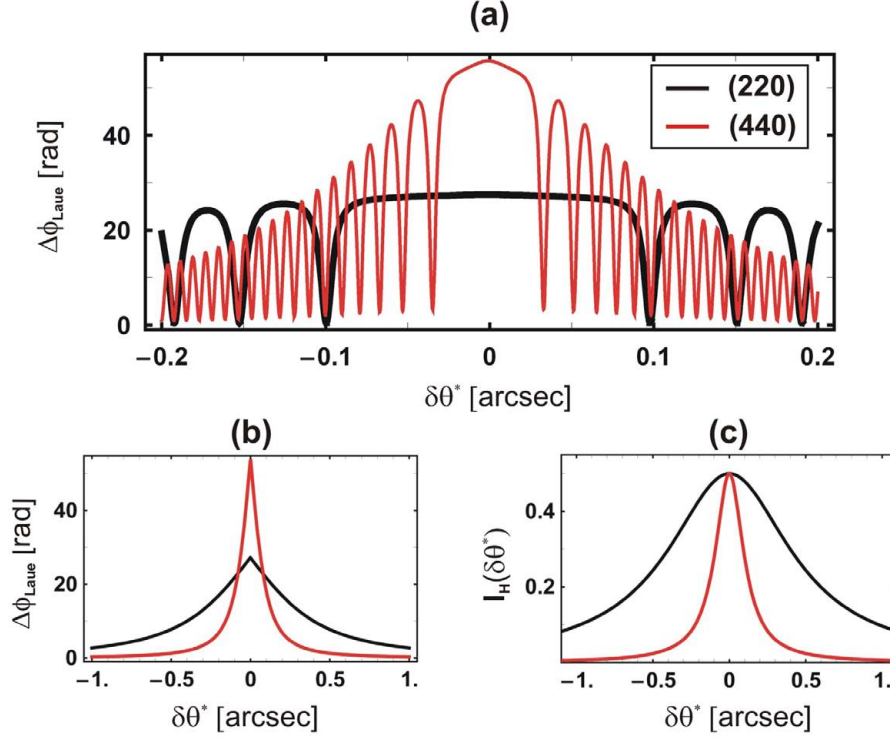


Figure 3.10: (a) Comparison of the phase difference $\Delta\phi_{Laue}(\delta\theta, \delta\theta^*)$ (3.13) of a crystal plate rotated by $\delta\theta = 0.002$ arc sec relative to another in exact Bragg condition for (220) and (440) reflection. (b) The same phase difference over a larger range of beam divergence and averaged over the Pendellösung structures using Eq. 2.37. (c) The reflectivity over the same range of beam divergence than in (b). (Parameters: $\theta_B = 45^\circ$, $D = 3\text{mm}$, Si-(220) reflection).

3.2.3 Wavelength distribution

Usually a neutron beam is not simply a mono energetic distribution of misset angles but is above all described by a distribution of wavelengths. This will have a further influence on the averaging of the Laue phase as

$$\phi_{Laue}(\delta\theta) = \phi_{Laue}(\lambda, \delta\theta_\lambda^*, \delta\theta) \quad (3.18)$$

where each λ consists of a distribution $\delta\theta_\lambda^*$. While in the case of a phase shifter the $\delta\theta$ dependence on an arc second scale is negligible, the Laue phase depends on both the wavelength and for each wavelength on the beam divergence. The contribution of each wavelength is given by the average over the beam divergence, which has been discussed in the last subsection. Fig. 3.11 shows the phase

distribution within the beam divergence for two values of a typical wavelength distribution of $\Delta\lambda/\lambda \approx 5 \cdot 10^{-3}$. The main effect consists in a shift of the positions of the Pendellösung structures, which appear according to the condition:

$$A_H(\lambda)\sqrt{1+y^2(\lambda)} = (2n+1)\frac{\pi}{2} \quad (3.19)$$

where around Bragg the dependence on $y(\lambda)$ is dominated by $A_H(\lambda)$. Hence the phase distribution is almost repeated whenever

$$A_H(\lambda) \approx (2n+1)\frac{\pi}{2} \quad (3.20)$$

In general the arising phase distribution might result in significant changes of the phase average for small beam divergences, whereas for large beam divergences, the difference will be rather small. This suggests that the averaging over the wavelength distribution will have a small effect on the measured phase shift as well as on the visibility by a further reduction of the latter.

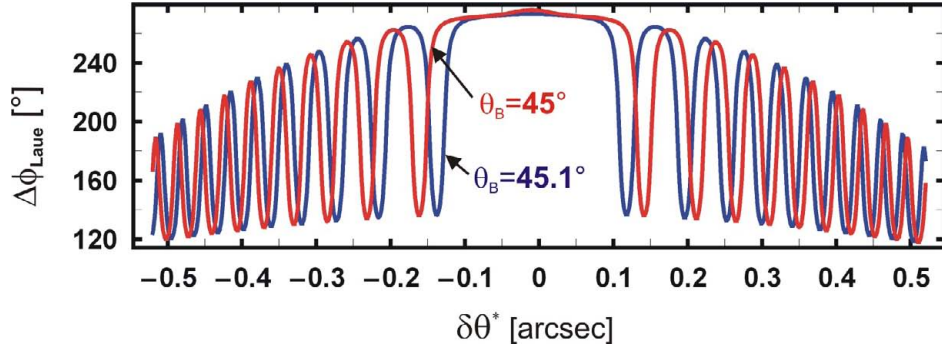


Figure 3.11: Phase difference $\Delta\phi_{Laue}(\delta\theta = 0.02'', \delta\theta^*)$ (3.13) within beam divergence $\delta\theta^*$ compared for two Bragg angles or wavelengths respectively: $\theta_B = 45^\circ \rightarrow \lambda = 2.7155\text{\AA}$ and $\theta_B = 45.1^\circ \rightarrow \lambda = 2.7203\text{\AA}$. (Other parameters: $D = 3\text{mm}$, Si-(220) reflection).

In this context it is interesting to note, that while in the case of a non-crystalline material or a crystal far off the Bragg condition, the wavelength distribution describes the phase and coherence behavior, in the case of a crystal close to the Bragg condition an energy independent, pure geometrical angle distribution is dominant.

3.2.4 Asymmetric intensities

Rotating a Laue crystal inside an interferometer also changes the beam path's intensity, as the transmitted intensity shows a strong angular dependence around

the Bragg condition. Asymmetric intensities in the two beam paths of the interferometer reduce the visibility according to [1]⁸

$$V = \frac{2\sqrt{I_1 I_2}}{I_1 + I_2} |\Gamma^{(1)}| \quad (3.22)$$

where $\Gamma^{(1)}$ is the first order coherence function. This can be also understood in the context of the visibility V and predictability P relation [28]:

$$P^2 + V^2 \leq 1 \quad (3.23)$$

as one in principle gains path information by a rotation of a Laue crystal inside an interferometer. This could be directly monitored by measuring the reflected intensity of the Laue crystal. The square relation between visibility and predictability (Eq. 3.23) is the reason that this intensity asymmetry has not a large influence on the visibility. In the extreme case of one additional Laue crystal in exact Bragg condition in one beam path and one rotated far off Bragg in the other path, the intensity ratio can be estimated to

$$\frac{I_1}{I_2} \approx \lim_{\delta\theta \rightarrow \infty} \frac{\int_{-\infty}^{\infty} P(\delta\theta, \delta\theta^*) d\delta\theta^*}{\int_{-\infty}^{\infty} P(0, \delta\theta^*) d\delta\theta^*} \approx 1.5. \quad (3.24)$$

where $P(\delta\theta, \delta\theta^*)$ is given by 3.17. Thus the visibility will still be $V \approx 0.975 \cdot \Gamma^{(1)}$. More precisely the intensity ratio depends on all the crystal thicknesses D_i of the interferometer and how the according Pendellösung structures of the transmitted and reflected intensities fit together. The problem of asymmetric intensities is not present in every setup, as for example in the setup shown in Fig. 3.3 the intensity modulation in both beam paths is equal.

3.2.5 Crystal alignment and the prism method

Summarizing there are four fundamental effects that influence the visibility and partly the measured phase shift

⁸Due to the strong nonlinearity of the Laue phase it is difficult to find analogies to the relations for the usual coherence function obtained to the relations for the usual coherence function obtained via a momentum distribution $\rho(k)$ and a spatial shift Δ

$$\Gamma^{(1)}(\Delta) = \int \rho(\mathbf{k}) e^{i\mathbf{k}\Delta} d\mathbf{k} \quad (3.21)$$

However one can at least define a related coherence function - depending on the involved crystal thicknesses, $\delta\theta$ and the beam divergence - via Eq. 3.22.

1. The defocusing effect - a geometrical effect related to interferometer geometry and beam spreading, with principal effects on the visibility.
2. The beam divergence - an effect related to phase averaging and thereby to a fundamental coherence property similar to the wavelength distribution in the case of a phase shifter
3. The wavelength distribution is another phase averaging effect related to coherence, which is however strongly dominated by the beam divergence
4. Intensity modulations within the beam paths, which might influence the visibility but also the weighting of the phase distributions concerning the phase averaging

However these effects can not be viewed independently but are strongly coupled. This already constitutes the basis for an understanding and description of experiments related to the Laue phase and in general measurements in a neutron interferometer around the Bragg condition.

Finally there remains the experimental problem of crystal alignment. The requirements are similar to the alignment of a split perfect crystal interferometer, which has so far only been realized for X-rays [13, 12, 14]. There are two critical axis of alignment. The first is the Bragg axis concerning the discussed misset angle $\delta\theta$. Hitherto considerations for a crystal plate with a thickness in the order of millimeters lead to the conclusion, that an alignment precision of at least 0.01 arc seconds is necessary to remain the visibility. Furthermore relative rotations in the order of 10^{-4} arc seconds might result in relative phase shifts in the order of degrees. Hence for a precise measurement a stability to at least this precision has to be maintained. The other sensitive axis corresponds to a rotation around the surface normal of the crystal plate. A misalignment with respect to the lattice planes of the interferometer lamellas might result in horizontal Moire fringes [8]. The period of the fringes is determined by the crystal lattice spacing d and the relative misalignment $\delta\alpha$

$$\Lambda = \frac{d}{\delta\alpha} \quad (3.25)$$

To ensure adequate visibility, this period should be significantly larger than the beam height, as usual neutron detectors integrate over the whole beam area. The requirement $\Lambda \gg 1\text{cm}$ demands an accuracy of $\delta\alpha \lesssim 10^{-3}$ arc sec. To achieve and especially remain such an accuracy with respect to two axis during the time of the experiment constitutes a severe technical challenge. Additionally there could be problems due to small disturbing crystal strains by the support of the sample crystal. In the context of a measurement of the neutron-electron scattering length

A. Ioffe [8] has therefore proposed to cut the sample crystals together with the neutron interferometer so that they are monolithically fixed to it. The necessary rotation can instead be achieved by a beam deflection relative to the sample crystal. The idea of this approach is similar to the technique of building a perfect crystal interferometer. Instead of trying to align perfect crystals, one can use the prealignment achieved by crystal growing. Fig. 3.12 shows a possible setup, where instead of rotating lamella L_2 , the beam is deflected in front by using the sketched prism arrangement. Altogether four prisms are needed to compensate defocusing effects within the interferometer.

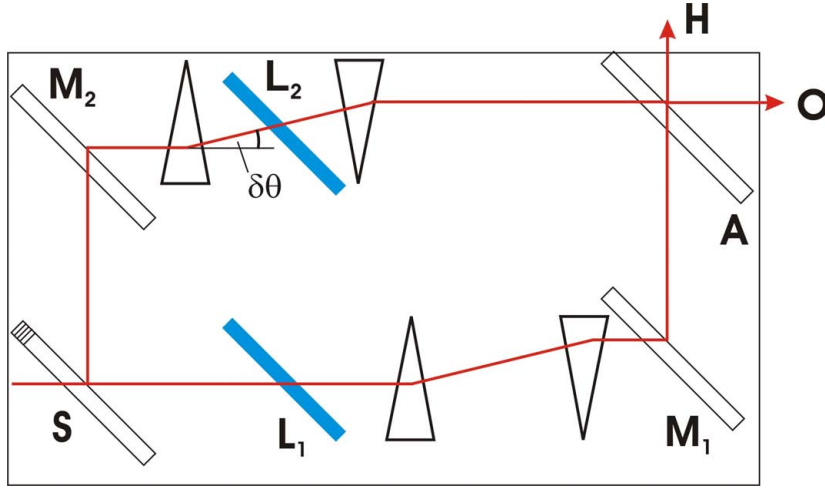


Figure 3.12: Possible setup to measure the Laue phase induced by L_2 relative to L_1 via beam deflection in front of L_2 . The beam paths within the prisms and lamellas are simplified.

To continuously change the beam deflection $\delta\theta$ in front of the crystal slabs, prisms with apex angle β are rotated by an angle α around the incident beam direction, Fig. 3.13, as to first order there is only a sensitivity relative to the crystal lattice planes. The relevant beam deflection is then given by

$$\delta\theta = \delta \sin \alpha \quad (3.26)$$

where $\delta \propto (1 - n)$ (chapter 6) is the refraction angle of the prism. Due to $(1 - n) \approx 10^{-5}$ a very high resolution in $\delta\theta$ can be achieved. The final setup and the measurements will be discussed in chapter 7.

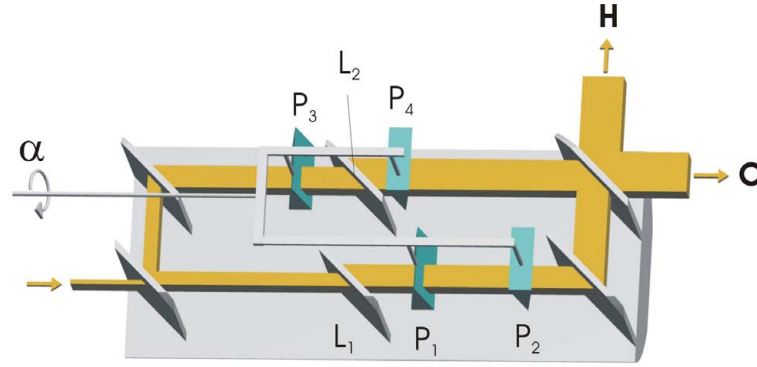


Figure 3.13: Continuous tuning of the relevant beam deflection $\delta\theta = \delta \cdot \sin \alpha$ in the scattering plane by a rotation of the prisms with beam deflection δ by an angle α around the incident beam direction. Fig. 3.12 corresponds to the case $\alpha = 90^\circ$.

Chapter 4

Numerical interferometer calculation

In the last chapter we have shown that a simple use of Eq. 2.33 will not give a satisfactory description of a Laue crystal inside a neutron interferometer. It is necessary to take the beam divergence and the wavelength distribution into account. A first approach for a phase calculation could consist in an averaging of Eq. (3.13) over both of these distributions of the incoming beam $P(\lambda)$ and $P(\delta\theta^*)$

$$\begin{aligned}\phi(\delta\theta) &= \langle \langle \Delta\phi_{Laue}(\delta\theta, \delta\theta^*) \rangle_{\delta\theta^*} \rangle_{\lambda} \\ &= \frac{\int_{-\infty}^{\infty} P(\lambda) \int_{-\infty}^{\infty} P(\delta\theta^*) \cdot P_I(\delta\theta^*, \delta\theta, D_i) \Delta\phi_{Laue}(\delta\theta, \delta\theta^*) d\delta\theta^* d\lambda}{\int_{-\infty}^{\infty} P(\lambda) \int_{-\infty}^{\infty} P(\delta\theta^*) \cdot P_I(\delta\theta^*, \delta\theta, D_i) d\delta\theta^* d\lambda} \quad (4.1)\end{aligned}$$

Here it is important to introduce another distribution function $P_I(\delta\theta^*, \delta\theta, D_i)$ that takes a further modification of the incoming $\delta\theta^*$ distribution by all interferometer lamellas into account. As it is necessary to resolve the Pendellösung structures¹ this distribution function depends on all crystal lamella thicknesses D_i . In general however $|\delta\theta|$ is not equal for both beam paths, thereby the intensities are asymmetric and consequently expression 4.1 is not strictly correct. The defocusing discussed in the last chapter is another aspect that would not be included in this approach. In fact one needs a model that does not only take the beam properties but the whole interferometer geometry into account. Additionally it would be desirable to obtain information on the visibility. Such a model can consist in spherical wave theory applied to the whole interferometer setup.

¹For example for one single sample crystal the transmission factor has its minima at the Pendellösung plateaus. Thereby these would give a minor contribution to the phase average. Another crystal of the same thickness in the beam, where a reflection is of interest, could however enlarge this contribution.

Just recently such a model with an accompanying program has been developed by H. Lemmel [26, 16, 29], which can now be adapted to our problem. Alternatively one could also apply an incoherent model by integrating the intensities of plane waves over the beam divergence and fitting the intensities similar to the subsequent discussion.

4.1 Spherical wave model

Spherical waves can be considered as a coherent superposition of plane waves with a certain angular divergence. This is an important observation, as the plane wave solutions for dynamical diffraction theory are well known. We have already stated, that in the surrounding of the Bragg condition the beam divergence is much more important than the wavelength distribution. To simplify the model and especially save computational time, we are here considering a monochromatic beam with a given wavelength. Another restriction is a reduction of the problem to a plane². In fact thereby one does not create a three-dimensional spherical wave but rather a two-dimensional beam with a representation in polar coordinates. For this beam one can now consider a certain misset angle distribution $g(\delta\theta)$ relative to the Bragg angle determined by the wavelength. The wave function in momentum space now reads

$$\psi(\mathbf{k}) = \psi(k, \delta\theta) = \delta(k - k_0)g(\delta\theta) \quad (4.2)$$

The wave function in real space is obtained by a Fourier transform

$$\begin{aligned} \psi(\mathbf{r}) &= \frac{1}{2\pi} \int d^2k \psi(\mathbf{k}) e^{i\mathbf{k}\mathbf{r}} = \frac{1}{2\pi} \int_{-\pi}^{\pi} d\delta\theta \int_0^{\infty} dk k e^{i\mathbf{k}\mathbf{r}} \delta(k - k_0) g(\delta\theta) \\ &= \frac{k_0}{2\pi} \int_{-\pi}^{\pi} d\delta\theta e^{i\mathbf{k}_0\mathbf{r}} g(\delta\theta) \end{aligned} \quad (4.3)$$

One can think of such a wave function as originating from a point source, as it would be created by a plane wave incident on an extremely narrow slit. In this case one could use a Gaussian angle distribution

$$g(\delta\theta) = \frac{1}{\sqrt{2\pi\sigma_\theta^2}} e^{\frac{-\delta\theta^2}{2\sigma_\theta^2}} \quad (4.4)$$

where σ_θ is the width of the $\delta\theta$ distribution. This width of the beam divergence together with the distance to the source $\rho = |\mathbf{r} - \mathbf{r}_0|$ determine the intensity

²The dimension normal to this plane is of no significance, as long as effects of the vertical divergence of the incoming beam can be neglected.

distribution and the related beam width σ_ζ , at the transversal coordinate ζ [26]:

$$\begin{aligned} |\psi(\rho, \zeta)|^2 &= \frac{1}{\sqrt{1 + k_0^2 \rho^2 \sigma_\theta^4}} e^{\frac{-\zeta^2}{2\sigma_\zeta^2}} \\ \sigma_\zeta^2 &= \frac{1}{2} \left(\frac{1}{k_0^2 \sigma_\theta^2} + \sigma_\theta^2 \rho^2 \right) \end{aligned} \quad (4.5)$$

Via this relation one can calculate the position \mathbf{r}_0 of the point source, if a certain beam width at a certain distance ρ is desired. In reality the angular acceptance

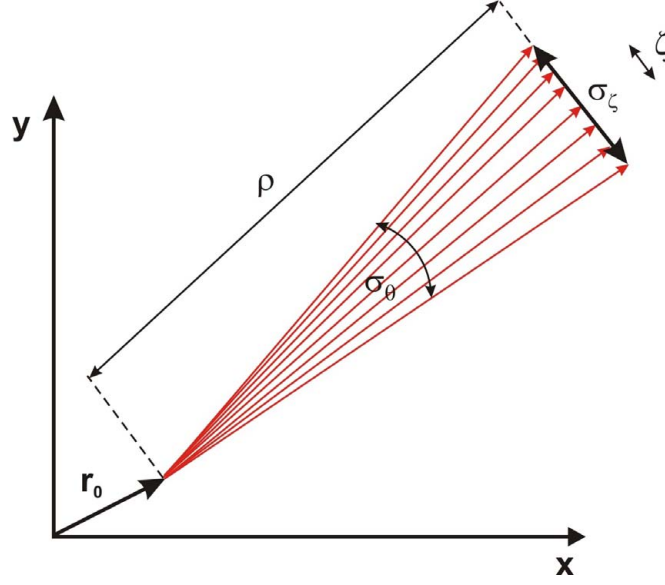


Figure 4.1: A spherical beam with divergence σ_θ can be described as a coherent superposition of a divergent bundle of plane waves. Beam width σ_ζ and source distance ρ determine each other.

of the interferometer is restricted to the arc second range. If one chooses $\sigma_\theta \gg \Delta\theta_{1/2}$ most of the plane wave contributions will not give any contribution to the interference pattern. In addition large beam divergences would require long computation times. Choosing $\sigma_\theta \approx \Delta\theta_{1/2}$ in the Gaussian distribution would however underestimate plane wave contributions for $0 < \delta\theta^* \lesssim \Delta\theta_{1/2}$ as normally in an experimental setup there are no beam collimations of the order of arc seconds. Thus using a square function for the angle distribution

$$g(\delta\theta) = \theta(\delta\theta + \sigma_\theta) - \theta(\delta\theta - \sigma_\theta) \quad (4.6)$$

seems more appropriate. In this case the beam profile is also a square function with width

$$\sigma_\zeta = \sigma_\theta \cdot \rho \quad (4.7)$$

at distance ρ . In comparison to the originally implemented Gaussian distribution it is sufficient to choose σ_θ in the order of several $\Delta\theta_{1/2}$ to include the relevant contributions accepted by the interferometer lamellas. Furthermore, there is another reason for preferring a square distribution. If a perfect crystal monochromator is used - as in the case of instrument S18 - the incoming angular distribution per wavelength should be determined by the reflection width of the monochromator. This width is just given by the Bragg reflection width of the monochromator, where the Bragg reflection curve for thick crystals is well described by

$$\begin{aligned} R(\delta\theta) &= 1 & |y(\delta\theta)| < 1 \\ R(\delta\theta) &= 1 - \sqrt{1 - \frac{1}{y(\delta\theta)^2}} & |y(\delta\theta)| > 1 \end{aligned} \quad (4.8)$$

In the most important range $|y(\delta\theta)| < 1$ it is thereby given by a square function. However the half width of the Bragg reflection curve is rather $y_H = \frac{4}{\sqrt{3}} \approx 2.3$ and thereby a factor of approximately 1.15 larger than the plateau. Fig. 4.2 (a) compares the Bragg reflection curve with a Gaussian- and square distribution of width $\sigma_\theta = \delta\theta_{y=1}$, whereas Fig. 4.2 (b) shows a comparison with the averaged reflectivity of one Laue crystal, which is a measure for the angular acceptance of the interferometer.

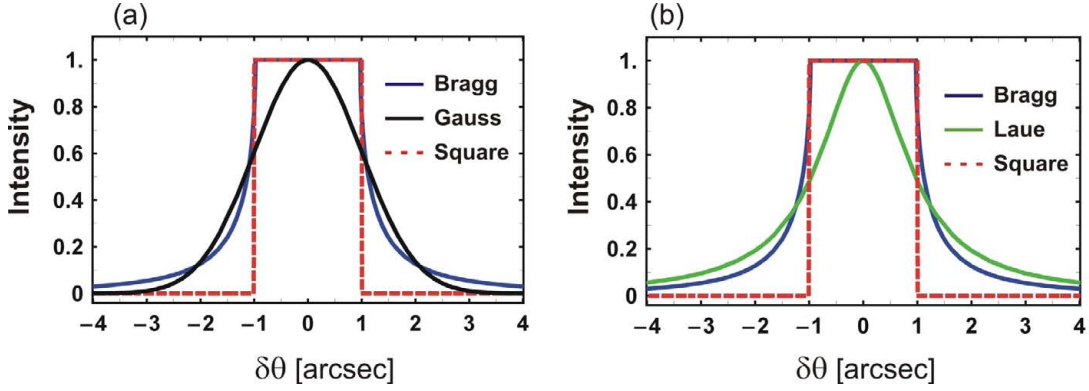


Figure 4.2: Bragg reflection curve for (220) reflection at $\theta_B = 45^\circ$ compared with an angular square- and Gaussian distribution with $\sigma_\theta = 1''$ (a) and an according Laue reflection curve (b).

Another possibility consists in the use of a mosaic crystal as monochromator. As this type of monochromator consists of many small perfect crystals with a certain angle distribution much larger than the Darwin width of the single crystals the beam divergence of the incoming beam in this case would be large in comparison to $\Delta\theta_{1/2}$. In this case a square function with $\sigma_\theta \gg \Delta\theta_{1/2}$ should be appropriate for the incoming beam.

For the numerical calculation it is of course useful to use the dimensionless y parameter instead of the miset angle $\delta\theta$

$$\begin{aligned} g_{square}(y) &= \theta(y + \sigma_y) - \theta(y - \sigma_y) \\ g_{Gaussian}(y) &= \frac{1}{\sqrt{2\pi\sigma_y^2}} e^{-\frac{y^2}{2\sigma_y^2}} \\ \psi(\mathbf{r}) &= \int dy e^{i\mathbf{k}_0 \mathbf{r}} g(y) \end{aligned} \quad (4.9)$$

Eq. 4.9 constitutes a suitable normalized representation for the incoming beam. Considering now a simple setup with only one crystal in Laue orientation the transmitted and reflected wave functions can be calculated via

$$\begin{aligned} \psi_t(\mathbf{r}) &= \int dy e^{i\mathbf{k}_0 \mathbf{r}} g(y) t(y) \\ \psi_r(\mathbf{r}) &= \int dy e^{i\mathbf{k}_H \mathbf{r}} g(y) r(y) \end{aligned} \quad (4.10)$$

This approach can be easily extended to a specific arrangement of crystal plates like a neutron interferometer. The two beam path contributions $\psi_{OI,II}(\mathbf{r})$ to the O-beam are given by an integral over the plane wave solutions $\psi_{OI,II}(\mathbf{r}, y)$

$$\psi_{OI,II}(\mathbf{r}) = \int g(y) \psi_{OI,II}(\mathbf{r}, y) dy \quad (4.11)$$

The absolute square of the superposition of the two wave functions yields the intensity of the O-beam at a specific point \mathbf{r} .

$$\begin{aligned} \psi_O(\mathbf{r}) &= \psi_{OI}(\mathbf{r}) + \psi_{OII}(\mathbf{r}) \\ I_O(\mathbf{r}) &= |\psi_O(\mathbf{r})|^2 \end{aligned} \quad (4.12)$$

$I_O(\mathbf{r})$ yields the intensity profile in the O-beam, an integral over this profile or rather the transverse coordinate ζ yields the total O-beam intensity

$$I_O = \int I_O(\mathbf{r}) d\zeta \quad (4.13)$$

Applying an auxiliary phase shift χ via $\psi_{O,I}(\mathbf{r}) e^{i\chi}$ to one beam path, one obtains similar to the experimental case an intensity $I_O(\chi)$ that can be fitted by a (co-) sine function to obtain both phase shift ϕ and visibility V

$$I_O(\chi) = I_{O,mean} [1 + V \cos(\phi + \chi)] \quad (4.14)$$

The same procedure is valid for the H-beam. Carrying out the involved integrals numerically it is important to choose the step size Δy small enough to resolve

all Pendellösung structures and to resolve the structures in the transversal beam profile in the case of the ζ integration. This approach has been implemented by H. Lemmel in the program *ifmsim* [26, 16, 29]. With this program any possible interferometer geometry can be analyzed. Just recently this program has been adopted to our needs, as one can also rotate specific lamellas relative to the others and the incident beam. The most important parameters that can be chosen by the user are

- exact interferometer geometry (lamella distances, thicknesses, lattice plane orientation)
- angle $\delta\theta$ of each lamella relative to the ideal Bragg condition
- type of reflection (lattice plane distance)
- Bragg angle
- beam type: square or Gaussian distribution
- beam divergence σ_θ
- beam width σ_t (this does not make any difference for our calculations but might be useful for calculating beam profiles)
- angle α of the incoming beam (center) relative to the interferometer (Position in the rocking curve)
- physical quantities like b_{ne} , B (Eq. 2.71)

In the following the results for some interesting configurations are shown. Most of the calculations have been performed for both square and Gaussian beam distribution, with rather small differences for the same σ_θ . In the following usually the results for the square distribution are shown if not explicitly mentioned.

In addition numerical calculations by a direct integration of the phase shift have been carried out. A comparison will be given in Fig. 4.9.

4.2 One crystal plate in one beam path

One of the conclusions of the last chapter has been, that one single crystal plate inserted close to the Bragg condition into a neutron interferometer will decrease if not destroy the visibility. Applying the spherical wave model more quantitative estimations shall now be given. Therefore the configuration shown in Fig. 4.3 is

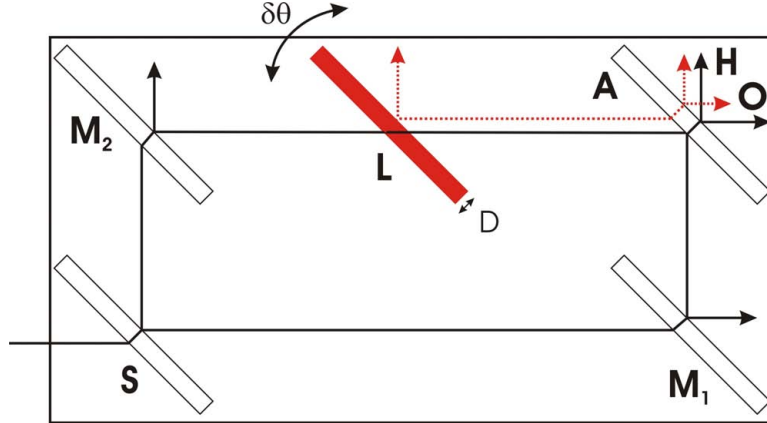


Figure 4.3: Neutron interferometer with an additional crystal lamella L. The visibility can be studied either as a function of the thickness D or by a rotation of the plate with fixed thickness by $\delta\theta$.

considered, where first the additional crystal lamella is assumed to be aligned in perfect Bragg condition ($\delta\theta = 0$).

Now the visibility can be studied as a function of the crystal thickness D . The result is shown in Fig. 4.4 for the (a) (220) and (b) (440) reflection. Depending somewhat on the beam divergence σ_θ the visibility is rapidly destroyed at a thickness of $D \gtrsim 20\mu\text{m}$ (220) and $D \gtrsim 40\mu\text{m}$ (440), although some damped reappearance of visibility can be observed at larger thicknesses. A comparison with the Laue phase for small crystal thicknesses (Appendix A), reveals that the sharp drop of the visibility at $D \gtrsim \Delta_H/2$ is explained by the jump of the asymptotes from 0 to $\pm\pi$. Thereby the phase distribution strongly increases to a range of 2π . Hence in this regime also the visibilities are governed by the Pendellösung length. The dependence of the Pendellösung length on the order of reflection

$$\Delta_H \propto m \quad (4.15)$$

explains the faster decrease of the visibility for the (220) reflection.

How does this compare to the case, if the crystal plate would have not been cut in Laue orientation and would thereby just act as a phase shifter? There the visibility is simply described by the incident wavelength distribution. It is now interesting to note, that the sample crystal³ is just orientated in the con-

³Here it is assumed that the sample crystal has the same lattice orientation as the interferometer and is made of the same material. In the case, that crystals of another orientation or material are inserted, the configuration is in general between the configuration for longitudinal and transversal coherence. Moreover in this case the crystal would be in a dispersive arrangement, where the influence of the wavelength distribution becomes crucial.

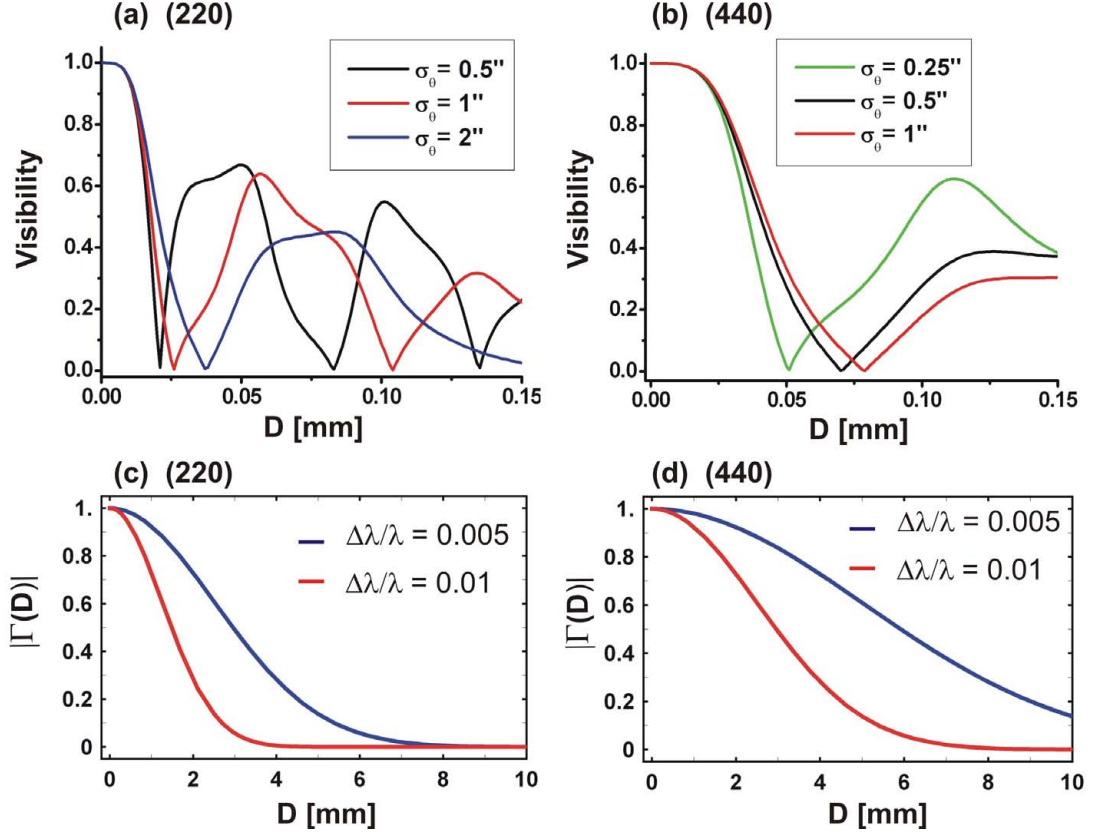


Figure 4.4: Visibility for one additional Si-crystal plate in one path of a neutron interferometer as a function of the thickness: in exact Bragg condition for the (220) (a) and (440) (b) reflection and for the crystal plate orientated far off a Bragg condition (220) (c) and (440) (d), where the wavelength distribution $\Delta\lambda/\lambda$ determines the coherence function.

figuration related to the longitudinal coherence length⁴. The visibility is in this case proportional to the longitudinal coherence function. Assuming a Gaussian momentum distribution of width δk one obtains a Gaussian coherence function

$$|\Gamma(\Delta_L)| = |\Gamma(D)| = e^{-(\Delta_L \delta k)^2/2} = e^{-(\Delta\phi)^2/2}$$

$$\Delta_L = -\frac{Nb_N \lambda^2 D_0}{2\pi \cos \theta_B} \quad (4.16)$$

with a corresponding width of phase shift distribution

$$\Delta\phi = -\frac{\lambda Nb_N D_0}{2\pi \cos \theta_B} \frac{\Delta\lambda}{\lambda} \quad (4.17)$$

⁴Here the definition of the longitudinal coherence function normal to the crystal lamellas [1] is considered.

This coherence function for both reflections is shown in Fig. 4.4 for two typical values of a wavelength distribution $\Delta\lambda/\lambda$. Whereas in the case of the crystal in Bragg condition, thicknesses in the range of $10\mu\text{m}$ already decrease the visibility significantly, here thicknesses in the order of millimeters are needed to create the same effect. This reveals the much stronger effect of the phase averaging by the beam divergence around Bragg in comparison to the usually considered case of a phase shifter described by the incident wavelength distribution.

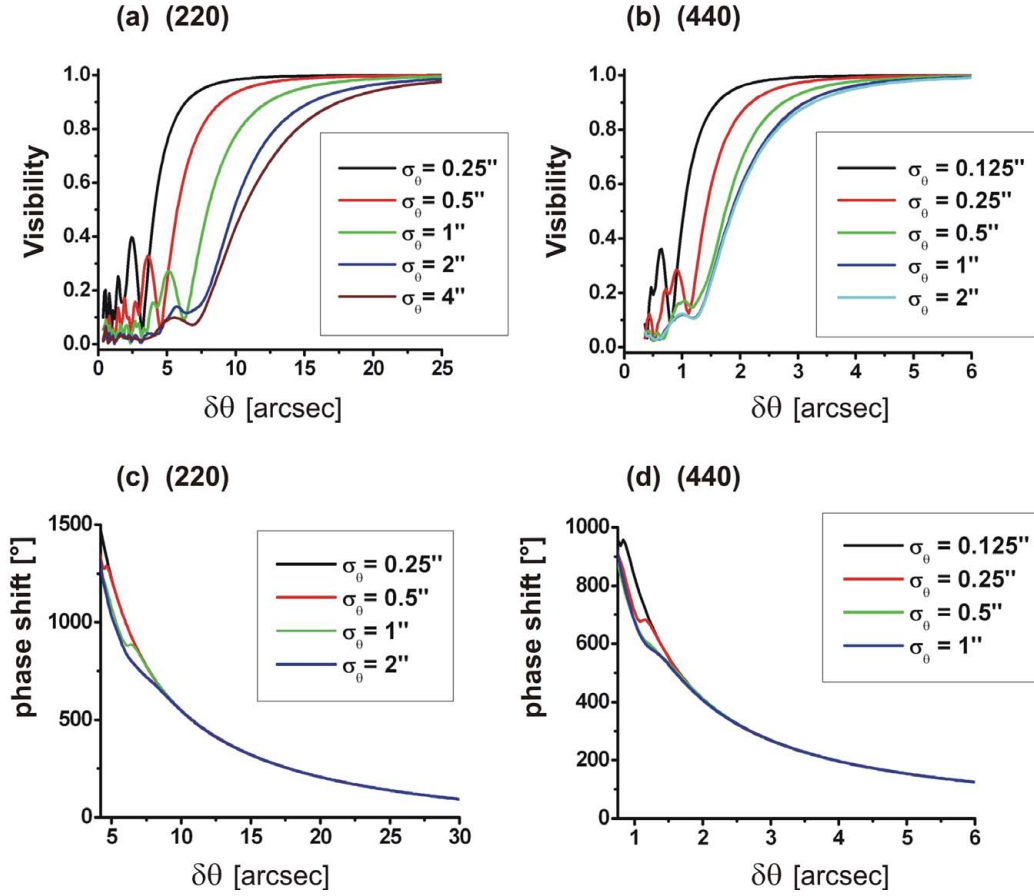


Figure 4.5: Thick Si-crystal lamella (3 mm) in one path of a neutron interferometer. Visibility and phase shift for the (220) and (440) reflection as a function of a rotation $\delta\theta$ relative to $\theta_B = 45^\circ$ (Fig. 4.3). The pure nuclear phase shift is subtracted as offset.

Let's now consider the additional crystal plate to be of the same thickness than the other interferometer lamellas ($D = 3\text{mm}$). In exact Bragg condition the visibility is of course destroyed almost completely, but what happens if one rotates this plate continuously off Bragg?

Fig. 4.5 (a), (b) shows that the visibility is restored several arc seconds away

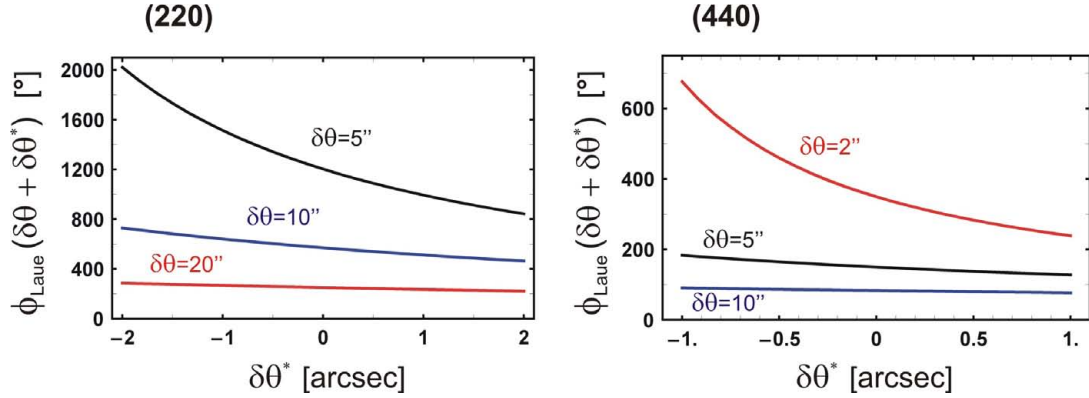


Figure 4.6: Phase distributions within the angular distribution $\delta\theta^*$ according to Fig. 4.5. A phase offset is subtracted.

from the exact Bragg condition, with a strong dependence on the beam divergence. However there is a quite large range of many arc seconds around Bragg, where the beam divergence has a dominant influence on the visibility. This range depends on the Darwin width (Eq. 2.27) whereby for example the (220) reflection is affected over a significantly larger range than the higher order reflections. The phase shift (Fig. 4.5 (c), (d)) strongly ascends, as the Bragg condition is approached. On the other hand it shows outside the immediate surrounding of the Bragg condition only a weak dependence on the beam divergence. For $\delta\theta \gg \Delta\theta_{1/2}$ even the single plane wave solution for $\delta\theta^* = 0$ is a good approximation. This can be understood by the phase distribution within the beam divergence (Fig. 4.6). Several Darwin widths off Bragg, this distribution is almost linear and antisymmetric around $\delta\theta^* = 0$. Thus the average phase shift is almost not affected by the divergence, whereas $\langle\delta\phi^2\rangle$ and thereby the visibility (3.10) are strongly connected to the beam divergence.

Summarizing, the coherence properties in the case of a perfect crystal are dominated several arc seconds off a Bragg condition by the beam divergence, whereas far off the wavelength distribution dominates. In between there is a region $\delta\theta \lesssim 1'$ where both coherence properties are relevant. This transition range of course depends on both the type of reflection and the associated Darwin width in combination with the beam divergence as well as the wavelength distribution.

4.3 One crystal plate in each beam path

Now we will study the configuration that we have already discussed in chapter 3, where one crystal plate is placed in each beam path. In this case the visibility

corresponds just to the visibility of the empty interferometer. The interesting part begins, if now one crystal plate is rotated relative to the other one, that is kept in exact Bragg condition (Fig. 4.7).

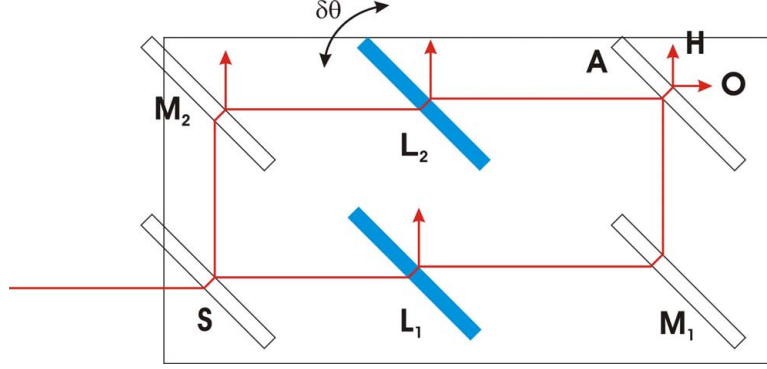


Figure 4.7: One additional crystal lamella inside of each beam path of the interferometer. One crystal lamella is rotated while the other is kept in exact Bragg condition.

Fig. 4.8 (a), (b) shows the visibility as a function of the rotation $\delta\theta$. Besides the case $\sigma_\theta \ll \Delta\theta_{1/2}$ the calculated visibility is roughly independent of the beam divergence. Considering now the phase shift (Fig. 4.8 (a), (b)), a completely different picture can be observed. Here one obtains a strong dependence on the beam divergence. The steepness of the phase shift decreases significantly with increasing σ_θ . This behavior can be understood by the already discussed phase distribution in Fig. 3.9, 3.10. Here the Pendellösung structures in the vicinity of $\delta\theta^* = 0$ play a dominating part for the mean phase fluctuation $\langle\delta\phi^2\rangle$. Thus $\langle\delta\phi^2\rangle$ is almost not enlarged when the beam divergence is increased to larger values of $\delta\theta^*$, which anyhow give a decreasing contribution to the interference pattern. In the case of $\langle\phi\rangle$ however, the contributions for $\delta\theta^* \gtrsim \Delta\theta_{1/2}$ still lower the phase shift. Here the influence on phase shift and visibility is just contrary to the one found in Fig. 4.5. Thus each possible configuration has to be analyzed separately to make conclusions on the influence of σ_θ on the phase and coherence behavior. Regarding the visibility, a reduction to approximately 0.5 is obtained by a rotation of only $0.02''$ for the (220) and $0.01''$ for the (440) reflection. The stronger decrease for higher order reflections is mainly explained by the larger steepness and the associated phase averaging discussed in Fig. 3.10. Although the calculated phase shift depends strongly on the beam divergence, in general one can say, that higher order reflections show - just as expected from the case of a single plane wave - a steeper curve. Very close to $\delta\theta = 0$ the calculated phase shift is approximately linear in $\delta\theta$, for larger $\delta\theta$ the steepness of the curve

gets weaker and ripply structures appear. These stem from the Pendellösung structures that are washed out by the averaging over the beam divergence. For small σ_θ they are still more pronounced as it can be seen for the (440) reflection at $\sigma_\theta = 0.125''$.

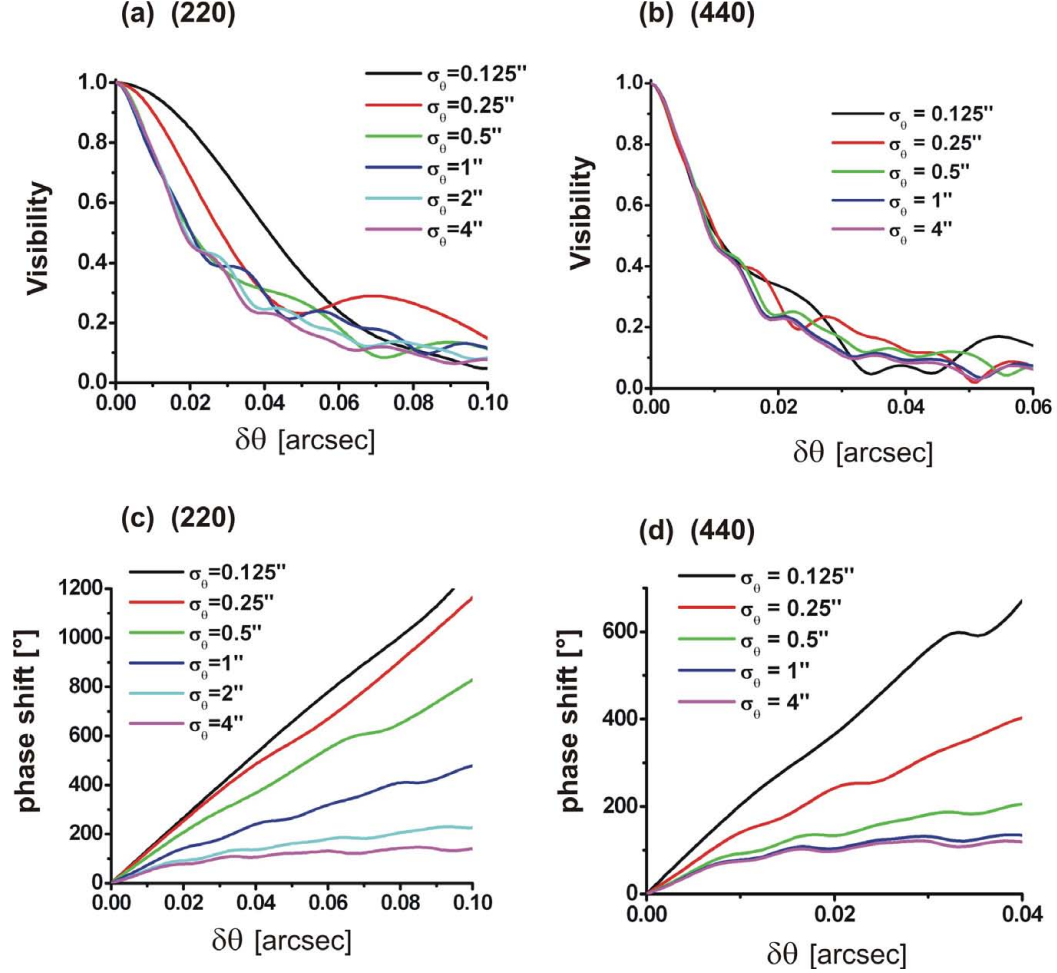


Figure 4.8: Visibility and phase shift for the (220) and (440) reflection using configuration (Fig. 4.7). Thickness of all lamellas: $D = 3\text{mm}$.

Influence of the beam divergence

In Fig. 4.9 (a) the calculated phase shift for a fixed plate rotation $\delta\theta$ is shown as a function of the beam divergence. In the limit of very small divergences $\sigma_\theta \ll \Delta\theta_{1/2}$ the phase shift approaches the plane wave result (Eq. 2.33). In the other limit of large beam divergences $\sigma \gg \Delta\theta_{1/2}$ the phase shift approaches a constant value.

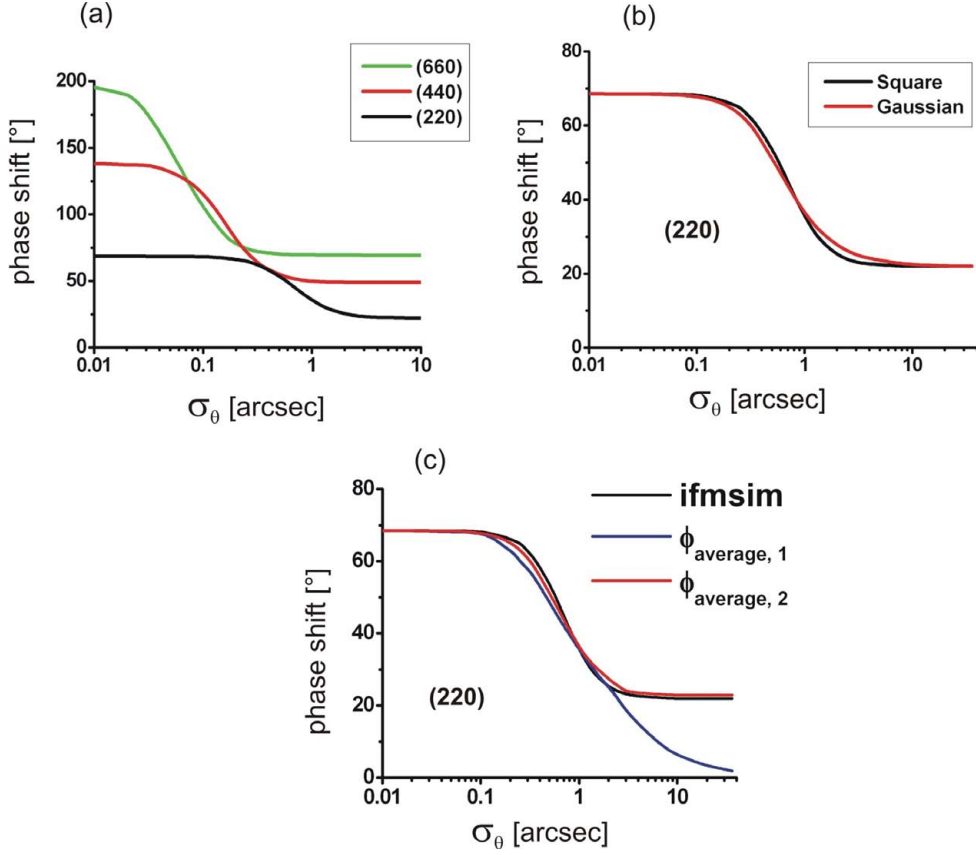


Figure 4.9: (a) Calculated phase shift as a function of the beam divergence for a fixed beam deflection of $\delta\theta = 0.0036''$ and several reflections. (b) Comparison of the square distribution with a Gaussian distribution (4.4) (c) comparisons with directly averaged phase distributions according to Eq. 4.19 ($\phi_{average,1}$) and Eq. 4.1 ($\phi_{average,2}$, monochromatic beam assumed). Same parameters as in Fig. 4.8.

This is expected as plane waves far off the Bragg angle can give no significant contribution to the interference pattern and the essential contributions are already included within the smaller beam divergences. This constant value for small $\delta\theta$ is approximately

$$\lim_{\sigma_\theta \rightarrow \infty} \phi_{spherical}(\delta\theta) \gtrsim 0.3\Delta\phi_{Laue}(\delta\theta, 0) \quad (4.18)$$

Thus it is a little bit lower than the estimated average omitting the Pendellösung structures (Eq. 3.16).

Between these two limits - determined by the Darwin width - one obtains a strong dependence of the phase shift on the divergence. Consequently the position of the drop in Fig. 4.9 is different for different reflections. The limit of large

σ_θ is already well approximated for $\sigma_\theta \approx 4\Delta\theta_{1/2}$, so one does not need to accomplish the calculations for large σ_θ , which would result in long computation times. Thereby the essential angular regime determined by the effective reflectivities of the interferometer lamellas, makes life - in this respect - a lot easier.

Fig. 4.9 (b) compares the same curve to a calculation assuming a Gaussian instrument width function (Eq. 4.4). For the same σ_θ the Gaussian includes additional contributions in the regime $|\delta\theta^*| > \sigma_\theta$, while it underestimates contributions for $|\delta\theta^*| \leq \sigma_\theta$. The difference between the calculated phase shifts is not very striking. Moreover in Fig. 4.9 (c) a comparison to a simple phase averaging

$$\langle\phi(\delta\theta)\rangle = \frac{1}{2\sigma_\theta} \int_{-\sigma_\theta}^{\sigma_\theta} \Delta\phi_{Laue}(\delta\theta, \delta\theta^*) d\delta\theta^* \quad (4.19)$$

and the phase average calculated via Eq. 4.1 is shown, where a monochromatic beam has been assumed. The simple averaging over the phase function can be used as an approximation for $\sigma_\theta \lesssim \Delta\theta_{1/2}$ whereas for $\sigma_\theta \gg \Delta\theta_{1/2}$ the contributions for larger $\delta\theta^*$ are overestimated and the average approaches zero in the limit $\sigma_\theta \rightarrow 0$. On the other hand taking the phase average according to Eq. 4.1 gives a rather good approximation over the whole range of beam divergences, despite the disregard of the asymmetry between the two beam paths.

Beam alignment in the rocking curve

If a perfect crystal monochromator is used, the phase shift can also depend on the alignment between monochromator and interferometer. This determines the angle of the incident beam spectrum relative to the interferometer lamellas. Fig. 4.10 shows the effect on the phase, if the incident beam is shifted by an angle α relative to the exact Bragg condition of the interferometer lamellas. Such a relative shift has a similar effect than a larger beam divergence, as the averaged phase shift contains more contributions with large $\delta\theta^*$. One could even choose $\alpha \gg \Delta\theta_{1/2}$. In this case the interfering intensity would become very small. On the other hand the phase averaging within the interferometer would be much less severe and calculations show that the sample lamella can be rotated over a significantly larger range of $\delta\theta$ until the visibility is lost.

Influence of the crystal thickness

Fig. 4.11 shows the visibility and the phase shift as a function of the sample crystal thickness D , equal for both additional crystals. As $\phi_{Laue} \propto D$ the visibility decreases faster, while the steepness of the phase shift increases with larger crystal thickness. Thus the gained phase shift is counteracted by a loss of visibility.

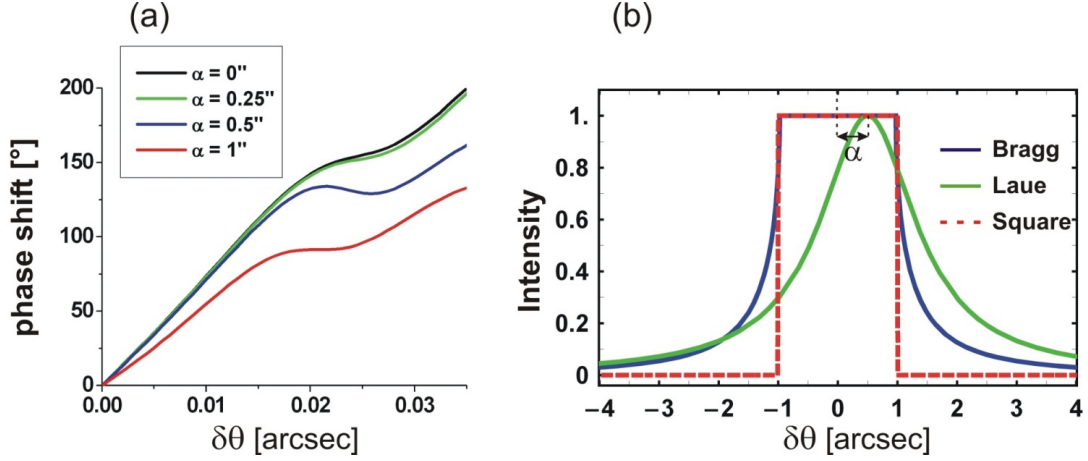


Figure 4.10: (a) Phase shift as a function of a beam misalignment (b) α relative to the interferometer. As incident beam a square function with $\sigma_\theta = 1''$ is used. Other parameters as in Fig. 4.8.

Hence there seems to be almost no advantage in choosing a specific thickness, except for special experimental considerations. If one uses prisms - as suggested in subsection 3.2.5 - it is difficult to create large $\delta\theta$, thus in this case thick crystal lamellas can help in accessing large phase shifts. As the phase shift depends on the beam divergence, a fixed divergence of $\sigma_\theta = 4''$ - approximately equal to the limit $\sigma_\theta \rightarrow \infty$ has been chosen. The crystal thickness is also a possibility to improve the angular sensitivity of the phase shift, which could be interesting for the measurement of very small beam deflections.

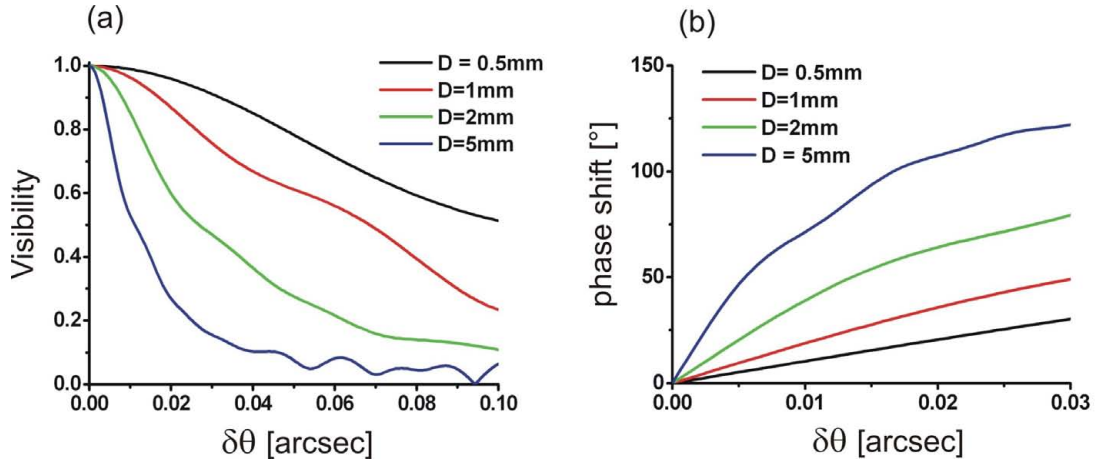


Figure 4.11: Calculated visibility (a) and phase shift (b) for several crystal thicknesses. Configuration as in Fig. 4.7, $\sigma_\theta = 4''$.

Influence of the wavelength distribution

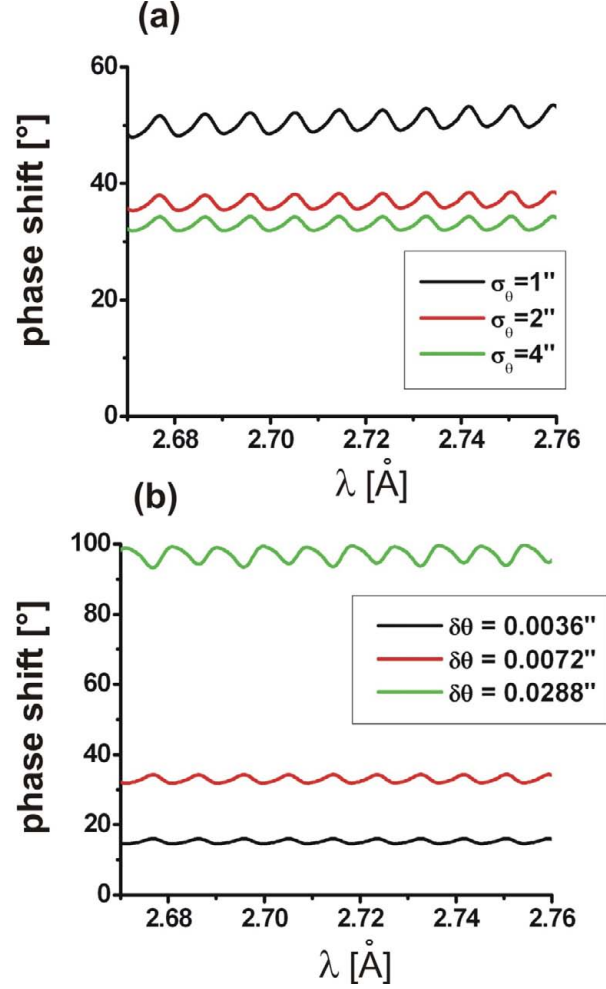


Figure 4.12: Calculated phase shift as a function of the Bragg angle θ_B or equivalently wavelength λ . Configuration as in Fig. 4.7. (a) $\delta\theta = 0.0072''$ for several σ_θ (b) $\sigma_\theta = 4''$ for several $\delta\theta$.

So far a monochromatic beam has been considered. Now we will discuss the variation for different wavelengths and thereby the impact of the wavelength distribution. Therefore the visibility and phase shift can be calculated as a function of the wavelength or Bragg angle. As the visibility is virtually independent of the Bragg angle, we will here only discuss the phase shift. For the phase shift one finds to first order an oscillatory behavior with comparatively small amplitude (Fig. 4.12). This oscillation is determined by the change of the Pendellösung length as the wavelength is varied (compare Fig. 3.11). Accordingly the condition for two successive minima λ_1 and λ_2 of this oscillatory curve is given by (Eq.

3.20)

$$A_H(\lambda_1) - A_H(\lambda_2) = \pi \left(\frac{D}{\Delta_H(\lambda_1)} - \frac{D}{\Delta_H(\lambda_2)} \right) = \frac{\pi}{2} \quad (4.20)$$

The amplitude of this oscillation increases with $\delta\theta$ and decreases with σ_θ . This wavelength dependence leads to a further averaging of the phase shift $\langle\phi(\delta\theta, \lambda)\rangle_{\delta\theta^*}$ gained by the monochromatic spherical wave calculation over the (normalized) wavelength distribution $P(\lambda)$

$$\phi(\delta\theta) = \langle\langle\phi(\delta\theta, \lambda)\rangle_{\delta\theta^*}\rangle_\lambda = \int_{-\infty}^{\infty} P(\lambda) \langle\phi(\delta\theta, \lambda)\rangle_{\delta\theta^*} d\lambda \quad (4.21)$$

However if one chooses the Bragg angle for the calculation approximately at the mean value of this oscillatory curve, one can omit this further averaging. This reflects the fact, that the influence of the wavelength distribution in the considered range is not crucial in comparison to the beam divergence. A small influence on the visibility remains, as the wavelength distribution creates a mean fluctuation $\langle\delta\phi^2\rangle$ that increases with $\delta\theta$. Thus one obtains a further decrease of the visibility

$$V(\delta\theta) = \tilde{V}(\delta\theta) e^{-\langle\delta\phi^2(\delta\theta)\rangle/2} \quad (4.22)$$

where $\tilde{V}(\delta\theta)$ is the calculated visibility for a monochromatic beam. From Fig. 4.12 it can be observed that in the relevant regime $\langle\delta\phi^2(\delta\theta)\rangle < \frac{1}{10}\langle\phi(\delta\theta)\rangle$. Thus uncertainties in the beam divergence might result in even larger uncertainties of the visibility (Fig. 4.8).

4.3.1 Defocused arrangement of two crystal plates

Finally we investigate the case, that in one beam path the plate is inserted before the mirror, in the other after the mirror. In 3.2.1 it has already been pointed out that this configuration is not optimal as it leads to a severe defocusing problem. As this setup has been proposed in [7] for a measurement of the neutron-electron scattering length, estimations on the visibility while rotating both lamellas off Bragg are of basic interest. As the article gives no information on the planned sample crystal thicknesses or exact orientation⁵, the calculations have been performed for a (220) lattice orientation at $\theta_B = 30^\circ$ for $D = 3\text{mm}$ and $D = 1\text{mm}$ (Fig. 4.13).

The visibility and phase shift strongly depend on the thickness of the crystal plate. Whereas measurements as close as $\delta\theta = 2''$ seem possible for $D = 1$

⁵At NIST interferometers with (220) as well as (111) lattice orientation are used. Moreover the sample Laue crystal could in principle be cut in even another orientation than the interferometer. This would however correspond to a dispersive arrangement.

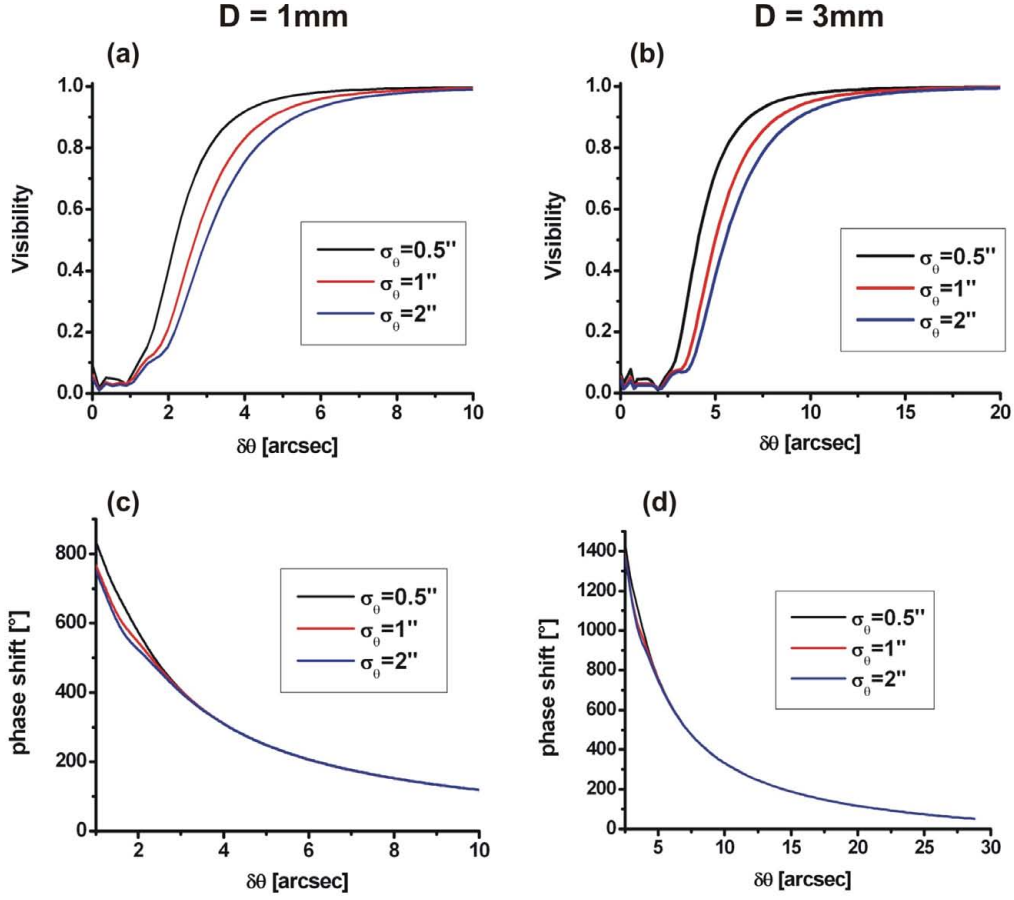


Figure 4.13: Calculated visibility and phase shift for the setup shown in Fig. 3.3 at $\theta_B = 30^\circ$. Two lamella thicknesses (D) and several beam divergences are compared. A phase offset is subtracted.

mm, for $D = 3\text{mm}$ the visibility is already significantly reduced at $\delta\theta = 5''$, which is in good agreement with Fig. 3.1. This is closer to Bragg than with the one plate setup at 45° though (Fig. 4.5). The reason is the reduced effective range of the Laue phase at smaller Bragg angles (Fig. 2.7). This however also results in a reduced phase sensitivity when comparing with Fig. 4.5 and for different thicknesses. Hence increased phase sensitivity is to some extent always counteracted by a loss in visibility due to phase averaging. Moreover increased phase sensitivity implies also a larger dependence on the actual beam divergence. Comparing Figs. 4.13 c,d and 4.5 it is obvious that the phase curves for different beam divergences start to show a significant difference just in the region the visibilities decrease. Concerning the goal of the experiment - a measurement of the neutron electron scattering length b_{ne} - it is interesting to note, that reduced phase sensitivity by decreasing crystal thickness or Bragg angle (compare Fig.

4.14 and Fig. 2.13) results also in a reduced sensitivity to b_{ne} over the whole range of $\delta\theta$. Moreover it does not seem possible to measure the phase shift over the whole aimed range $-10'' < \delta\theta < 10''$ [7]. Though measuring the visibility and phase shift within the accessible range could be still interesting. Nevertheless it has still to be shown if this setup can be used for a precision measurement of b_{ne} .

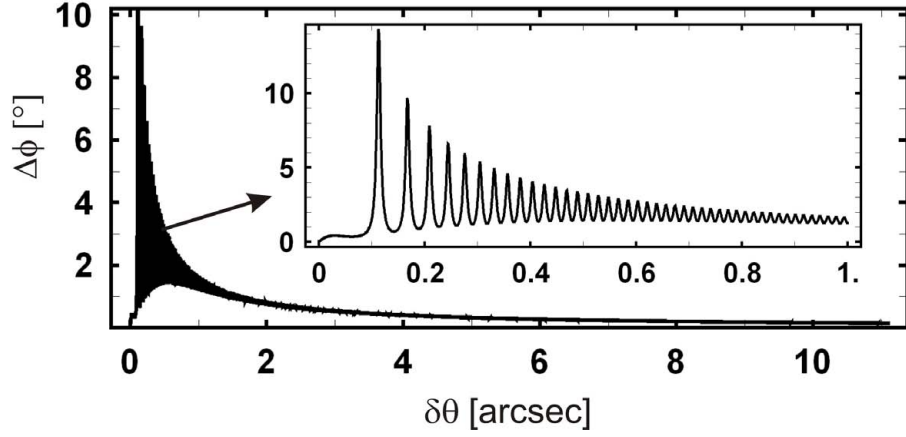


Figure 4.14: Difference in Laue phase (Eq. 2.62) for two disputed values of b_{ne} (2.57) at $\theta_B = 30^\circ$. (Other parameters: Si-(220) reflection, $D = 3\text{mm}$).

Chapter 5

Interferometer

5.1 Interferometer preparation

5.1.1 Planning of the interferometer

The most essential requirement for an experiment dedicated to a measurement of the Laue phase is a suitable neutron interferometer. According to our strategy of using prisms for beam deflection relative to monolithically fixed lamellas, we have the following basic requirements

- Interferometer with at least two additional lamellas according to Fig. 3.7 (b)
- path length and beam separation allowing sufficient space for the required prism operations
- Accurate crystal orientation to the symmetric case or alternatively precise measurement of the actual orientation. Precise crystal orientation will additionally simplify the sample alignment in non dispersive position for the accurate measurement of nuclear scattering lengths.
- Thick interferometer base to reduce perturbations by crystal bending

The problem with conventionally used symmetric and skew-symmetric types (Fig. 5.1 (a), (b)) is the severe limitation of the path length, which strongly depends on the diameter of the silicon ingot. A new skew-symmetric interferometer geometry [30, 31] uses a different crystal orientation where the (110) lattice planes enclosing a 45° angle to the (100) ingot orientation are used. Here the beams are traveling along the crystal axis (Fig. 5.1 (c)), hence the path length is only limited by the ingot length. The diameter of the ingot only limits the beam

separation, which is usually still larger than in the original types. An interesting feature of this geometry with $\theta_B = 45^\circ$ is that both the first (220) with $\lambda = 2.72\text{\AA}$ and second order reflection (440) with $\lambda = 1.36\text{\AA}$ lie within the neutron spectrum available at S18. On the downside the intensity at the first order is significantly lower than at the usually employed interferometers at $\theta_B = 30^\circ$ with $\lambda \approx 1.9\text{\AA}$.

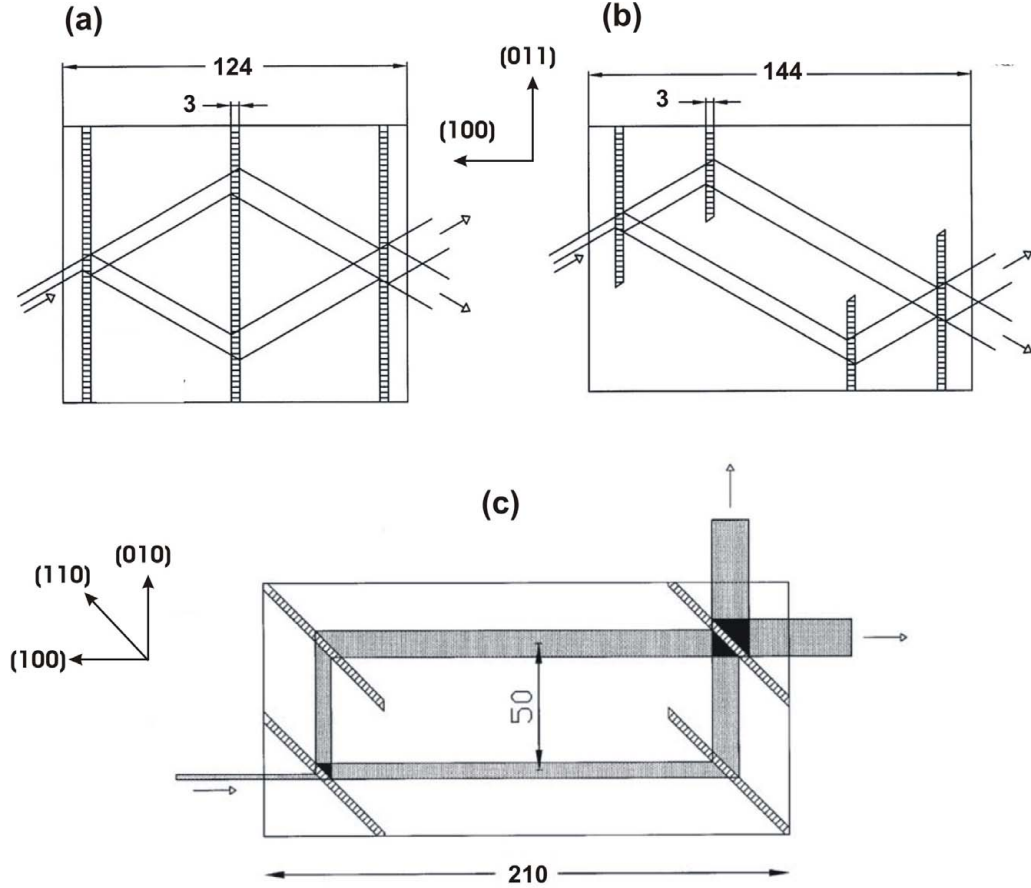


Figure 5.1: Three different IFM types: (a) symmetric 3 blade interferometer (b) skew-symmetric interferometer and (c) the new skew-symmetric type using a $\theta_B = 45^\circ$ geometry.

For the final interferometer dimensions the total path length and the lamella size have been optimized to the required prism configurations, while maintaining the required focusing conditions [25]. On the other hand the interferometer should not be larger than necessary, as thereby also the sensitivity to external disturbances increases. As the main planned experiment should consist in a beam deflection relative to one sample lamella while not to the other, a prism configuration as shown in Fig. 5.2 is necessary. In this configuration the beam

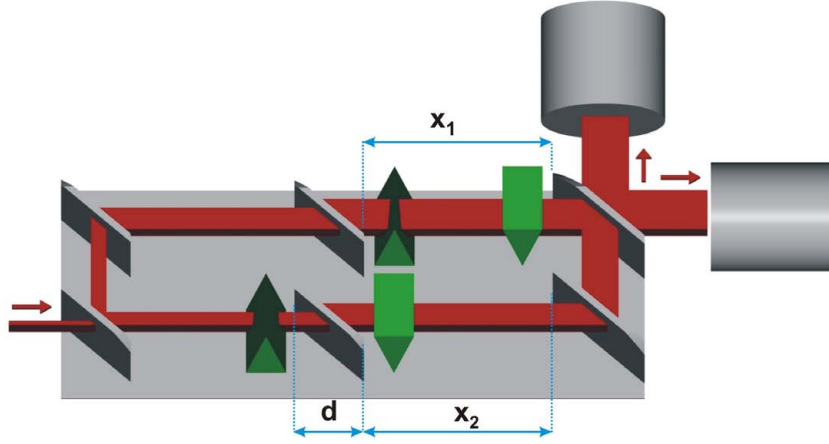


Figure 5.2: One of the essential prism arrangements determining the interferometer dimensions.

displacement by both prism sets is equal. Hereby for example the lamella width d and the partial path lengths $x_{1,2}$ are determined. The lamella sizes have been optimized to the desired beam geometry, taking the beam spreading due to the Borrmann fan into account. In a first layout it seemed to be advantageous to cut the two sample lamellae displaced (Fig. 5.2 $x_1 \neq x_2$), whereby the use of larger prisms would have been possible. Moreover extraordinary thick sample lamellae would have given an even higher phase sensitivity. Finally we have chosen equal thickness for all lamellae and a design that also enables further use of the interferometer in double loop configuration. Moreover in this layout it is possible to deflect the beam in front of both lamellae simultaneously and study relative deflections (compare 7.2.5).

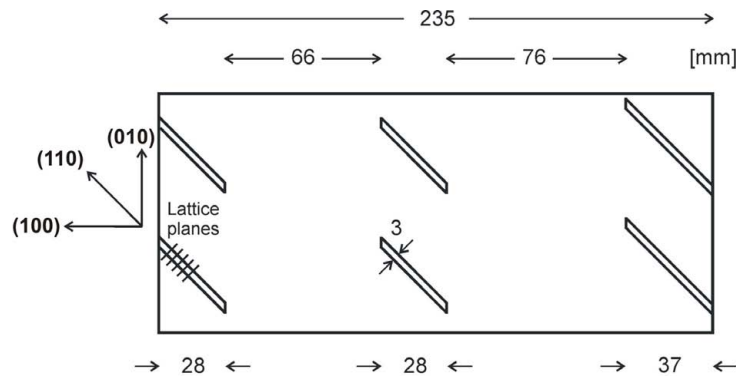


Figure 5.3: Finally planned geometry of the interferometer.

Fig. 5.3 shows the finally planned dimensions of the interferometer¹(Table 5.1), more detailed plans are given in Appendix B. This constitutes the plan for the hitherto largest perfect crystal neutron interferometer.

Interferometer length	23.5 cm
Path length	25 cm
Beam separation	5 cm
Full enclosed beam area (loop 1/2)	100 (45 /55) cm ²
Lamella height	5cm
Lamella thickness	0.3cm
Base thickness	3.4cm

Table 5.1: Geometric parameters of the new interferometer.

5.1.2 Crystal selection and orientation

Crystal selection

For the interferometer a float-zone grown 4 inch silicon ingot from Wacker-Sitronic (Burghausen) with fourfold symmetry and cubic lattice oriented in (100) direction has been chosen. The initial length of the crystal amounted to 40cm, ingots of length 1m are available though. Hitherto there have been good experiences with this type of ingots, that are to a high degree free of dislocations. Disturbing lattice distortions may occur via axial and radial carbon and oxygen impurities [32]. These amount to [33]

$$\begin{aligned}\frac{\delta d_L}{d_L} &= -6.9 \cdot 10^{-24} N_O \\ \frac{\delta d_L}{d_L} &= 4.4 \cdot 10^{-24} N_C\end{aligned}\tag{5.1}$$

where d_L is the lattice spacing and the impurities for the chosen quality amount to

$$\begin{aligned}N_C &= 2 \cdot 10^{15} \text{cm}^{-3} \\ N_O &= 1.4 \cdot 10^{15} \text{cm}^{-3}\end{aligned}\tag{5.2}$$

¹From a later point of view it would maybe have been better to make the first loop smaller and hence increase the size of the second. The reason for the chosen sample lamella positions has been due to a planned arrangement with large 90° prisms which has not been used finally in the experiment.

Axial gradients can be avoided to a high degree, if intermediate pieces of long ingots are chosen. Radial gradients on the other hand appear mainly close to the surface. Hence the beam geometry should be chosen accordingly.

Crystal orientation

Usually for crystal orientation we employ the X-ray Laue camera of our institute. Hereby with some effort a precision of 10 arc minutes is possible. To avoid remarkable corrections from the asymmetric case (subsection 2.2.3) a much higher precision $\gamma < 30''$ is required. Such precision is possible with the X-ray diffractometer of our co-operation partner at the PTB Germany. This diffractometer has been especially adapted for the precise lattice orientation of a large crystal as large as ours, where we have already cut the initial 40cm ingot down to 25 cm at our institute. Special adjustment of the employed four-fold (220) silicon monochromator leads to an accuracy of ± 0.2 arc sec. This is less than one tenth of the achievable rocking curve width (≈ 2.6 arc sec) for etched crystals. Perpendicular to the thereby obtained orientation of the (110) crystal lattice planes an auxiliary mirror is aligned and fixed (Fig. 5.4 (a)). This is performed by an especially adjusted autocollimator, which constitutes the main source of uncertainty (± 1 arc sec). This is well within the necessary accuracy though.

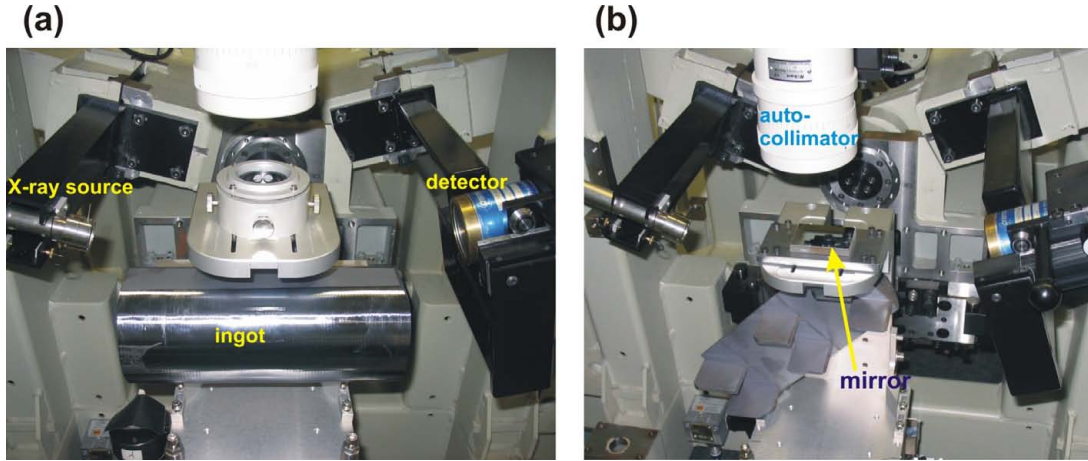


Figure 5.4: (a) Orientation of the ingot on the X-ray diffractometer (b) an auxiliary mirror is orientated via an autocollimator on the X-ray diffractometer parallel to the (110) lattice vector for the final interferometer.

For the finished interferometer the same method has been used to determine the orientation of the finally obtained lamella surfaces to the lattice planes (Fig. 5.4 (b)).

5.1.3 Crystal machining and fine grinding

Preliminary machining

The hitherto machined interferometers could be cut at the surface grinding machine at our institute. With the present size this is no more possible as the plan parallel transfer of the cutting wheel is limited. Thus the preliminary cutting has been performed at the PTB Meyer Burger grinding machine employing bronze-bonded diamond wheels. In a first step the flat base and top are cut off, then the crystal is glued with its base on an especially adapted metal plate for fixing on the goniometer of the grinding machine. After cutting out the material in between the three lamella pairs (Fig. 5.5 (a)) employing a 0.3mm thick diamond coated wire saw, an 8mm thick diamond cutting wheel has been used to cut out the lamellas (Fig. 5.5 (b)). As during the later preparation processes - fine grinding and etching - the thickness will be further reduced and moreover later reparations of the crystal have been expected, the planned lamella thickness at this step has been $3.3\mu\text{m}$.

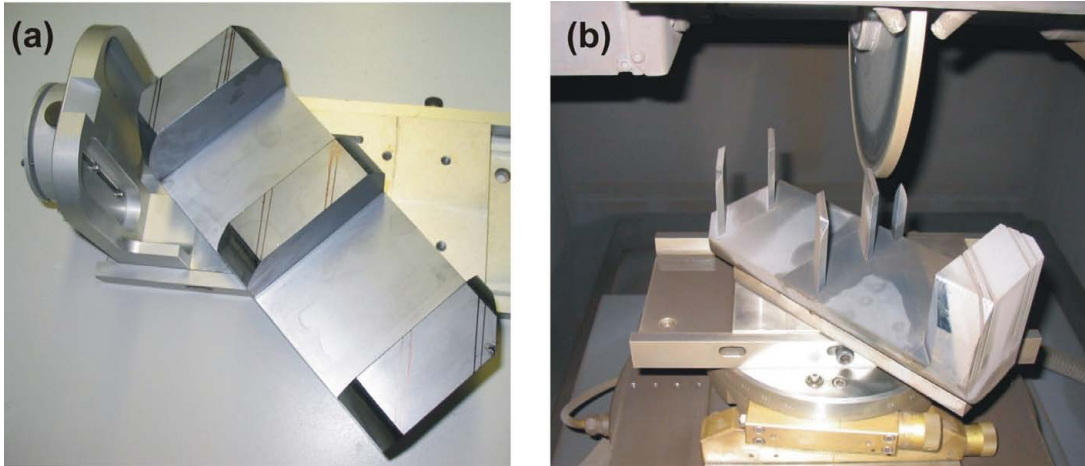


Figure 5.5: (a) ingot after base and top cutting, additionally the silicon in between the lamella pairs has been cut out (b) cutting of the lamellas with a diamond cutting wheel.

The cutting process is already important for the accuracy of the overall geometry and the orientation of the lamellas. The surface quality is determined by the later fine grinding though. The measured geometry at this step (compare subsec. 5.1.5) showed an average lamella thickness of $3.287(4)\text{mm}$. The maximum difference between two lamellas was $10\mu\text{m}$. Again using the X-ray diffractometer an auxiliary mirror has been aligned perpendicular to the (110) lattice planes, as a reference orientation for the subsequent fine grinding process.

Fine grinding

To obtain the final geometric accuracy and surface quality, the interferometer has been fine grinded at G. Rauch company. Here a similar surface grinding machine with a diamond cutting wheel is used to finish the geometry by an iterative pendular grinding process ($v \approx 20$ cm/s) along the lamella surfaces. The orientation of the surfaces is obtained by accurate alignment of the cutting wheel according to the auxiliary mirror.

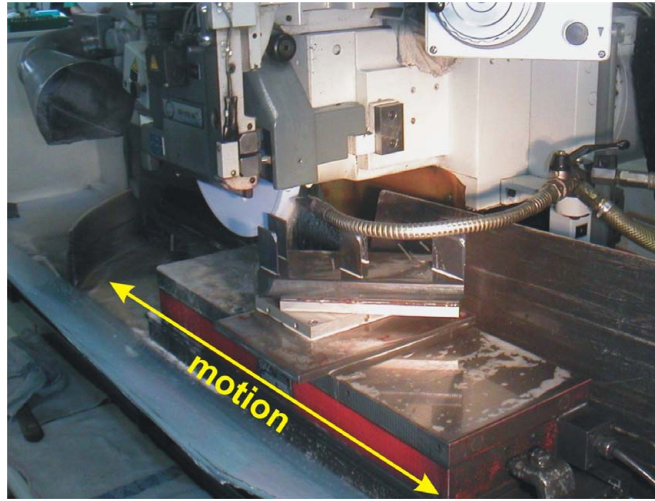


Figure 5.6: Fine grinding of the interferometer. The interferometer is moved with approximately $v \approx 20$ cm/s along the diamond cutting wheel - in the photo actually a corundum wheel is employed - until the desired lamella thickness is reached.

Usually this fine grinding procedure leads to an accuracy of approximately $3\mu\text{m}$. Unfortunately, due to fixed time schedules for testing at S18 in Grenoble, the procedure could not be finished properly and furthermore a not optimal corundum wheel had to be used. Hence the thickness errors have accumulated up to $17\mu\text{m}$. This explains the poor results of the first interferometer test (compare section 5.2). In a second step the interferometer has been fine grinded again with a newly-acquired diamond cutting wheel. This time the geometric errors have been below $3\mu\text{m}$. The remaining geometric imperfection has a minor influence on the visibility [25, 31], which will be more influenced by thermal gradients at the interferometer, lattice distortions due to crystal bending and vibrations. In addition to the described fine grinding process an alternative approach using a coordinate milling machine [34] has been tested with two interferometers that had to be repaired after damage to the surface structure. Due to the size of the interferometer this procedure is extremely time-consuming - 20 days for six

lamellas. An attempt with 10 times faster grinding than usually applied for X-ray interferometers at the PTB yielded visibilities below 5% at usual etching depths of approximately $30\mu\text{m}$. Hence this technique results in a more pronounced surface damage and shows no advantage. Moreover even for the optimal (slow) procedure the measured surface roughness is larger than $5-10\mu\text{m}$ which can only be reduced by large etching depths. The difference to the normal fine grinding process is even optical visible at the lamella surfaces (Fig. 5.7).

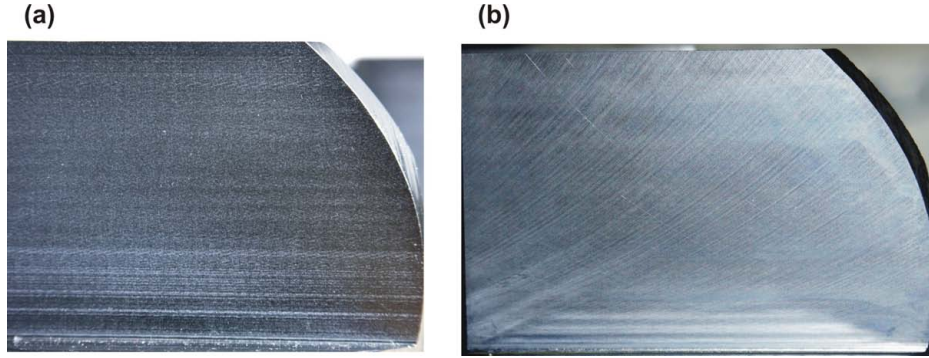


Figure 5.7: Surface pattern after fine grinding (a) employing a coordinate milling machine and (b) employing the usual fine grinding method.

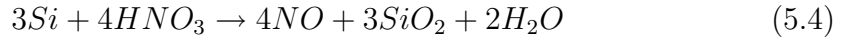
5.1.4 Etching

The final step in interferometer preparation consists in the removal of the damaged perfect crystal structure at the lamella surfaces due to the cutting and fine grinding process. Furthermore etching reduces the surface roughness below $1\mu\text{m}$. The etching depth D_e is a crucial parameter in interferometer preparation and has to be optimized in two respects. The minimum etching depth depends on the cutting process. Fulminating diamond grains or abrupt changes in the cutting speed or cooling flow can cause deep rills and long-ranging lattice deformations. Presuming smooth cutting and grinding the minimum etching depth is $15\mu\text{m}$, in some cases remaining lattice distortions up to $30\mu\text{m}$ etching depth may occur. On the upper side etching is accompanied by unavoidable convex-shaped thickness errors due to higher acid flow and thereby etching speed at the crystal edges. Hitherto experiences for a typical lamella size show a relative thickness gradient from the center to the edges of

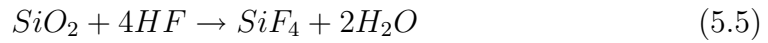
$$\frac{\Delta D_e}{D_e} \geq 0.2 \quad (5.3)$$

Such a gradient within the beam area results in a decrease of the visibility. Hence the etching depth should be chosen as small as possible, otherwise the utilizeable

beam area is reduced. This thickness gradient is also one of the reasons why the chosen neutron beam paths should be close to the center of the lamellas. The actual etching process is carried out in an appropriately sized and acid-resistant reservoir, that is embedded in a large water vessel for cooling. During several recently carried out etching processes² we have optimized the etching speed. An acid mixture of hydrofluoric acid (HF 40% pA) and Nitric acid (HNO_3 60% pA) is used in relative concentration 1 : 60. Nitric acid oxidizes the silicon surface



which is removed by the hydrofluoric acid



in the form of SiF_4 . During this process the concentration of HF is reduced. Hence it is necessary to continuously add hydrofluoric acid according to the removed silicon mass Δm during etching

$$+ \Delta HF(ml) \approx 0.02\Delta m(mg) \quad (5.6)$$

If bubbles of SiF_4 occur during the etching process at the surface of the lamellas these have to be removed by moving the whole crystal to guarantee homogeneous etching. This movement leads to enhanced acid flow and hence increased etching speed though. Thus extensive cleaning - both mechanical and chemical - of the lamella surfaces together with the optimized acid mixture turned out to be essential for the accurate control of the etching speed. Applying the described procedure we could extremely good stabilize the etching rate to $\approx 0.3\mu m/min$ ³. The accurate knowledge of the etching rate is essential for choosing the proper etching time. After etching the etching depth can be determined by the mass difference Δm of the crystal before and after etching. Via

$$\Delta D(\mu m) = \frac{10 \cdot \Delta m(mg)}{2.33 \cdot O(cm^2)} \quad (5.7)$$

the etching depth ΔD can be calculated by the known surface area O . Additionally the etching depth and furthermore thickness gradients can be determined by

²During this work also several interferometers for colleagues have been etched after a damage of the crystal surface.

³Formerly the etching speed has been chosen larger, by a mixture of approximately 1 : 20 [34]. Such highly concentrated mixtures are also used for X-ray interferometers [13], resulting in high etching depths and strongly convex shaped surfaces. Anyhow for X-ray interferometers this problem is of minor importance, as the beam size can be chosen small in comparison to neutron interferometers.

accurate geometric measurements of the crystal geometry before and after etching. These measurements confirm the accurate accomplishment of the etching procedure.

5.1.5 Final geometric measurements

In a final step the geometry of the crystal is measured with a Zeiss-Prismo coordinate measuring machine at G. Rauch company. For this a 1mm ruby sensor sphere with small contact force (0.1N) to avoid scratches on the lamella surfaces is applied. The reproducibility within the interferometer geometry is of the order of $1\mu\text{m}$. These measurements have been applied between several preparation stages, thus we obtained valuable information not only on the overall geometry but also on the etching procedure and thickness gradients on the crystal lamellas.

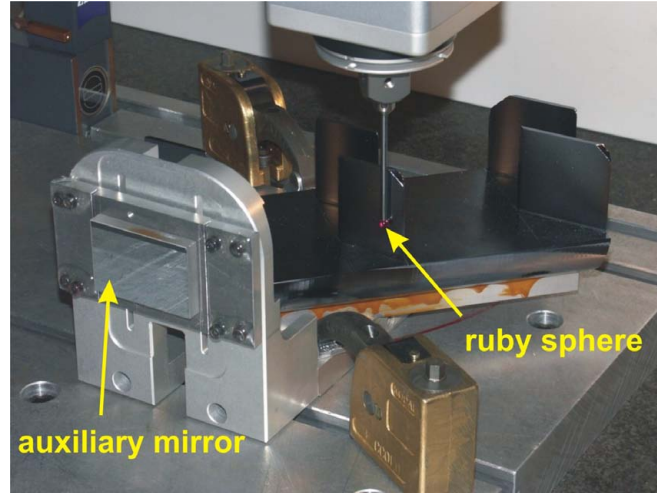


Figure 5.8: Measuring of the interferometer geometry together with an auxiliary mirror that is aligned parallel to the (110) lattice vector.

After the last etching once again an auxiliary mirror has been aligned perpendicular to the (110) lattice planes (5.1.2). Including the mirror in the geometric measurement (Fig. 5.8) revealed the final orientation between lamella surface and the (110) lattice vector, thus the angle of asymmetry γ . This amounted to

$$\gamma_{average} = 13.5''(\pm 5'') \quad (5.8)$$

in the relevant lamella areas, where the error contributions are $\pm 0.2''$ from the diffractometer, $\pm 1''$ from the autocollimator and $\pm 4''$ via the coordinate measurement. This is surprisingly small concerning the long preparation history and

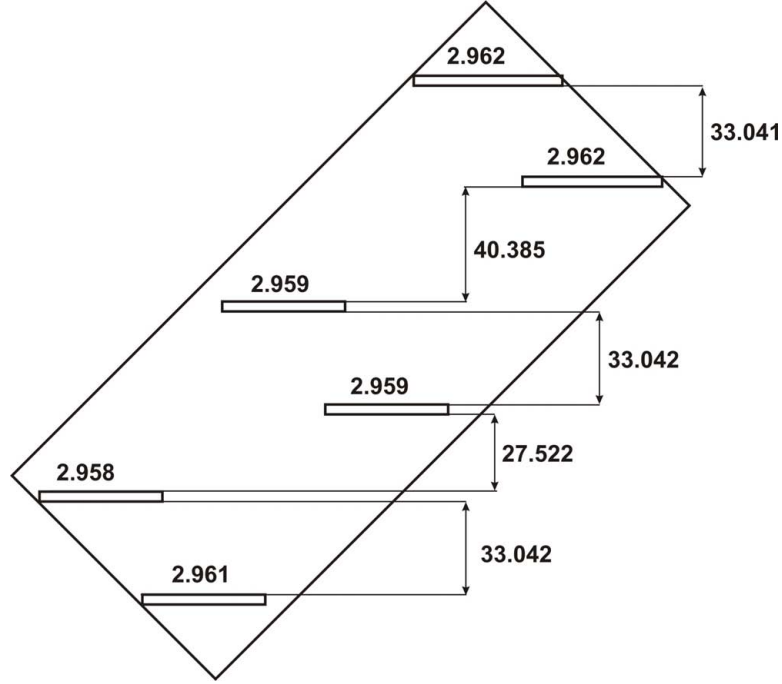


Figure 5.9: Finally measured geometry of the interferometer. Dimensions in millimeters.

should be sufficient concerning the estimations in subsection 2.2.3. In fact, this is the first neutron interferometer oriented symmetrically to such high accuracy.

Fig. 5.9 shows the final geometry of the interferometer. The average lamella thickness in the illuminated area has been measured to $\bar{D} = 2.960\text{mm}$, the maximum thickness difference between two lamellas to $4\mu\text{m}^4$. The same accuracy is fulfilled for the relevant lamella distances guaranteeing the focusing conditions. The surface flatness has been measured to $1.8\mu\text{m}$ in the beam area on average.

A short overview of the preparation history and resulting visibilities is given in Tab. 5.2.

5.2 Interferometer testing

The test of the interferometer has been performed at the instrument S18, ILL in Grenoble. Actually there have been three tests and interim optimization of the preparation. Here only the results after the final preparation stage are discussed.

⁴Moreover a slightly vertically wedge shaped form at some of the lamellas has been measured which should be of minor importance.

Step	total etching depth	max. error (μm)	visibility
Fine grinding	-		-
Etching	31.4(10)	17(1)	< 0.2
Fine grinding	-	3(1)	-
Etching	23.7 (10)	-	0.45
Etching	32.7(10) (measured: 31.2(10) μm)	4(1)	0.6

Table 5.2: Final steps of the interferometer preparation and resulting geometrical errors and the visibility measured at the (220) reflection. The given values of the etching depth are calculated from the etching process.

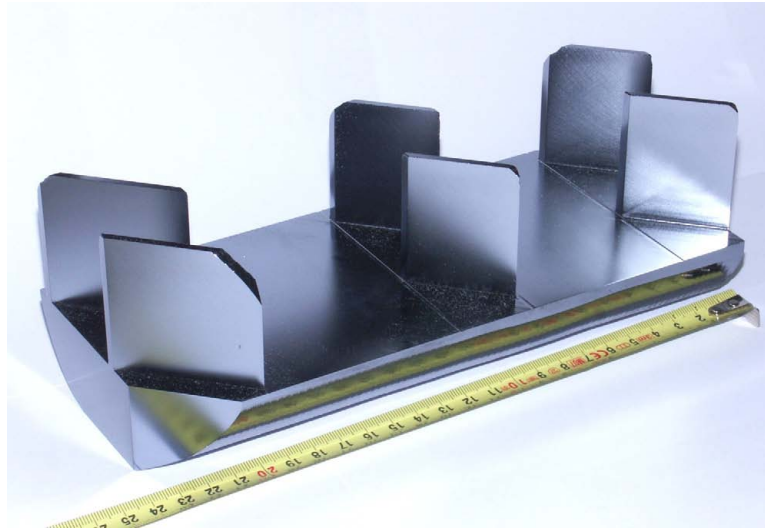


Figure 5.10: Finished interferometer

5.2.1 Rocking curve

Up to now in neutron interferometric experiments at S18 the second order reflection could be neglected - as in the usually used $\theta_B = 30^\circ$ setup - or has been separated as far from the first order, so that the latter is not contaminated. However one of the advantages of a perfect crystal monochromator is the possibility to separate higher order reflections in the rocking curve and thus make use of them. Hence the goal has been to separate the second order reflection far enough to avoid contamination from the comparatively broad first order. The use of higher order reflections is interesting for systematic precision measurements and might be also useful for the experimental discrimination between topological and dynamical phase shift. In a later stage even the (660) and (880) could be found in the rocking curve. This has been accomplished by the use of six 140° prisms

(Appendix C). Fig. 5.11 shows the obtained rocking curve.

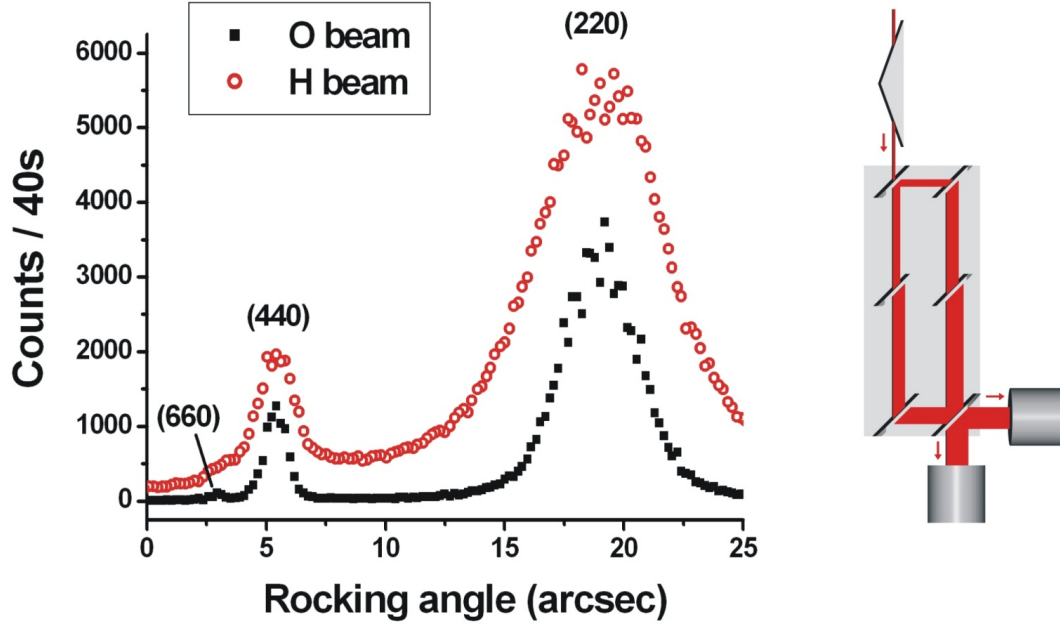


Figure 5.11: Rocking curve in interferometric configuration, showing the separation from the (220) to the (660) reflection in O and H-beam. Here the zero position is arbitrary according to the goniometer encoding.

Whereas the (220) reflection is almost perfectly separated from the other reflections in the O-beam, at the positions of the higher order reflections remain small contributions from other harmonics. This is even more pronounced in the H-beam with higher peak width, where it becomes difficult to resolve the (660) reflection. In the O-beam the contaminations have been corrected by interpolating the corresponding peak profiles and thereby weighting the λ contributions. As the angular width of the reflection curves reduces according to

$$\Delta\theta_{1/2} \propto \lambda^2 \propto \frac{1}{m^2}. \quad (5.9)$$

high angular stability between monochromator and interferometer are required for measurements at higher order reflections. This constitutes a problem as non systematic drifts of the piezo could be observed.

5.2.2 Visibility measurements

Whereas optimizing and moreover maintaining the visibility of a perfect crystal interferometer is not trivial usually, it turned out to be even more challenging in

the case of the new large interferometer. The main disturbances such as temperature gradients and vibrations strongly increase with the size of the interferometer. Moreover intrinsic or residual strains due to crystal mounting are more likely to appear at large lamella distances. These result in space dependent phase patterns - Moires - and thereby reduce the visibility when position-insensitive gas detectors are used. This has been addressed by choosing an accordingly thick interferometer base. One of the problems in the case of a lack of visibility consists in the location of the actual cause. Moreover for a new interferometer one has no reference for the achievable performance, and problems with the crystal can not be excluded. This has been a severe uncertainty factor in the first two tests.

Crystal support

With the present size of the interferometer the limit of the support table at S18 has been reached. Thus a new aluminium table with 30cm diameter and 1cm glass plate has been installed⁵. On this glass plate many combinations of underlays have been tested (a selection is shown in Tab. 5.3). Satisfying results could only be obtained with a stack of papers though.

Support	V (220)	V (440)
Thin carton 0.5mm	0.1	
Plexiglas 5mm	0.1	
Plexiglas 5mm + rubber mat 2mm	0.17	
Plexiglas + rubber mat + sheets of paper 1.5mm	0.27	
Plexiglas + thin smooth tissue	0.23	
Damping rubber mat 10mm	0.38	< 0.1
Tissue + Plexiglas + sheets of paper 1mm	0.51	0.4
Sheets of paper 1.5mm or hydrophobic tyvek	0.6	0.73

Table 5.3: Selection of several tested crystal supports. The underlay is placed on a glass plate of 1cm thickness and 30cm diameter. The best measured visibilities V are shown.

To more systematically investigate this behavior a position sensitive ND&M detector (App. E) with $50\mu\text{m}$ resolution has been employed in the O-beam⁶.

⁵The glass plate is mounted on three fine thread screws, by which the ρ axis relative to the monochromator is adjusted. This axis corresponds to a rotation around the surface normal of the lamellas.

⁶Another interesting possibility of this detector is the measurement of beam profiles in the interferometer output ports, and comparison with calculations from dynamical diffraction

The investigation of phase dependent patterns is well established in X-ray interferometry [35, 13]. However due to the relatively small count rates in neutron interferometry⁷ and accordingly long measurement times, sufficient phase stability has to be guaranteed. At least in the case of non vanishing visibility this stability can be monitored via the intensity of the H-beam. For the clear discrimination of phase dependent patterns from pure intensity distributions, at least two images with different phase shifter position are required.

Fig. 5.12 confirms the absence of Moire fringes for the best underlay for the (220) and (440) reflection. The integral visibility for 1.5cm (width) x 2.5cm (height) beam size yielded still 36%. Thus for this setup intrinsic strains and induced contact strains due to crystal support could be excluded to a high degree.

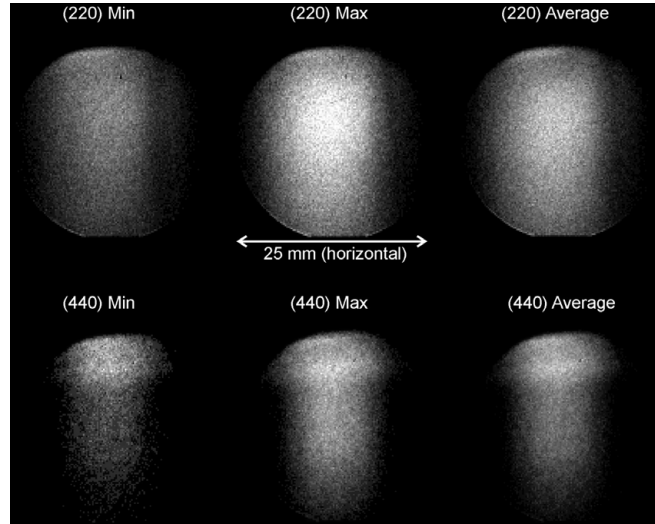


Figure 5.12: Intensity distribution in the O-beam with phase shifter in O-minimum (left), O-maximum (middle) position and phase averaged (right). Average pixel counts $\bar{N}((220), Min - Max) = 96 - 195/pixel$, $\bar{N}((440), Min - Max) = 33 - 73/pixel$.

Fig. 5.13 (c) shows an intrinsic Moire detected in the forerunner interferometer that has not been present after the original preparation [30], whereas in Fig. 5.13 (d) -(e) horizontal Moires detected at a suboptimal underlay (damping rubber mat Tab. 5.3) are shown. Horizontal Moire patterns result from small lattice rotations $\Delta\rho$ - around the axis normal to the lamella surfaces - relative to other

theory. This can also give valuable information on the actual beam width at the positions of the prisms and thereby the possible rotation angle in the Laue phase experiments.

⁷The count rates at $\theta_B = 45^\circ$ are even significantly below the usually used $\theta_B = 30^\circ$ geometry.

interferometer lamellas. Thereby fringes with spacing

$$\Lambda_R = \frac{d}{\Delta\rho} \propto \frac{1}{m} \quad (5.10)$$

are generated. Consequently the period of such fringes is smaller for higher order reflections m (Fig. 5.13 (d) -(e)) and these are more sensitive to relative lattice distortions. In general there is the requirement $\Delta\rho \ll 0.001''$. On the other hand the higher sensitivity of the higher order reflections can be used as a test for the crystal support. Employing the position sensitive detector, fringe spacings that can no more be observed in (220) reflection are still observable in (440) reflection. Hence a further optimization is possible.

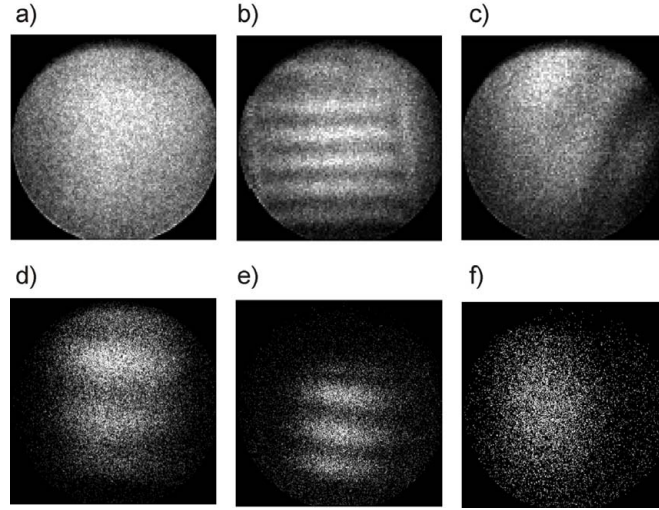


Figure 5.13: a) No Moires in the new interferometer with optimal underlay in (220). b) Artificial Moires with a 1.9° Al-wedge. c) Intrinsic Moire in another large interferometer. d) Intrinsic Moire in the new interferometer with suboptimal underlay (damping rubber mat). e) Same setup but (440) reflection. f) Retrieval of a homogeneous phase profile by putting weights on the interferometer base.

Besides the change of crystal supports, one can try to place weights on the interferometer base and systematically improve via observation of the Moire fringes. Fig. 5.13 (f) shows a compensation by weights of the Moire shown in (e). Due to the thick base the interferometer is not very sensitive to weights though⁸.

⁸An alternative approach consists in placing thin strips of paper etc. below the interferometer base and thereby systematically improve the Moire patterns. This however turned out to be not very efficient. Most of the time the Moire fringes would only become denser and the visibility became worse.

Another strategy is the use of wedges with opening angle β in one beam path. Thereby an artificial fringe pattern with period [13]

$$\Lambda_w = \frac{\lambda}{\delta_{wedge}(\beta, \lambda)} = \frac{\pi}{\lambda N b_N} \cot \frac{\beta}{2} \propto m \quad (5.11)$$

is created (Fig. 5.13 (b)), which can be used to compensate the horizontal Moire fringes due to lattice rotations:

$$\begin{aligned} \Lambda_w &= \Lambda_R \implies \\ \beta &= 2 \arctan \frac{\pi \Delta \rho}{2d^2 N b_N \sin \theta_B} \end{aligned} \quad (5.12)$$

Hence for higher order reflections one needs wedges with larger apex angle, as on the one hand the horizontal fringes are denser on the other hand stronger refracting wedges are needed to obtain the same fringe distance than for larger λ . Anyhow this type of compensation is not optimal for our experiment, where additional material in one beam path might decrease the visibility and moreover gives further limits to the available space for prism and phase shifter positioning.

Visibility performance

The actual visibility tests have been performed by scanning a $6 \times 6 \text{ mm}^2$ entrance slit across the lamella surface. In the horizontal direction the possible beam width has been limited to approximately 1.5 cm due to the fore prisms⁹. The beam height has been limited to approximately 2.5 cm, where the upper half of the lamellas have been illuminated. This included the beam height optimal for the prism experiments, i.e. 10 -20 mm below the upper edge of the lamellas. Within this area no significant visibility variations could be observed.

Fig. 5.14 shows the best visibility scans for the (220) to (660) reflections and Tab. 5.4 summarizes the measured values. The H-beam visibility for the (440) and (660) is comparatively small due to the contamination by the broad (220) and (440) H-beam respectively. For the visibility values given in Tab. 5.4 corrections for background and contributions from other harmonics have been performed. As stated above higher order reflections are more sensitive to suboptimal crystal support. On the other hand one finds a better performance at optimal crystal support. This can be understood by the reduced sensitivity to lattice vibrations, as the time of flight through the interferometer is proportional to λ . Another

⁹Translating the interferometer induces too much uncertainties for a real comparison and a translation of the fore prisms is time-consuming, as precise prism alignment - and masking by cadmium - is required to avoid contamination by background and other harmonics.

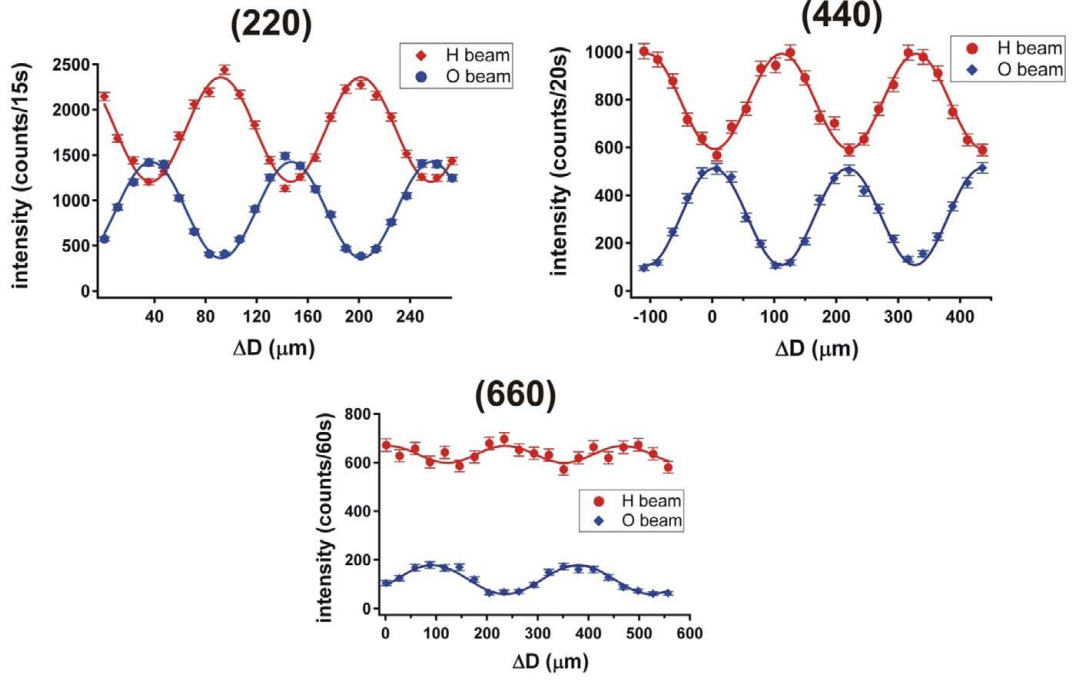


Figure 5.14: Unprocessed visibility scans for different wavelengths as a function of the path difference ΔD by the silicon phase shifter.

interesting point is the reduced sensitivity due to small geometric errors resulting in a slight defocusing of the interferometer. For the ideal geometry¹⁰ a defocusing Δx of the analyzer plate results in [25]

$$V = \left| 1 + \frac{2\pi\Delta x}{\Delta_H} - \frac{5}{9} \left(\frac{2\pi\Delta x}{\Delta_H} \right)^2 \right| e^{-\frac{2\pi\Delta x}{\Delta_H}} \quad (5.13)$$

where the visibility reduction is described by the ratio between Δx and the Pendellösung length Δ_H . As

$$\Delta_H \propto \frac{m}{\tan \theta_B} \quad (5.14)$$

the sensitivity to this type of geometric errors is reduced as shown in Fig. 5.15 (b).

¹⁰Here the mirror lamella D_M is assumed to be equally thick than the analyzer and beam splitter lamellas D . For the geometry $D_M = 2D$ the sensitivity to defocusing can be further reduced as

$$V = \left| 1 + \frac{2\pi\Delta x}{\Delta_H} - \frac{5}{17} \left(\frac{2\pi\Delta x}{\Delta_H} \right)^2 \right| e^{-\frac{2\pi\Delta x}{\Delta_H}}$$

This could be advantageous in the $\theta_B = 45^\circ$ geometry, that is more sensitive to geometric errors. However it is not possible to use this strategy for our interferometer, where also the double loop configuration is an interesting option.

reflection	wavelength (\AA)	relative intensity	peak width	visibility
(220)	2.72	1	3.2''	0.596(10)
(440)	1.36	0.3	0.9''	0.733(20)
(660)	0.91	0.03	0.4''	0.850(60)
(880)	0.68	0.01	0.3''	> 0.5

Table 5.4: Selectable wavelengths at 45° Bragg angle and best obtained values for the visibility after correction for background and contamination by other harmonics.

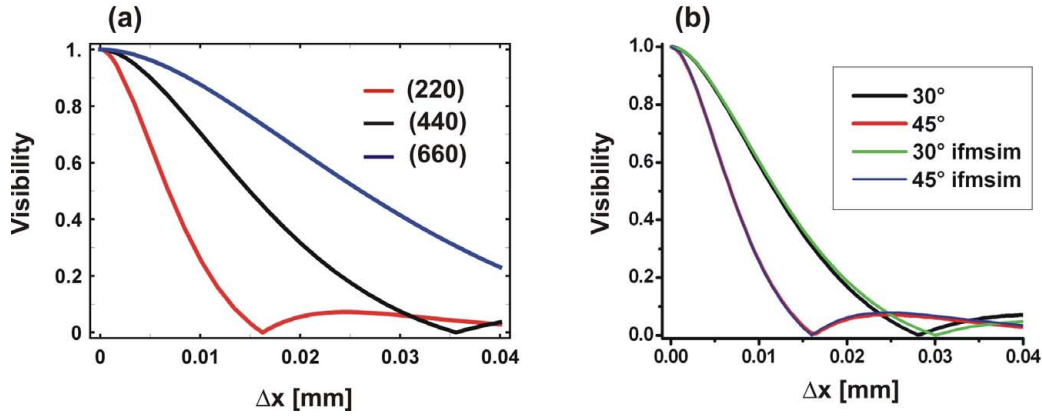


Figure 5.15: Defocusing due to translation of the analyzer lamella by a distance Δx . (a) Visibility reduction for (220) and (440) reflection at $\theta_B = 45^\circ$ (b) for (220) at $\theta_B = 45^\circ$ and $\theta_B = 30^\circ$, compared with spherical wave calculation using *ifmsim* at $\sigma_\theta = 4''$.

Moreover the used $\theta_B = 45^\circ$ geometry is a factor $\tan 45^\circ / \tan 30^\circ \approx 1.7$ more sensitive to geometric errors (Fig. 5.15 (b)). In the latter case Eq. 5.13 has been compared with calculations by spherical wave theory (chapter 4), resulting in good agreement. This reveals the usefulness of *ifmsim* for the estimation of geometrical errors in interferometer geometry. In this respect the exact interferometer geometry has been analyzed and the theoretical values have been calculated. The calculated values are shown in Tab. 5.5 and compared with the best measured values.

In the same way the single loops have been analyzed. A comparison between calculated and measured values is given in Tab. 5.6. However the measured visibilities are probably not the best achievable ones, as the main focus of testing has been on the performance of the large loop, that is used for the experiments.

The calculations can also be used to evaluate possible improvements by selective etching at specific lamellas. In the present case however the main visibility

reflection	wavelength (\AA)	calculated visibility	measured visibility
(220)	2.72	89(4)	0.596(10)
(440)	1.36	97(2)	0.733(20)
(660)	0.91	99(1)	0.850(60)
(880)	0.68	99(1)	> 0.5

Table 5.5: Comparison of calculated visibility for the exact interferometer geometry with the measured values after correction for background and contamination by other harmonics. The errors for the calculated visibilities have been determined by assuming small variations in the geometry within the precision of the geometry measurement.

reflection	area	calculated visibility	measured visibility
1. Loop	45cm^2	92(3)	0.635(10)
2. Loop	55cm^2	91(3)	0.54(1)

Table 5.6: Comparison of calculated (220) visibility for the first and second loop with the best measured values.

reduction is obviously not due to interferometer geometry.

The (880) reflection

Finally it was also possible to resolve the (880) reflection. Fig. 5.16 (a) shows a zoom into the (660) and (880) region of the rocking curve. Despite the difficulties concerning the necessary angular stability and resolution due to the extremely small width of the (880) peak it was possible to reproduce an oscillation with approximately the correct period $\lambda \approx 0.68\text{\AA}$ at the position of the peak. Although at this beam line measurements below $\lambda \approx 1\text{\AA}$ are rather challenging the measurements at the (660) and (880) orders are to our knowledge the shortest wavelengths hitherto used in neutron interferometry¹¹. This is insofar interesting, as almost all other approaches are into the direction of cold and ultra cold neutrons. Moreover the use of several harmonics is of essential interest with respect to precision measurements such as for the neutron-electron scattering length, the Debye Waller factor of silicon and gravitational short Range interactions (7.3).

Visibility within the rocking curve

In another measurement the visibility as a function of the position in the rocking curve has been measured. This is of interest with respect to remaining inter-

¹¹To our knowledge $\lambda \approx 0.95\text{\AA}$ [36] has been the smallest wavelength so far.

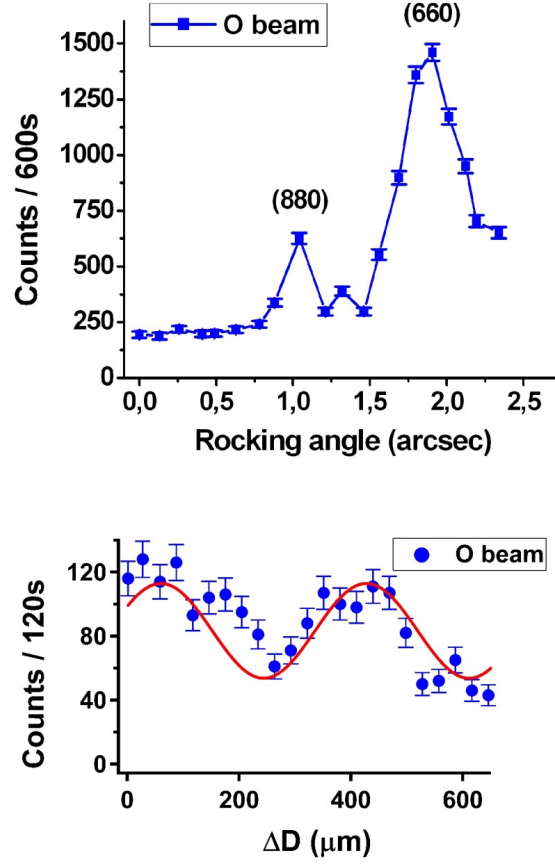


Figure 5.16: Rocking curve between (660) and (880) reflex and visibility scan at the (880) peak.

ference able contribution of for example the (220) reflection at the position of the higher order reflections. Another aspect consisted in a preliminary study of the dependence of the Laue phase on the rocking position (chapter 7).

Fig. 5.17 shows the average intensities normalized with respect to the maximum together with the measured visibilities¹² (corrected for the average back-

¹²In addition a variation of the phase shift of the empty interferometer within the rocking curve could be measured. This should not be the case in ideal interferometer geometry. However in the non-ideal geometry like for a defocused interferometer the phase shift can depend on the miset angle of the incident beam [25]. Hence a variation of the incident beam spectrum by a variation of the angle between monochromator and interferometer can change the phase shift. Just recently a more accurate measurement of this feature has been addressed with a different interferometer in 30° geometry. Placing a diffracting sample in front of the interferometer reduced this phase variations due to a broadening of the rocking curve (private communication with H. Lemmel). Therefore a mosaic crystal would be optimal for higher phase stability.

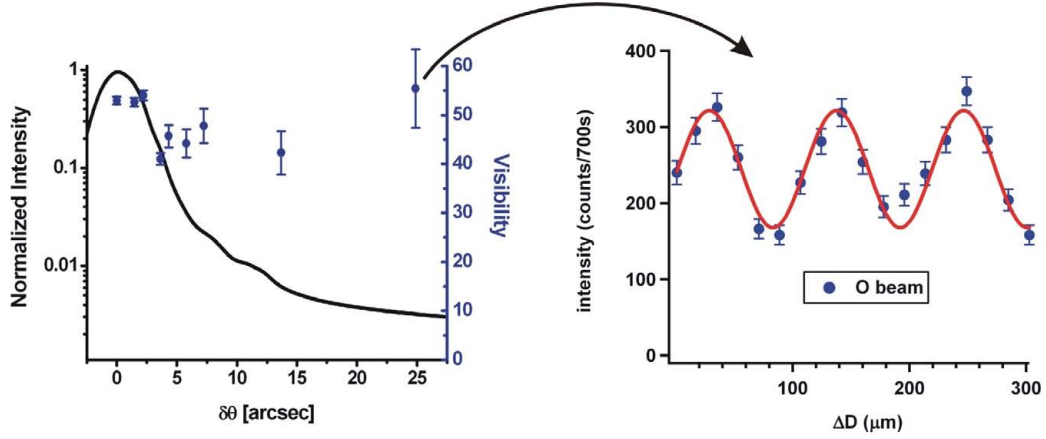


Figure 5.17: Visibility (with background correction) and average intensity within the rocking curve and unprocessed scan for $\delta\theta \approx 25''$.

ground) within the rocking curve (the higher order reflections are at negative angles). One has to be careful with interpretations of the measured visibility variations, as the measurements had to be performed serially. Moreover the measurement times at the low intensities far off the maximum are quite long and phase drifts might have a negative influence on the visibility¹³. All the more the visibilities obtained up to $\delta\theta = 25''$ are remarkable. This is already more than ten five times the FWHM off Bragg. Also from a theoretical point of view interference at such large angles comes out naturally, in praxis it's astonishing. Probably it is possible to measure visibilities at even larger angles and one can thereby to some extent distinguish interfere able contributions from background. It is also interesting to note that by a measurement at the side of the rocking curve containing the higher order reflections, one would again expect to measure interfere able (220) contributions after scanning over all higher order contributions.

Stability problems

Summarizing the interferometer test we have

- successfully tested the presently largest perfect crystal neutron interferometer
- shown the use of up to four wavelengths without changing the beam geometry or interferometer setup

¹³These measurements have only been possible during a time of high phase stability.

- Systematically investigated the influence of crystal support and space dependent phase patterns employing a position sensitive detector
- investigated and discussed some aspects of the interferometer performance with respect to higher order reflections

Unfortunately there remained a fundamental stability problem concerning the interferometer performance. For instance recurring visibility losses have been observed, continuously and in time scales between one and many hours. This resulted in severe problems concerning the available measurement time and the accuracy of the phase measurements. As it might be useful for the further investigation of this phenomenon, an overview of addressed approaches is given in the following

- Employing the ND&M camera allowed to distinguish effects from the crystal support from other disturbances. Taking images in the O-beam - optionally with the help of an auxiliary wedge to create an artificial pattern for reference - gives information on principal interference and phase stability even if no visibility can be found with the position insensitive detector. However in the times of visibility loss, also the spatial phase patterns vanished.
- Sometimes the loss of visibility has been accompanied by strong phase drifts - an indication for a temperature drift of the whole setup - but not all the time.
- A careful monitoring of the temperature close to the interferometer, within the S18 housing, the guide hall, the beam guide and even the temperature outside didn't show any distinct correlation. A similar observation had been made before [37], although some correlation between guide hall temperature and phase stability had been found then.
- Although due to the type of time structure of the visibility loss vibrations seemed to be a rather unlikely cause, trials with optimal and suboptimal damping¹⁴ especially during the time of high visibility have been performed. Additionally the influence of magnitude and frequency of vibrations has been studied using a loud speaker close to the interferometer. As main conclusion vibrations can be excluded to a high degree as cause of the discussed visibility problems.

¹⁴Even the optical bench has been fixed, still showing a remarkable value of visibility.

- Although non polarized neutrons have been used, as pointed out by H. Rauch, disturbances from the large magnetic field (up to 15 Tesla) of the neighboring instrument might result in disturbing phase shifts and thereby visibility losses. Neither measurements directly at the interferometer nor a monitoring of the absolute magnetic field of the neighboring instrument did show any correlation with the visibility.
- The rather unusual crystal support by a stack of papers raised the question, if the support might be unstable or humidity might cause problems. However monitoring of phase patterns by a wedge has shown a simple loss of the visibility but no change in the structure of the fringes. Furthermore paper together with silica gel and instead of paper hydrophobic tyvek have been tried, without any improvement.
- As temperature gradients at the interferometer seemed to be the main source, the aluminium interferometer table has been isolated to gradients emerging from the bottom, and a weak heat source in the form of a small lamp has been tested around the interferometer. This probably has been too rough as the visibility could only be decreased, in extreme cases even the intensities changed, as due to temperature variations the reflectivities change.
- As the interferometer - just as in the case of previous interferometers - has been housed in a box with foil windows, the density of this box has been studied. Sometimes small holes seemed to be better, with increasing hole size however the phase drift also increased. An attempt to cover the box with aluminium foil, to avoid a sort of greenhouse effect, did show no improvement.
- Finally the identical setup as usually used for the experiments with polarized neutrons has been used, employing water cooled coils with adjustable temperature around the interferometer. Although measurements before and after ours with a small interferometer in the identical setup (except the angle of the optical bench) have shown good visibility, no improvement could be achieved.
- During times of visibility reduction still better values could be achieved in the single loops. Additionally also in the case of the small interferometers regularly slight reductions in the order of 10% of the visibility are detected, without an obvious reason. This suggests that the problem is more pronounced for large interferometers.

Although no final conclusion on this can be made, the most likely source still seems to consist in small thermal gradients at the interferometer lamellas and/or the overall temperature stability. However it should be noted that in no case vertical Moires could be detected, which are likely to appear by thermal gradients between beam splitter and analyzer lamella [38, 39]. An improvement should be addressed via the installation of more reliable¹⁵ temperature sensors at S18, and attempts with infrared diodes (J. Summhammer) around the interferometer, for a fine tuning of the lamella temperature. Additionally upcoming measurements at NIST with the same interferometer shall bring more insight into this problem.

¹⁵Despite the theoretical accuracy of $0.01^{\circ}C$ the sensors turned out to be not very reliable.

Chapter 6

Prisms in neutron interferometry

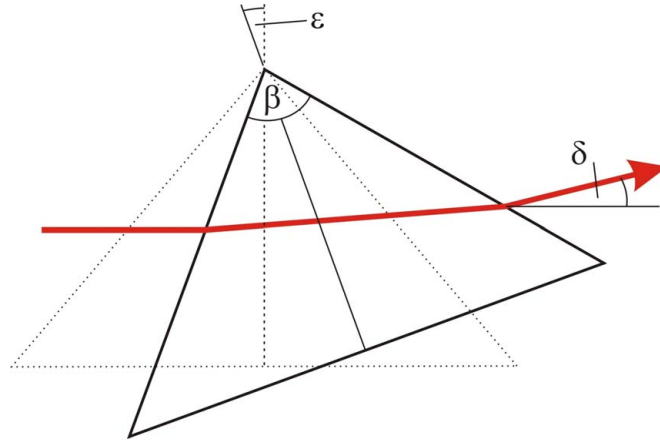


Figure 6.1: Beam deflection δ by a prism in asymmetric ($\epsilon \neq 0$) configuration.

Optical components such as prisms and lenses in light optics make use of the fact that light waves are refracted when they pass from one medium to another. Therefore the media are characterized by their index of refraction n . This description can be also applied to neutron optics where the index of refraction is given by

$$n = 1 - \frac{\lambda^2 N b_N}{2\pi} \quad (6.1)$$

This can be used for neutron beam deflections by prisms, where the angle of deflection δ reads (Fig. 6.1)

$$\delta = 2(1 - n) \frac{\sin \beta}{\cos \beta + \cos 2\epsilon} \quad (6.2)$$

This expression simplifies in the symmetric case ($\epsilon = 0$)

$$\delta = 2(1 - n) \tan \frac{\beta}{2} \quad (6.3)$$

For most materials b_N is positive, thus δ is positive in contrast to light optics. As for thermal neutrons $1 - n$ is of the order of 10^{-5} , the beam deflection is extremely small, in the order of arc seconds or below. The strong dependence on the wavelength $1 - n \propto \lambda^2$ leads to a strong dispersion, which can be used for the separation of wavelengths. Fig. 6.2 (a) shows the strong increase of the beam deflection with the apex angle. A further increase can be gained by the asymmetric rotation ϵ (Fig. 6.2(b)). However in the extreme case of $\epsilon \lesssim \pi/2 - \beta/2$, the utilizeable beam width becomes very small. In another interesting approach a perfect silicon prism has been used to significantly enhance the deflection close to a Bragg condition [40]. This method is connected to our study of the increasing phase shift around the Bragg condition. Anyhow using such a prism for beam deflection the strong dispersion of the beam deflection close to Bragg would complicate the experiment significantly. Moreover the justage of this kind of silicon prism would be almost as delicate as the justage of a sample Laue crystal inside the interferometer.

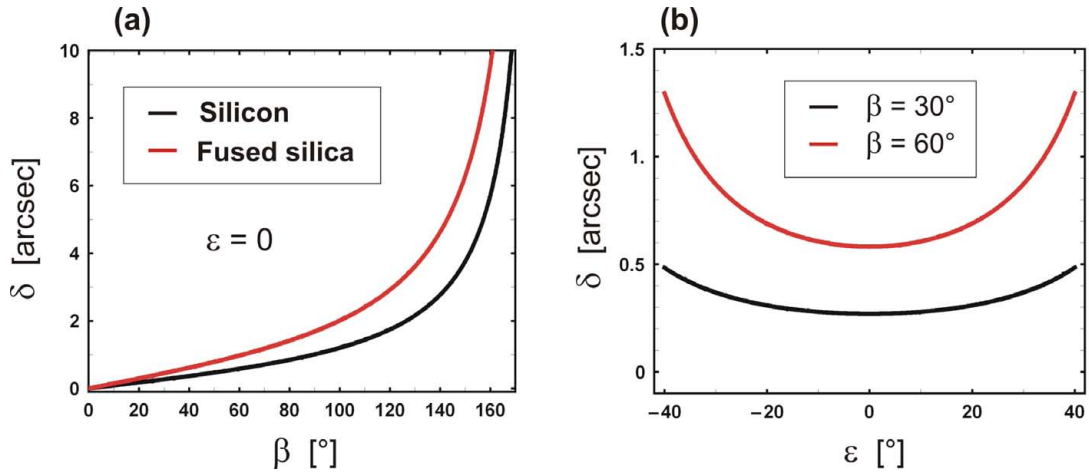


Figure 6.2: (a) beam deflection in the symmetric case as a function of the apex angle β (b) beam deflection as a function of the asymmetric rotation ϵ for a silicon prism of apex angle β .

Concerning neutron interferometry, so far prisms have been applied in two cases: First for the separation of wavelengths before the interferometer (App. C), secondly within an interferometer for the creation of position dependent phase patterns (section 5.2). In the latter case the beam deflection is however extremely

low in the order of $0.01''$. Hitherto there have been no experiences with strong deflecting prisms inside a neutron interferometer, where the coherence properties of the neutron beam become crucial. However parallel to our investigations, similar experiments have been carried out at NIST [41, 42].

6.1 Materials

There are several possibilities to increase the beam deflection in neutron optics. One can choose long wavelengths or a large apex angle β eventually combined with an asymmetric rotation ϵ . However in a perfect crystal neutron interferometer one is limited to the range of thermal neutrons and the beam height in combination with the path length limit the apex angle and ϵ . Thus to obtain sufficient deflection the choice of appropriate prism materials becomes important as $1 - n \propto Nb_N$. Furthermore the requirements in interferometry are much higher than in other neutron optical experiments. The use of prisms has to maintain the coherence between both beams and should not disturb precise phase measurements. Especially inhomogeneities causing variations of the scattering length density Nb_N and variations δD of the thickness D over the beam diameter can cause a severe reduction of the visibility by phase averaging. Such a variance of the phase $\langle \delta\chi^2 \rangle$ over the beam diameter gives rise to a damping factor (3.10) for the coherence function. For a Gaussian distribution of the variations δN , δD , δb_N one obtains a coherence function [1, 43]

$$\begin{aligned}
 |\Gamma(\Delta)| &= \Gamma_D(\delta D)\Gamma_D(\delta N)\Gamma_D(\delta b_N)|\Gamma(\Delta)|_0 \\
 &= \exp\left(\left[-\left(\frac{\delta D}{D}\right)^2 + \left(\frac{\delta N}{N}\right)^2 + \left(\frac{\delta b_N}{b_N}\right)^2\right](\Delta_0 k_0)^2/2\right)|\Gamma(\Delta)|_0 \\
 &= \exp\left(-\left[\left(\frac{\delta D}{D}\right)^2 + \left(\frac{\delta N}{N}\right)^2 + \left(\frac{\delta b_N}{b_N}\right)^2\right]\left(\frac{Nb_N\lambda D}{\cos\theta}\right)^2/2\right)|\Gamma(\Delta)|_0
 \end{aligned} \tag{6.4}$$

where θ is the angle between surface normal and wave vector \mathbf{k} . $|\Gamma(\Delta)|_0$ is the coherence function omitting all variations concerning the material and is usually described by the width of the wavelength distribution $\Delta\lambda/\lambda$. Variations of the nuclear scattering length δb_N for example due to a mixture of isotopes are in most cases of minor importance. The influence of the thickness and density variations increases with λ^2 . Thus at the first order reflection with $\lambda = 2.72\text{\AA}$ our setup is much more sensitive to surface roughness and inhomogeneities than at the usually used 1.9\AA at $\theta_B = 30^\circ$ or at the higher order reflections. The influence

of the variation δD is independent of the absolute thickness and thus a pure surface effect, however scales with the number of surfaces n by a factor \sqrt{n} . In the applied prism arrangements there are at least four surfaces per beam path. Thus δD should optimally be in the range $\delta D \lesssim 1\mu\text{m}$. The variation of δN on the other hand increases strongly with the absolute thickness D . Normally only relatively thin phase shifters are used in neutron interferometers. Hence there are only very few experiences with thicknesses $D \gtrsim 1\text{cm}$ [44] and problems probably due to material inhomogeneities have been encountered [23]. Thus the investigation of possible materials for prism fabrication is essential.

6.1.1 Material candidates

Hitherto there have been experiences with several materials for phase shifters, mainly with silicon, aluminium, bismuth and thin plates of fused silica. For aluminium for example problems concerning the quality of the material have been encountered [23]. On the other hand it is desirable to especially investigate materials with strong refraction for the fabrication of prisms. Therefore we have the following requirements on prism materials

- extremely homogeneous (negligible variations δN)
- absorption negligible
- large scattering length density Nb_N for sufficient beam deflection
- high surface quality (negligible variations δD)
- reasonable material and production costs
- producibility with high geometric accuracy

Table 6.1 shows a list of elements that are possible constituents because of their small absorption and scattering cross sections.

Table 6.2 shows a selection of materials that could be suitable for prisms. The materials in brackets are only of theoretical interest, as they would yield extremely high refraction. Affordable fabrication of suitable diamond prisms would be unrealistic. In the case of ^{58}Ni the magnetic domain structures result in a critical inhomogeneity of the material. Inhomogeneities are a problem of several metals with high scattering length density such as iron, copper. E. Jericha had an interesting suggestion as to use D_2O in cuvettes in prism form. Nevertheless the accurate fabrication of the cuvettes and the problem to guarantee a homogeneous density over the volume might cause problems. Pyrolytic graphite might be

Isotope	b_{nuc} [fm]	σ_{coh} [barn]	σ_{incoh} [barn]	σ_{abs} [barn]
2H	6.674(6)	5.592(7)	2.05(3)	0.000519(7)
9Be	7.79(1)	7.63(2)	0.0018(9)	0.0076(8)
C	6.6484(13)	5.551(2)	0.001(4)	0.00350(7)
O	5.805(4)	4.232(6)	0.000(8)	0.00019(2)
^{19}F	5.654(12)	4.017(14)	0.0008(2)	0.0096(5)
^{23}Na	3.63(2)	1.66(2)	1.62(3)	0.530(5)
Mg	5.375(4)	3.631(5)	0.08(6)	0.063(3)
^{27}Al	3.449(5)	1.495(4)	0.0082(6)	0.231(3)
Si	4.15071(22)	2.1633(10)	0.004(8)	0.171(3)
^{31}P	5.13(1)	3.307(13)	0.005(10)	0.172(6)
S	2.847(1)	1.0186(7)	0.007(5)	0.53(1)
Ca	4.70(2)	2.78(2)	0.05(3)	2.83(2)
Ge	8.185(20)	8.42(4)	0.18(7)	2.20(4)
^{93}Nb	7.054(3)	6.253(5)	0.0024(3)	1.15(6)
Pb	9.401(2)	11.115(7)	0.0030(7)	0.171(2)
^{209}Bi	8.532(2)	9.148(4)	0.0084(19)	0.0338(7)
^{58}Ni	14.4(1)	26.1(4)	0	4.6(3)

Table 6.1: Various elements - or alternatively specific isotopes - that are interesting as components for neutron optical components [45].

an interesting candidate, but it is difficult to obtain sufficient large pieces of homogeneous material for testing or prism fabrication. Especially interesting are materials that are used for light optical components, as in this case experience in prism fabrication can be guaranteed. Concerning these there would be of course a lot of other possibilities such as $LiNbO_3$, CaF_2 , ZnS , BaF_2 , RuF , ZrO_2 , $ZrSiO_4$, SnO_2 , $CaCO_3$, NaF , SrF_2 ..., which however do not give an advantage in refraction in comparison to the listed materials.

In this context it is interesting to note that in the recent years the interest in strongly refracting neutron optical devices such as prisms and (Fresnel-)lenses has grown from the side of applied neutron optics such as SANS. Therefore several projects especially investigating components for cold neutrons have been initiated. Especially MgF_2 seems to be very promising [46, 47, 48, 49]. Other components have been built from MnF_2 [50] (with however non-negligible absorption in the thermal neutron range) and vitreous silica [51]. Another promising candidate is the amorphous perfluoropolymer CYTOP ($C_6F_{10}O$) with relatively large refraction $Nb_N = 4.5 \cdot 10^{14} m^{-2}$ and a high degree of homogeneity. Nevertheless at the moment only thin sheets of thicknesses in the order of $100\mu m$ are available.

Material		$\rho [g \cdot cm^{-3}]$	$Nb_N [10^{10} cm^{-2}]$	$\delta (\beta = 30^\circ)$
Silicon	<i>Si</i>	2.33	2.07	0.27''
Aluminium	<i>Al</i>	2.7	2.08	0.27''
Bismuth	<i>Bi</i>	9.78	2.35	0.31''
Lead	<i>Pb</i>	11.34	3.09	0.40''
Fused silica	<i>SiO₂</i>	2.201	3.46	0.45''
Germanium	<i>Ge</i>	5.323	3.61	0.46''
Quartz	<i>SiO₂</i>	2.65	4.18	0.54''
Magnesiumfluorid	<i>MgF₂</i>	3.177	5.11	0.66''
Silicon carbide	<i>SiC</i>	3.21	5.22	0.68''
Sapphire	<i>Al₂O₃</i>	3.99	5.74	0.74''
Magnesiumoxid	<i>MgO</i>	3.585	5.99	0.77''
Heavy water	<i>D₂O</i>	1.1047	6.36	0.82''
Graphite	<i>C</i>	2.25	7.5	0.96''
Beryllium	<i>Be</i>	1.848	9.62	1.23''
(Diamond)	<i>C</i>	3.51	11.7	1.53''
(Nickel58)	⁵⁸ <i>Ni</i>	8.908	13.2	1.72''

Table 6.2: Materials that could be interesting for strong refracting prisms in neutron optics and the calculated scattering length density Nb_N . As an example the beam deflection for a symmetric 30° prism is given.

These can be grooved and afterwards stacked, resulting in large beam deflections [52, 53]. This method is not easily applicable to neutron interferometry, as it is difficult to avoid thickness gradients over the neutron beam, resulting in a strong reduction of the visibility. This again shows the much higher restrictions in neutron interferometry in comparison to the usual needs in neutron optics.

6.1.2 Testing materials

For the purpose of testing several candidates for prism fabrication, thick plan parallel plates of these materials with good surface quality have been ordered. The length of these test plates was larger than the beam separation in our interferometer, so that they reached through both paths. The product $\Gamma_D(\delta D)\Gamma_D(\delta N)\Gamma_D(\delta b_N)$ is obtained by the visibility reduction

$$V_{red}(\lambda) = \frac{V_{sample}(\lambda)}{V_{empty}(\lambda)} \quad (6.5)$$

relative to the visibility of the empty interferometer V_{empty} . The results are shown in Table 6.3 together with measured values of Σ_{SANS} (Eq. 6.10).

Material	specification	thickness	V_{red}	Σ_{SANS}
$AlMgSi0.5$	wrought	2 cm	0.96(1)	0.03
$AlMgSi1$	wrought	2 cm	0.10(2)	0.19
$Al99.5$	wrought	2 cm	0.72(3)	0.06
$AlMg4.5Mn$	cast	0.5 cm	0.35(3)	0.73
Fused silica	grade 2F	1 cm	0.94(3)	0.0084
Fused silica	Suprasil,	6 cm	0.00(1)	0.09
Fused silica	Infrasil	-	-	0.05
Fused silica	SQ0	-	-	0.01
MgF_2	VUV, single crystal	1 cm	0.92(3)	0.0015
Al_2O_3	single crystal	1 cm	0.98(2)	0.01
Be	S200F	0.5 cm	0.00(1)	

Table 6.3: Materials tested for visibility reduction at $\lambda = 2.72\text{\AA}$ and/or small angle scattering. The surface roughness of all plates tested for visibility has been significantly below $1\mu\text{m}$.

Small angle scattering measurements

Another approach consisted in a qualitative measurement of small angle scattering from the samples. This has the advantage that these measurements are not restricted to plan parallel plates of good surface quality. Thus also other test pieces that are available without special preparation can be tested for material inhomogeneities.

Small angle scattering refers to the scattering from small structures of size d characterized by a variation of the scattering length density Nb_N , which according to Eq. 6.4 decrease the coherence function. This scattering is characterized by a momentum transfer q that is inversely proportional to the structure size:

$$\begin{aligned}
 q &= \frac{2\pi}{d} \\
 q &= \frac{2\pi}{\lambda} \cdot 2 \sin \frac{\theta}{2}
 \end{aligned} \tag{6.6}$$

where the q is related to the scattering angle θ . Concerning the momentum transfer and thus the structure size, two techniques are established

- SANS (Small angle neutron scattering) for structure sizes below $1\mu\text{m}$

$$10^{-3} < q \tag{6.7}$$

Due to the relatively large scattering angles a two dimensional detector in a distance defined by the expected scattering angles is used.

- USANS (Ultra Small angle neutron scattering) for structure sizes in the range of micrometers

$$2 \cdot 10^{-5} < q < 5 \cdot 10^{-3} \text{Å}^{-1} \quad (6.8)$$

The small scattering angles are detected by the application of a Bonse-Hart camera (Fig. 6.3) [54].

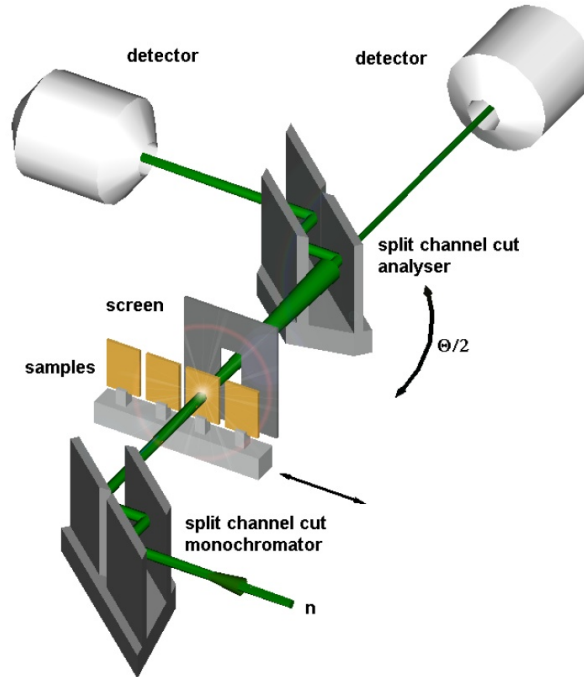


Figure 6.3: Sketch of a Bonse-Hart camera employed for USANS measurements [55].

A first simple approach could consist in a measurement of the small angle cross section Σ_{SANS} integrated over most of the q range. This can be easily carried out during measurements in the interferometric setup [23] (Fig. 6.4 (a)). Blocking one beam path and placing the test plate in the other path, the scattered neutrons will increase the transmitted beam intensity at the analyzer lamella, thereby increasing the O-beam intensity and decreasing the H-beam intensity. Thus Σ_{SANS} adds to the total cross section

$$\Sigma_{tot} = \Sigma_{absorption} + \Sigma_{scattered} = N \cdot (\sigma_a + \sigma_s) \quad (6.9)$$

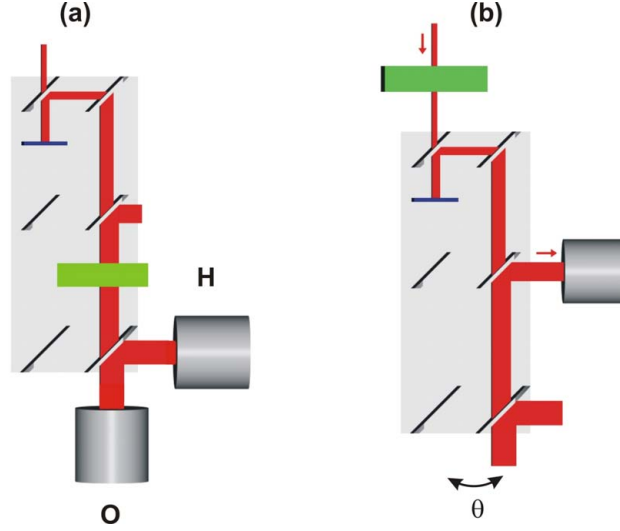


Figure 6.4: (a) Setup for the measurement of the total and small angle scattering cross sections with a neutron interferometer (b) USANS equivalent measurement with the interferometer

for the H-intensity while it has to be subtracted for the O-intensity:¹

$$\begin{aligned} \frac{I_{H,sample}}{I_{H,empty}} &= e^{-(\Sigma_{tot} + \Sigma_{SANS})D} \\ \frac{I_{O,sample}}{I_{O,empty}} &= e^{-(\Sigma_{tot} - \Sigma_{SANS})D} \end{aligned} \quad (6.10)$$

Measuring both intensities yields Σ_{tot} and Σ_{SANS} . Table 6.3 compares visibility measurements with measurements of Σ_{SANS} . It is obvious that larger Σ_{SANS} decrease the visibility. However it is desirable to obtain more information on the structure sizes inside the material, as structures larger than $1\mu\text{m}$ are mainly responsible for visibility reductions [56]. Therefore USANS measurements can give the necessary information. In the case of different aluminium alloys we had the possibility to make measurements with the USANS-setup at S18 at 1.9\AA , shown in Fig. 6.5.

It is difficult to obtain measurement time for this purpose and desirable to perform such measurements together with visibility measurements. Therefore we have employed the interferometer as an USANS device as shown in Fig. 6.4. Instead of the usual threefold Bragg reflection by the analyzer here a threefold

¹The range of measured scattering angles θ is limited by the distance and opening area of the O-detector. Neutrons scattered outside this angle of acceptance $\theta \gtrsim 2^\circ$ will here give a contribution to Σ_{tot} .

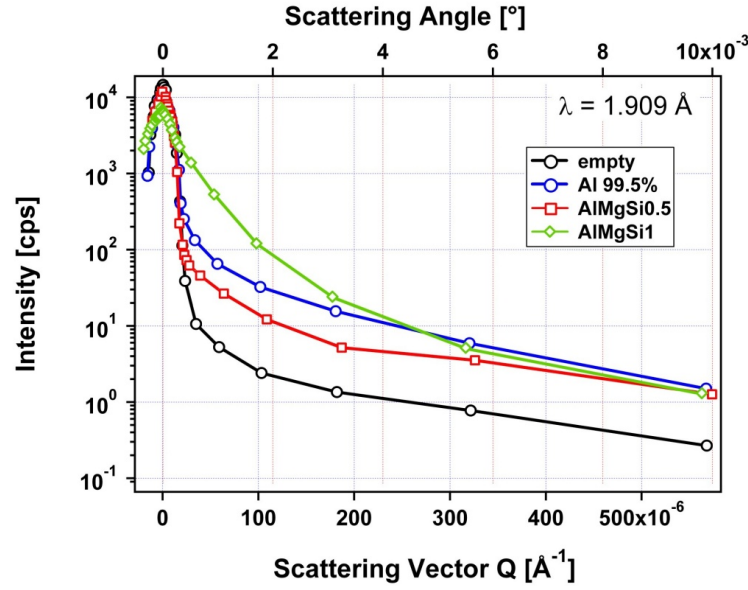


Figure 6.5: USANS measurements for several aluminium alloys, applying the conventional Bonse-Hart camera at $\lambda = 1.9\text{\AA}$.

Laue reflection is employed². Concerning the reflected intensity (Fig. 6.6, App. D) this setup is not competitive to the usual Bonse-Hart camera. Nevertheless it is sufficient for our needs.

Fig. 6.7 (a) shows qualitatively the same results as obtained by the usual USANS setup (Fig. 6.5). These measurements in comparison with Tab. 6.3 clearly show that enlarged small angle scattering at inhomogeneities in the size of micrometers is related to a significant loss of visibility.

Hence it is advisable to test each non-crystalline material before prism fabrication, as a large variation of usability has been confirmed, with a strong dependence on the manufacturing process.

In the following some comments on some of the tested materials are given.

Single crystals

One finds especially good results for single crystals like silicon, MgF_2 and sapphire, which is expected due to their homogeneity. USANS measurements similar to Fig. 6.7 (b) have shown no detectable small angle scattering. Using single crystals as phase shifters or prisms one has to consider the crystal orientation,

²Concerning the monochromator in the usual setup, also there a threefold Bragg-reflection is employed, in the case of the monochromator for the interferometer, there is only one Bragg reflection.

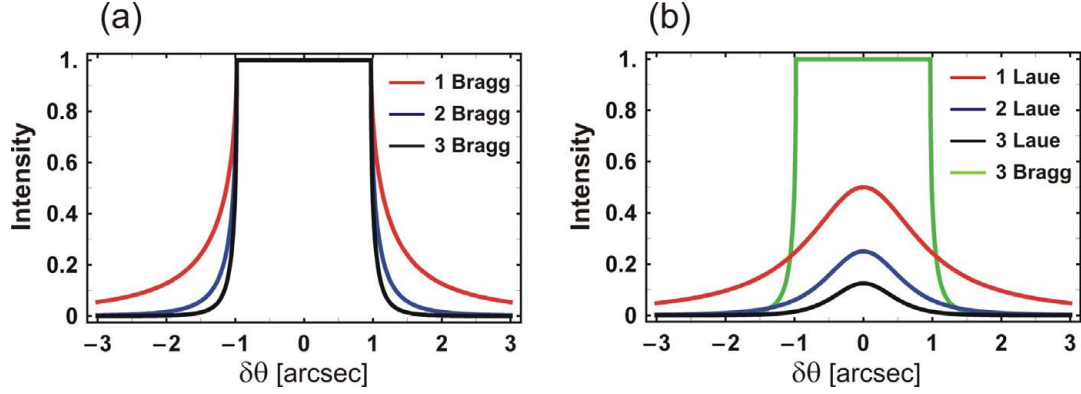


Figure 6.6: (a) Multiple Bragg reflections and (b) Multiple Laue reflections compared with a threefold Bragg reflection for (220) reflection at $\theta_B = 45^\circ$. In all cases the average over the Pendellösung oscillations has been taken.

as remarkable phase effects from dynamical diffraction occur many arc minutes off the exact Bragg condition. Concerning the strongly refracting materials like MgO , MgF_2 and Al_2O_3 there are experiences in manufacturing from light optics. However the standard size of crystals is rather limited (MgO), and due to the hardness of the materials it is difficult to polish the surfaces to the desired flatness. Nevertheless it was possible to find manufacturers, that could in principle handle at least Al_2O_3 and MgF_2 to the desired precision and size. Unfortunately it was not possible to order prisms in the final phase of the project, due to the prices: approximately 9000 Euro for 4 MgF_2 prisms and approximately 6000 Euro for 4 Al_2O_3 prisms (dimensions similar to the ones shown in Fig 6.12).

Fused silica

There have been already many good experiences with thin pieces of fused silica in neutron interferometry, where it is routinely used for example for cuvettes in scattering lengths measurements. In a measurement with Suprasil³ with a however extremely thick sample $D \approx 6$ cm the visibility has been destroyed completely [57]. Additionally slightly enhanced small angle scattering in comparison to other tested silica types could be confirmed (Tab. 6.3, Fig. 6.7), which has not been expected from the stated homogeneity. Thus further tests with silica have been performed. However all further tested pieces have shown a high degree of homogeneity and negligible USANS (Fig. 6.7). The tested Suprasil turned out to be an outlier. One especially prepared test plate (Silo, grade 2F, Tab. 6.3) has main-

³Linos Photonics GmBH, Göttingen, Germany

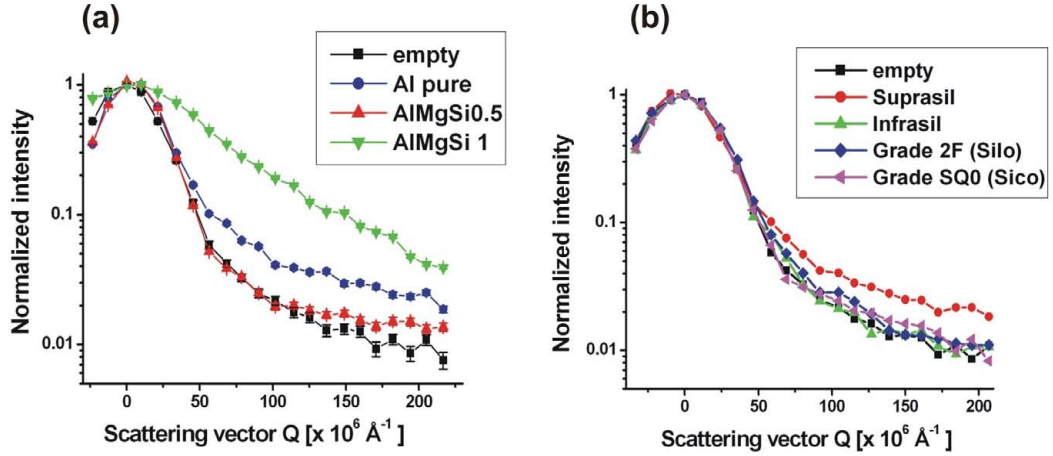


Figure 6.7: (a) USANS measurements applying the interferometer setup (Fig. 6.4) at $\lambda = 2.72 \text{ \AA}$ for several aluminium alloys $D = 2 \text{ mm}$ (b) for several types of fused silica $D = 1 \text{ mm}$.

tained the visibility to a high degree. Thus fused silica seems to be a promising candidate. Furthermore the fabrication of silica prisms is comparatively easy and cheap. On the downside silica offers only slight enhanced refraction in comparison to silicon or aluminium. Moreover due to inhomogeneities on the nanometer scale there is a remarkable loss of intensity due to scattering in a wide range of angles.

Aluminium

Concerning refraction, aluminium is not really a prime candidate. However it offers large advantages concerning the fabrication and also the price. For example it is possible to manufacture a joined prism set, that is cut from one block as shown in Fig. 6.8. This is extremely useful as most alignment problems can be circumvented.

Furthermore aluminium is routinely used for phase shifters in neutron interferometry. Though usually only pieces of several millimeters are used and for thick plates problems have been reported [23]. In a first approach for prism manufacturing pure, wrought (99.5) aluminium and cast *AlMg4.5Mn* have been used, as these have suggested for their homogeneity from the manufacturer. Unfortunately severe problems concerning the visibility have been encountered in our first measurements. Thus tests on several aluminium alloys have been performed. The best usability has been found for wrought *AlMgSi0.5*. The large difference in homogeneity between *AlMgSi0.5* and *AlMgSi1* might probably also explain the encountered problems in [23], as *AlMgSi1* is mainly used for thicker



Figure 6.8: Connected set of two 25° aluminium prisms, that are cut from one aluminium block.

aluminium bars. In general before the fabrication of neutron optical devices in interferometry, a test of the material is strongly advisable, as results between different manufacturers might vary. Concerning the surface quality, electrical discharge machining, has been used. This technique allows to cut connected forms (Fig. 6.8) to a high geometrical precision. The emerging roughness is of the order $\delta D \approx 1.5\mu\text{m}$. This roughness can be further reduced by electrochemical polishing below $1\mu\text{m}$. A comparison in a visibility measurement of a test plate before and after electrochemical polishing⁴, has shown no detectable difference. Thus the surface quality directly obtained from electrical discharge machining is sufficient for aluminium phase shifters and prisms in interferometry.

Beryllium

Beryllium would be ideal concerning the strong refraction. Moreover there has been already an application to X-ray interferometry [58]. Unfortunately the tested material (Tab. 6.3) revealed extremely strong small angle scattering. Placing a 5mm thick plate in front of the interferometer lead to a broadening of the rocking curve to almost one arc minute! Thus no visibility has been preserved despite an extremely good surface quality of the tested plate. The reason is the

⁴Performed by Henkel Beiz- und Elektropolier technik GmbH, Waidhofen an der Thaya. 15 to $20\mu\text{m}$ at each surface have been removed during the polishing process.

manufacturing of usually available beryllium is by compressing, resulting in an inhomogeneous density. Single crystals can in principle be grown, which is complex and costly though. Furthermore beryllium components should be handled with care anyhow, due to its toxicity.

6.2 Prism design and alignment

The accurate alignment together with accurate fabrication is essential for the maintenance of the visibility and moreover for precise phase measurements. In general one can say that for larger wavelengths ((220) reflection) the requirements are higher than for shorter wavelengths ((440) reflection) due to the strong dispersion of the index of refraction. Moreover for the use of strongly refracting prisms these requirements are higher and have to be taken into account accordingly.

In this context it is interesting to note that also the prism design has an impact on the alignment requirements. Practically one normally uses either symmetric prisms or orthogonal prisms (Fig. 6.9). The orthogonal prisms can be understood as an asymmetric rotation of a symmetric prism by $\epsilon = \beta/2$. Thus the beam deflection is somewhat stronger than in the symmetric case

$$\begin{aligned}\delta_{orth}(\beta) &= \delta_{sym}\left(\beta, \epsilon = \frac{\beta}{2}\right) = 2(1-n)\frac{\sin\beta}{\cos\beta + \cos\beta} = (1-n)\tan\beta > \\ &> 2(1-n)\tan\frac{\beta}{2} = \delta_{sym}(\beta)\end{aligned}\quad (6.11)$$

This enhancement is especially significant for $\beta \rightarrow 90^\circ$, while it is of minor importance for $\beta \lesssim 45^\circ$. However concerning misalignments with respect to ϵ the error in beam deflection is significantly larger for orthogonal prisms

$$\begin{aligned}\delta_{orth}(\delta\epsilon) &\propto \frac{\sin\beta}{\cos\beta + \cos[2(\beta/2 + \delta\epsilon)]} \\ &= \frac{\tan\beta}{2} + \frac{\tan^2\beta}{2}\delta\epsilon + \frac{1}{2}(\tan\beta + \tan^3\beta)\delta\epsilon^2 + O(\delta\epsilon^3) \\ \delta_{sym}(\delta\epsilon) &\propto \tan\frac{\beta}{2} + \frac{2\sin\beta}{(1+\cos\beta)^2}\delta\epsilon^2 + O(\delta\epsilon^4)\end{aligned}\quad (6.12)$$

This refers to the fact that the symmetric layout just corresponds to the case where the beam deflection has its minimum (Fig. 6.2 (b)), hence $\frac{\partial\delta(\beta,\epsilon)}{\partial\epsilon}(\epsilon=0) = 0$. Thus alignment errors there only contribute to second order in $\delta\epsilon$. A similar statement can be made for errors concerning the apex angle β

$$\begin{aligned}\delta_{orth}(\beta + \delta\beta) &\propto \frac{\tan\beta}{2} + \frac{1}{2}(1 + \tan^2\beta)\delta\beta + O(\delta\beta^2) \\ \delta_{sym}(\beta + \delta\beta) &\propto \tan\frac{\beta}{2} + \frac{1}{1+\cos\beta}\delta\beta + O(\delta\beta^2)\end{aligned}\quad (6.13)$$

As $\frac{1}{2}(1 + \tan^2 \beta) > \frac{1}{1 + \cos \beta}$ for $0 < \beta < \pi/2$, the required accuracy of prism fabrication is usually higher for orthogonal prisms. This is not as striking as in the case of the misalignment though. These considerations show a clear preference for symmetric prisms. However there are practical reasons to choose the orthogonal design:

- A pair of orthogonal prisms needs less space in a neutron interferometer (Fig. 6.9)
- Sometimes the fabrication or alignment is easier or more efficient (for example in the case of the combined set of aluminium prisms or in the case of the self-made silicon prisms)
- For the measurement of the vertical coherence function both prism sets can be separated to double the vertical displacement between the two beam paths (section 8.3)

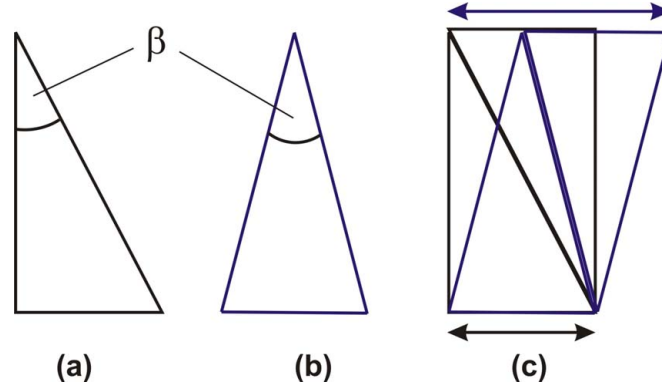


Figure 6.9: Usual prism designs (a) orthogonal (b) symmetric and (c) the minimum spatial requirement for a set of two compensating prisms.

There are several possibilities for misalignment. In the following several principal effects shall be discussed that influence either the visibility or the phase shift.

- An angle α between the two path contributions (Fig. 6.10 (a)) leads to a horizontal phase (Moire-) pattern with vertical spacing

$$\Lambda = \frac{\lambda}{\alpha} \quad (6.14)$$

The period of these fringes has to be much larger than the beam height: $\Lambda = \frac{\lambda}{\alpha} \gg h \approx 1\text{cm}$. Thus one obtains for example for $\lambda = 2.72\text{\AA}$: $\alpha \ll$

0.005". The angle α may result from a not perfect compensation of a pair of prisms in one beam path⁵. This can for example result from unequal apex angles of the single prisms, from asymmetric rotations of one prism relative to the other (Fig. 6.10 (b)) or from a rotation of one prism relative to the other around the beam axis. The latter case is additionally accompanied by a thickness gradient over the width and height of the prism set, resulting in a phase gradient when the set is translated through the beam. The case of asymmetric misalignment with respect to ϵ depends on the prism design. Assuming $\lambda = 2.72\text{\AA}$ in the case of an orthogonal silicon prism ($\beta = 30^\circ$) one obtains $\delta\epsilon \lesssim 1.5^\circ$ while in the case of an symmetric prism $\delta\epsilon \lesssim 7^\circ$ would be sufficient, to avoid the discussed fringes within the beam height. The influence of such a rotation on the measured phase shift has to be analyzed accordingly.

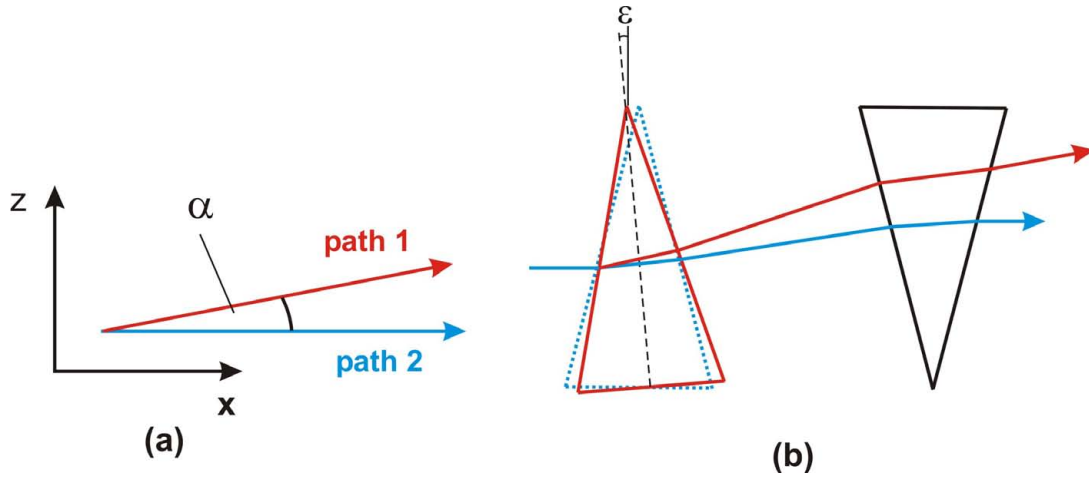


Figure 6.10: (a) An angle α between two beams leads to a horizontal phase pattern (b) Asymmetric rotation of one prism as a source of such an angle.

- A not perfect compensation within a prism set might additionally result in beam deflections relative to the lattice planes of successive lamellas with an accompanying phase shift and result on the visibility if the deflection has a component in the scattering plane. As the phase shifts are of the order 1° for $\delta\theta = 0.0001''$, accurate compensation within one prism set is

⁵During a rotation of a prism set around the beam axis the phase pattern shows also an according angle. This has been explicitly tested during the stepwise rotation of a 1.9° Al-wedge in one of the interferometer paths. However the fringe visibility decreases due to the additional deflection component in the scattering plane, which reduces the overall visibility.

required. For 2.72\AA and a silicon prism with 30° apex angle for example a misalignment of the order of $1'$ with respect to a rotation around the beam axis would yield such an effect.

- A shift Δ of one beam path relative to the other (Fig. 6.11) results in a decrease of the visibility according to the related coherence length (chapter 8). Such a shift in vertical direction might occur from unequal prism separation distances in the two beam paths or in longitudinal direction by an unequal thickness of the whole prism set due to a translation of one prism vertically relative to another (Fig. 8.10).

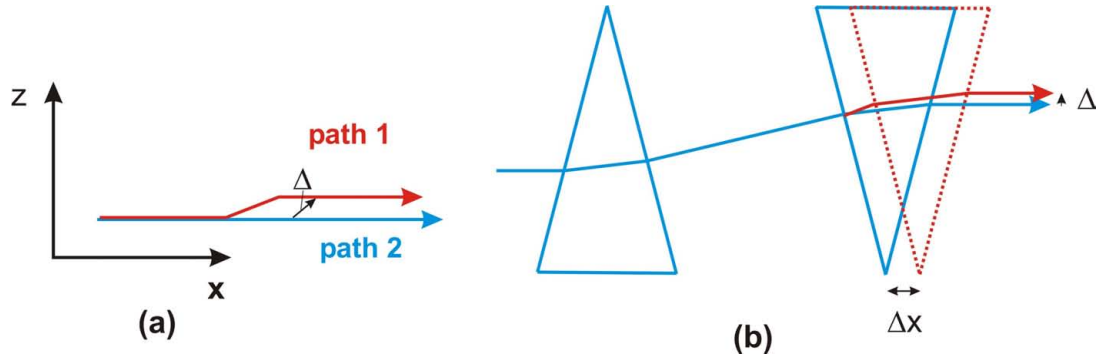


Figure 6.11: (a) A displacement Δ between two beam paths in an interferometer reduces the coherence function according to $\Gamma(\Delta)$. (b) a difference of Δx between the two beam paths leads to a vertical displacement between the two beams.

6.2.1 Preparation of silicon prisms

As silicon is well established in neutron interferometry, we decided to prepare Si-prisms at our institute.

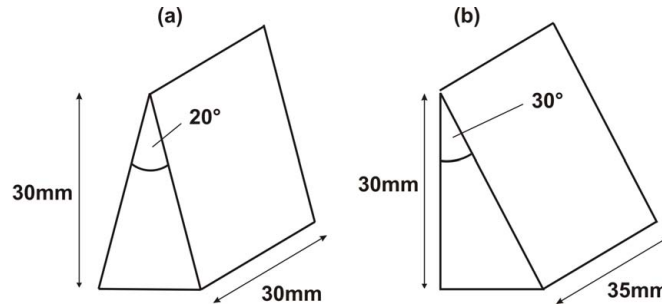


Figure 6.12: Geometry of the cut perfect crystal silicon prisms.

In a first attempt⁶ twelve symmetric 20° (Fig. 6.12 (a)) have been cut. Furthermore four additional 140° prisms⁷ for wavelength separation in front of the interferometer have been cut. As raw material a 20cm long oddment of the four inch crystal used for the interferometer has been used. To avoid the vicinity of reflecting lattice planes during the experiment, the crystal has been orientated accordingly employing an X-ray-Laue camera. The same technique has been applied to check this symmetry for several orientations of the finished prisms, as these are rotated through the neutron beam. The cutting of the prisms has been performed using the grinding machine at our institute employing a bronze-bonded diamond wheel. The same machine has in the past also been used for cutting most of the interferometers. Using this machine plan parallel serrations can be performed. Careful rigging of the machine allows distance errors between the serrations below approximately $3\mu\text{m}$. The angle between serrations can be adjusted using a goniometer with an accuracy of $1'$. Nevertheless during the process of prism cutting only an accuracy of approximately $3'$ could be guaranteed. For the cutting process the crystal has to be glued on a Tampax-glass plate that is mounted on a steel plate for fastening on the grinding machine. For the gluing an epoxy resin⁸ at 120° melting temperature has been used. The gluing process is extremely important for the stability of the crystal and thereby the achieved cutting accuracy and surface quality.

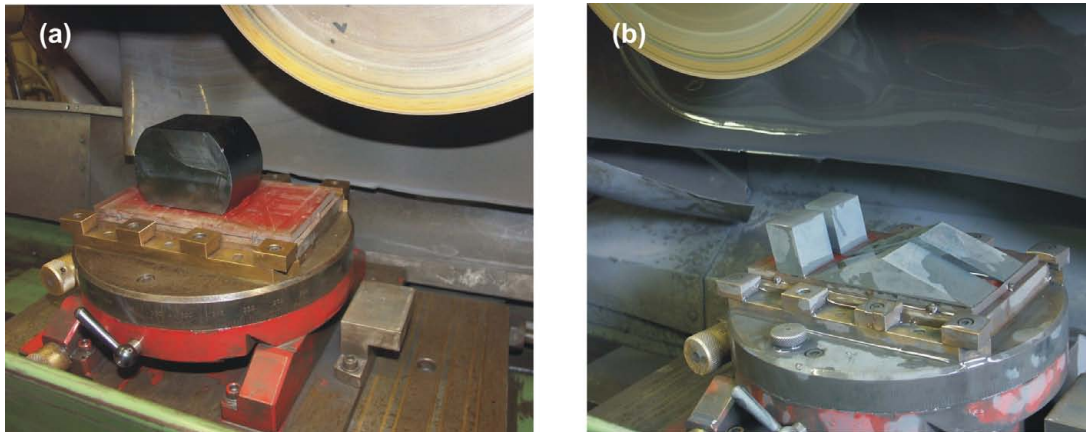


Figure 6.13: (a) one of the used ingot pieces after preliminary cuttings (b) 140° prisms after final separating cut. By a final separating cut of the two small pieces the 20° prisms are obtained.

The cutting process is very time consuming as many serrations with interme-

⁶In this part Robert Farthofer participated for his diploma thesis[57].

⁷Two 140° prisms had been already cut earlier for the instrument S18.

⁸Vinnapas B60, Wacker Polymer Systems

diate changing of the crystal position and thereby gluing are necessary to obtain the final prisms. For high surface quality a final cutting speed of approximately 4mm/min has been employed. Unfortunately problems with unbalance of the diamond cutting wheel have been encountered probably due to a recent reinstallation of the grinding machine. Thereby some of the prisms have been damaged. Moreover the accuracy of gluing with respect to the orthogonality between the prism sides and the cutting wheel has not been optimal. This resulted in a thickness gradient over the prism width [57]. Furthermore the course of cutting has not been optimal, especially concerning the insufficient chamfer of the 20° prism edge and unequal thicknesses between the single prisms.

Etching of prisms

As the prisms are not used as beam splitters, the removal of the damaged surface structure after the cutting process is of minor importance in comparison to the interferometer lamellas. On the other hand silicon is rather brittle after the cutting, which is especially a problem at the edges of the prisms. This brittleness can be significantly reduced by etching the surface. The etching process is similar to the etching of the interferometer, however some specifics shall be mentioned here. As after an etching of approximately 50 – 100 μ m the silicon surface becomes reflective to light, this can in principle be used for the control of prism justage by an autocollimator or a Laser reflection. In this first approach we however neglected the effect of the appearance of a convex-shaped thickness gradient induced by etching, which has a severe influence on phase measurements. Furthermore after the etching process it turned out that the etching speed for the prisms had been severely underestimated by the usual rate of 0.3 μ m/min (chapt. 5). In fact the etching rate had been approximately 0.6 μ m/min for the 20° prisms and 0.5 μ m/min for the simultaneously etched 140° prisms. The reason is the much smaller structure of the prisms in comparison to the interferometer, combined with the need to move the prisms in the utilized etching vessel more than usual. This leads to a strongly increased acid flow, which increases the etching speed. Altogether, instead of the aspired 50 μ m the 20° prisms had been etched 100 μ m. By the resulting curved prism surface and together with the insufficient cutting accuracy the prisms have proven to be useless for precise phase measurements. However they could be used for the measurement of the vertical coherence function (chapter 8).

Second prism set

In a second attempt 30° prisms (Fig.6.12 (b), Fig. 6.14) have been cut. Together with the enlarged apex angle this time orthogonal prism design has been used, as the procedure of cutting has been simplified thereby. Furthermore the gluing on the Tampax-glass plate has been significantly optimized, resulting in a set⁹ of four prisms with identical apex angle and negligible thickness gradient. This time the etching depth has been reduced to $8(0.5)\mu\text{m}$, the etching speed however also here was approximately $0.5\mu\text{m}/\text{min}$.

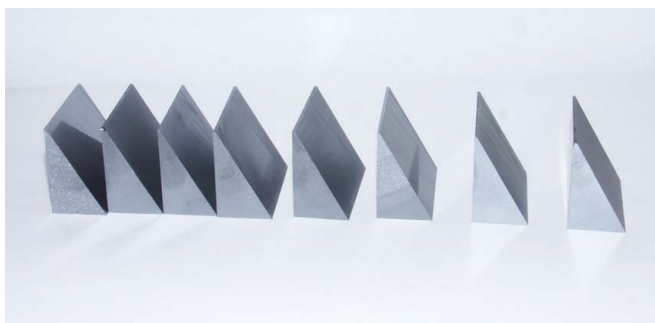


Figure 6.14: Two finished sets of orthogonal 30° silicon prisms.

Additionally several large silicon phase shifters for S18 have been prepared in this process.

⁹Altogether two sets have been cut, to have a backup if a prism should have been damaged during the cutting process or later.

Chapter 7

Laue phase measurement

7.1 Experiment

7.1.1 Idea of the experiment

As suggested in chapt. 3, 4 the main approach of our experiment consists in a measurement of a phase shift obtained by beam deflection relative to one lamella while a second one in the other beam path remains in exact Bragg condition (Fig. 3.12). As numerical calculations (chapt. 4) show a strong reduction of the visibility already for small beam deflections, one is here limited to the immediate vicinity of Bragg. Alternatively one could also measure over a larger range of $\delta\theta$ in a larger distance to Bragg (Fig. 4.5). Nevertheless there are several reasons for choosing the region around Bragg:

- The vicinity of the Bragg condition has not even qualitatively been reached.
- At Bragg the phase shift shows the strongest angular dependence and thereby sensitivity.
- The study of the strong effect on the coherence properties there is another interesting aspect.
- The possibility to observe Pendellösung structures.
- Starting in the well defined Bragg condition reduces uncertainties.
- Large beam deflections $\delta\theta > 1''$ by prisms are difficult to achieve.
- The stronger sensitivity to higher order reflections around Bragg. For these large beam deflections due to prism refraction would be even more challenging.

For the actual measurement four prisms are needed as shown in Fig. 7.1. One prism P_3 deflects the beam relative to lamella L_2 , whereas P_4 realigns the beam back to avoid further phase shifts at successive lamellas. In the other beam path one needs an identical set P_1 and P_2 to compensate for the beam displacement by the first prism set.

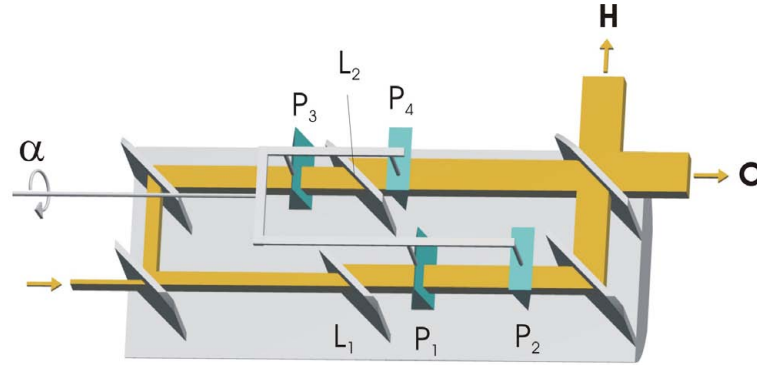


Figure 7.1: Sketch of the main measurement: the prism set $P_3 - P_4$ creates a beam deflection relative to lamella L_2 . The obtained phase shift is measured relative to lamella L_1 in Bragg position.

7.1.2 Experimental devices

Concerning the rotation of the prisms an approach has been chosen, where both prism sets are rotated simultaneously via one single axis of rotation. Thereby the realization with only one motor driven goniometer is relatively easy and identical rotation in both beam paths can be guaranteed. On the other hand this has the disadvantage, that the axis of rotation is several centimeters away from the beam and thereby the prisms move through the beam (Fig. 7.2). Hence there are several issues:

- As one illuminates different prism areas, thickness gradients or varying surface quality will lead to unwanted variations. of the phase shift and/or visibility
- The angle of rotation is limited
- To guarantee a sufficient angle of rotation a certain prism height and width is required. A larger prism height leads inevitably to larger prism thickness with higher requirements on the material.

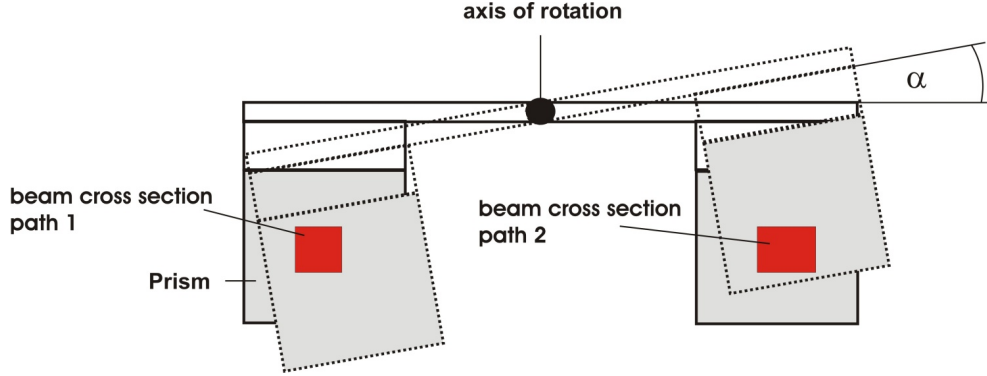


Figure 7.2: View normal to the beam: The prisms move through the neutron beam during the rotation by an angle α . For the beam cross section the beam spreading by the Borrmann fan and the vertical divergence have to be considered. Hence the beam cross sections are unequal in the two beam paths.

To avoid the stated problems one could also choose the axis of rotation for both beam paths separately centered to each beam. Hence the whole range of rotation $\alpha = 0^\circ \rightarrow 90^\circ$ would be accessible, and prisms with smaller apex angle and/or height could be used, significantly reducing the problem caused by large thicknesses due to material inhomogeneities. Therefore special goniometers with large aperture around the center of rotation to hold the single prisms would have to be used. Nevertheless precise adjustment of the prisms would be complicated thereby, thus for the beginning the more simple approach has been taken. The actual geometry of the axis of rotation relative to the prisms has been optimized according to the planned beam and lamella geometry and prism size.

To take into account intrinsic phase shifts that occur simply by the rotation of the prisms through the beam, a measurement as shown in Fig. 7.3 is required. The total phase shift is then the difference between the phase shifts measured by the configurations Fig. 7.3 and Fig. 7.1.

For the realization of the required operations - together with the measurement of the vertical coherence function discussed in section 8 - a special prism holding device (Fig. 7.4) has been constructed together with the machine shop of the atomic institute. This device allows the separation of the single prisms as needed for the measurement of the vertical coherence function and a rotation of both sets relative to the beam. As the motor drives¹ are quite close to the interferometer lamellas, especially small, low power motor drives have been ordered to avoid

¹Linear Motor drive: M-111.1DG, goniometer: M-116. DG, both using a DC-motor and installed at C-809.40 control. All from PI Physik instruments GmbH & Co. KG, Germany.

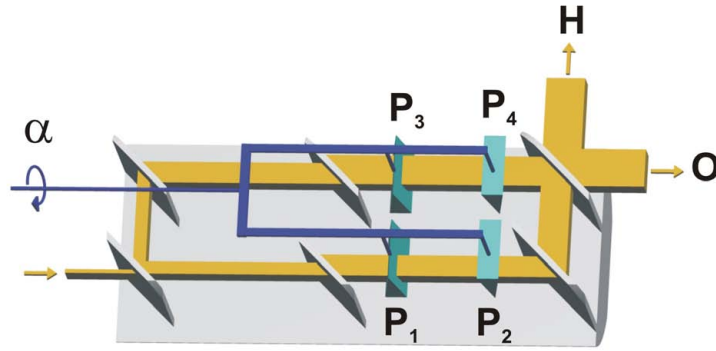


Figure 7.3: Measurement of a possible intrinsic phase shift.

thermal gradients. Moreover the whole holding device is thermally isolated from the robot that is used for positioning relative to the interferometer.

Prisms

For the measurements several sets of prisms have been used

- self fabricated 30° orthogonal silicon prisms (6.2.1)
- 25° and 15° $Al/99.5$ prisms in connected design (Fig. 6.8), which have however shown a significant reduction of the visibility (6.1.2)
- 25° $AlMgSi0.5$ prisms in connected design

The geometry of the connected prism sets has been measured by the same coordinate measurement machine used for the interferometer (Fig. 5.8), where also deformation effects via the mounting by screws have been studied. The precision of the apex angle turned out to be better than 1' while thickness gradients over the prism surfaces were at least below $5\mu m$ resulting in very good geometry. The single prisms had to be fixed on the holding device by gluing². This has been performed using a mask to define the plane parallelism of the prism surfaces and the prism faces. Finally it is also important to ensure precise parallelism between the two sets in the two beam paths.

²Concerning the small glued surface problems with the stability of the glue have been encountered. Additionally glue on the illuminated surfaces - which easily happens with thin fluid glues - has to be avoided. The best results for aluminium and silicon - after proper cleaning of the surfaces - have been obtained by the two-component DELO-DUOPOX 01 rapid, 2K-Epoxy.

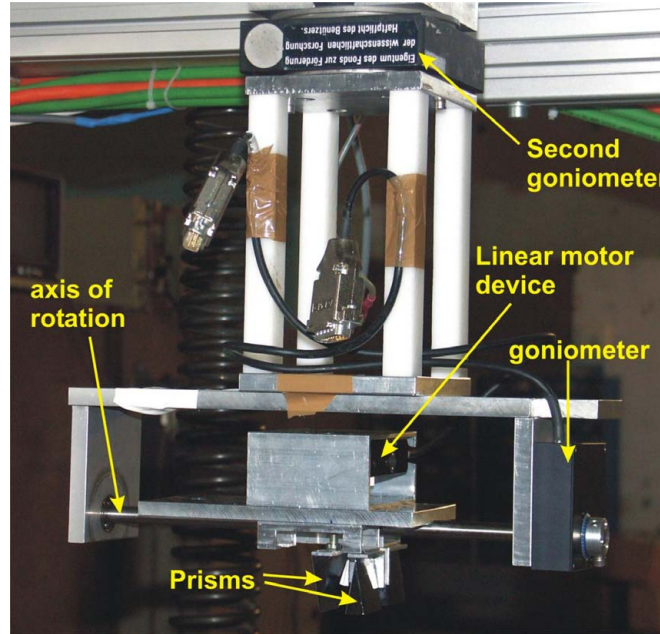


Figure 7.4: Prism holding device. The second goniometer is for adjusting the angle of the rotation axis parallel to the beam path.

Measurement method

For precise phase measurements parallel instead of serial measurement of interferograms is required. Thereby at each phase shifter position a measurement with and without sample is performed. Thus phase drifts of the interferometer caused by the environment cancel. This method is sometimes also referred to as "in-out"-measurement. In our case this would mean, that interferograms with and without prisms are measured in parallel. Moving the comparatively large prism holding device in and out of the beam paths constitutes a not negligible source of disturbance though. Furthermore the implemented course of motions has to be extremely accurate and reliable, otherwise the interferometer can be damaged easily. Hence for the main measurement an optimized approach has been chosen. The prism holding device remained always in the "in"-position, and parallel measurements have been performed between the $\alpha = 0$ position and the desired α values. Nevertheless also in this case accurate alignment of the whole holding device and a detailed test of the prism rotation is required, as the prisms are rather close to the interferometer lamellas. This method is not applicable for the measurements discussed in 7.2.5. Here one needs an absolute reference for the phase shift. Consequently it is at least necessary to perform one measurement where the prisms are moved in and out of the beam paths.

7.2 Results

The measurements have been performed at the instrument S18, ILL. Unfortunately the useable measurement time and precision have been severely limited by the visibility problems discussed in 5.2.2. If possible the measurements have been employed by two different prism sets to get rid of systematic effects. In the following the beam deflection is calculated from the rotation angle via Eq. 3.26 and the according prism refraction (chapter 6).

Due to the good geometry of the combined prism sets the intrinsic phase shifts turned out to be almost negligible, whereas in the case of the silicon prisms a not negligible correction remained. Also a slight variation of the visibility was detected. For the results in the following the visibility has been normalized to these measured curves. In general the precision of the visibility and phase results is given by both measurements (Fig. 7.1) and (Fig. 7.3). Consequently the error bars in the following show some variations because some of the measurements could not be finished to the desired precision.

The measurements are compared with numerical calculations as described in chapter 4 where the exact interferometer geometry according to Fig. 5.9 has been implemented.

7.2.1 Visibility

(220) reflection

Fig. 7.5 (a) shows the measured visibility by two prism sets for the (220) case and a Gaussian fit through both data sets. For both the symmetry of the curve is shifted relative to the expected zero position. Although the initial prism position can only be aligned approximately to the zero position, determined by the lattice planes of the interferometer, this shift is too large to be explained by this uncertainty. The shift is approximately equal for both prism sets and amounts to

$$\delta\theta_{shift} = -0.0080(4)'' \quad (7.1)$$

whereas it is different concerning the rotation angle α :

$$\begin{aligned} \alpha_{shift, Si} &= -1.7(1)^\circ \\ \alpha_{shift, Al} &= -2.0(1)^\circ \end{aligned} \quad (7.2)$$

This is another hint, that the shift is not due to the uncertainty of the zero position. A discussion of possible reasons for this shift will be given in subsection

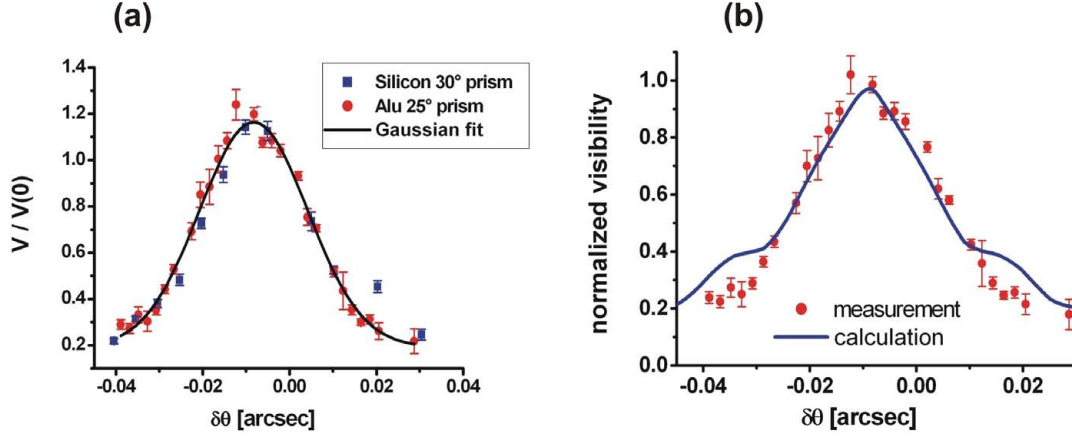


Figure 7.5: Visibility at the (220) reflection measured by two prism sets. (a) compared with a Gaussian fit (b) normalized relative to the maximum and compared with an accordingly shifted numerical calculation for $\sigma_\theta = 1.25''$.

7.2.4. By this shift the visibility in fact increases to a maximum, with approximately 15% higher visibility than in the zero position. The most interesting aspect is the width of this visibility curve with

$$\delta\theta_{FWHM} = 0.037(1)'' \quad (7.3)$$

which experimentally demonstrates the strong effect of the Laue phase shifts on the coherence. In Fig. 7.5 (b) the measurement is normalized to the maximum value of the fitted curve and compared with the calculated curve³, that is shifted accordingly. Obviously the calculations give a good estimation for the visibility reduction.

(440) reflection

For the (440) reflection the measurement for only one prism set (25° aluminium prisms) could be finished properly, however a few points measured with 15° aluminium prisms have been in good agreement.

Similar to the (220) reflection a shift relative to the expected zero position has been detected (Fig. 7.6 (a)). Here the shift amounted to

$$\begin{aligned} \delta\theta_{shift} &= -0.0045(3)'' \\ \alpha_{shift} &= -4.7(2)^\circ \end{aligned} \quad (7.4)$$

³As shown in chapter 4 the visibility depends only marginally on the beam divergence. Here the beam divergence with the best fit to the phase values has been chosen.

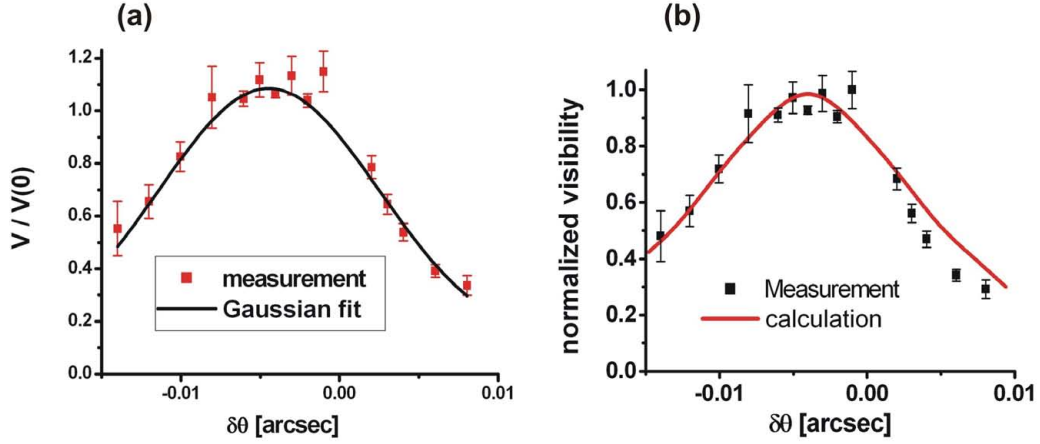


Figure 7.6: Visibility at the (440) reflection: (a) compared with a Gaussian fit (b) normalized relative to the maximum and compared with an accordingly shifted numerical calculation for $\sigma_\theta = 1.25''$.

Whereas with respect to $\delta\theta$ the shift is roughly half the one in the case of the (220) reflection, the α position is more than twice as large. This is another strong argument against a dependence on the absolute prism position. Here the shift results in an increase of approximately 10% from the zero position to the maximum of the visibility curve. The width of the visibility curve is

$$\delta\theta_{FWHM} = 0.018(1)'' \quad (7.5)$$

which is half the width of the (220) curve and demonstrates the much stronger phase averaging in the (440) case. Finally Fig. 7.6 (b) gives a comparison with the calculated curve which again shows good agreement.

7.2.2 Phase shift

(220) reflection

After correcting for the intrinsic phase shift good agreement between the results for both prism sets could be achieved (Fig. 7.7 (a)). Interestingly also the phase curve is not symmetric around the expected position but shows exactly the same shift as found for the visibility curve (7.1). This shift is especially characterized by the asymmetric appearance of a wiggled structure stemming from the Pendellösung structures. The observation of these structures in the measurement is an extremely interesting fact. Consequently for the phase shift an averaging over these structures as in principle done by Eq. 2.37 is not sufficient, to explain the details of the phase curve. The shift detected equally in the phase as the visibility

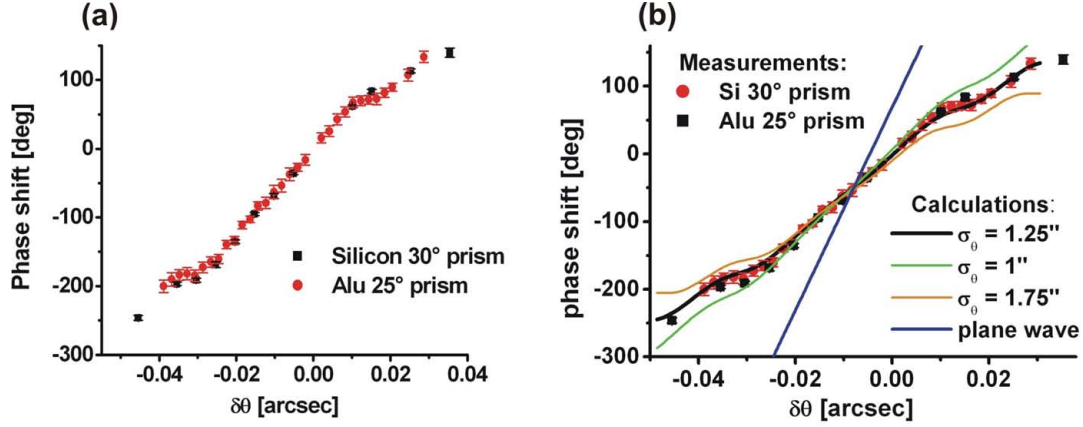


Figure 7.7: Phase shift at the (220) reflection (a) measurements for two prism sets (b) compared with the plane wave solution and calculated values including the best fitting beam divergence.

measurements is a good justification, for also shifting here the calculated curves by the same value (Fig. 7.7(b)). After this shift one finds exactly the same symmetry within calculated and measured phase curves. Furthermore for the best fitting divergence ($\sigma = 1.25''$) one finds a good fit even to the Pendellösung structures. Moreover it is obvious that a simple plane wave model would significantly overrate the slope of the phase shift. Larger beam divergences than the best fit would underestimate the slope though. Consequently the phase shift can not be explained by the limit to large beam divergences. In fact the best fitting divergence is close to the half-width of the Bragg reflection curve ($\sigma \approx 1.15''$) of the perfect crystal monochromator. Calculations comparing a phase averaging according to Eq. 4.1 with $\sigma = 1.25''$ and on the other hand applying a Bragg reflection curve and taking the integration boundaries to infinity in fact show a very good match. However in this region of beam divergence the phase shift is quite sensitive to small changes of the beam divergence (Fig. 4.9) and beam misalignments (Fig. 4.10). Despite the phase averaging the measured angular sensitivity around the Bragg condition

$$\left. \frac{\phi(\delta\theta)}{\delta\theta} \right|_{\delta\theta=0} \approx \frac{6^\circ}{0.001''} \quad (7.6)$$

is still remarkable.

(440) reflection

For the (440) reflection only one measurement could be finished satisfactorily.

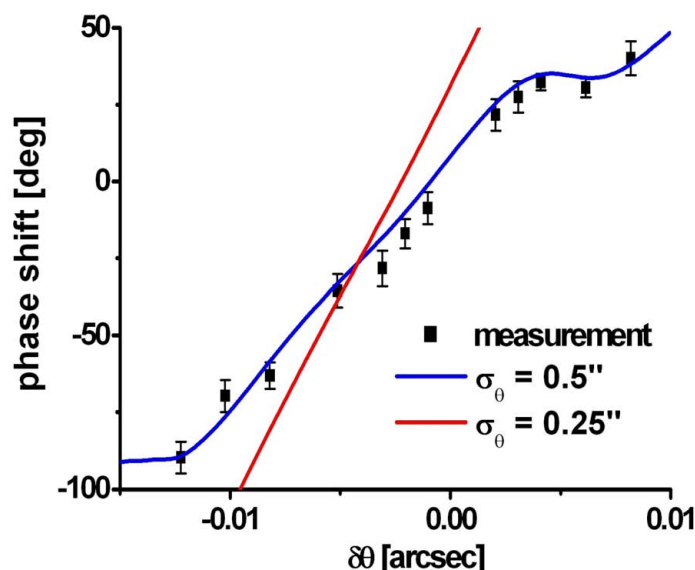


Figure 7.8: Phase shift at the (440) reflection compared with the best fitting beam divergence and half of this value which is close to the expected width resulting from the monochromator.

Also here one finds the same shift (7.4) for the phase curve as for the visibility. The calculated values are adjusted accordingly. Moreover there are Pendellösung structures visible in the measured curve and it is possible to find a good fit for the measured values ($\sigma_\theta = 0.5''$). However this divergence is approximately twice as large as the expected divergence from the monochromator ($\sigma_\theta \approx 0.29''$). Taking this divergence, the slope of the phase curve would be significantly overrated. In fact the best fitting beam divergence is already close to the limit of large divergences (Fig. 4.9). This is astonishing due to the good agreement with the monochromator width for the (220) reflection. One problem of the (440) reflection constitutes the strongly reduced peak width in comparison to the (220) reflection. Hence there is a larger sensitivity to small misalignments between monochromator and interferometer. In fact during all measurements non-systematic drifts⁴ of the piezo used for the adjustment of the rocking position have been observed. Especially concerning the higher order peaks it turned out to be difficult to maintain the position in the peak maximum. Moreover due to the finite resolution of the rocking axis the peak maximum can be only resolved to approximately $0.2''$ ⁵. This uncertainty is of similar order than the beam divergence of the monochromator. As shown in Fig. 4.10 misalignments of this order have a similar effect

⁴With strong variations the order $0.1 - 0.5''$ on average over one hour.

⁵A higher resolution can be chosen but the piezo will not move reliably then.

than an increased beam divergence of approximately $2\sigma_\theta$. Hence the stability and resolution of the rocking position is a likely explanation for the discrepancy, although a final conclusion on this can not be made and should be clarified in future measurements. Another open question is the influence of slight deviations from the perfect alignment between monochromator and interferometer according to the so called ρ axis (axis normal to the lamella surface).

Despite the relatively large effective beam divergence the angular sensitivity still amounts to

$$\left. \frac{\phi(\delta\theta)}{\delta\theta} \right|_{\delta\theta=0} \approx \frac{8.5^\circ}{0.001''} \quad (7.7)$$

and is thereby larger than in the (220) case. The fact that the phase shift around Bragg is twice as large as in the (220) case still becomes obvious from the correct description of the visibilities.

7.2.3 Studying the beam divergence

Hitherto the perfect crystal monochromator has been identified as the main source for the beam divergence incident on the interferometer. However it would be desirable to obtain more experimental insight into the influence of the beam divergence on the phase shift. Hence for future measurements the following attempts could be of interest

- In the case of a mosaic crystal as monochromator as employed at NIST, the beam divergence is much larger than the Darwin width. Consequently the phase shift should approach the limit of large beam divergences (Fig. 4.9) and should show a smaller slope than with our setup. Despite the reduced angular sensitivity this has the advantage of a strongly reduced uncertainty concerning the accurate modeling of the beam divergence and the exact rocking position.
- To increase the angular sensitivity and moreover study the case of small beam divergences, one can place a narrow absorbing entrance slit on the front and back side of the beam splitter lamella [59] of the interferometer. Due to the strong angle amplification one can thereby select a certain beam divergence that is smaller than the Darwin width. Another possibility could be to post-select small divergences after the analyzer lamella by a similar technique and thereby obtain the visibility and phase results for small divergences. Nevertheless in both approaches the intensity is dramatically reduced.

- One can study the influence of the beam divergence by placing a narrow spaced lattice with vertical orientation in front the interferometer. Thereby the incoming beam should be diffracted, corresponding to a slightly enlarged beam divergence. Hence the slope of the measured phase shift should decrease accordingly.

In general the dependence of the phase shift on the rocking position and adjustment of the ρ axis between interferometer and monochromator should be measured systematically. This would be extremely time-consuming though. In general a better resolution and higher stability of the rocking axis is desirable.

7.2.4 Shift of phase and visibility curves

There remains the problem of the discussed shift of the phase and visibility curves. As already stated the shift cannot be addressed to an absolute rotation angle of the prisms as different angles have been observed for different reflections and also different prism sets. Although a slight offset due to the unknown zero position of the prisms can not be excluded, we found

$$\begin{aligned} |\delta\theta_{shift,(220)}| &= 0.0080(4)'' \\ |\delta\theta_{shift,(440)}| &= 0.0045(3)'' \end{aligned} \quad (7.8)$$

So far we have analyzed the following effects resulting from interferometer geometry and the prism configuration.

- The shift looks rather similar to the shift arising from the case when the lattice planes are not orthogonal to the lamella surface (section 2.2.3). This kind of shift is proportional to $1/m^2$ (Eq. 2.77) though and not to $1/m$ as found in our measurements. Furthermore the measured shift for the (220) case would amount to $\gamma \approx 0.5^\circ$ which is the precision of the usually oriented interferometer. In our case the precision has been a factor of hundred better and the shift would be below $\delta\theta = 10^{-4}''$, thus not resolvable. Hence this cannot be the source of the shift.
- One could think of this shift as a result of the not perfect interferometer geometry. For example one could imagine that in the case of a slightly defocused interferometer, one compensates for this by the beam deflection relative to one lamella, which to some extent also constitutes a defocusing in ideal geometry (compare section 3.2.1). However the exact interferometer geometry has been implemented for the calculations, but both visibility and phase shift remained symmetric. Moreover several variations of the actual

as well as of the ideal geometry including unequal lamella thicknesses⁶ and distances have been studied. None of these geometries has shown a shift though. As an example the visibility and phase shift in the case of a simple defocused interferometer - distance to the analyzer lamella increased by $4\mu\text{m}$ - is shown in Fig. 7.9. Both curves are perfectly symmetric with respect to the Bragg angle. Anyhow the non ideal interferometer geometry is a rather

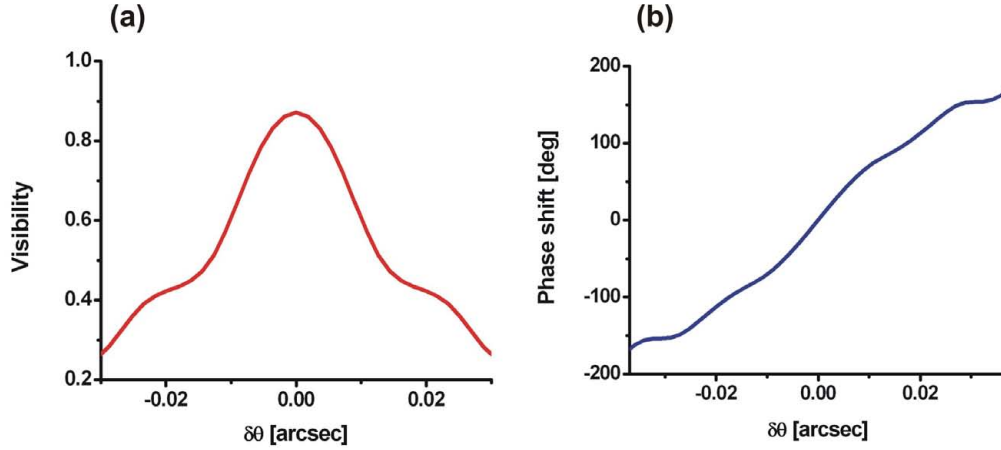


Figure 7.9: Calculated visibility and phase shift of setup Fig. 7.1 for a defocused interferometer (distance to the analyzer lamella increased by $4\mu\text{m}$).

unlikely cause for the discussed shift. The calculated visibilities for the present geometry (Tab. 5.5) are too high to explain the obtained increase of the visibilities (15% for the (220) and 10% for the (440) reflection).

- The smaller shift in the case of the (440) reflection might be addressed to the decreased prism refraction which is however $\propto \lambda^2$. In fact there is an effect stemming from the usage of prisms. So far we have only regarded the contribution into the scattering plane $\delta_{eff} = \delta \sin \alpha$. This is due to the fact, that to first order the exact Bragg condition is only violated in this plane. However to second order one in principle also violates the Bragg condition by a deflection normal to this plane. One can think of this as a violation of the Bragg condition normal to the lattice vector which is according to the cosine function second order in $\delta\theta$ while the usually regarded violation is

⁶Here special attention has been given to the effect of unequal thickness of the two additional lamellas, although they have been confirmed to be equally thick within the known precision of $1\mu\text{m}$ (Fig. 5.9). Besides the numerical simulations it can be shown that the obtained phase distribution according to Fig. 3.9 is symmetric with respect to $\delta\theta = 0$ and leads to a reduction of the visibility.

parallel to the lattice vector and thereby first order in $\delta\theta$. Another viewpoint is the change of the wavelength while maintaining the Bragg condition. The wave vector here is projected to the scattering plane via

$$k_{eff} = k \cos \delta \approx k \left(1 - \frac{\delta^2}{2}\right) \quad (7.9)$$

whereby the wavelength is changed to

$$\lambda_{eff} \approx \lambda \left(1 + \frac{\delta^2}{2}\right) \quad (7.10)$$

The difference between the Bragg angle between λ_{eff} and λ thus amounts to

$$\sin \theta_{B,eff} - \sin \theta_B = \frac{1}{2d}(\lambda_{eff} - \lambda) \approx \frac{1}{2d}\lambda \frac{\delta^2}{2} = \sin \theta_B \frac{\delta^2}{2} \quad (7.11)$$

As $\frac{\delta^2}{2} < 10^{-12}$ for the used prisms - in the case of the (220) reflection - the according shift is of the order $10^{-7''}$, hence much smaller than the measured effect.

Of course as explanation could remain some kind of crystal imperfection or strain, but this is almost impossible to account for. Additionally one would expect detectable Moire patterns, which we didn't find with our position sensitive detector.

Coriolis force and gravitational interaction

Recently D. Petrascheck suggested the Coriolis force by the earth rotation $\omega = 7.29 \cdot 10^{-5} s^{-1}$ acting along the neutron beam path as cause of the detected shift. This can in general lead to beam deflections relative to the interferometer lamellas. The Coriolis force is given by

$$\mathbf{F}_{cor} = 2m_n \mathbf{v} \times \boldsymbol{\omega} \quad (7.12)$$

The relevant deflection component is parallel to the lattice vector \mathbf{H} and yields

$$F_{H,cor} = 2m_n v \cdot \omega \cdot \sin \theta \cdot \cos \theta_B \quad (7.13)$$

Here θ is the angle between $\boldsymbol{\omega}$ and \mathbf{v} and is determined by the colatitude angle (Grenoble: 45.18°) and the exact interferometer orientation at 45° Bragg angle (47° to the east from the north direction). During a time of flight $\Delta t = L/v$ the momentum component parallel to the lattice vector changes by

$$\Delta p_H = \hbar \Delta k_H = F_H \Delta t = 2m_n L \cdot \omega \cdot \sin \theta \cdot \cos \theta_B \quad (7.14)$$

It is here interesting to note that the change in momentum Δp_H is independent of the neutron velocity as the Coriolis force depends itself on the velocity. The relevant beam deflection can then be calculated via

$$\Delta\delta\theta = \frac{\Delta k_H}{k} \cos\theta_B \quad (7.15)$$

An important observation here is that

$$\Delta\delta\theta_{Coriolis} \propto \frac{1}{m} \quad (7.16)$$

with m the order of reflection. This is just what has been found in the experiment.

Moreover if the lattice planes are tilted by an angle α relative to the vertical direction the beam deflection by the gravitational force of the earth results also in a beam deflection relative to the lattice planes. The relevant component of the gravitational force is

$$F_{H,grav} = m \cdot g \cdot \sin\alpha \quad (7.17)$$

As here the force is independent of the velocity, the resulting beam deflection is

$$\Delta\delta\theta_{grav} \propto \frac{1}{m^2} \quad (7.18)$$

which is not what we found in the experiment. However the potential angle α has not been determined during our measurements and a slight correction from gravitational beam deflection might remain. Here it is interesting to note that tilts of the order of 1° result in similar beam deflections than caused by the Coriolis force.

Both effects have in common that they are proportional to the path length of the neutron L . Consequently the larger the distance of lamellas to the beam splitter, the larger they are affected by the Coriolis and gravitational force. All things considered the beam deflection relative to each lamella is different, which is equivalent to the case that all six lamellas would be tilted against each other. This together with the non ideal interferometer geometry constitutes the most general problem of a six lamella interferometer. As neutron interferometers are rather sensitive to beam deflections this also implies, that the Coriolis force and/or the gravitational force reduce the visibility of an interferometer according to its path length L . Hence there seems to be a limit for even larger interferometers. However one could try to compensate for the resulting beam deflections by using appropriate wedges. This could be an interesting method for future measurements with large interferometers. Indeed our method corresponds to some extent to a compensation by wedges, as we improve the visibility by beam deflection relative to one lamella. Implementing all resulting deflections from the Coriolis force

into the interferometer simulation indeed shows a shift, which is approximately half of the measured shift. A more accurate investigation should be aimed for in upcoming measurements, when also the exact tilt of the lattice planes should be determined. Another interesting observation is that deflecting the beam with respect to L_1 instead of L_2 (Fig. 7.1) should yield a shift of equal magnitude but opposite sign. Unfortunately this measurement configuration has not been possible during the available measurement time.

7.2.5 An approach beyond Bragg

By the hitherto approach one is limited to the close vicinity of Bragg due to the rapid destruction of the visibility. On the other hand starting off Bragg one is limited to the region several arc seconds off Bragg (section 4.2). To access the region in between one has to compensate the arising phase distribution in one beam path to some extent in the other. This can be performed by rotating both crystal lamellas or alternatively deflect the beam in front of both (Fig. 7.10).

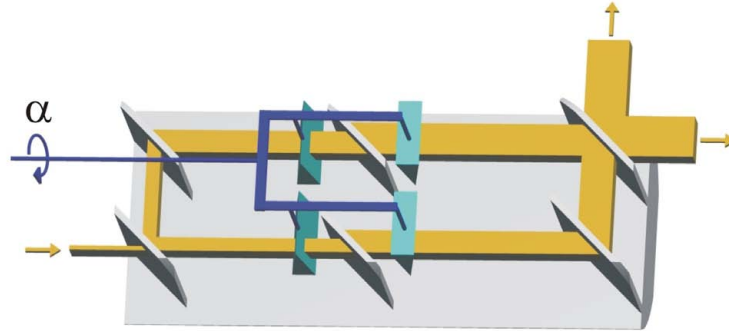


Figure 7.10: Equal beam deflection in front of both sample lamellas.

In this simple experiment one shifts the phase curves in both beam paths by exactly the same $\delta\theta$ (Fig. 3.8) and creates the same phase distribution in both beam paths

$$\Delta\phi(\delta\theta, \delta\theta^*) = \phi_{Laue, I}(\delta\theta + \delta\theta^*) - \phi_{Laue, II}(\delta\theta + \delta\theta^*) = 0 \quad (7.19)$$

Hence the relative phase shift for all plane wave components $\delta\theta^*$ is zero. Moreover the manipulation of the beam path intensities is equal whereby the visibility is equal to the visibility of the undisturbed interferometer. With respect to phase shift and coherence this approach is similar to applying equal spatial shifts by phase shifters in both beam paths. The difference here is that instead of a phase

shift linear proportional to the wavelength, one here deals with a strongly non-linear phase shift that is manipulated by its angular sensitivity rather than by a spatial shift.

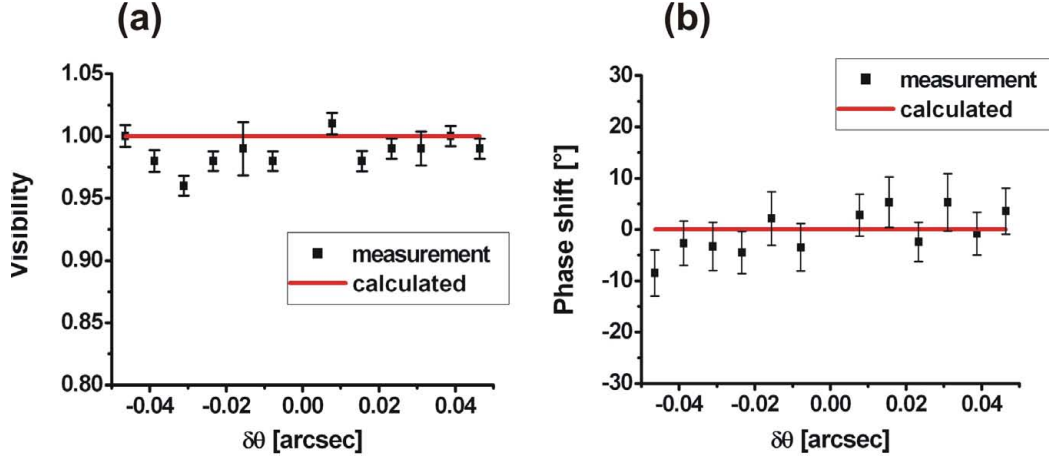


Figure 7.11: Equal beam deflection $\delta\theta$ in front of both sample lamellas (Fig. 7.10) using the (220) reflection: (a) normalized visibility (b) phase shift.

The accuracy of the results is rather poor due to the especially pronounced stability problems of the interferometer during these measurements. Anyhow one finds the expected constancy of phase shift and visibility. The outcome of this measurement is to some extent trivial, but constitutes the basis for the following measurements. Moreover the manipulation on the neutron beam is rather complex, as strong modifications to phase, beam geometry and beam intensities⁷ are generated. It demonstrates that the process of dynamical diffraction maintains the coherence of the neutron beam, a fact that is however already incorporated in the functionality of the interferometer itself.

Differential rotation

To measure a phase shift as a function of the deflection angle, one has to apply an offset to one of the beam deflections: $\delta\theta$ in one beam path, $\delta\theta + \delta$ in the other:

$$\Delta\phi(\delta, \delta\theta, \delta\theta^*) = \phi_{Laue, I}(\delta\theta + \delta + \delta\theta^*) - \phi_{Laue, II}(\delta\theta + \delta\theta^*) \quad (7.20)$$

This idea is related to a measurement of the slope of the phase function, which would be only true for a single plane wave though. In principle the whole complex

⁷The intensity in the output beams increases by almost forty percent over the displayed range in Fig. 7.11.

system of interferometer and beam divergence creates a special phase distribution that is measured as a function of $\delta\theta$. In praxis this measurement is carried out by two prism sets slightly tilted $(\delta\alpha)^8$ against each other, that are rotated by an angle α together (Fig. 7.12):

$$\begin{aligned}\alpha_1 &= \alpha \\ \alpha_2 &= \alpha + \delta\alpha\end{aligned}\tag{7.21}$$

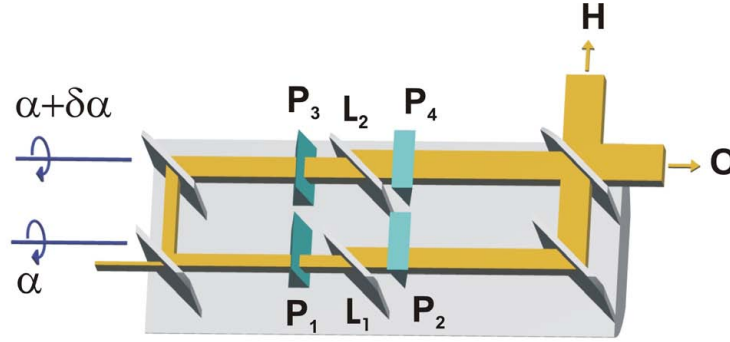


Figure 7.12: Measurement method where one prism set is rotated by $\alpha_1 = \alpha$ while in the other beam path the set is rotated slightly shifted $\alpha_2 = \alpha + \delta\alpha$.

For this experiment of course a measurement of the intrinsic phase analogous to Fig. 7.3 is required. Fig. 7.13 compares the measured visibilities and phase shifts with calculated values. As in the phase measurements for beam deflection relative to one lamella only (Fig. 7.7), one finds the best fitting beam divergence to be $\sigma_\theta \approx 1.25''$. Even though the large error bars due to visibility and stability problems are quite large, the central peak in the calculated curves seems to come out in the measurements. Beyond that the accuracy is too poor for a comparison with the damped oscillatory behavior found in the calculations. It is important to note, that the slight shift of the central peak is not related to the asymmetry of the original phase measurement (section 7.2.4) but is due to the relative prism rotation⁹. Phase shift and visibility thereby reach their maximum when both sets

⁸This method does not accurately correspond to constant δ , due to the non-linearity of the sine function: $\sin(\alpha + \delta\alpha) - \sin(\alpha) = \sin(\delta\alpha) + (\cos(\delta\alpha) - 1) \cdot \alpha - \frac{\sin(\delta\alpha)}{2}\alpha^2 + O(\alpha^3) = \delta\theta(1 - \frac{\alpha^2}{2}) + (\sqrt{1 - \delta\theta^2} - 1) \cdot \alpha + O(\alpha^3)$ thereby one obtains corrections that gain importance with increasing α and $\delta\alpha$. Either one accounts for this in the evaluation or the relative tilt $\delta\alpha$ is adjusted accordingly.

⁹Upcoming measurements with higher precision should reveal if this is really the case if the influence of the Coriolis force is taken into account.

lead to a perfect antisymmetric deflection: $\delta/2$ and $-\delta/2$ respectively. The phase offset of approximately 55° results from the relative beam deflection $\delta \approx 0.009''$ (compare Fig. 7.8).

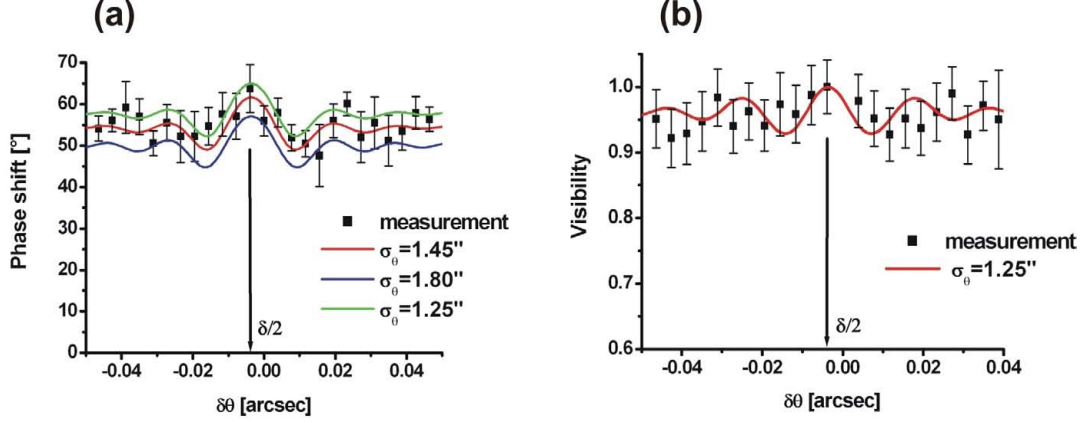


Figure 7.13: Measured and calculated visibility and phase shifts by the setup Fig. 7.12 for the (220) reflection.

So far the range of $\delta\theta$ has not been extended in comparison to the original measurement method 7.1. This was due to the relatively small prism refraction and the geometry of prism rotation. Anyhow it has been shown qualitatively that one can perform a phase measurement around Bragg without (significant) visibility reduction. Hence this approach should be applicable to a larger range of $\delta\theta$.

7.3 Outlook: Precision measurements?

One of the motivations to study the Laue phase might of course be S. A. Werner's proposal to use it for a precision measurement of the neutron electron scattering length (subsection 2.2.2). Might this or another precision measurement be possible? We first summarize some of the aspects discussed in chapt. 2, 3:

- The sensitivity to the neutron-electron scattering length is on average the largest around the Darwin width of the reflection.
- This sensitivity reduces for higher order reflections, thus the (220) reflection would be most sensitive.
- Increasing the crystal thickness and the Bragg angle also increases the phase sensitivity for b_{ne} . However increased phase sensitivity is counteracted by reduced visibility over a larger range of $\delta\theta$.

At this point it is important to note that further studies are required. The main idea of this work consisted in a fundamental investigation of the principal phase properties, effects on the visibility and possible experimental approaches. This constitutes the most important stage before even thinking about a precision measurement. Hence the fairest answer to this question would probably be: It is still too early, to answer this question.

Nevertheless some comments on this shall be given in the following: We have already discussed several challenges during the treatment of a single plane wave (subsection 2.2.2). A fundamental problem - independent of the concrete setup - consisted in the present uncertainty of the Debye Waller factor resulting in a larger uncertainty of the atomic scattering length than by the neutron electron scattering length. However using several reflections might help in measuring both effects. Alternatively one could measure the Debye Waller factor by a precision measurement of the Laue phase in the X-ray case, employing a similar X-ray setup. This would additionally have the advantage of higher precision according to higher intensities and visibilities. Provided that the required precision of the Debye Waller factor has been gained, what sensitivity remains for divergent beams where one takes the average over many plane waves?

In the following we still neglect variations of the crystal thickness and the wavelength and fix these values as well as the Debye Waller factor. Fig. 7.14 shows the calculated phase difference

$$\Delta\phi_{\sigma\theta}(\delta\theta) = \phi_{\sigma\theta}(b_{ne}(1), \delta\theta) - \phi_{\sigma\theta}(b_{ne}(2), \delta\theta) \quad (7.22)$$

for the method shown in Fig. 7.1 and the values given in Eq. 2.57. There remains still some $\delta\theta$ dependent phase sensitivity, which would even increase further for larger $\delta\theta$. These measurements due to the strongly reduced visibility would be useless though. It is obvious that this phase difference depends significantly on the thickness and Bragg angle.

Hence one could aim for an optimal combination of crystal thickness and Bragg angle. Nevertheless to achieve the required phase accuracy also the knowledge of the absolute value of $\delta\theta$ has to be within 10^{-4} ". Moreover the beam divergence for modeling should be known within 10^{-2} " and an equivalent effect concerning the position in the rocking curve has to be considered. Otherwise the absolute phase uncertainty due to these effects would be as large as the phase difference by the present uncertainty in the neutron electron scattering length. The problem of the absolute beam divergence and/or rocking position could probably be significantly reduced using a mosaic crystal, although also the phase sensitivity is reduced for larger beam divergences (Fig. 7.14 (c)).

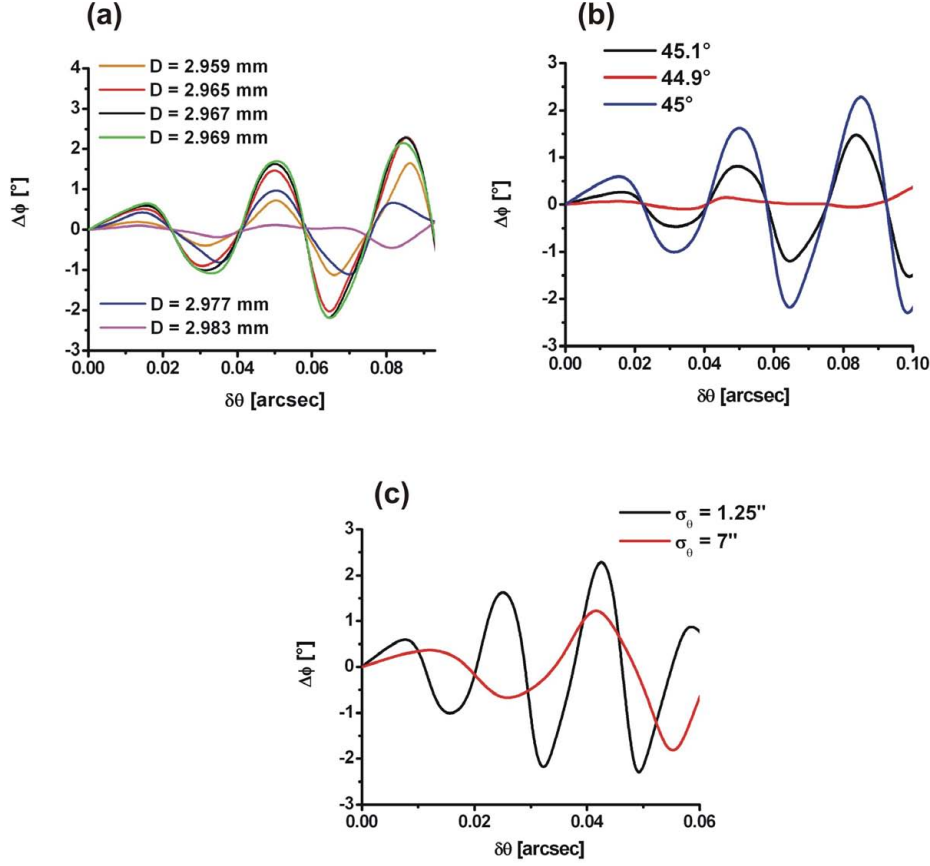


Figure 7.14: Calculated phase difference 7.22 according to Fig. 7.1 as a function of $\delta\theta$ for (220) reflection. (a) in dependence of the lamella thickness ($\theta_B = 45^\circ$, $\sigma_\theta = 1.25''$), (b) of the Bragg angle ($D = 2.967$ mm, $\sigma_\theta = 1.25''$) and (c) of the beam divergence ($\theta_B = 45^\circ$, $D = 2.967$ mm).

Similar calculations for the approach discussed in subsection 7.2.5 over a large range of $\delta\theta$ only reveal phase differences well below 1° . These phase differences of course depend on the relative rotation δ . Nevertheless even for relatively large δ where the visibility would already drop significantly, no satisfying sensitivity can be achieved.

The third possibility - a measurement far off Bragg - would have the advantage of reduced dependence on the accurate modeling of the beam divergence, as to first order already the plane wave solution is a good approximation. However the obtainable phase difference over the accessible region while maintaining a reasonable degree of visibility is also here in the order of 0.5° (compare Figs. 4.5, 2.13, 4.14, 4.13). At such precision the absolute value (or at least the angular difference) of $\delta\theta$ has to be known to approximately $0.001''$, as otherwise this

uncertainty would create larger phase differences. This is not trivial at distances $\delta\theta > 1''$.

The stated phase sensitivities still neglect the distributions arising from the variation of the crystal thickness and the averaging over the wavelength distribution. The knowledge of these quantities should be in the same order as the aimed precision of the atomic scattering length (10^{-4}).

Just recently there has been a further proposal [9] showing interest in neutron interferometric measurements of the Laue phase. This proposal is dedicated to the investigation of non-Newtonian gravity theories, where one assumes corrections to the usual $1/r$ law at short distances described by the effective range λ according to

$$V(r) = -G \frac{m_n M}{r} (1 + \alpha_G e^{-r/\lambda}) \quad (7.23)$$

where α_G is a dimensionless parameter and m_n and M are the two interacting masses. Thereby a further term b_G adds to the atomic scattering length

$$b_{atom} = b_N + Z[1 - f(q)]b_{ne} + f_G(q)b_G \quad (7.24)$$

with

$$\begin{aligned} b_G &= -\frac{2m_n^2 M G \alpha_G \lambda^2}{\hbar^2} \\ f_G(q) &= \frac{1}{1 + (q\lambda)^2} \end{aligned} \quad (7.25)$$

Although two unknown scattering lengths b_G and b_{ne} enter, one could measure both - or rather measure b_{ne} and find constraints for b_G - by measuring at different q or reflections respectively. This is possible as the form factors $f(q)$ (Eqs. 2.58, 7.25) show a different q dependence. Obviously this proposal neglects the uncertainty and q dependence of the Debye-Waller factor, but however shows the broad interest in related phase measurements - ranging from crystal physics to elementary particle physics.

Anyhow besides experimental problems with the setup¹⁰ and the present uncertainty of the Debye Waller factor it still has to be shown to what principal accuracy one can measure and model the Laue phase. Therefore more accurate measurements are required. Furthermore one should also give thought to the modeling, including the detailed reflection curve of the monochromator into the program. Although preliminary calculations do not show a large effect, for precision measurements this would be inevitable.

¹⁰At the moment the achievable phase precision at S18 can not be guaranteed below 0.5° due to systematic phase drifts and instability of the rocking axis. These problems are even larger for the employed 45° large scale interferometer. The problem of the rocking axis could maybe be improved by employing a mosaic crystal.

7.3.1 Future approaches

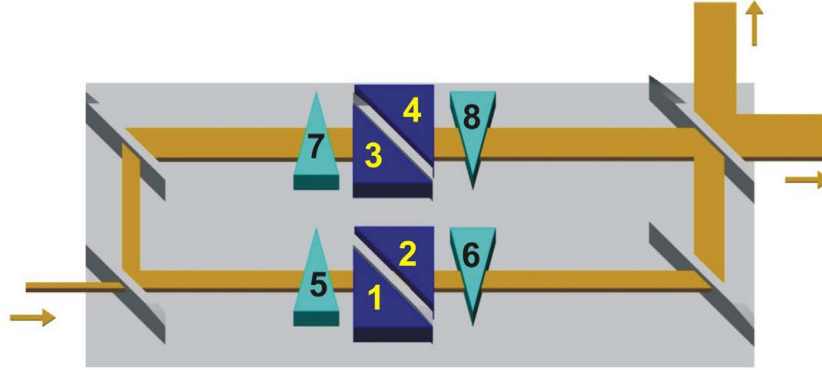


Figure 7.15: Optimized position for a fixed prism set (prisms 1-4) to set the sample lamellas to a certain value off Bragg. By an additional rotatable prism set (prisms 5-8) one changes the overall beam deflection.

Proceeding with Laue phase measurements a detailed study of the influence of the beam divergence and its manipulation as discussed in subsubsection 7.2.3 should be addressed. Furthermore a new interferometer with significantly thicker sample lamellas could be interesting due to the higher angular sensitivity. Besides the continuation of the already applied measurement methods the already discussed measurement further off Bragg could be interesting. Therefore one can deflect the beams in both paths with a fixed strong deflecting prism set to a certain value and then modify the overall deflection by additional prisms as up to now. In the present interferometer one can optimize the position of the fixed prism set as shown in Fig. 7.15 without losing place for the rotatable prism set. It should be noted that the study of phase shifts by dynamical diffraction theory is also interesting with respect to split crystal interferometers which have so far only been realized for X-rays[13, 12]. In this case however also phase shifts from crystal reflection are involved and have to be analyzed. An equivalent setup to measure at least the sensitivity with respect to the Bragg axis¹¹ is shown in Fig. 7.16.

¹¹ The sensitivity with respect to a rotation around the axis of the incoming beam is quite large though. Concerning the rotation around the Bragg axis in the suggested setup this would be equivalent to a rotation of the lamellas around their center. In the real split crystal case there is one axis of rotation for both lamellas additionally leading to a length change in the beam paths.

This measurement would be quite straight forward with the present equipment. Accompanied by numerical calculations this could reveal interesting information on the realization of a split crystal interferometer.

Moreover one should give thought to the extraordinary angular sensitivity of the phase shift which could become interesting for the precise detection and measurement of beam deflections, similar to the angle amplification effect [59].

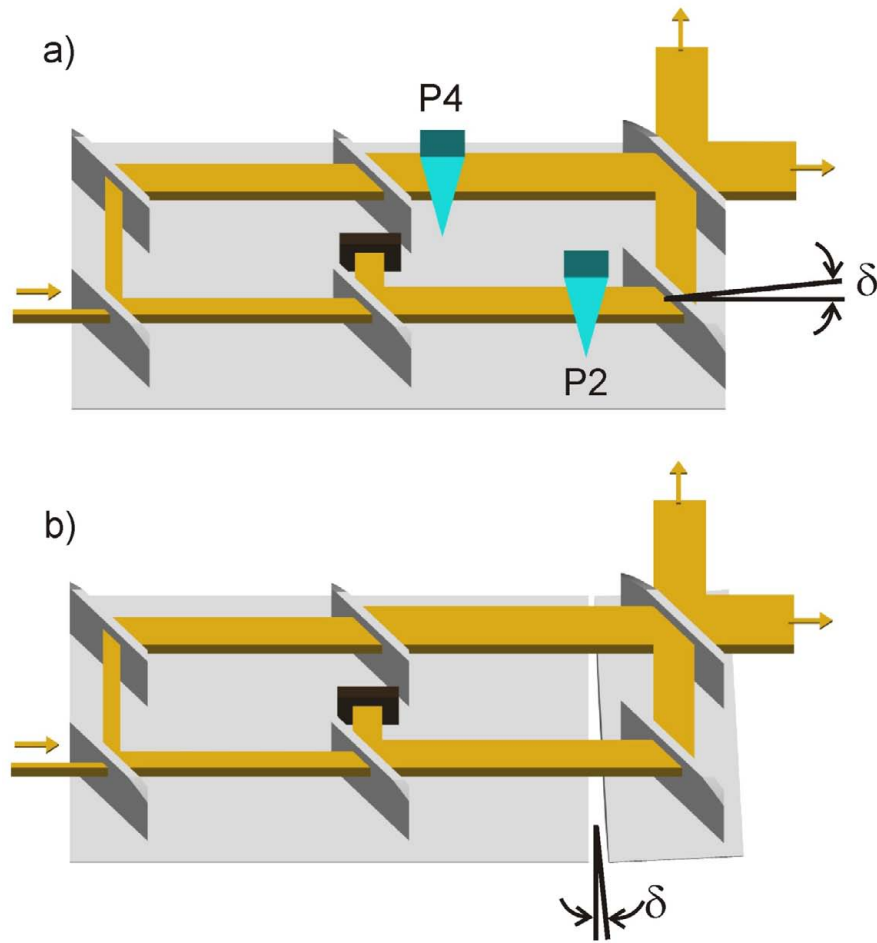


Figure 7.16: Simulation of a split interferometer by using two prisms with equal distance to the recombining lamella (a). Lattice rotation in the split interferometer (b), largely exaggerated.

Chapter 8

Vertical coherence function

The investigations for prisms in neutron interferometry and the related adjustment challenges due to the coherence properties of the neutron beam lead to the idea, to use prisms for the measurement of coherence functions in the interferometer. This is based on the idea, that the neutron beam is deflected by one prism and can be deflected back to the original direction via another prism. According to the separation of the two prisms one obtains a spatial shift Δ of the neutron beam in one beam path related to the coherence function $\Gamma(\Delta)$. This approach is especially attractive for the measurement of the vertical coherence function which has so far only been studied once at $\theta_B = 30^\circ$ by a different method [23].

8.1 Calculation of the spatial shift

First we have to investigate the direction and magnitude of the spatial shift generated by a compensated prism set as shown in Fig. 8.1.

Although usually symmetric or orthogonal prisms will be used, the derivation for the general case shall be given. In general the total spatial shift of a specific arrangement is a sum of all single spatial shifts of the neutron beam:

$$\Delta = \sum_i \Delta_i \quad (8.1)$$

Considering the separated prism set one can think of it as an arrangement of one large slab defined by the effective thickness $L = L_0 + x$ and surface normal \hat{s}_0 , minus the slab defined by the separation of the prisms x and the surface \hat{s}_1 . In general the spatial shift for a slab with surface normal \hat{s} , thickness D and neutron

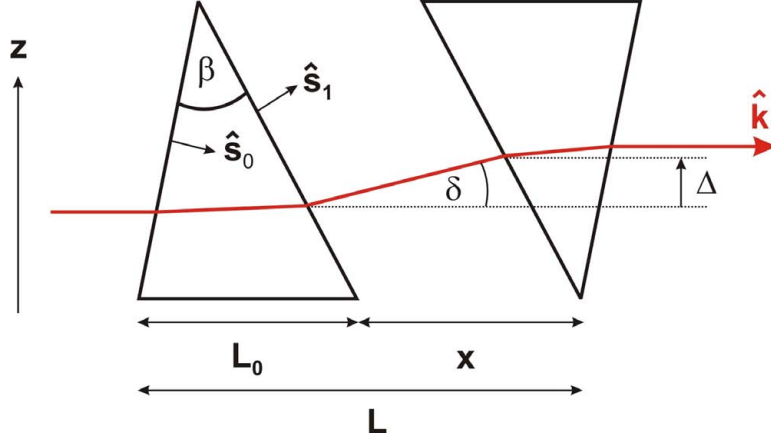


Figure 8.1: Compensated prism set and arising vertical shift Δ by separating a distance x .

wave unit vector \hat{k} is given by¹

$$\Delta = \frac{(n-1)\hat{s}}{(\hat{k} \cdot \hat{s})^2} D = \frac{(n-1)\hat{s}}{(\hat{k} \cdot \hat{s})} D_{eff} \quad (8.3)$$

where $D_{eff} = \frac{D}{(\hat{k} \cdot \hat{s})}$ denotes the effective thickness or path length of the neutron beam in the slab. Thereby one finds for the spatial shift of the large slab

$$\Delta_L = \frac{(n-1)\hat{s}_0}{(\hat{k} \cdot \hat{s}_0)} (L_0 + x) \quad (8.4)$$

whereas the spatial shift of the separation part is

$$\Delta_x = \frac{(n-1)\hat{s}_1}{(\hat{k} \cdot \hat{s}_1)} x \quad (8.5)$$

Thus one obtains for the spatial shift of one separated prism set

$$\begin{aligned} \Delta_{tot}(x) &= \Delta_L - \Delta_x \\ &= (n-1) \left(\frac{L_0 + x}{(\hat{k} \cdot \hat{s}_0)} \hat{s}_0 - \frac{x}{(\hat{k} \cdot \hat{s}_1)} \hat{s}_1 \right) \\ &= (n-1) \left(L_0 \frac{\hat{s}_0}{(\hat{k} \cdot \hat{s}_0)} + x \cdot \left[\frac{\hat{s}_0}{(\hat{k} \cdot \hat{s}_0)} - \frac{\hat{s}_1}{(\hat{k} \cdot \hat{s}_1)} \right] \right) \end{aligned} \quad (8.6)$$

¹In the literature one finds $\Delta = (n-1)\hat{s}D$ [60, 1] or $\Delta = \frac{(n-1)\hat{s}}{(\hat{k} \cdot \hat{s})} D$ [61, 62] which however do not yield the correct phase shift

$$\chi = \Delta \cdot \mathbf{k} = (n-1)kD_{eff} = -Nb_N\lambda D_{eff}. \quad (8.2)$$

The sign convention is according to the surface vectors shown in Fig. 8.1.

The relative spatial shift between the two beam paths, where in one beam path the prism set is separated by a distance x , while it is joined ($x = 0$) in the other, then reads

$$\begin{aligned}\Delta_{rel}(x) &= \Delta_{tot,I}(x) - \Delta_{tot,II}(x=0) \\ \Delta_{rel}(x) &= (n-1)x \cdot \left[\frac{\hat{s}_0}{(\hat{k} \cdot \hat{s}_0)} - \frac{\hat{s}_1}{(\hat{k} \cdot \hat{s}_1)} \right]\end{aligned}\quad (8.7)$$

We now have to evaluate the term²

$$\frac{\hat{s}_0}{(\hat{k} \cdot \hat{s}_0)} - \frac{\hat{s}_1}{(\hat{k} \cdot \hat{s}_1)} \quad (8.9)$$

Using the definitions by Fig. 8.2 one obtains

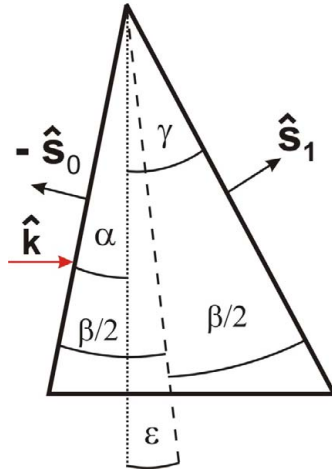


Figure 8.2: Angle definition for a prism with apex angle β when regarded as a symmetric prism rotated by an angle ϵ .

$$\begin{aligned}\hat{k} \cdot \hat{s}_0 &= \cos \alpha \\ \hat{k} \cdot \hat{s}_1 &= \cos \gamma\end{aligned}\quad (8.10)$$

²In the case of symmetric prisms this expression immediately simplifies via $\hat{k} \cdot \hat{s}_0 = \hat{k} \cdot \hat{s}_1 = \cos \frac{\beta}{2}$ and $\hat{s}_0 - \hat{s}_1 = -2 \sin \frac{\beta}{2} \cdot \hat{z}$ to $-2 \tan \frac{\beta}{2} \hat{z}$ and thereby

$$\Delta_{rel}(x) = 2x(1-n) \cdot \tan \frac{\beta}{2} \hat{z} = x\delta \hat{z} \quad (8.8)$$

where δ is the deflection angle by the prism.

and

$$\begin{aligned}\hat{s}_0 &= \begin{pmatrix} \cos \alpha \\ \sin \alpha \end{pmatrix} \\ \hat{s}_1 &= \begin{pmatrix} \cos \gamma \\ \sin \gamma \end{pmatrix}\end{aligned}\tag{8.11}$$

Hence we arrive at

$$\begin{aligned}\frac{\hat{s}_0}{(\hat{k} \cdot \hat{s}_0)} - \frac{\hat{s}_1}{(\hat{k} \cdot \hat{s}_1)} &= \begin{pmatrix} 1 \\ \tan \alpha \end{pmatrix} - \begin{pmatrix} 1 \\ \tan \gamma \end{pmatrix} = \begin{pmatrix} 0 \\ \tan \alpha - \tan \gamma \end{pmatrix} \\ &= \hat{z} \cdot (\tan \alpha - \tan \gamma)\end{aligned}\tag{8.12}$$

Consequently the relative spatial shift has only a component in vertical direction. Any prism can be viewed as a symmetric prism with opening angle β and asymmetric rotation ϵ , hence according to Fig. 8.2

$$\begin{aligned}\alpha &= \epsilon - \frac{\beta}{2} \\ \gamma &= \epsilon + \frac{\beta}{2}\end{aligned}\tag{8.13}$$

and

$$\frac{\hat{s}_0}{(\hat{k} \cdot \hat{s}_0)} - \frac{\hat{s}_1}{(\hat{k} \cdot \hat{s}_1)} = \hat{z} \cdot \left[\tan \left(\epsilon - \frac{\beta}{2} \right) - \tan \left(\epsilon + \frac{\beta}{2} \right) \right]\tag{8.14}$$

After some manipulation one can rewrite this into

$$\frac{\hat{s}_0}{(\hat{k} \cdot \hat{s}_0)} - \frac{\hat{s}_1}{(\hat{k} \cdot \hat{s}_1)} = -\hat{z} \cdot \left[2 \frac{\sin \beta}{\cos \beta + \cos 2\epsilon} \right]\tag{8.15}$$

Summarizing the relative spatial shift reads

$$\Delta_{rel}(x) = 2x \cdot (1 - n) \cdot \frac{\sin \beta}{\cos \beta + \cos 2\epsilon} \cdot \hat{z} = x \cdot \delta(\beta, \epsilon) \cdot \hat{z}\tag{8.16}$$

where in the last step Eq. 6.2 has been used. Consequently we found for any compensated prism set that the obtained spatial shift has only a vertical component which is directly given by the prism deflection angle δ and the separation x between the two prisms. This is just what one would expect.

This setup is relatively easy to realize in comparison to the hitherto applied method [60, 23]. Interestingly the same idea has independently and parallel been invented and applied at NIST [42].

8.2 Vertical momentum distribution

The coherence function is in general related via a Fourier Transform [1] to the momentum distribution

$$\Gamma(\Delta) = \int \rho(\mathbf{k}) e^{i\mathbf{k}\Delta} d^3k \quad (8.17)$$

Consequently a measurement of the vertical momentum distribution $\rho_z(k_z)$ yields the vertical coherence function $\Gamma(\Delta_z)$. For the measurement of the vertical momentum distribution a horizontal slit of 1 mm height has been placed after the fore prisms for wavelength separation (App. C).

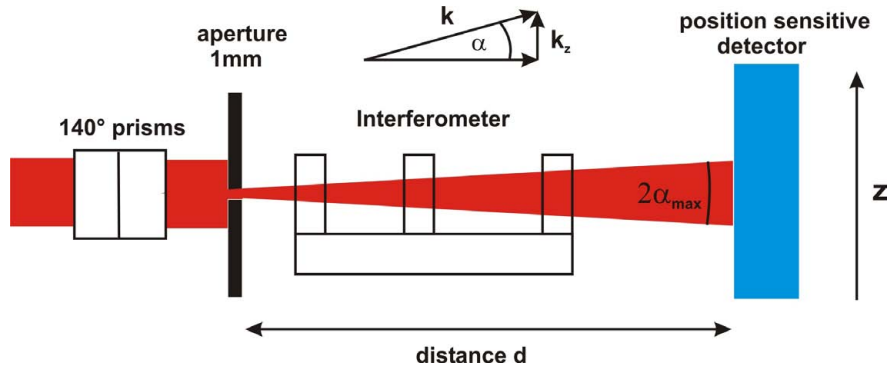


Figure 8.3: Measurement of the vertical intensity profile using a position sensitive detector. Via the interferometer and prisms the different harmonics can be separated.

If now the position sensitive detector (App. E) is placed into a certain distance d (Fig. 8.3) one finds according to the geometry given by d and the position z on the detector the vertical angular³ and thereby the momentum distribution. For our setup it is essential to place the interferometer between slit and detector to separate the different harmonics, which would otherwise overlap. This has the disadvantage of strongly reduced intensity⁴ and accordingly long measurement times, but on the other hand there is the possibility to obtain the momentum distribution for several harmonics, by choosing the according peaks in the rocking curve.

³In addition the vertical angular divergence gives important information on the increasing beam height within the interferometer which is especially important in large interferometers as ours. The increased beam height gives for example further restrictions for the possible rotation angle in Fig. 7.2.

⁴To obtain maximum intensity all beam paths have been opened. In order to avoid the appearance of remaining visibility fringes at the detector, the phase shifter has been rotated during the whole measurement time to average out all phase effects.

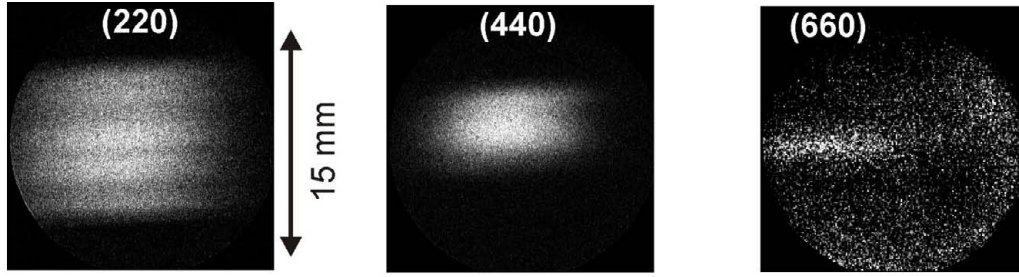


Figure 8.4: Measured intensity distribution employing the position sensitive detector according to Fig. 8.3.

Fig. 8.4 shows the obtained images⁵ for the (220) to the (660) reflection, where the latter constituted the largest challenge concerning the intensity and peak stability. From the images it is obvious that the vertical extension and thereby the angular divergence strongly reduces for higher order reflections, which is shown explicitly in Fig. 8.5. Here the intensities have been integrated over the horizontal direction.

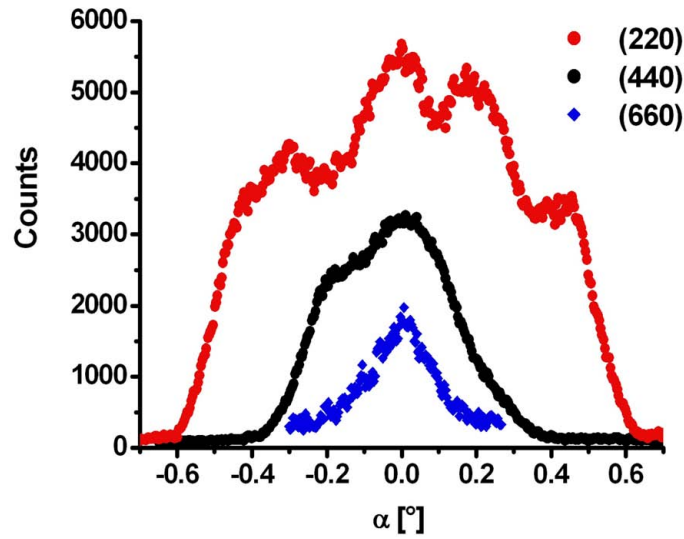


Figure 8.5: Vertical angular distributions of several harmonics after integrating over the horizontal direction.

⁵Actually several images with different vertical positions of the aperture (Fig. 8.3) within the beam height have been taken. The variations of the momentum distributions within the beam height were negligible. Due to the employed fore prisms the possible variation of aperture position was rather limited though.

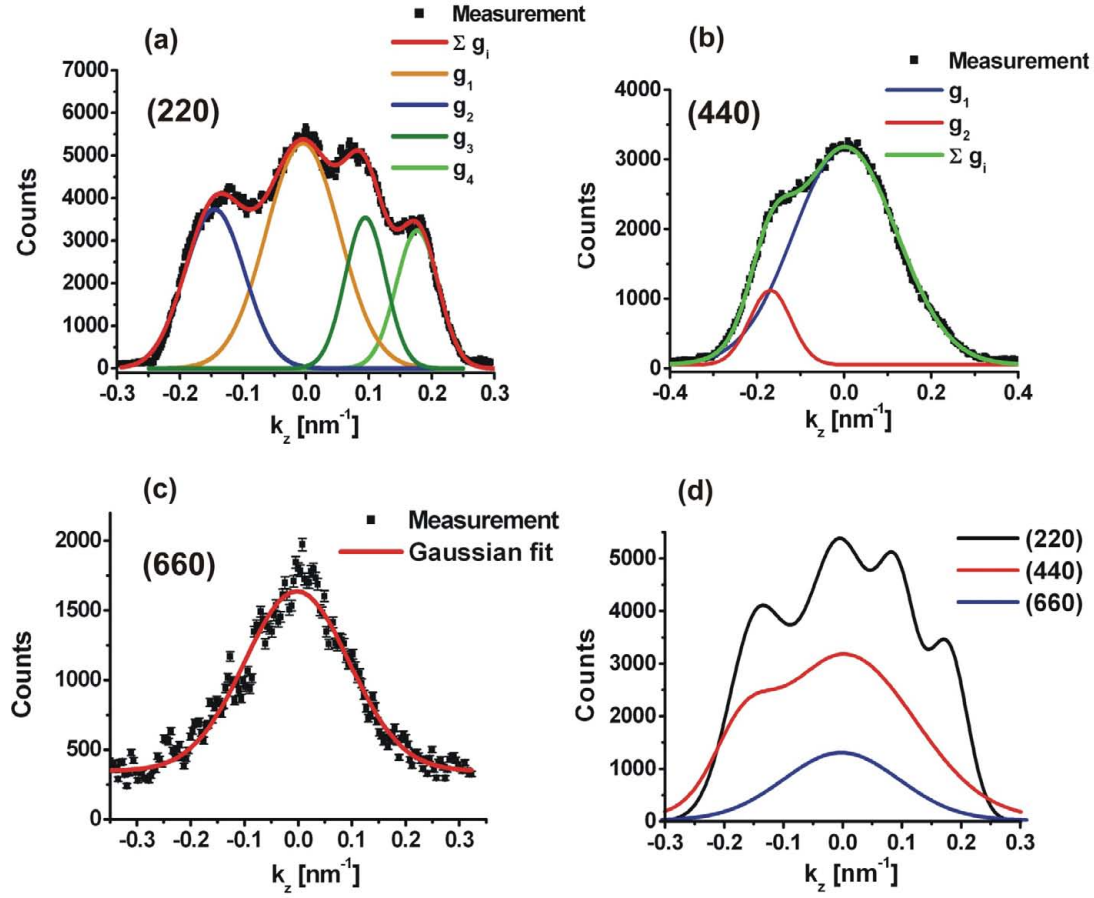


Figure 8.6: Vertical momentum distribution for three reflections, fits by sums of Gaussian functions (a)-(c) and comparison of the fitted distribution (d).

The (440) intensity distribution is by a factor of two narrower than the (220) profile. This can be explained by the wavelength-proportional critical angle for total reflection in the beam guide

$$\alpha_{max} = \lambda \sqrt{\frac{Nb_N}{\pi}} \quad (8.18)$$

Thereby the super mirror beam guide $H25^6$ can be identified as the main source for the vertical beam divergence, as by a collimator within the beam the angular divergence would be equal for different wavelengths. The thereby calculated

⁶This neutron guide consists of a complex multilayer coating by nickel-titan with $m \approx 2$. Here m is the factor gained in comparison to using only nickel.

angles of total reflection amount to

$$\begin{aligned}\alpha_{max,(220)} &\approx 0.54^\circ \\ \alpha_{max,(440)} &\approx 0.27^\circ \\ \alpha_{max,(660)} &\approx 0.18^\circ\end{aligned}\tag{8.19}$$

For the (220) and (440) reflection the measured angular distributions are in reasonable agreement with these values. The vertical divergence of the (660) reflection is slightly smaller than expected. This has to be explained by the non-optimal guiding behavior in the sub-Angstrom regime.

From this angular distributions one derives the momentum distributions (Fig. 8.6) via $k_z = k \sin \alpha$. Contrary to the angular distributions one finds approximately the same width of the momentum distributions. This is due to the relation

$$k_{z,max} = k \cdot \alpha_{max} \propto \frac{2\pi}{\lambda} \lambda \approx const.\tag{8.20}$$

The momentum distributions are not simple Gaussian distributions but show a specific structure, which can be fitted by sums of Gaussian distributions though⁷ (Fig. 8.6). For Gaussian momentum distributions with width δk_z the related coherence function is also Gaussian:

$$\Gamma(\Delta_z) = e^{-\frac{(\Delta_z \delta k_z)^2}{2}}\tag{8.21}$$

In this case the vertical coherence length Δ_z^c is defined when the coherence function has decayed to a value $1/e$. Consequently the coherence length and the momentum width δk_z are directly related via

$$\Delta_z^c \cdot \delta k_z = \frac{1}{2}\tag{8.22}$$

Hence the coherence length of the (440) and (220) reflection should be approximately equal whereas the (660) distribution results in a larger coherence length. In Fig. 8.7 the related coherence functions $\Gamma(\Delta_z)$ derived via Fourier transforms⁸

⁷The (660) reflection has been fitted by a simple Gaussian function although a slightly better fit could be gained by including another Gaussian function. However at this level of resolution, the structures are not conclusive and an estimation for the width of the curve is sufficient. Hence also the derived vertical coherence function is Gaussian, although a more precise measurement might result in deviations as for the other reflections.

⁸For the (220) and (440) reflection the Fourier transforms for the fit functions and directly applied to the data via a Fast-Fourier transform are almost identical. In the (660) case the result for the Fourier transform of the fit function is shown.

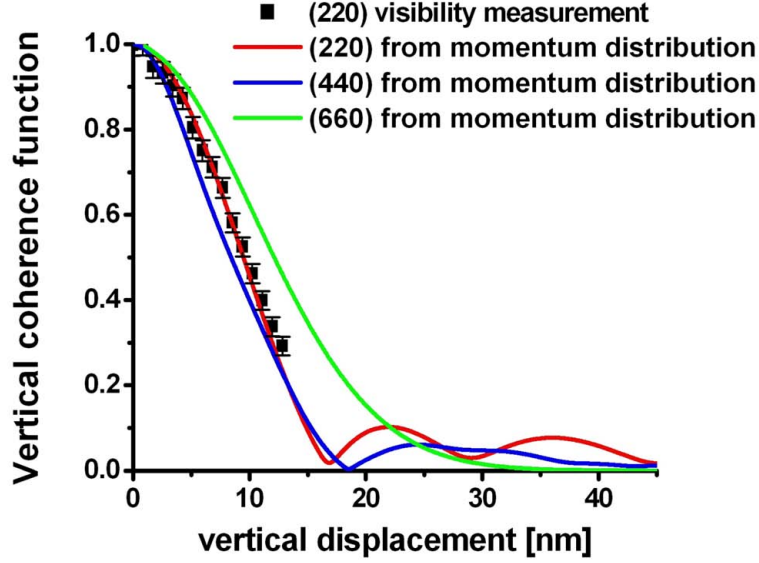


Figure 8.7: Vertical coherence function derived from the vertical momentum distributions (solid lines) and comparison with visibility measurements using the prism method.

are shown. Despite slight deviations in the coherence functions, the coherence length for the (220) and (440) reflection is approximately equal and amounts to

$$\Delta_z^c \approx 11\text{nm} \quad (8.23)$$

This is in good agreement with the derived coherence length for a different wavelength ($\lambda = 1.91\text{\AA}$, [23]). The coherence length for the (660) reflection is according to the reduced width of the momentum distribution

$$\Delta_{z,(660)}^c \approx 15\text{nm} \quad (8.24)$$

It is also obvious that the deviation from a single Gaussian behavior of the momentum distributions leads to a non Gaussian form of the coherence function with a damped reappearance of the visibility at large Δ_z .

For the (220) reflection these measurements have been compared with measurements by the prism method. At the time of this experiment⁹ the first set of self fabricated silicon prisms with suboptimal geometry have been used, resulting only in measurements up to approximately Δ_z^c . Nevertheless good agreement

⁹This measurement has been performed together with Robert Farthofer[57] for testing the usage of prisms in neutron interferometry. Due to the concentration on interferometer testing and Laue phase measurements there has been no possibility to continue these measurements.

with the coherence function determined by the momentum distribution has been found. As the prism refraction increases proportional to λ^2 , the data for the (440) reflection has been even more limited in the range of Δ_z and is not shown here. An interesting feature of this experiment is, that the spatial shift is purely vertical. Consequently contrary to the measurements of the longitudinal and transversal¹⁰ coherence function no phase shift arises during the prism separation

$$\phi(x) = \Delta \cdot \mathbf{k} = x \cdot \delta(\beta, \epsilon) \cdot \hat{z} \cdot k \cdot \hat{x} = 0 \quad (8.25)$$

Fig. 8.8 shows this feature observed during our measurement. The phase uncertainty due to the overall low visibility is relatively large, a linear fit through the data confirms this property accurately though.

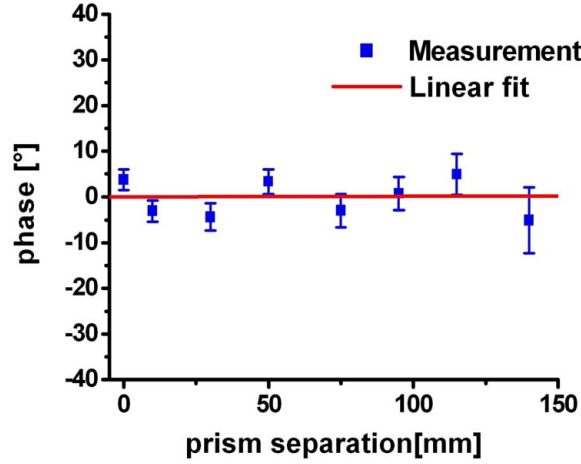


Figure 8.8: Measured phase shift during prism separation.

8.3 Outlook

A direct measurement of the coherence function with prisms would be desirable also for the higher order reflections. Furthermore one should aim to resolve the slight reappearance of the visibility at vertical displacements beyond the coherence length. Large displacements are especially difficult for the higher order reflections due to the strongly reduced prism refraction. Besides the application of strongly refracting prisms, the orthogonal prism design would be especially

¹⁰Here the definition for longitudinal and transversal with respect to the lattice vector is used [1]. Sometimes these directions are defined according to the neutron wave vector though.

useful. As shown in Fig. 8.9 this enables to double the spatial shift, if the sets in the two beam paths are rotated by 180° against each other and one separates both prism sets simultaneously.

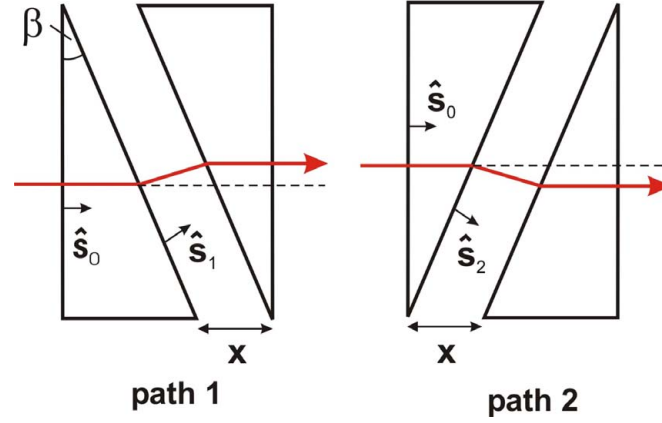


Figure 8.9: Arrangement of orthogonal prisms to double the spatial shift between the two beam paths.

An alternative and much faster method of a coherence measurement would be the measurement of intensity changes in the O- and H-output as a function of the prism separation. If the initial phase - preferable at the O-beam minimum or maximum - is known and phase stability can be maintained during prism separation, then the visibility is completely determined by the intensity modulations. For instance, intensity changes become constant if the visibility approaches zero. This is a special feature of this type of measurement as no phase shift arises during the prism separation (Eq. 8.25). By adjusting the prisms in the horizontal position (δ_y) one derives the coherence function transversal to the beam. The coherence measurement in longitudinal direction can be achieved in the non-dispersive arrangement with phase plates of various thicknesses, or continuously, with two prisms moving against each other in order to smoothly vary the thickness (Fig. 8.10).

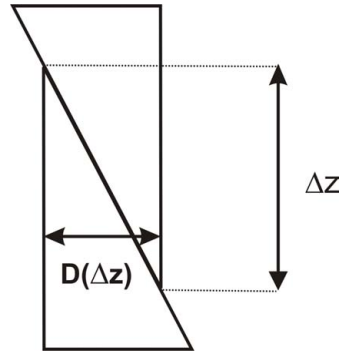


Figure 8.10: Variation of the effective thickness $D = D(\Delta z)$ by sliding two prisms along each other.

Appendix A

Laue phase: special cases

In Eq. 2.42 an expansion for small $\delta\theta$ has been given. For the further considerations the term $\frac{\sin 2\theta_B}{v_H} \tan A_H \delta\theta$ has been dropped. This is only a good approximation for the case $A_H \gg 1$ and simultaneously $\tan A_H \lesssim 1$. There are two cases where these conditions are not fulfilled

- For thin crystals where the thickness is of similar order than the Pendellösung length
- for

$$A_H = \frac{\pi D}{\Delta_H} \approx (2n + 1) \frac{\pi}{2} \quad (\text{A.1})$$

which corresponds to the case that the Pendellösung structure discussed in 2.2.2 is very close to the exact Bragg condition

In these cases the first order expansion reads

$$\phi_{Laue}(\delta\theta) = \phi_{Laue}(0) + \delta\theta \cdot \frac{\sin 2\theta_B}{v_H} (A_H - \tan A_H) + O(\delta\theta^3) \quad (\text{A.2})$$

Hitherto the phase function has been considered as steadily increasing. However now

$$A_H - \tan A_H < 0 \quad \text{for} \quad A_H < \frac{\pi}{2} \implies D < \frac{\Delta_H}{2} \quad (\text{A.3})$$

This implicates, that for thicknesses smaller than half of the Pendellösung length the slope of the phase function is negative in the vicinity of Bragg. Furthermore the slope of the phase function becomes extremely large at $D \approx \frac{\Delta_H}{2}$

$$\begin{aligned} \lim_{D \rightarrow \Delta_H/2-} (A_H - \tan A_H) &\rightarrow -\infty \\ \lim_{D \rightarrow \Delta_H/2+} (A_H - \tan A_H) &\rightarrow +\infty \end{aligned} \quad (\text{A.4})$$

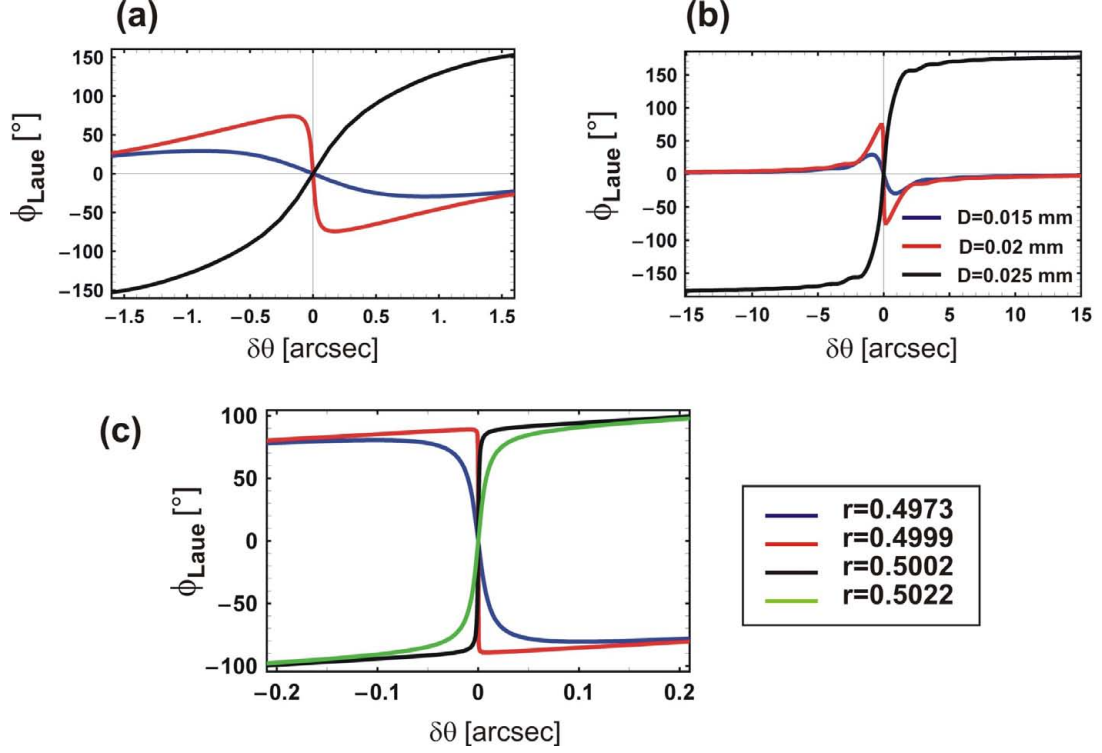


Figure A.1: Laue phase for small thicknesses: (a) around Bragg and (b) in the limit of the asymptotes. (c) shows the case closely around $r = \frac{D}{\Delta_H} = 0.5$. According to the chosen parameters $\Delta_H = 40.622\mu\text{m}$. The constant $\phi_{Laue}(0)$ has been subtracted.

and changes the sign from $D < \frac{\Delta_H}{2}$ to $D > \frac{\Delta_H}{2}$. This evolution of the phase function is shown in Fig. A.1.

In Fig. A.1 (b) another interesting feature can be observed, concerning the asymptotes

$$\begin{aligned} \lim_{\delta\theta \rightarrow \pm\infty} \phi_{Laue}(\delta\theta) - \phi_{Laue}(0) &= 0 & D &\lesssim \frac{\Delta_H}{2} \\ \lim_{\delta\theta \rightarrow \pm\infty} \phi_{Laue}(\delta\theta) - \phi_{Laue}(0) &= \pm\pi & D &\gtrsim \frac{\Delta_H}{2} \end{aligned} \quad (\text{A.5})$$

Thus the asymptotes are separated exactly by 0 or 2π respectively. The transition between these two cases occurs exactly at $D = \frac{\Delta_H}{2}$. Another interesting observation is

$$|\phi_{Laue}(D_1, \delta\theta)| > |\phi_{Laue}(D_2, \delta\theta)| \quad \text{for} \quad \frac{\Delta_H}{2} \lesssim D_1 \lesssim D_2 \quad (\text{A.6})$$

This behavior of the Laue phase for small thicknesses is important for an understanding of the calculated visibilities presented in Fig. 4.4. Let's now consider

the case $D > \Delta_H$. Here the slope of the phase function at Bragg is only negative for $A_H < \tan A_H$. Whereas this condition has been fulfilled over the whole first half of the period of the tangent, this range where $A_H \lesssim (2n+1)\frac{\pi}{2}$ significantly decreases with increasing D/Δ_H as shown in Fig. A.2.

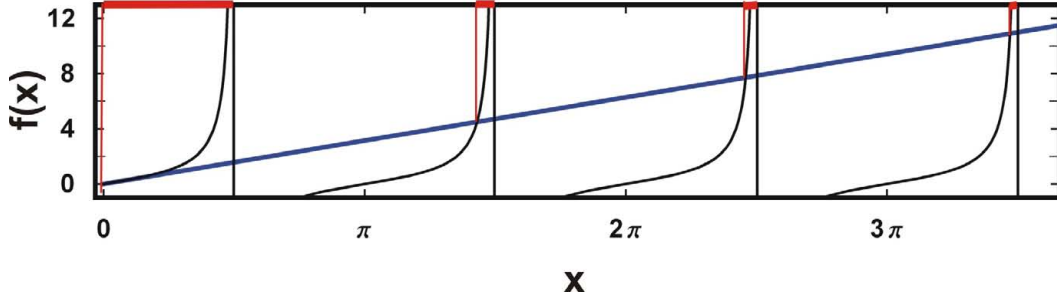


Figure A.2: Comparison of $\tan x$ (black curve) with x (blue curve) The regions where $\tan x > x$ are highlighted by a red line.

In these increasingly narrow areas the slope of the phase function at Bragg is still negative though, as shown in Fig. A.3.

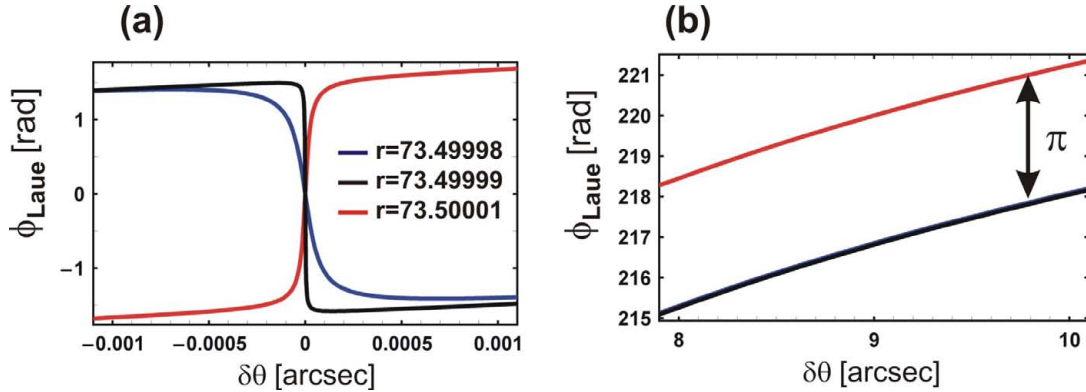


Figure A.3: The case of $D \approx (2n+1)\frac{\Delta_H}{2}$. Here $D \approx 73.5\Delta_H \approx 2.9857\text{mm}$. (a) shows the evolution of the Laue phase around Bragg depending on $r = \frac{D}{\Delta_H}$. (b) shows the Laue phase further away. The phase curves for $r < 73.5$ and $r > 73.5$ are separated by π in the limit of the asymptotes. The constant $\phi_{Laue}(0)$ has been subtracted.

Similar to the case of $D = \frac{\Delta_H}{2}$, here the distance between the asymptotes changes by exactly 2π :

$$\begin{aligned} \lim_{\delta\theta \rightarrow \pm\infty} \phi_{Laue}(\delta\theta) - \phi_{Laue}(0) &= \pm n\pi & D < (2n+1)\frac{\Delta_H}{2} \\ \lim_{\delta\theta \rightarrow \pm\infty} \phi_{Laue}(\delta\theta) - \phi_{Laue}(0) &= \pm(n+1)\pi & D > (2n+1)\frac{\Delta_H}{2} \end{aligned} \quad (\text{A.7})$$

Thus every time the thickness reaches another uneven multiple of half of the Pendellösung length, the separation of the asymptotes changes by 2π . As for $D < \frac{\Delta_H}{2}$ the asymptotes are zero, the asymptotes are always separated by a multiple of 2π as discussed in subsection 2.2. Eq. A.8 gives also the correct limit in comparison with Eq. 2.45, where the value A_H can take every value. Thus the asymptotes go to the closest lower or upper bound multiple of π rather than to A_H exactly:

$$\begin{aligned} \lim_{\delta\theta \rightarrow \pm\infty} \phi_{Laue}(\delta\theta) - \phi_{Laue}(0) &= \pm \left\lfloor \frac{A_H}{\pi} \right\rfloor \pi & \left| \frac{A_H}{\pi} - \left\lfloor \frac{A_H}{\pi} \right\rfloor \right| > \left| \frac{A_H}{\pi} - \left\lceil \frac{A_H}{\pi} \right\rceil \right| \\ \lim_{\delta\theta \rightarrow \pm\infty} \phi_{Laue}(\delta\theta) - \phi_{Laue}(0) &= \pm \left\lceil \frac{A_H}{\pi} \right\rceil \pi & \left| \frac{A_H}{\pi} - \left\lceil \frac{A_H}{\pi} \right\rceil \right| < \left| \frac{A_H}{\pi} - \left\lfloor \frac{A_H}{\pi} \right\rfloor \right| \end{aligned} \quad (A.8)$$

This separation of the phase curves takes already place closely around Bragg (Fig. A.3 (a)). The discussed cases $D = (2n + 1)\frac{\Delta_H}{2}$ are also just the case where the Pendellösung structure appears exactly at the Bragg condition, hence where the transmitted intensity has a minimum at $\delta\theta = 0$. Here the Pendellösung structure shows no more a phase "plateau" but a distinct change of the slope. Actually also the Pendellösung structures at $\delta\theta \neq 0$ are not really plateaus, but also there remains a slight change of the slope to negative values Fig. A.4, that however decreases with increasing $\delta\theta$.

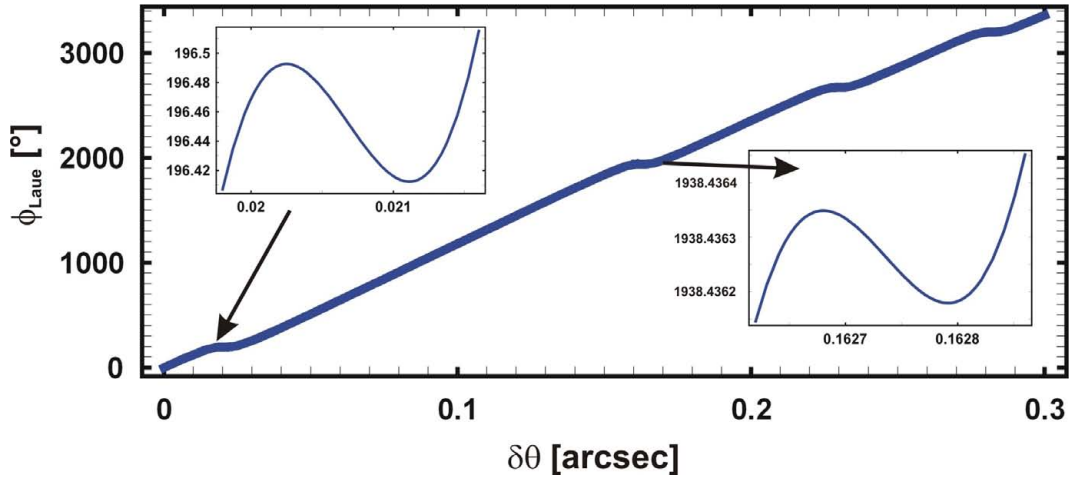


Figure A.4: Zoom into the Pendellösung structure plateaus of the Laue phase.

Hence the Laue phase is not a steadily increasing function over all angular range. Of course instead of varying the thickness the same holds for a variation

of the Pendellösung length via a variation of the scattering length or the Bragg angle.

Appendix B

Interferometer cutting drafts

The plans for the first cutting: In view of the further preparation steps, the initial lamella thickness has been planned to $D = 3.3\mu\text{m}$.

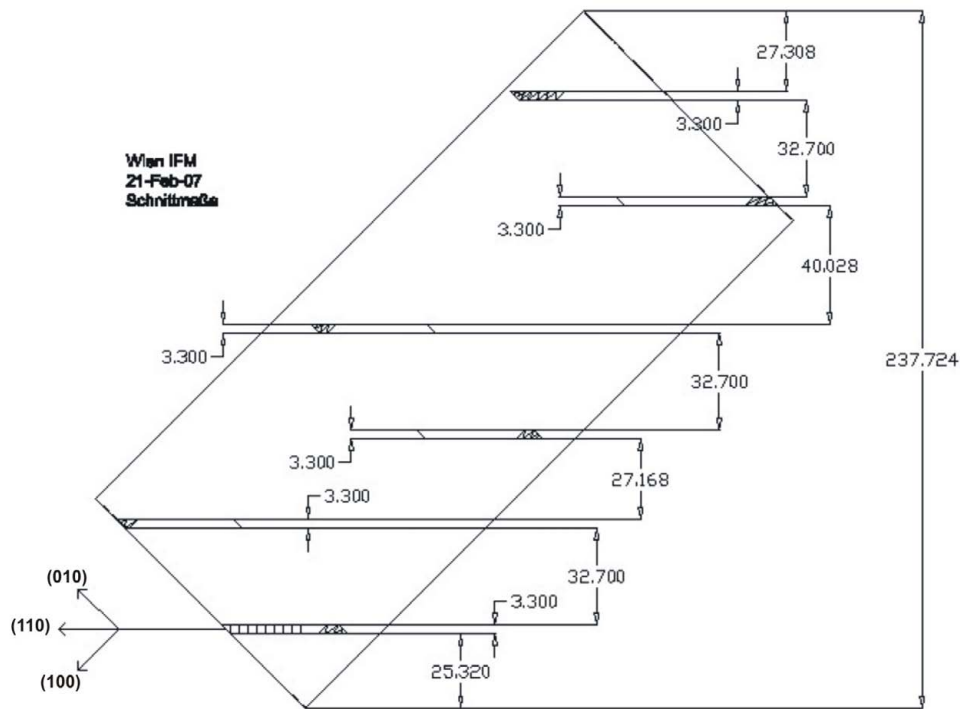


Figure B.1: Aimed lamella thicknesses and distances after the first cutting process.

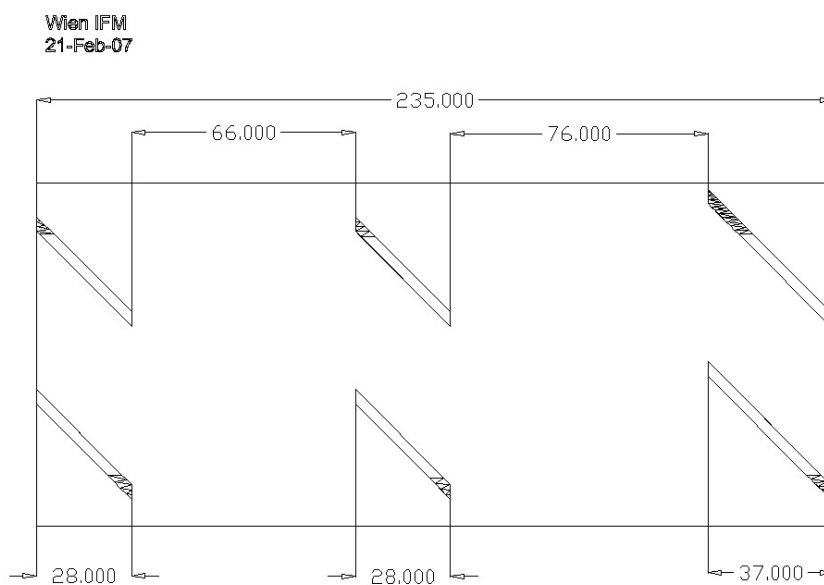


Figure B.2: Horizontal projection and lamella widths.

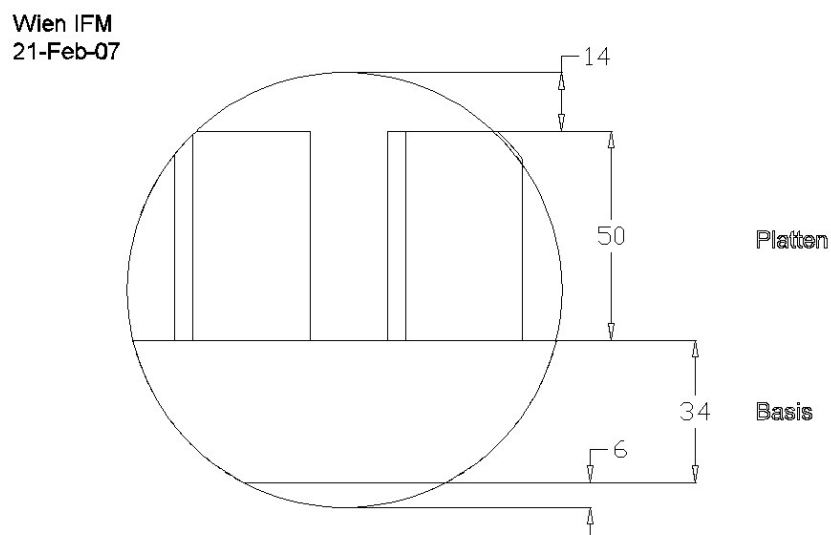


Figure B.3: Front elevation.

Appendix C

Rocking curves

The separation of the higher order reflections has been accomplished using six 140° perfect crystal silicon prisms, that have been fabricated during this work at the atomic institute (6.2.1). The prism deflection is strongly dispersive, yielding a total deflection δ as a sum¹ of the individual deflections by n prisms with apex angle β_i ²

$$\delta(\lambda) = \sum_{i=1}^n \delta_i = \lambda^2 \sum_{i=1}^n \frac{Nb_N}{\pi} \tan \frac{\beta_i}{2} \quad (\text{C.1})$$

Hence the separation between two wavelengths becomes

$$\Delta\delta_{prism}(\lambda_1, \lambda_2) = \delta(\lambda_1) - \delta(\lambda_2) = (\lambda_1^2 - \lambda_2^2) \sum_{i=1}^n \frac{Nb_N}{\pi} \tan \frac{\beta_i}{2} \quad (\text{C.2})$$

Moreover the combination of a perfect crystal monochromator with the interferometer leads to an intrinsic separation of the wavelengths. This is due to the asymmetry of the Bragg reflection curve with respect to $\delta\theta$, although it is symmetric with respect to y (Eq. 4.8). According to Eqs. 2.75, 2.74

$$\begin{aligned} y &= -\frac{(b-1)v_0 + 2b \sin 2\theta_B \delta\theta}{2\sqrt{|b|}v_H} \\ b &= 1 \quad \text{Laue case} \\ b &= -1 \quad \text{Bragg case} \end{aligned} \quad (\text{C.3})$$

¹Corrections to the asymmetric case by the deflection of the previous prisms can be neglected, as the deflections are only in the range of arc seconds. The error by manual alignment of the prisms is much higher.

²Here symmetric alignment of the prisms is assumed. One can even enhance the deflection by an additional asymmetric angle ϵ . The useable beam width for the interferometer would become smaller though.

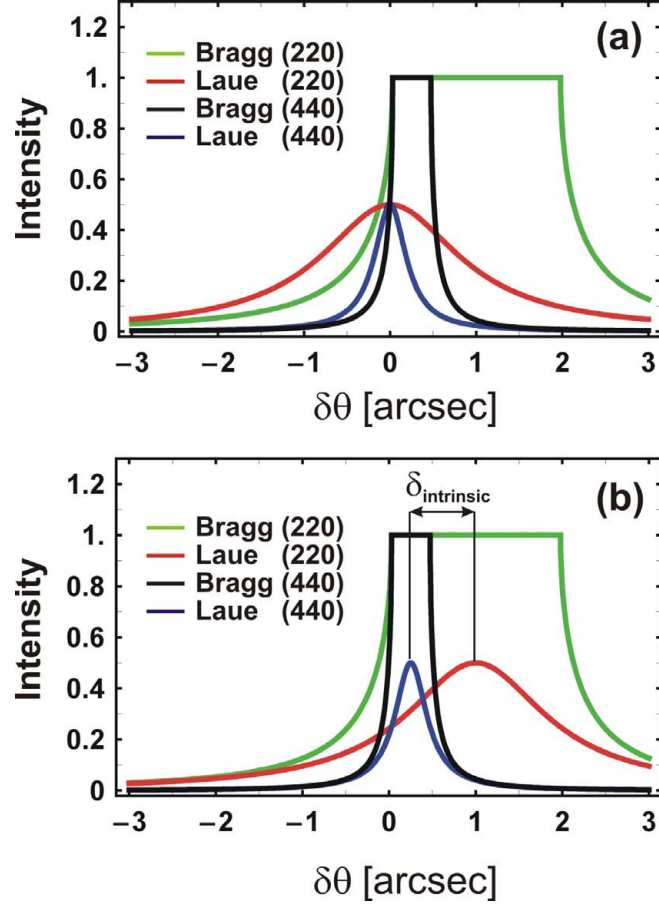


Figure C.1: (a) Shift between Bragg- and Laue reflections curves. (b) Laue curves centered relative to the according Bragg curves and intrinsic separation thereby.

In the Laue case the center of reflection is still θ_B while in the Bragg case it is shifted to ($y = 0$):

$$\begin{aligned}\theta &= \theta_B - \theta_{\text{shift}} \\ \theta_{\text{shift}} &= \frac{v_0}{\sin 2\theta_B} = \lambda^2 \frac{Nb_N}{\pi \sin 2\theta_B}\end{aligned}\tag{C.4}$$

This relative shift of the Bragg- to the Laue reflection curve is shown in Fig. C.1.

To obtain the maximum intensity both curves are centered to each other, which results in different angles for different reflection orders, as θ_{shift} depends on λ .

Thus an intrinsic separation between two orders of reflection m_1 and m_2 can

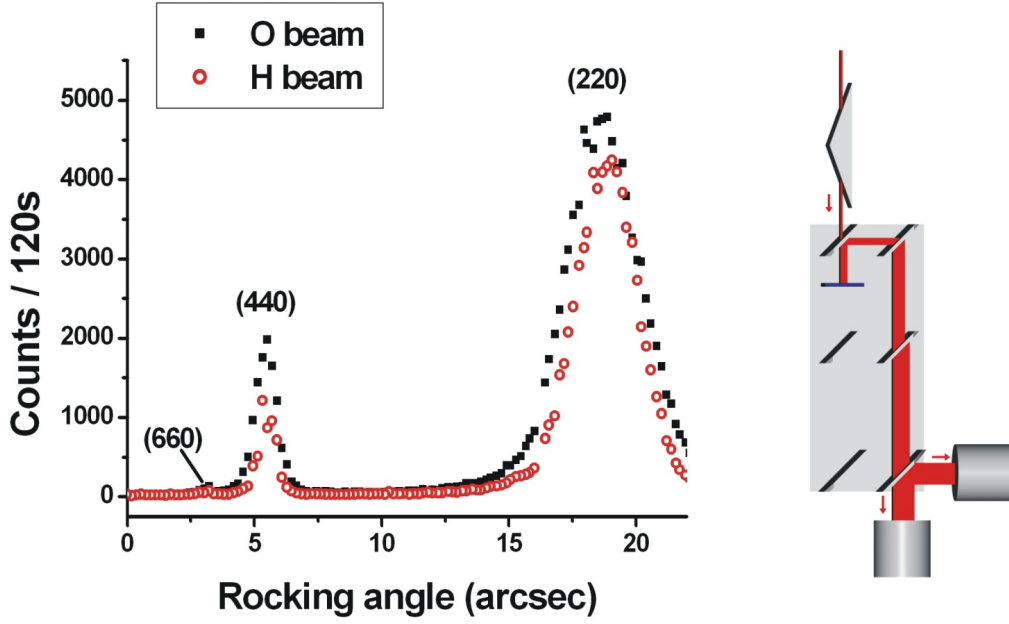


Figure C.2: Rocking and wavelengths separation in non-interferometric configuration (one beam path blocked). The zero position here is arbitrary according to the goniometer encoding.

be observed

$$\delta_{intrinsic}(m_1, m_2) = \theta_{shift}(m_1) - \theta_{shift}(m_2) = (m_1^2 - m_2^2) \cdot \lambda_{220}^2 \cdot \frac{Nb_N}{\pi \sin 2\theta_B} \quad (C.5)$$

Altogether the obtained wavelength separation yields

$$\begin{aligned} \Delta\delta(m_1, m_2) &= \Delta\delta_{prism}(\lambda_1, \lambda_2) \pm \delta_{intrinsic}(m_1, m_2) \\ &= (m_1^2 - m_2^2) \cdot \lambda_{220}^2 \cdot \frac{Nb_N}{\pi} \cdot \left(\sum_{i=1}^n \tan \frac{\beta_i}{2} \pm \frac{1}{\sin 2\theta_B} \right) \end{aligned} \quad (C.6)$$

where the plus/minus sign depends on the assembly of the prism arrangement relative to the direction of the intrinsic separation. To obtain maximal separation the prism arrangement should be chosen accordingly. By rotating the prisms by 180° , one can easily measure the intrinsic separation as half of the difference between the measured total separations. Tab. C.1 shows the calculated separations. Good agreement with the measured values has been found, although in our experiments the exact separation has been of minor importance.

reflections	intrinsic separation	prism separation	total separation
(220) - (440)	0.75''	12.41''	13.16''
(440) - (660)	0.14''	2.3''	2.44''
(660) - (880)	0.05''	0.8''	0.85''

Table C.1: Theoretical separation between several reflection orders at $\theta_B = 45^\circ$, without prisms (intrinsic), by six 140° prisms omitting the intrinsic separation and totally.

Appendix D

Reflectivity of Laue-USANS

Here a short comparison of the reflectivity and thereby the intensity ratio between the usually applied USANS method and our interferometric method in Laue geometry (Fig. 6.4) is given. The reflectivity of a threefold Bragg reflection is calculated via

$$\begin{aligned} R_{Bragg,tot} &= \int_{-\infty}^{\infty} R_{H,Bragg}^3(y) dy \\ &= \int_{-1}^1 1 dy + 2 \cdot \int_1^{\infty} \left(1 - \sqrt{1 - \frac{1}{y^2}}\right)^3 dy \\ &= \frac{9\pi}{2} - 12 \approx 2.14 \end{aligned} \tag{D.1}$$

and in the case of the Laue reflection one obtains

$$\begin{aligned} R_{Laue,tot} &= \int_{-\infty}^{\infty} R_{H,Laue}^3(y) dy \\ &= \int_{-\infty}^{\infty} \left(\frac{1}{2(1+y^2)}\right)^3 dy \\ &= \frac{3\pi}{64} \approx 0.15 \end{aligned} \tag{D.2}$$

where the averages over the Pendellösung oscillations according to Eqs. 4.8, 2.26 have been taken. Hence the intensity ratio yields

$$\frac{R_{Bragg,tot}}{R_{Laue,tot}} \approx 14.5 \tag{D.3}$$

Appendix E

Position sensitive detector

For the detection of spatial dependent phase patterns and the measurement of the vertical momentum distribution a position sensitive detector has been employed. This ND&M detector¹ had been used before at S18 for neutron phase tomography [63] but had been rejected afterwards. Therefore we have reinstalled this detector on a suitable computer containing an ISA slot. Now this detector is again available for the measurement of intensity distributions within beams and spatial dependent phase patterns (compare section 5.2). Additionally this detector can now be used for neutron imaging at low intensity beam lines such as the one at our institute. An according test on resolution and usability has been performed [64] and shall be summarized in this chapter.

E.0.1 General features

The ND&M camera is a compact neutron detector, which consists of a handmonitor and a readout unit. The handmonitor contains a ${}^6\text{LiF}-\text{ZNS}(\text{Ag})$ scintillator coupled to a micro-channel plate image amplifier with 25mm opening, the output of which is projected to a phosphor screen (Fig. E.1). Moreover the handmonitor can be used as a stand-alone device for beam alignment. For quantitative imaging it is attached to a readout unit, which consists of a mirror, a high speed lens, and a low noise CCD camera with 512×512 pixels and $11 \times 11 \mu\text{m}^2$ resolution. The readout unit is connected to the ND&M realtime centroiding processor in the host PC. Special features of this detector are single neutron counting and a high optical resolution of $50 \mu\text{m}$, realized by an electronic centroiding procedure of the light spots on the screen. Single neutron counting is accomplished by the high readout rate of the CCD frames, thereby avoiding an overlap of the light spots on the single digitized image. Frames with overlapping spots are discarded. Each

¹ND&M Felber, Raum, Rausch GBR, D-85356 Freising

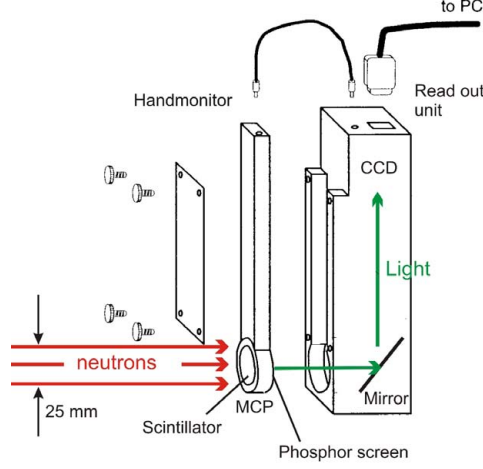


Figure E.1: Outline of the ND&M micro-channel detector

digitized video frame runs through a two-dimensional convolver where the frames are correlated with idealized model distributions of scintillation light spots. This allows very effective noise discrimination. The centroids of the spots and their peak value are determined in realtime and can be viewed at the PC monitor. The host PC sums up the spatial distribution of incoming neutrons with 16 bit dynamic range. A demonstration of the efficient electronic noise suppression and the homogeneous intensity profile in the central beam area is shown in Fig. E.2.

E.0.2 Characterization of the resolution

The spatial resolution at our beam line is primarily limited by the collimation ratio $L/D = 130$, i.e, the ratio between collimator length $L = 2600$ mm and aperture $D = 20$ mm. This results in a geometric unsharpness

$$U_g = L_{S-D} \frac{D}{L} \quad (\text{E.1})$$

determined by the sample-to-detector distance L_{S-D} , which should therefore be minimized. The second blurring effect is the intrinsic unsharpness in the sensitive layer. A thin layer narrows the spread of secondary radiation in the converter, thereby reducing the detector blurring at the cost of detection efficiency. To compare the spatial resolutions a sharp edge (Fig. E.2) fabricated of a $25\mu\text{m}$ thick gadolinium foil with 5.1% neutron transmission was placed directly on the scintillator (Fig. E.2). The measured edge spread function (ESF) and its derivative, the line spread function (LSF), can be approximated by a Lorentzian model if image blurring predominantly emerges in the converter. The ESF parameters

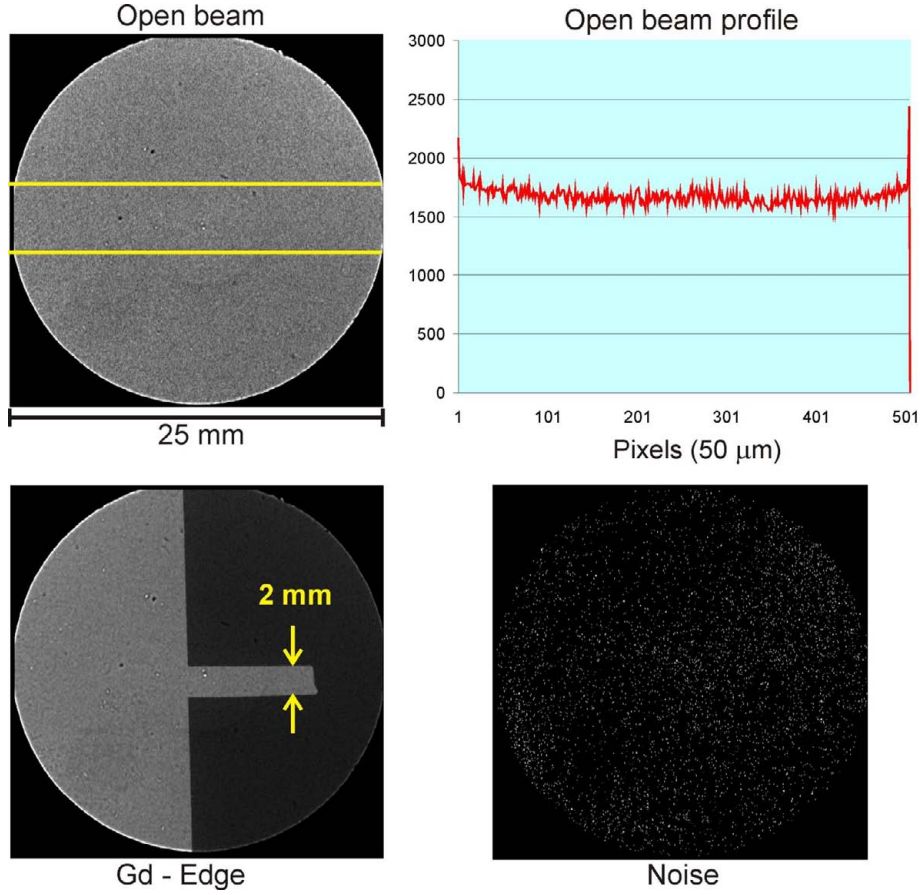


Figure E.2: The ND&M open beam analysis yields a rather homogeneous profile with intensity variance $\sigma = 1.2 \times \sqrt{N_{average}}$. The measured intrinsic noise was 8200 counts in 28 hours on the whole sensitive area.

$p_{1,2,3}$ and λ are fitted to the measured edge profile with the resolution parameter λ as result. The latter is important for the resolution given by the full-width half-maximum (FWHM).

$$\begin{aligned}
 ESF(x) &= p_1 + p_2 \cdot \arctan[\lambda(x - p_3)] \\
 LSF(x) &= \frac{d}{dx} ESF(x) \\
 FWHM(\lambda) &= \frac{2}{\lambda}
 \end{aligned} \tag{E.2}$$

Fig. E.3 shows the fits for the gadolinium edge horizontally and vertically. The corresponding resolutions are

$$\begin{aligned}
 \text{horizontal:} & \quad 50 \pm 15 \mu\text{m} \\
 \text{vertical:} & \quad 80 \pm 15 \mu\text{m}
 \end{aligned} \tag{E.3}$$

thereby yielding a slightly better resolution in horizontal direction, due to the CCD readout procedure.

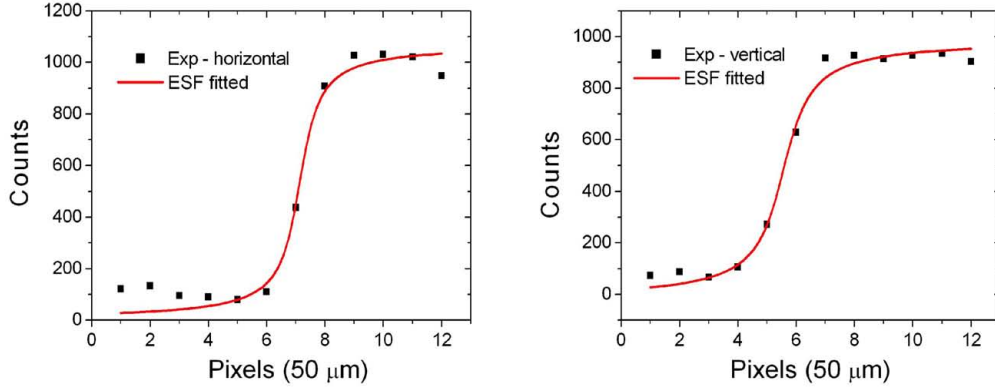


Figure E.3: ESF resolution with the ND&M camera evaluating the edges of a $25\mu\text{m}$ thick gadolinium foil horizontally and vertically.

In an alternative approach a specially developed gadolinium layer of $6\mu\text{m}$ thickness with periodic structures has been employed [65]. Fig. E.4 B, C shows the image of a star consisting of a structure of transparent lines with periodicity between 500 and $50\mu\text{m}$. The resolution is marked by concentric rings corresponding to 500 , 400 , 300 , 100 and finally $50\mu\text{m}$ for the ring in the center.

Detector	Spatial resolution	n/ γ -ratio	Intrinsic noise/pixel
^6Li - ND&M	$50(80) \mu\text{m}$	40	$3 \times 10^{-7}/s$
^6Li -thin-plate	$150 \mu\text{m}$	500	$300 + (0.4/s)$
Gd-NIP	$40 \mu\text{m}$	50	$4 \times 10^{-5}/s$

Table E.1: Summary of detector characteristics and comparison with the other two available detectors at our imaging beam line: a $100\mu\text{m}$ thin-plate scintillator (^6Li -thin-plate) and an imaging plate detector with $25\mu\text{m}$ scanning resolution (Gd-NIP).

Fig. E.4 D shows the image of a grid with line widths down to $50\mu\text{m}$ embedded in the same gadolinium layer. It is obvious that line structure down to $50\mu\text{m}$ and probably below can easily be resolved, while the detection of periodic structures is restricted by the pixel resolution to approximately $100\mu\text{m}$. Finally the same images have been made with a 7 bit film converter. A comparison of Fig. E.4 A, B, C shows the advantage of the 16 bit digitized imaging.

Furthermore the neutron-to gamma ratio was determined to approximately a value of 40 (Tab. E.1) by comparing the intensities with open and closed boron

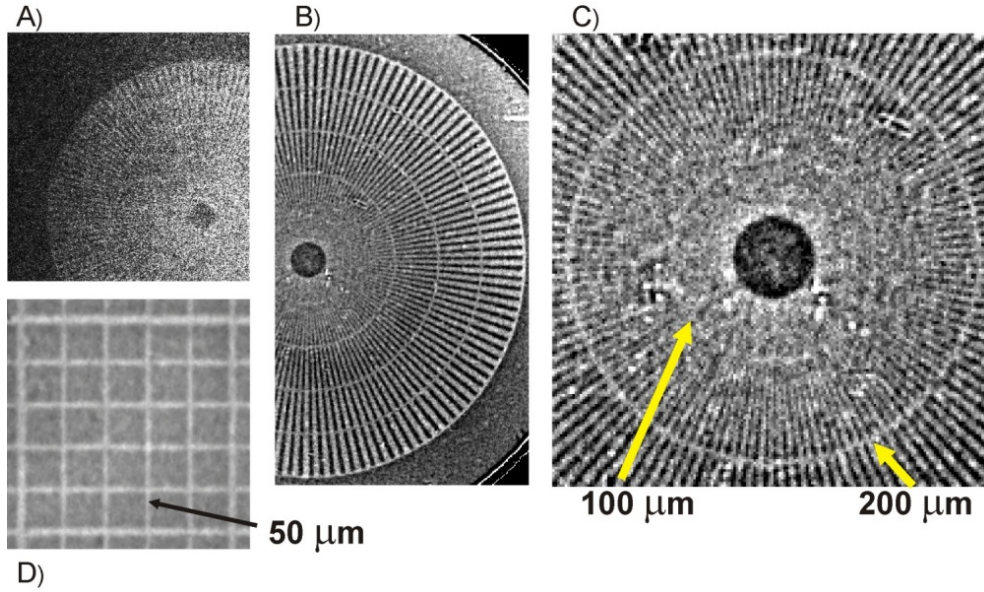


Figure E.4: Imaging of an artificial test mask of transparent lines etched in a $6\mu\text{m}$ gadolinium layer. A) Siemens star imaged with a X-ray film (Structurix D7, 35 min exposure) with gadolinium converter and 7 bit image gradation; the resolution of periodic line structures is approx. $200\mu\text{m}$. B) ND&M image with approx. $100\mu\text{m}$ line pair resolution. C) Zoom in the inner zones of the star, one recognizes that the resolution below $100\mu\text{m}$ is limited by the pixel size. D) ND&M image of the grid, the finest lines have $50\mu\text{m}$ width with 30 % elevated transmission.

beam shutter. Concerning the usability for radiography a severe limitation for neutron imaging is the maximum acceptable count rate of approx. 3000n/s in the whole detector field to avoid overlapping light spots on the phosphor screen. This limit counteracts the high efficiency of approx. 40%, as one has to attenuate the beam at our beam line. Nevertheless due to its effective noise suppression and high efficiency the ND&M camera is interesting for NR/NT applications with weak beams of the order $10^3 - 10^4\text{n/s}$ (compare Tab. E.1). Based on these results we have applied this detector for neutron radiography mainly in the investigation of the homogeneity of the neutron transmission through boron alloyed steels accompanied by Monte Carlo simulations. This however is beyond the scope of this work [66].

Bibliography

- [1] H. Rauch and S. A. Werner. *Neutron interferometry*. Clarendon Press, Oxford, 2000.
- [2] S. A. Werner. Gravitational and magnetic field effects on the dynamical diffraction of neutrons. *Phys. Rev. B*, 21:1774, 1980.
- [3] H. Rauch and D. Petrascheck. *Grundlagen für ein Laue-Neutroneninterferometer - Teil 1*. AIAU 74405b, 1974.
- [4] H. Rauch and D. Petrascheck. *Dynamical Neutron Diffraction and Its Application*, chapter 9. Springer Verlag, 1978.
- [5] C. G. Shull. Observation of Pendellösung fringe structure in neutron diffraction. *Phys. Rev. Lett.*, 21:1585, 1968.
- [6] C. G. Shull and J.A. Oberteuffer. Spherical-wave neutron propagation and Pendellösung fringe structure in silicon. *Phys. Rev. Lett.*, 29:871, 1972.
- [7] F. E. Wiedtfeldt, M. Huber, T. C. Black, H. Kaiser, M. Arif, D. L. Jacobson, and S. A. Werner. Measuring the neutron’s mean square charge radius using neutron interferometry. *Physica B*, 385-386:1374–1376, 2006.
- [8] A. Ioffe and M. Vrana. A new neutron interferometry approach in the determination of the neutron-electron interaction amplitude. *Appl. Phys. A*, 74:314, 2003.
- [9] G. L. Greene and V. Gudkov. Neutron interferometric method to provide improved constraints on non-Newtonian gravity at the nanometer scale. *Phys. Rev. C*, 75:015501, 2007.
- [10] W. Graeff, W. Bauspiess, U. Bonse, and H. Rauch. A new neutron interferometry approach in the determination of the neutron-electron interaction amplitude. *Acta cryst. A*, 34, supplement:238, 1978.

- [11] H. Rauch. Wave-particle properties measured by neutron interferometry. *Nucl. Instr. Meth. Phys. Res. A*, 284:156–160, 1989.
- [12] U. Bonse and E. te Kaat. A two-crystal x-ray interferometer. *Z. Phys.*, 214:16, 1968.
- [13] P. Becker and U. Bonse. The skew-symmetric two-crystal x-ray interferometer. *J. Appl. Cryst.*, 7:593, 1974.
- [14] H. Uebbing. *Aufbau und Messungen mit dem Zweikristall-Röntgen-Neutronen- Interferometer*. PhD thesis, University of Dortmund, Dortmund, 1991.
- [15] H. Rauch, H. Lemmel, M. Baron, and R. Loidl. Measurement of a confinement induced neutron phase. *Nature*, 417:630–632, 2002.
- [16] H. Lemmel. *Confinement induced neutron phase*. PhD thesis, TU Wien, Atominstitut, Wien, 2006.
- [17] V. F. Sears. Electromagnetic neutron-atom interactions. *Physics Reports*, 141, 5:281–317, 1986.
- [18] Y. A. Alexandrov, M. Vrana, G.J. Menrique, T.A. Machekhina, and L.N.Sedlakova. *Sov. J. Nucl. Phys.*, 44:900, 1986.
- [19] Yu. A. Alexandrov. Intrinsic charge radius of the neutron: discrepancy between Garching and Dubna results. *Phys. Rev. C*, 49:R2297, 1994.
- [20] L. Koester, W. Waschkowski, L.V.Mitsyna, G.S. Samosvat, P. Prokofjevs, and J. Tambergs. Neutron-electron scattering length and electric polarizability of the neutron derived from cross sections of bismuth and of lead and its isotopes. *Phys. Rev. C*, 51:3363, 1995.
- [21] S. Kopecky, J. A. Harvey, N. W. Hill, M. Krenn, M. Pernicka, P. Riehs, and S. Steiner. Neutron charge radius determined from the energy dependence of the neutron transmission of liquid ^{208}Pb and ^{209}Bi . *Phys. Rev. C*, 56:2229, 1997.
- [22] V. V. Nesvizhevsky, G. Pignol, and K. V. Protasov. Neutron scattering and extra-short-range interactions. *Phys. Rev. D*, 77:034020, 2008.
- [23] M. Baron. *Messung von Quantenzuständen im Neutroneninterferometer*. PhD thesis, TU Wien, Atominstitut, Wien, 2005.

- [24] N. M. Butt, J. Bashir, B. T. M. Willis, and G. Heger. Compilation of temperature factors of cubic elements. *Acta Cryst. A*, 44:396, 1988.
- [25] H. Rauch and D. Petrascheck. *Grundlagen für ein Laue-Neutroneninterferometer - Teil 2*. AIAU 76401, 1976.
- [26] H. Lemmel. Dynamical diffraction of neutrons and the transition from the beam splitter to the phase shifter case. *Phys. Rev. B*, 76:144305, 2007.
- [27] K. Hirano and A. Momose. Investigation of the phase shift in x-ray forward diffraction using an x-ray interferometer. *Phys. Rev. Lett.*, 76:3735, 1996.
- [28] M. Zawisky, M. Baron, and R. Loidl. Three-beam interference and which-way information in neutron interferometry. *Phys. Rev. A*, 66:063608, 2002.
- [29] H. Lemmel. Ifmsim - simulation software for neutron interferometers. 2007.
- [30] M. Zawisky, M. Baron, R. Loidl, and H. Rauch. Testing the worlds largest monolithic perfect crystal neutron interferometer. *Nucl. Instr. Meth. Phys. Res. A*, 481:406, 2002.
- [31] R. Jäger, P. Becker, N. M. Durakbasa., U. Kuetgens, P.H. Osanna, E. Seidl, and M. Zawisky. Optimizing performance of neutron interferometers. *Proceedings of XVI IMEKO World Congress 200*, VIII:127–132, 2000.
- [32] W. Zulehner, D. Huber, R. G. Seidensticker, and R. B. Heimann. *Crystals*. Springer Verlag, 1982.
- [33] D. Windisch and P. Becker. Lattice distortions induced by carbon in silicon. *Philosophical Magazine*, A58:435, 1988.
- [34] P. Becker, U. Bonse, A. Dettmer, F. Dubus, and M. Zawisky. Neutron interferometer with very thin lamellae. *Cryst. Res. Technol.*, 36:589, 2001.
- [35] P.H. Bezirganyan, V. G. Aslanyan, and S. E. Bezirganyan. Interpretation of interference patterns obtained from x-ray laue interferometers in primary plane waves. *Phys. Stat. Sol. (a)*, 110:359, 1988.
- [36] K. C. Litrell, B. E. Allman, and S. A. Werner. Two-wavelength-difference measurement of gravitationally induced quantum interference phases. *Phys. Rev. A*, 56,3:1767, 1997.
- [37] Simon Mayer. Experimente zur Phasenstabilität eines Neutroneninterferometers. Master’s thesis, TU Wien, Atominstitut, Wien, 2003.

- [38] U. Bonse and M. Hart. Moire patterns of atomic planes obtained by x-ray interferometry. *Z. Phys.*, 190:455–467, 1965.
- [39] M. Hart. Review lecture: Ten years of x-ray interferometry. *Proc. R. Soc. Lond.*, 346:1–22, 1975.
- [40] M. Strobl, W. Treimer, C. Ritzoulis, A. G. Wagh, S. Abbas, and I. Manke. The new V12 ultra-small-angle neutron scattering and tomography instrument at the Hahn-Meitner institut. *J. Appl. Cryst.*, 40:463–465, 2007.
- [41] D. A. Pushin, M. Arif, D. L. Jacobson, Changwoo K. Doe, and D. G. Cory. Reciprocal space neutron imaging. *Physica B*, 385-386:1402–1404, 2006.
- [42] D.A. Pushin, M. Arif, M. G. Huber, and D.G. Cory. Measurements of the vertical coherence length in neutron interferometry. *Phys. Rev. Lett.*, 100:250404, 2008.
- [43] Treimer. *Entwicklung eines Neutroneninterferometers*. PhD thesis, TU Wien, Atominstitut, Wien, 1992.
- [44] H. Rauch and U. Bonse. *Neutron interferometry*. Oxford science publications, 1979.
- [45] Atomic institute. Neutron scattering lengths and cross sections. pages 1–10, 2001.
- [46] H. M. Shimizu. Development of neutron optical devices. *Appl. Phys. A*, 74:326–328, 2002.
- [47] S. M. Choi, J. G. Barker, C. J. Glinka, Y. T. Cheng, and P. L. Gammel. Focusing cold neutrons with multiple biconcave lenses for small-angle neutron scattering. *J. Appl. Cryst.*, 33:793–796, 2000.
- [48] T. Adachi, K. Ikeda, T. Oku, K. Sakai, S. Suzuki, J. Suzuki, H. M. Shimizu, K. C. Littrell, C.-K. Loong, W. Lin, J. Guo, N. Mitsuishi, S. Morita, and H. Ohmori. Recent progress in the development of concave Fresnel lenses for neutrons. *J. Appl. Cryst.*, 36:806–808, 2003.
- [49] T. Adachi, T. Oku, S. Morita, H. Ohmori, Y. Takizawa, H. M. Shimizu, C.-K. Loong, K. C. Littrell, and R. Goyette. Development of neutron compound refractive optics: a progress report. *Appl. Phys. A*, 74:180–182, 2002.

- [50] W. M. Gibson, A. J. Schultz, J. W. Richardson, J. M. Carpenter, D. F. R. Mildner, H. H. Chen-Mayer, M. E. Miller, E. R. Maxey, and R. Youngman. Convergent-beam neutron crystallography. *J. Appl. Cryst.*, 37:778–785, 2004.
- [51] T. Oku, S. Morita, S. Moriyasu, Y. Yamagata, H. Ohmori, Y. Takizawa, H.M.Shimizu, T. Hirota, Y. Kiyanagi, T. Ino, M. Furusaka, and J. Suzukui. Development of a Fresnel lens for cold neutrons based on neutron refractive optics. *Nucl. Instr. Meth. Phys. Res. A*, 462:435–441, 2001.
- [52] T. Shinohara, K. Hirota, T. Adachi, K. Ikeda, H. M. Shimizu, J. Suzuki, and T. Oku. Thermal neutron refraction by material prism. *Physica B*, 385-386:1232–1235, 2006.
- [53] T. Shinohara, T. Adachi, K. Ikeda, T. Morishima, K. Hirota, H.M. Shimizu, T. Oku, and J. Suzuki. Development of an optical device for thermal neutrons by amorphous perfluoropolymer. *Nucl. Instr. Meth. Phys. Res. A*, 529:134–137, 2004.
- [54] U. Bonse and M. Hart. *Small-Angle X-Ray scattering*. Gordon and Breach, New York, 1967.
- [55] M. Villa. *Optimiertes Kristalldesign für ein Doppelkristall-Diffraktometer*. PhD thesis, TU Wien, Atominstitut, Wien, 2001.
- [56] H. Rauch and E. Seidl. Neutron interferometry as a new tool in condensed matter research. *Nucl. Instr. Meth. Phys. Res. A*, 255:32, 1987.
- [57] R. Farthofer. Strahlmanipulation mit Prismen im Perfektkristall-Neutroneninterferometer. Master’s thesis, TU Wien, Atominstitut, Wien, 2008.
- [58] M. Deutsch and M.l Hart. Noninterferometric measurement of the x-ray refractive index of beryllium. *Phys. Rev. B*, 30:643, 1984.
- [59] S. Kikuta, I. Ishikawa, K. Kohra, and S. Hoshino. Studies on dynamical diffraction phenomena of neutrons using properties of wave fan. *J. Phys. Soc. Japan*, 39:471, 1975.
- [60] H. Rauch, H. Wöwlitsch, H. Kaiser, R. Clothier, and S.A. Werner. Measurement and characterization of the three-dimensional coherence function in neutron interferometry. *Phys. Rev. A*, 53:902, 1996.

- [61] H. Rauch, H. Wöwlitsch, R. Clothier, H. Kaiser, and S.A. Werner. Time-of-flight neutron interferometry. *Phys. Rev. A*, 46:49, 1992.
- [62] D. L. Jacobson, S. A. Werner, and H. Rauch. Spectral modulation and squeezing at high-order neutron interferences. *Phys. Rev. A*, 49:3196, 1994.
- [63] F. Dubus, U. Bonse, T. Biermann, M. Baron, F. Beckmann, and M. Zawisky. Tomography using monochromatic thermal neutrons with attenuation and phase contrast. *Proceedings of SPIE*, 4503:359–370, 2002.
- [64] M. Zawisky, F. Hameed, E. Dyrnjaja, and J. Springer. Digitized neutron imaging with high spatial resolution at a low power research reactor: I. Analysis of detector performance. *Nucl. Instr. Meth. Phys. Res. A*, A 587:342–349, 2008.
- [65] C. Grünzweig, G. Frei, E. Lehmann, G. Kühne, and C. David. Highly absorbing gadolinium test device to characterize the performance of neutron imaging detector systems. *Rev. Sci. Instrum.*, 78:053708, 2007.
- [66] M. Zawisky, F. Hameed, E. Dyrnjaja, J. Springer, and H. Rohatsch. Digitized neutron imaging with high spatial resolution at a low power research reactor: II. Applications with steel and rock samples. *to be published*.